5-2021

Isomotive dielectrophoresis for enhanced analyses of cell subpopulations.

Mohamed Zakarya Rashed
University of Louisville

ISOMOTIVE DIELECTROPHORESIS FOR ENHANCED ANALYSES OF CELL SUBPOPULATIONS

By
Mohamed Zakarya Rashed
M.Sc. in Nanotechnologies for ICTs, 2014

A Dissertation
Submitted to the Faculty of the
J.B. Speed School of Engineering of the University of Louisville
in Partial Fulfillment of the Requirements
for the Degree of

Doctor of Philosophy
in Electrical Engineering

Electrical and Computer Engineering
University of Louisville
Louisville, Kentucky

May 2021

ISOMOTIVE DIELECTROPHORESIS FOR ENHANCED ANALYSES OF CELL SUBPOPULATIONS

By

Mohamed Zakarya Rashed
M.Sc. in Nanotechnologies for ICTs, 2014

Dissertation approved on

April 30, 2021

by the following dissertation Committee:

Dissertation Director
Stuart J. Williams, PhD.

John F. Naber, PhD,

Cindy K. Harnett, PhD.

Shamus McNamara, PhD.

DEDICATION

For my Dad, Zakarya Rashed & My mom, Sadia Kamal, and Andrey Shchetinin.

ACKNOWLEDGMENTS

First and foremost, I would like to thank God for providing the chance to do this research, giving me the motivation, resources, opportunities, and placing great and helpful people through the course of my graduate studies.

I would like to express my deepest appreciation to my committee chair and mentor, Dr. Stuart J. Williams. His constant scientific advice, personal support, and infinite patience with me were crucial during my graduate studies. Above all, he mentored my growth as a researcher and scientist, pushing me to do things that helped me to develop my skills and I will forever be grateful.

I would like to deeply thank Dr. John Naber for his support throughout my graduate studies, Dr. Cindy Harnett for allowing me to use her lab equipment, and Dr. Shamus McNamara for his guidance in L-Edit and Covontor simulation. Thanks a lot for taking the time to serve as my committee members.

I would also like to sincerely thank Dr. Carlotta Guiducci and Dr. Kevin Keim for hosting me for 5-months internship at CLSE lab (EPFL, Switzerland). I have enjoyed this fruitful collaboration, mentorship, and expertise gained during the course of this internship. Special thanks to everyone else at CLSE lab for having me there as your guest.

I am very grateful to Dr. Michael Menze, Dr. Jonathan Kopechek, and Dr. Susan Hendricks for their biological training, cell supplies and fruitful collaboration that made this work accomplished in the best way. Without you, I would not have accomplished most of this work.

This project would have not been possible without the help of many others who trained me or taught me new techniques, as well as provided a useful piece of equip-

ment. My sincerest gratitude to the MNTC cleanroom staff, Dr. Julia Aebersold, Curtis Mckenna, Evgeniya Moiseeva, Michael Martin, and Jasmin Beharic. Special thanks to Dr. Mark Crain for his fruitful scientific discussions and training me on laser cutter and other tools.

Last but not least, I want to express my profound gratitude to my parents, sisters, and my wife. Thank you for being there for me all the time. I'm indebted for all your sacrifices that paved the way to me to focus on my research while providing me with your love and support.

Special thanks to everyone who I forgot to mention and they have supported me during this graduate studies.

Finally, I would like to acknowledge the financial support that made this work possible including the National Science Foundation under grant, and Swiss National Science Foundation.

ABSTRACT

ISOMOTIVE DIELECTROPHORESIS FOR ENHANCED ANALYSES OF CELL SUBPOPULTIONS

Mohamed Zakarya Rashed

April 27, 2021

As the relentless dream of creating a true lab-on-a-chip device is closer to realization than ever before, which will be enabled through efficient and reliable sample characterization systems. Dielectrophoresis (DEP) is a term used to describe the motion of dielectric particles/ cells, by means of a non-uniform electric field (AC or DC). Cells of different dielectric properties (*i.e.,* size, interior properties, and membrane properties) will act differently under the influence of dielectrophoretic force. Therefore, DEP can be used as a powerful, robust, and flexible tool for cellular manipulation, separation, characterization, and patterning. However, most recent DEP applications focus on trapping, separation, or sorting particles. The true value of DEP lies in its analytical capabilities which can be achieved by utilizing isomotive dielectrophoresis (isoDEP). In isoDEP, the gradient of the electric field-squared (∇E_{rms}^2) is constant, hence, upon the application of electric field, all particles/cells that share the same dielectric properties will feel the same constant dielectrophoretic force *i.e.,* translate through the micro-channel at the same velocity. However, DEP is not the only acting force upon particles inside an isoDEP device, other electrokinetics, including but not limited to electrothermal hydrodynamics, might act on particles simultaneously.

Within this dissertation, electrothermal-based experiments have been conducted to assess the effect of such undesired forces. Also, to maximize the relative DEP force over other forces for a given cell/particle size, design parameters such as microchannel width, height, fabrication materials, lid thickness, and applied electric field must be

properly tuned. In this work, scaling law analyses were developed to derive design rules that relate those tunable parameters to achieve the desired dielectrophoretic force for cell analysis. Initial results indicated that for a particle suspended in 10 mS/m media, if the channel width and height are below 10 particle diameters, the electrothermal-driven flow is reduced by ~ 500 times compared to the 500 μm thick conventional isoDEP device. Also, Replacing glass with silicon as the device's base for an insulative-based isoDEP, reduces the electrothermal induced flow by ~ 20 times.

Within this dissertation, different device designs and fabrication methods were attempted in order to achieve an isoDEP platform that can characterize and differentiate between live and dead phytoplankton cells suspended in the same solution. Unfortunately, unwanted electrokinetics (predicted by the previously mentioned scaling law analysis) prevented comprehensive isoDEP analysis of phytoplankton cells.

Due to isoDEP device limitations and other complications, other techniques were pursued to electrically characterize phytoplankton cells in suspension. An electrochemical-based platform utilizing impedance spectroscopy measurements was used to extract the electrical properties of phytoplankton cells in suspension. Impedance spectroscopy spectra were acquired, and the single-shell model was applied to extract the specific membrane capacitance, cytoplasm permittivity, and conductivity of assumingly spherical cells in suspension utilizing Maxwell's mixture theory of a controlled volume fraction of cells. The impedance of suspensions of algae were measured at different frequencies ranging from 3 kHz to 10 MHz and impedance values were compared to investigate differences between two types of cells by characterizing their change in cytoplasm permittivity and membrane capacitance. Differentiation between a healthy control and nitrogen-depleted cultured algae was attempted. The extracted specific membrane capacitances of *Chlamydomonas* and *Selenastrum* were 15.57 ± 3.62 and 40.64 ± 12.6 mF/m^2 respectively. Successful differentiation based on the specific membrane capacitance of different algae species was achieved. However, no significant

difference was noticed between nitrogen abundant and nitrogen depleted cultures.

To investigate the potential of isoDEP for cell analysis, a comparison to existing dielectrophoresis-based electrokinetic techniques was encouraged, including electrorotation (ROT) microfluidic platforms. The ROT microfluidic chip was used to characterize M17, HEK293, T-lymphocytes, and Hela single cells. Through hands-on experience with ROT, the advantages and disadvantages of this approach and isoDEP are apparent. IsoDEP proves to be a good characterization tool for subpopulation cell analysis with potential higher throughput compared to ROT while maintaining simple fabrication and operation processes.

To emphasize the role of dielectrophoresis in biology, further studies utilizing the 3DEP analytical system were used to determine the electrical properties of *Drosophila melanogaster* (Kc167) cells ectopically expressing Late embryogenesis abundant (LEA) proteins from the anhydrobiotic brine shrimp, *Artemia franciscana*. Dielectrophoretic-based characterization data demonstrates that single expression of two different LEA proteins, *Afr*LEA3m and *Afr*LEA6, both increase cytoplasmic conductivity of Kc167 cells to a similar extend above control values. The extracted DEP data supported previously reported data suggesting that *Afr*LEA3m can interact directly with membranes during water stress. This hypothesis was strengthened using scanning electron microscopy, where cells expressing *Afr*LEA3m were found to retain their spherical morphology during desiccation, while control cells exhibited a larger variety of shapes in the desiccated state.

TABLE OF CONTENTS

LIST OF TABLES

LIST OF FIGURES

CHAPTER I

INTRODUCTION

Motivation

Analysis and manipulation of single particles (or cells) in suspension has a pivotal role in many biomedical applications. Most of these biomedical applications require handling, separation and retrieval of specific cell subpopulation presented in heterogeneous populations. For an efficient biomedical device, such cell manipulation has to be label-free *i.e.,* does not rely on biochemical labels to target specific cell population. This is because label-based applications are expensive and require complex operating protocols. On the other hand, label-free applications depend on the particle's phenotype (eg., particle size and dielectric proprieties).

Dielectrophoresis is a label-free, electrostatic technique that can be used to characterize cell(s) based on its/their response to an induced non-uniform electric field. Unlike electrophoresis, DEP does not require the particle to carry a charge to feel the exerted DEP force. The polarization of a particle with DEP is based, in part, on the interfacial polarization at the interface of the liquid/particle boundary under an applied electric field. DEP is a well-known particle manipulation technique that has been able to capture, sort, concentrate, and characterize a variety of particles and biological entities as small as a few nanometers [2, 3]. DEP has been used to differentiate subpopulations of cells including live and dead bacteria [4] healthy and damaged phytoplankton [5], breast cancer sublines [6], circulating tumor cells from non-transformed cells [7], leukocyte subpopulations (T lymphocytes, B-lymphocytes, granulocytes, monocytes) [8], and blood types [9]. It is important to note that cells manipulated by DEP do not seem to be damaged from exposure to the applied field [10].

The most important characteristic of DEP for particle analysis is that by tracking the magnitude and direction of DEP-manipulated particles over a range of applied AC frequencies, the dielectric properties of the particles can be extracted and subsequently used for cell population identification or analyses. However, The primary disadvantage of current DEP systems is that the applied DEP force is spatially nonuniform, especially in three dimensions, making such cellular sub-population analysis nontrivial. Moreover, 3D electrode fabrication is nontrivial and typically requires complex microfabrication equipment and/or facilities. Other techniques that utilize glass/polymer structures, namely insulator-based DEP [11] and contactless DEP [12], may require large voltages (> 100 V), leading to unwanted electrokinetic effects which may induce device dielectric breakdown or disturb biological samples.

1 Isomotive DEP for Cell Analysis

In traditional DEP systems the force exerted on a particle is spatially non-uniform, typically by orders of magnitude over relatively short distances. For example, using coplanar electrodes the DEP force is greatest close to the surface of the electrodes but exponentially decreases with height above the electrode plane. Consider a 25 µm gap between two coplanar electrodes, the magnitude of the DEP force is approximately 100 times less for a particle 10 µm above the electrode edge compared to a distance of 1 µm [13]. Hence, an analytical DEP system is nontrivial because particles at different locations will be subjected to different DEP forces. To simplify analysis ∇E_{rms}^2 must be constant within the region of interest. Inspired by Pohl's design [14] (Fig. 1.1), Alen et. al [15] developed an Isomotive DEP (isoDEP)-based device for particle characterization.

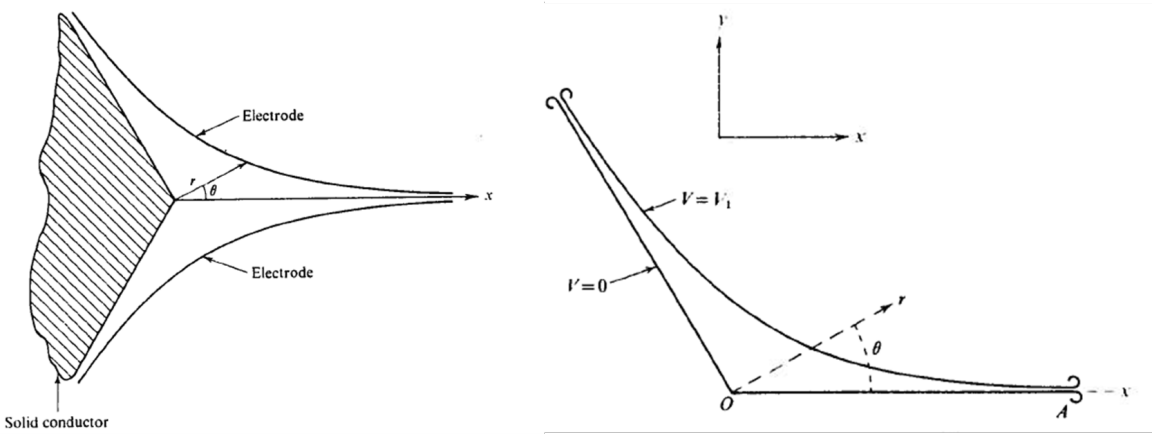

Figure 1.1. Pohl's first isoDEP design demonstration to produce a constant ∇E_{rms}^2 [14].

IsoDEP benefits from of the unique electrodes design such that a uniform DEP force is applied to all particles within the optical viewing area. The electrodes are designed such that the tracked identical particles within the viewing area are feeling the same uniform DEP force exerted upon the application of the electric field. As particle translation is a function of the polarizability of both the particles and suspending medium, the particles' size and shape, and the frequency of the electric field. Hence, it can be a good candidate for cell (particles) analysis. However, other electrokinetics act on the particles simultaneously, including electrothermal hydrodynamics. Hence, to maximize the DEP force relative to over electrokinetic forces, design parameters such as microchannel geometry, fabrication materials, and applied electric field must be properly tuned. Analysis of forces such as electrothermal heating induced forces can be assessed inside the isoDEP device to visualize its effect in order to eliminate its affect in the new designed devices.

The most significant undesired electrohydrodynamic force that occurs in an isoDEP device is derived from electrothermal (ET) hydrodynamics (Fig. 1.2) [16–18]. Therefore, purpose of this manuscript is to develop design rules for the geometrical configuration of an isoDEP system and develop scaling laws [19] to minimize ET flow

relative to isoDEP-induced particle translation for both microelectrode and insulative platforms. These design rules are based on analytical predictions, putting into account how the DEP and ET velocity scale with electrode size, applied voltage, fluid conductivity, and the size of the particles. This approach can be applied to other DEP systems that want to reduce unwanted ET flow. Reducing unwanted electrohydrodynamics enables analytical applications of DEP to electrically characterize cells.

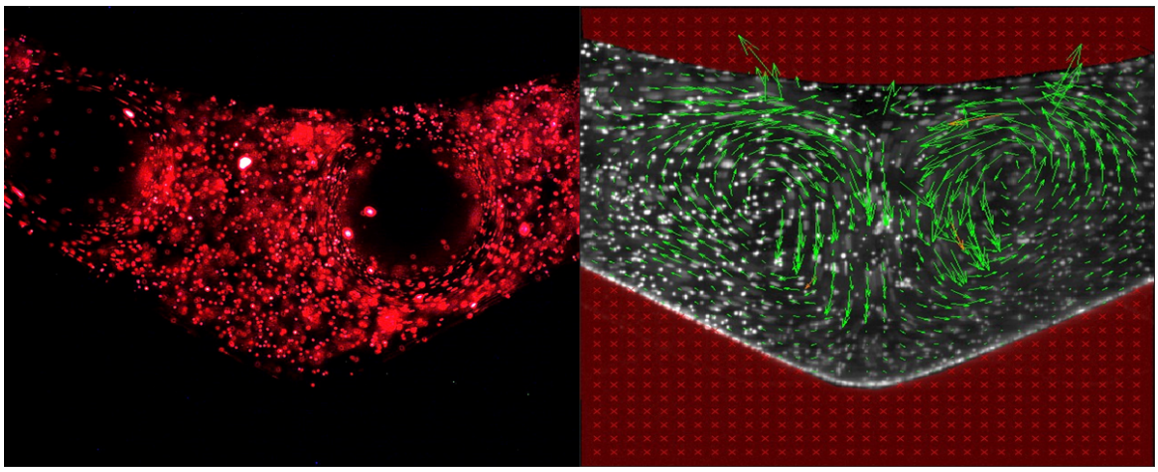

Figure 1.2. (Left) A microscopic image of 2 µm fluorescent particles inside isoDEP device showing formation of bubbles. (right) PIV vector analysis of the isoDEP device demonstrating formation of vortices.

2 Electrical Characterization of Phytoplankton

Phytoplankton are photosynthetic micro-organisms that play an indispensable role as indicators of the health and possible changes in most marine ecosystems. As autotrophs they form the basis of most aquatic food chains, and changes in their population health and productivity can have far reaching impacts [20, 21]. Due to their small size and fast metabolism, phytoplankton are the first to respond to environmental changes and can be used to predict how those changes, such as nutrient concentrations, dissolved oxygen, toxin presence, and even weather changes [20] will affect the wider ecosystem . As a result, they are often used as biosensors of a wide range of pollutants, including herbicides, pesticides, and toxic metals [22].

As the primary producers of most marine ecosystems, phytoplankton populations are a food source for a variety of marine life, from microscopic zooplankton to multiton whales [20]. Small fish and invertebrates feed on phytoplankton, and are then eaten by larger predators [20]. As a result, phytoplankton abundance directly affects the trophic structure of aquatic ecosystem. Phytoplankton population changes can also affect other marine life through "blooms", or periods of explosive population growth. Certain species of phytoplankton produce biotoxins and can cause toxin blooms that can kill marine life and contaminate seafood. Even non-toxic blooms

can be harmful, as the rapid growth and subsequent death depletes nutrients and oxygen, resulting in dead zones.

Electrochemical impedance spectroscopy (EIS) is a nondestructive tool that used to detects cellular response to the application of an AC signal over a frequency range [23]. EIS is a nondestructive, high throughput, characterization tool for studying cell behavior which can be used in sequence with other assays such as staining. EIS has been widely used to measure the dielectric properties of cell suspensions. It has been intensively used to monitor cell culture health, metabolism, viability, and proliferation (Fig. 1.3 [24, 25].

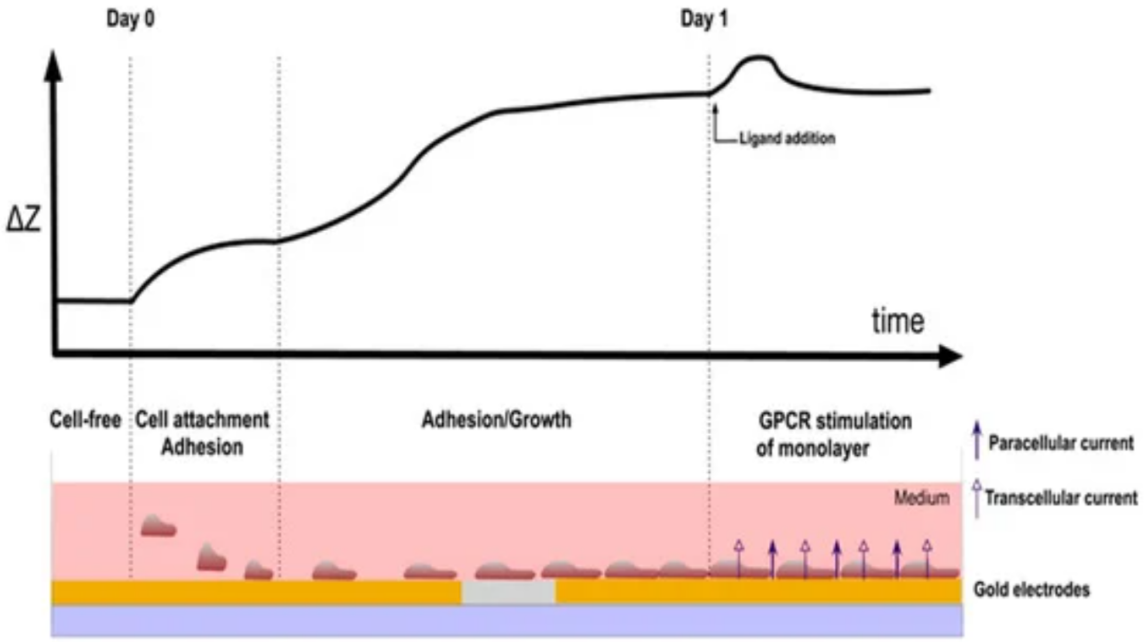

Figure 1.3. Illustration for the EIS-based assay for the detection of cell adhesion and growth. Reproduced from [1].

The purpose of analyzing the EIS data is to derive and characterize a load's (*i.e.,* cell suspension) electrical parameters and, although it doesn't directly measure physical phenomena, it is a reliable and sensitive technique [23]. To interpret impedance spectroscopy, a physio-chemical or measurement model must be used. Measurement modeling involves building a model using mathematical functions to explain the experimental impedance using a best fit method [23]. This method involves using good biological knowledge for cells in suspension in order to model their experimental data using equivalent circuit elements, such as resistors, capacitors, and inductors. The equivalent circuit method is simple and straightforward, but lacks high accuracy, which can cause inconsistency and degeneracy [26]. Physio-chemical modeling links the measured impedances and the measurement model to physio-chemical parameters of the process which provides higher accuracy than simply using an equivalent circuit, but obtaining the modeling parameters is highly complex and can lead to over-parameterization [26]. Once the circuit model is established, it can then be

used to track changes in electrical properties of a sample under test which indicate physiological changes inside the sample.

3 Investigating The Role of Late Embryogenesis abundant (LEA) Proteins

Anhydrobiosis, or "life without water," is a remarkable state of life where an organism has lost virtually all cellular water but is able to resume its life cycle upon rehydration. Understanding the molecular mechanism governing anhydrobiosis may lead to profound advances in engineering crop-desiccation tolerance and the ability to store biomedical relevant cell and tissue samples in the desiccated state as alternative to cryopreservation. Anhydrobiosis-related intrinsically disordered (ARID) proteins are found in all known anhydrobiotic species, spanning all domains of life, and have been linked to the successful entry and exit from anhydrobiosis, but the molecular mechanisms that lead to an increase in desiccation tolerance remain enigmatic.

The ability to enter and exit anhydrobiosis relies on an array of molecular mechanisms designed to repair and protect various cellular structures and macromolecules (*e.g.,* DNA, RNA, proteins, membranes, etc). Common anhydrobiotic strategies observed in animals include the accumulation of protective osmolytes, particularly trehalose, as well as the expression of a variety of ARID proteins, including late embryogenesis abundant (LEA) proteins [27, 28]. LEA proteins were originally discovered in plants, and predominantly occur in the late embryogenesis stage of anhydrobiotic seeds but were later also found in other plant tissues and in anhydrobiotic animals [29]. Several sequence-based grouping methods for LEA proteins have been described and this work will adapt the grouping scheme proposed by Tunnacliffe and Wise as a means to classify and organize groups of LEA proteins [30].

DEP is a very good candidate that can be used to gain insights into the molecular mechanisms of protection during water stress conferred by AfrLEA3m and AfrLEA6; two ARID proteins from the anhydrobiotic brine shrimp, *Artemia franciscana*.

Research Objectives

The proposed work herein entails the design, fabrication, characterization, and application of various microfluidic electrokinetic or field-based analytical platforms including electrode and insulator-based isoDEP devices, other DEP configurations, or electrode-based impedance spectroscopy systems. The design and fabrication of the isoDEP devices were based on the investigation and assessment of electrokinetic forces in an isoDEP analytical system to enhance its operation as well as maximize the DEP force relative to other unwanted electrokinetic forces by introducing design parameters for a specific isoDEP device. The isoDEP devices were then used to characterize and differentiate phytoplankton cell species that have been cultured in two different culturing environments with controlled nitrogen abundance. To operate the platform at high frequencies ($>$ 10 MHz), custom-built amplifier is designed to ensure high amplification at higher frequencies as well as, facilitating the portability of the platform. The isoDEP operation and performance was compared to other DEP plat-

forms including a commercially available system (Labtech International, East Sussex, UK). Also, further cell characterization techniques such as electrorotation (ROT) and electrochemical-based platforms were investigated. The specific objectives include:

1. Design, fabricate, and optimize the isoDEP chip/platform
2. Assess electrohydrodynamic forces that hinder the operation of an isoDEP device in order to maximize the DEP force
3. Characterize and differentiate between healthy and non-healthy phytoplankton cell species
4. Compare the contrast isoDEP device with electrorotation (ROT), electrochemical-based cell characterization techniques, and 3DEP (Labtech International, East Sussex, UK)
5. Utilize DEP-based technique to investigate the role of late embryogenesis abundant (LEA) proteins roles in desiccation tolerance in AfrLEA3m and AfrLEA6; two ARID proteins from the anhydrobiotic brine shrimp, *Artemia franciscana*

Table B.1 (Appendix B) lists the specific aims and their respective tasks with the current status of each task.

Dissertation Structure

This dissertation is organized in six chapters where Chapter 2 presents relevant DEP background including isoDEP for particle manipulation and its role in biomedical application as a tool for cell characterization with a review of theory and fabrication methods for several applications. Chapter 3 introduces the fabrication methods to achieve an isoDEP device. Additionally, complications and challenges in those fabrication processes are discussed. An assessment for electrothermal hydrodynamic forces within isoDEP device operation are investigated and, scaling law analysis and design parameters are developed for isoDEP device are derived to maximize the DEP force over these unwanted effects. Chapter 4 introduces two alternative characterization techniques for cell analysis. First part introduces impedance spectroscopy as a tool to differentiate between phytoplankton cells cultured in different nitrogen abundant environment. The underlying theory and equivalent circuit modeling that was utilized to extract cell parameters is described. The second part of the chapter discusses the role of electrorotation in characterization of M17, HEK293, T-lymphocytes cells. At the end of the chapter, a comparison between the resolution of each characterization techniques are compared with isoDEP device. Chapter 5 discusses the utilization of dielectrophoresis-based characterization platform for investigating the role of LEA proteins in desiccation tolerance in *Artemia franciscana* KC167 shrimp cells. Within this chapter, the validation of the dielectrophoresis-based platform was deliberated by comparing a confocal microscopy. Chapter 6 provides a concluding statement of the novel findings and limitations of isoDEP platform, in addition to a brief description of the future work that can proceed from this project.

CHAPTER II

ISOMOTIVE DIELECTROPHORESIS FOR PARTICLE ANALYSIS

This chapter discusses the theory of dielectrophoresis, isomotive dielectrophoresis as well as the advances in the field up to date. Some content (section 2) of this chapter is adapted from published work [31]

Introduction

The first integrated silicon chip was demonstrated over 60 years ago by scientists at Texas Instruments [32], who were able to miniaturize bulk electronic components such as transistors into a microscopic version that can be integrated in large numbers to achieve more complex calculations. Later on, researchers from other practices believed they can follow the same miniaturization trend to achieve patch and low cost fabrication [33]. Mechanical devices proved to be promising tools for chemical analysis and synthesis thanks to the obvious advantages of miniaturization of portability, lower cost consumption, shorter response time, less pollution, better process control etc.This trend, working hand in hand with development of lithography based micro- and nano-technology, revolutionized the field of multiple laboratories per chip or Lab-on-a-chip (LOC), which is also refereed to as Micro-total analysis system as well (μTAS).Research in LOC systems is extended towards fluid, droplet, and nanoparticles as well as proteins, DNA and virus [34–36]. One advantage of the LOC applications, the ability to effectively, dynamically and accurately manipulate and separate micro- and nano-scale particles in an aqueous solution is quite appealing in chemical, medical and biological fields. Among the technologies that have been developed and implemented in microfluidic microsystems for particle manipulation and separation, such as (I) mechanical manipulation of bioparticles (*i.e.,* plasma [37], blood cells [38], and circulating tumor cells [39]) based on size has been achieved by fabricating constriction structures within the microchannel (*i.e.,* pillar [40] , weir [41], and through-holes [42]). Despite several advantages these filter-based microfluidic devices have such as reproducibility and high labeling efficiency, there are many challenges including clogging, the heterogeneity of cell sizes within a population, fouling, and limited selectivity for biological assays. (II) acoustophoresis which is based on the concept that particles suspended in fluid experience an acoustic radiation force when they are exposed to an ultrasound. There are several applications regarding that combine laminar flow with an ultrasonic standing wave field with to separate yeast cells [43], blood cells [44] different-sized particles [45–48]. (III) optical trapping including optical tweezers and advanced techniques such as Rapid Electrokinetic Patterning (REP) [36] could tether biological molecules and particles in sub-micron

domain, which have been widely used as a tool for the manipulation and trapping of particles [49–52], however, its application in microfluidics is still limited due to the expensive instrumentation, complex operation,and complicated setup. (IV) hydrodynamic technique which presumes that at a low Reynolds number, particles will follow fluid streamlines, which has been applied within microchannels having micro-obstacle arrays, multiple side branch channels, or a pinched segment. Separation of blood plasma from the blood cells, malignant lymphocytes from healthy lymphocytes, different-sized polystyrene particles [53–58]. (V) magnetophoresis which is a label-based and passive method that is achieved by selectively bonding cells with magnetic beads, and then separating them by applying a magnetic field, in addition, the intrinsic magnetophoretic properties of particles or cells have been employed for separation and purification of living cells , red and white blood cells from whole blood [59–65]. (VI) Coulomb force and dielectrophoretic force, have been used to manipulate particles. A Coulomb force is responsible for induced movement of the charged particle generated by the interaction between the net charge on the particle and the applied electric field, this induced translation of the particle is known as electrophoresis (EP). Several the biological applications of EP have been well studied and demonstrated [66–69], However, for biological particles that are electrically neutral, EP may not applicable due to the absence of net charge.

Dielectrophoresis (DEP) force that arises from the interaction between the particle's dipole and a nonuniform electric field, can be used to manipulate neutral particles. DEP has attracted most attention due to its great advantages may prove to be the most popular method, because of its label-free nature. Unlike other techniques, DEP depends on the dielectric properties, which represent the structural, morphological, and chemical characteristics of bio-particles, allowing highly selective and sensitive analysis. DEP manipulation is straightforward and fully controllable by varying the frequency and magnitude of the applied electric field or the electric conductivity of the suspending medium. DEP is also easily and directly interfaced to conventional electronics, and can be used in the fabrication of LOC devices.In addition, DEP enables contact-free manipulation of particles with lower sample consumption and fast speed. DEP, first adopted by Pohl [70], is the translation of a polarizable particle when subjected to a non-uniform electric field. Hence, one requirement for the DEP force to be induced is the non-uniform electric field generated within the microfluidic device. Non-uniform electric field can either be generated by means of (i) insulator structures or (ii) by specially designed microelectrode arrays. Both the suspending medium and the dielectric particle become electrically polarized in an electric field, which separates the electric charge at the interface between liquid and solid. Depending on the relative polarizability of the suspending medium and particle, a net dielectrophoretic force will either repel the particle towards the region of lower electric field gradient (negative DEP) Fig. 2.1B, or attract the particle towards the region of higher electric field gradient (positive DEP) Fig. 2.1C. The frequency at which this transition occurs (*i.e.,* the frequency at which DEP force becomes zero) is called the cross-over frequency (COF).

One of the important applications of DEP is the selective separation of bio-

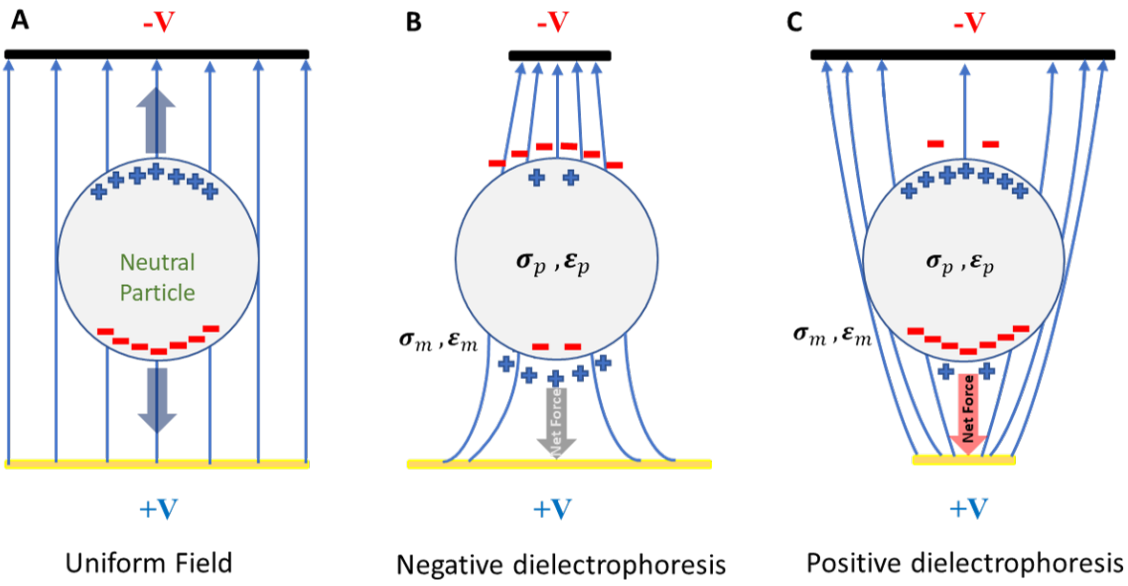

Figure 2.1. A schematic showing the difference between a particle suspended within a parallel plate and a point-plane electrode system. When the particle polarizes, the interaction between the dipolar charges with the local electric field produces a force. (A) No net forces. (B) Negative DEP net force (nDEP). (C) Positive DEP net force (pDEP).

particles, since DEP depends on the bio-particles' intrinsic electrical properties, electrokinetic manipulation techniques do not require any labeling. As mentioned previously, dielectric properties of a bio-particle depend on the morphology and chemical composition of the internal matrix of the bio-particle. Therefore, each bio-particle has its own dielectric signature that has been demonstrated for a variety of cells [71] Pohl. 1975, was the first to carryout the separation of viable and non-viable yeast cells, later he extended the experiments to separate other biological particles including red blood cells, canine thrombocytes, bacteria etc. By utilizing microelectrodes array design, Becker group, [72], performed a separation of human breast cancerous cells from normal blood cells utilizing the flow separation method. That is, a flow is used to carry two types of different cells in a microchannel. One type of cells is trapped on the electrode arrays located at the bottom of the channel, and the other type would be brought out of channel by the flow. The disadvantage of this strategy is the cell adherence to the electrodes need to be collected after the separation, Therefore, strategies combining the separating and collecting processes are of interest recently. Yang, et al. [73], performed the separation of human breast cells mixture with blood cells utilizing dielectrophoretic-field flow fractionation (DEP-FFF), which benefits from the velocity gradient in the flow profile to achieve a high selective separation. DED-FFF is another strategy in which a carrier flow is introduced with different speeds at different heights from the bottom surface. Cells are repelled from the electrodes under a negative DEP force. The cells with different dielectric properties would be found at different heights and therefore travel at different speeds with the

flow. However, the cells probably enter the channel with a Gaussian-shaped distribution which may cause overlap between the sub-populations of cells after separation.. Gascoyne's group managed to separate various cancerous cells from blood cells and normal murine erythrocytes from erythroleukemia cells and measured their dielectric properties by changing the frequency of the applied electric field till it reaches the COF of either of the cells [74]. Successful Separation of a mixture of bacteria was such as *Bacillus subtilis E. coli bacteria*, and *Micrococcus luteus* was performed by Markxa group [75]. Morgan, et al. [34] [76], demonstrated a separation of erythrocyte and leukocyte cells utilizing traveling wave DEP (TW-DEP), which is another recent and popular strategy in which electric fields rather than flow is used to give the cells a mean longitudinal velocity. Several applied electric fields are applied with continuous phase shift to give particles DEP forces in both vertical and horizontal directions.
The applications of DEP are very much to mention in one article, Moreover, a lot of research has been done in DEP manipulation of a variety of subimcron- and nanoparticles [77–79], proteins [80], DNA [81, 82] deoxyribonucleic acid [81], viruses [78], stem cells [83, 84], cancerous cells [85]. Recently DEP has been used to develop the fabrication of electronics by separation between metallic and semi-conducting single walled nanotubes (SWNTs) [86]. Metallic SWNTs are deposited to create thin film [87] while semiconducting SWNTs were used to fabricate electric transistors [88]. Relevant discussions about DEP and its application can be found explicitly in these literature reviews [89–98]. Although there are distinct advantages in using DEP to manipulate, concentrate, and sort particles, most of these applications did not fully utilize the analytical capabilities of DEP to measure particle's frequency-dependent response to the applied field. Hence, particle's phenotype can be concluded with higher throughput relative to existing techniques which perform extensive cell analysis. Such capabilities have been utilized by Allen, et al. [15], through electrokinetic analysis detailed dielectric measurements of individual cells is possible such that (i) cell sub-populations can be identified and/or (ii) variants within a cell population can be measured. Other merging commercially available analytical DEP systems of 3DEP (Labtech International, East Sussex, UK) and ApoStream (ApoCell, Houston, TX) verify such advantages and capabilities. The proposed work herein describes assessment of electrokinetic forces in an isoDEP analytical system to enhance its operation as well as maximize the DEP force relative to other unwanted electrokinetic forces by introducing design parameters for a specific isoDEP device. However, a fundamental understanding of DEP theory and other electrokinetic mechanisms is needed in order to provide a proper comparison of the isomotive dielectrophoresis (isoDEP) device [15] with existing techniques as well as develop the scaling law analysis for the isoDEP device.

Theoretical preliminaries

A brief derivation of the dielectrophoretic force analysis with a spherical homogeneous particle will be discussed here. Both the suspending medium and the particle are considered to be dielectrics, that is, materials that contain charges, which polarize

under the application of an external electric field. Because of the polarization of the particle and the medium are different, the surface charge at the interface between two dielectric materials is frequency dependent. A process known as Maxwell-Wagner (MW) interfacial polarization [99] explains the frequency dependent behavior of such systems.

For materials such as a biological or polymeric microparticles, this polarization largely involves the contribution of two charging components: (i) conductive component represented by the physical movement of free charges and (ii) dielectric displacement component represented by the field-induced perturbation of bound charges. Physically, surface charges induced at a particle interface are composed of free (conductive) and bound (dielectric) charges. Hence, this dual-charging behavior can be modeled by considering the material as a lossy dielectric, that is a material that has both a permittivity (ϵ) and conductivity (σ) The total current through this material is the same as if it were replaced with an equivalent electrical circuit comprised of a loss-free capacitor in parallel with a resistor,and is given by the sum of the current, I, through the capacitor (I_C) and the resistor (I_R) at a harmonic field with an angular frequency ω ($\partial/\partial t = i\omega$) [100] as

$$I = I_R + I_C = \frac{V}{R} + C\frac{\mathrm{d}V}{\mathrm{d}t} = V\frac{A}{d}(\sigma + i\omega\epsilon) \tag{2.1}$$

where V is the voltage drop across the circuit, $i^2 = -1$, $\omega = 2\pi f$ is the angular frequency of the AC electric field, where f is the ordinary frequency given in Hz, and $R = (1/\sigma)(d/A)$ and $C = \epsilon\frac{A}{d}$ are the resistance and the capacitance of the material, and A and $d$are the area and separation of the capacitor plates respectively. We can then write I as

$$I = \frac{i\omega A}{d}\left(\epsilon - \frac{i\sigma}{\omega}\right) \times V = \frac{i\omega A\epsilon^*}{d}V \tag{2.2}$$

Hence the relationship between the applied voltage and the experimentally observed current I is governed by the material's complex permittivity, ϵ^*, defined as

$$\epsilon^* = \epsilon - \frac{i\sigma}{\omega} \tag{2.3}$$

As we can see from Eq.(2.3), low frequency polarization is dictated by electrical conductivity. However, as electrical conduction involves the macroscopic movement of charge carriers (typically ions), there is a finite velocity at which ions can be conducted across the material. At high frequency, when ion conduction does not have time to occur, the polarization is driven by permittivity. The complex permittivity models the polarizable material as the electric equivalent to a resistor in parallel with a capacitor, which captures both low frequency conductive and high frequency dielectric charging mechanisms. AC frequencies between these two extremes are the key point of most DEP separation applications due to the different COF values attributed to different cellular dielectrophoretic behaviors. When an external electric field is

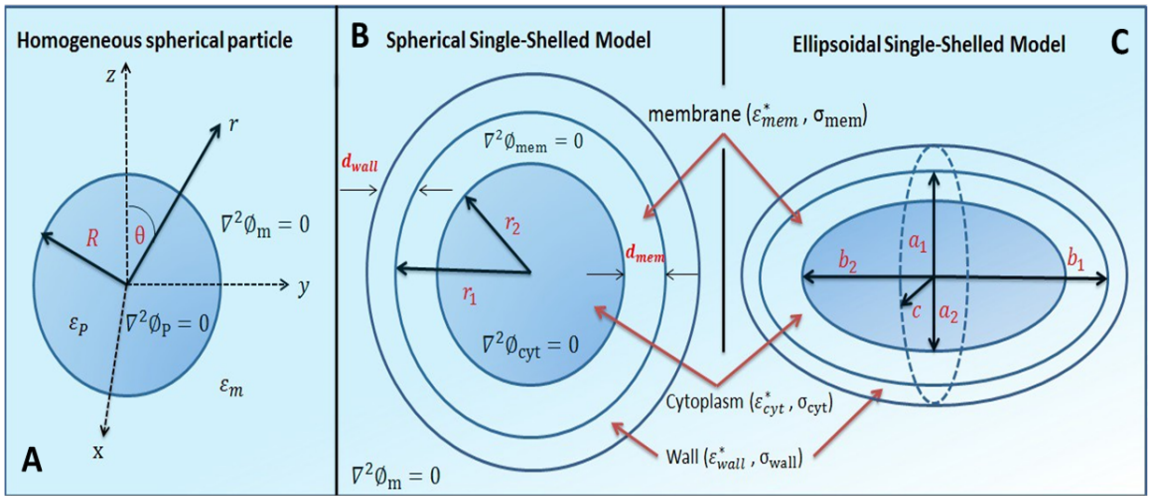

Figure 2.2. Schematic representation of different models used for derivation of the field induced dipole moment (P) used to derive the DEP force. (A) Homogeneous spherical particle ,f_{DEP}. (B) A single-shelled sphere showing a core (Cytoplasm) and outer shell (plasma membrane), with radii r_1, r_2, and membrane thickness. (c) Single-shelled ellipsoidal model for various cells with semi-axes $a > b > c$.

applied, charge of opposite sign accumulates at either side of the particle interface and forms an induced dipole around the particle.The induced dipole strength and direction depends upon the frequency and magnitude of the applied electric field, and on the electrical properties of both the the suspending medium and the particle. To determine the DEP force on the particle, we first have to calculate the particle-induced dipole moment which can be modeled using the simple well-known effective dipole method [99].

1.1 Effective dipole method and DEP force derivation

First, a spherical isotropic homogeneous particle, suspended in an electrolyte medium, with its center at the origin, is exposed to an electric field E. Hence, the problem becomes axially symmetric and 2-D in spherical polar coordinates. The field is assumed uniform far from the origin, and the potential both inside the particle (ϕ_P) and outside the particle (ϕ_m) can be calculated by solving the Laplace equation for each region (Fig. 2.2A). The Laplace operator in spherical coordinates is given by

$$\nabla^2 = \frac{1}{r}\frac{\partial}{\partial r}\left(r^2\frac{\partial}{\partial r}\right) + \frac{1}{r^2\sin\theta}\frac{\partial}{\partial\theta}\left(\sin\theta\frac{\partial}{\partial\theta}\right) + \frac{1}{r^2\sin^2\theta}\frac{\partial^2}{\partial\phi^2} \tag{2.4}$$

where r, θ and ϕ are the radial, polar and azimuthal coordinate variables. Due to polar axial symmetry, the azimuthal term in Eq.(2.4) is zero, and solutions ϕ_p and ϕ_m are given by

$$\phi_p = Br\cos\theta - Er\cos\theta \quad \text{for} \quad r \leq R \tag{2.5}$$

$$\phi_m = \frac{A}{r^2}\cos\theta - Er\cos\theta \quad \text{for} \quad r \geq R \tag{2.6}$$

where R is the particle radius. The constants A and B are determined by the appropriate boundary conditions at the particle–medium interface. First, we require the potential to be continuous across the interface

$$\phi_m - \phi_p = 0 \quad \text{at} \quad r = R. \tag{2.7}$$

Second, to satisfy charge conservation across the interface, its required to satisfy

$$J_m - J_p + \frac{\partial \sigma_f}{\partial t} = 0 \quad \text{at} \quad r = R. \tag{2.8}$$

recalling Ohm's law, $J_P = \sigma_p E_P$ and $J_m = \sigma_m E_m$ are the normal ohmic current inside and outside the particle. Physically, the ohmic current describes the conductive charging component from mobile charge being driven to the interface by the electric field.The field-driven induced displacement of the free unpaired surface charges due to the dielectric polarization,is represented by σ_f. The displacement current due to these charges is

$$\epsilon_p E_p - \epsilon_m E_m = \sigma_f \quad \text{at} \quad r = R. \tag{2.9}$$

Hence, the total current (conduction + displacement) at the interface,can be calculated by combining Eq.(2.8) and Eq.(2.9) to be

$$\epsilon_p^* E_p \frac{\mathrm{d}\phi_p}{\mathrm{d}n} - \epsilon_m^* \frac{\mathrm{d}\phi_m}{\mathrm{d}n} \quad \text{at} \quad r = R. \tag{2.10}$$

Physically, Eq.(2.10) describes how the normal component of the electric field, $\frac{\mathrm{d}\phi_p}{\mathrm{d}n}$, at the particle surface changes such that $\epsilon_i \frac{\mathrm{d}\phi_p}{\mathrm{d}n}$ remains continuous across the interface. Employing boundary conditions given by Eq.(2.7)and Eq.(2.10) with Eq.(2.5) and (2.6), the solution coefficients A and B are then

$$A = \frac{\epsilon_p^* - \epsilon_m^*}{\epsilon_p^* + 2\epsilon_m^*} R^3 E \quad \text{and} \quad B = \frac{3\epsilon_p^*}{\epsilon_p^* + 2\epsilon_m^*}. \tag{2.11}$$

The medium potential function Eq.(2.5) is thus given as

$$\phi_m = -\left(\frac{\epsilon_p^* - \epsilon_m^*}{\epsilon_p^* + 2\epsilon_m^*}\right) Er\cos\theta + Er\cos\theta \tag{2.12}$$

As we can see, Eq.(2.12) is the linear sum of the electrostatic potential due to the induced external field (Er $\cos\theta$) (second term) and electric dipole (first term). The first term is the potential generated outside a lossy dielectric sphere, polarized by an imposed field E. Here, due to the imposed polar symmetry, the electric dipole term in Eq.(2.12) is physically identical to the potential produced by a finite two-point dipole, that is, two point charges ($+q$ and $-q$) separated by a distance vector $\mathbf{d}$. The electric potential due to such a two-point dipole, ϕ_{dipole}, with an effective dipole

moment $\mathbf{P}$ in a dielectric medium of permittivity ϵ_m can be derived from Coulomb's law and given as [99]

$$\phi_{\text{dipole}} = \frac{p\cos\theta}{4\pi\epsilon_m r^2} \tag{2.13}$$

Comparing the induced dipole term in Eq.(2.13) to Eq.(2.12), the effective field induced dipole moment of the particle is

$$\mathbf{P} = 4\pi\epsilon_L R^3 \left(\frac{\epsilon_p^* - \epsilon_m^*}{\epsilon_p^* + 2\epsilon_m^*}\right) E = 4\pi\epsilon_m R^3 (f_{\text{cm}}) E \tag{2.14}$$

where f_{cm} is the *Clausius-Mossotti* (CM) factor which provides a measure the effective polarization strength.

$$f_{\text{cm}} = \left(\frac{\epsilon_p^* - \epsilon_m^*}{\epsilon_p^* + 2\epsilon_m^*}\right) \tag{2.15}$$

By summing all the electric forces acting on the positive and negative charges constituting the dipole moment, p, the net DEP force acting on the particle can be obtained. If the field is uniform, the total force on the particle will be zero, as the electric force on the two charges ($+q$ and $-q$) will completely cancel one another. However, If the electric field is nonuniform, the two charges will experience different values of the imposed electric field, and the induced dipole will experience a net force, and this the main mechanism of DEP technique.

An important key assumption that the induced dipole moment is small compared to the length scale of the electric field non-uniformity. Physically, this occurs when the particle radius is much smaller than the characteristic separation length of the applied voltage (*i.e.,* the electrode separation length).If this is valid, then the force on such a small dipole is [99]

$$f_{\text{DEP}} = p \cdot \nabla E \tag{2.16}$$

Employing an exponential time dependence $e^{j\omega t}$ for the electric field, the instantaneous applied field at time t and location r is given by

$$E(r,t) = Re[E(r)e^{j\omega t}], \tag{2.17}$$

where $i^2 = -1$ and Re[...] is the real part of the complex phasor $E = E\cos\omega t + iE\sin\omega t$. By using this notation, we are essentially accounting for contributions from both the magnitude and the phase of the electric field to the induced dipole moment, as the field is moving sinusoidally in time. Combining Eq.(2.14) and Eq.(2.17), and taking the time-average, we obtain the well-known time-averaged DEP force for a lossy spherical particle

$$\langle f_{\text{DEP}} \rangle = 2\pi\epsilon_m R^3 Re[f_{\text{cm}}] \nabla |E|^2 \tag{2.18}$$

Equation 2.18, is a dipole approximation and higher order multipole terms are neglected, multipoles should be incorporated for systems where the length scale of the electrode geometry is on the order of the particle size being manipulated [101], which

is not the scope of this work. It also assumes a stationary field; however, if there is a spatial non-uniformity in the electric field's phase ψ, the extended DEP force is given by

$$\langle f_{\mathrm{DEP}} \rangle = 2\pi\epsilon_m R^3 Re[f_{\mathrm{cm}}]\nabla|E|^2 + 4\pi\epsilon_m R^3 Im[f_{\mathrm{cm}}](E_x^2\nabla\psi_x + E_y^2\nabla\psi_y + E_z^2\nabla\psi_z) \quad (2.19)$$

The second term in Eq.(2.19) is dependent on the imaginary part of the Clausius-Mossotti factor and the spatial non-uniformity of the field's phase. In particular, a rotating field will induce particle rotation, which electrorotation (ROT) technique is based on. As discussed earlier, the total charging current contains elements of both macroscopic movement of free charge (conductive polarization) and displacement of bound charge (dielectric polarization) at the particle−medium interface. The net direction and magnitude of the induced dipole moment, and the resulting DEP force, depends upon these two charging mechanisms, which are captured in the frequency dependent CM factor, f_{cm}. Where $Re[f_{\mathrm{cm}}]$ value is between +1 and -0.5 (Fig .2.3 Left). When f_{cm} is positive, the induced DEP force displaces the particle up the field gradient towards regions of high electric field intensity, known as positive DEP (pDEP). If f_{cm} is negative, the particle will be displaced down the field gradient into regions of low field intensity, known as negative DEP (nDEP). The frequency where the CM factor equals zero is known as the COF, which, as we shall see, provides a very useful way to experimentally characterize cells using DEP.As conductive polarization involves ion migration, it is limited by the speed at which ions can electro-migrate to the particle interface. Typically, the mobile ions take a few microseconds to reach equilibrium, and at low frequency they can keep pace with the changing field. However, at a high enough frequency, the charges will not have enough time to respond. Dielectric polarization, on the other hand, involves relatively fast charge segregation at the molecular level. Consequently, conductive polarization is favored at low frequency below the characteristic inverse MW relaxation timescale, $1/\tau_{MW}$,

$$\frac{1}{\tau_{MW}} = \frac{1}{2\pi}\left(\frac{\sigma_p + 2\sigma_m}{\epsilon_p + 2\epsilon_m}\right) \quad \sim \quad \mathrm{COF} \quad (2.20)$$

while dielectric polarization dominates at high AC frequency. The COF separates these two distinct, and often competing, polarization mechanisms where dielectric polarization begins to overtake conductive charging, a phenomenon known as *dispersion*. A particle with a greater conductivity ($\sigma_p < \sigma_m$) and lower permittivity ($\epsilon_p < \epsilon_m$) than the suspending media. Below the COF, charge will be driven to the particle interface via conductive polarization. In this case, because the particle is more conductive than the media, more charge will build up just inside the particle interface than outside, and in a non-uniform electric field, the particle will be displaced to the high field region (pDEP). If the frequency is increased such that it exceeds ∼O(1/tMW), the free charge will no longer have enough time to respond. As such, the induced dipole magnitude and direction will be driven by the polarization of bound charge. Because the particle permittivity is less than the media, more charge will begin to accumulate just outside the particle interface, and if placed in a non-uniform field, the particle will now be driven to regions of low field intensity (nDEP).

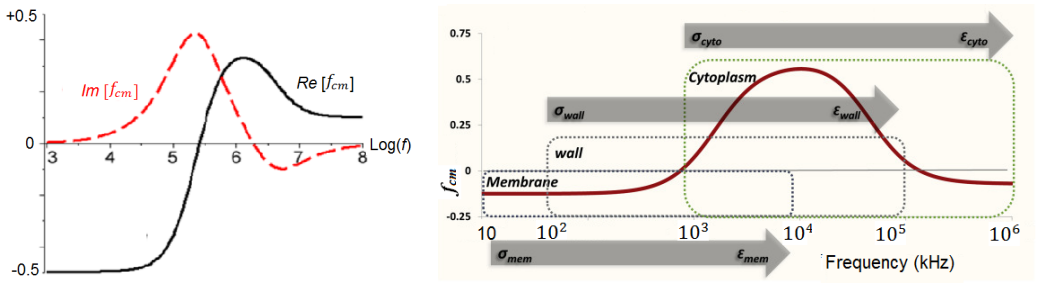

Figure 2.3. Schematic representation of the Clausius-Mossotti factor (f_{cm}): (*Left*) using a homogeneous spherical particle model. (*Right*) using two-shell dielectric model, indicating regions wherein each sub-cellular phenotype dominates. (Right) reproduced with permission from [102]

1.2 DEP-shell model

The CM factor given in Eq.(2.14) is valid only for homogeneous spherical particles. Biological particles, however, are often complex, non-spherical, heterogeneous structures with a cell membrane, cytoplasm and internal organelles, each possessing their own distinct electrical properties. When working with biological particles of this nature, the DEP model must be modified to account for these differences. The above theoretical approach can be expanded to account for differences in cell shape and the presence of a cell membrane and internal cell structures. Irimajiri, et al.[103], developed this "multi-shell" model by considering each structure (cell membrane, cytoplasm, nucleus, etc.), Fig. 2.2b, as a homogeneous particle suspended in medium, with the medium itself modeled as the layer surrounding it. In this process, each layer in the cellular domain is modeled as an individual electrical shell. As mentioned earlier, the effective dipole method is again applied to the multi-shell domains. As shown in Fig. 2.2b, the cell membrane introduces a second interface that can undergo MW polarization and produce an additional dipole moment. As such, biological particles commonly have at least two MW relaxation processes, which, as expected, can often lead to at least two crossover frequencies. The single-shell model is developed by first considering the electrostatic potential in each of three domains: the cytoplasm, the cell membrane and the suspending media. Assuming each domain is satisfied by the Laplace equation, and employing the same boundary conditions given in Eqs.(2.7) and (2.10) for each of the two interfaces, we can solve for the induced electrostatic potential in each domain. However, in this case two interfaces are considered: the cell membrane–medium and the cytoplasm–membrane, and each one must be considered separately. The new expression for the DEP force on a single-shelled lossy spherical particle is given by

$$\langle f_{\mathrm{DEP}} \rangle = 2\pi\epsilon_m R^3 Re\left(\frac{\epsilon^*_{eff} - \epsilon^*_m}{\epsilon^*_{eff} + 2\epsilon^*_m}\right)\nabla|E|^2, \tag{2.21}$$

where an effective complex permittivity of the shelled particle ϵ^*_{eff} replaces ϵ_p in the CM factor given in Eq.(4.15). Hence, the electric potential outside the layered

particle is identical from that of a homogeneous sphere. The charging characteristics of both interfaces are therefore captured in the effective complex permittivity term ϵ^*_{eff} , given as [99, 100],

$$\epsilon^*_{eff} = \epsilon^*_m \frac{\left(\frac{r_2}{r_1}\right)^3 + 2\frac{\epsilon^*_{cyt}-\epsilon^*_{mem}}{\epsilon^*_{cyt}-2\epsilon^*_{mem}}}{\left(\frac{r_2}{r_1}\right)^3 + \frac{\epsilon^*_{cyt}-\epsilon^*_{mem}}{\epsilon^*_{cyt}+2\epsilon^*_{mem}}} \tag{2.22}$$

where ϵ^*_{mem} and ϵ^*_{cyt} are the complex permittivity of the cell membrane and cytoplasm, respectively, r_1 and r_2 are the inner and outer cell radii as determined by the cell membrane thickness. The most important characteristic of DEP for particle analysis is that by tracking the magnitude and direction of DEP-manipulated particles over a range of applied AC frequencies, the dielectric properties of the particles can be extracted and subsequently used for cell population identification or analyses.

1.3 Non-spherical cells DEP model

DEP behavior of the viable and non-viable yeast cells was described by single-shell DEP model [104], recently Oblak, et al. [105], used this model to quantify the electrical properties between normal and electroporated mouse melanoma cells. However, bioparticles are non-spherical in nature. For example, bacteria have a rod-like cylindrical shape and erythrocytes are usually discoid in shape. Although some Phytoplankton species' cells are spherical in shape, Fig .2.4a. However, different species of Phytoplankton cells, Fig .2.4b,c, are non spherical in nature. As one of the main aims of this work to characterize the dielectric properties of phytoplankton, a quick derivation of the non-spherical DEP model will be discussed briefly. Unlike the spherical case, the dipole moment for a non-spherical cell differs along each semi-axis a, b and c, as shown in Fig. 2.2c. Since each axis has a different dispersion, the particle orientation in response to the electric field can vary according to the frequency applied. A rod-shaped particle at low frequencies, may experience pDEP, hence will align its longest axis parallel to the electric field. The induced charge along this axis has the greatest effective dipole moment and will exert the greatest torque on the particle. As the frequency is increased and the long axis dipole begins to disperse, the particle will rotate 90 degrees and align perpendicular to the field [106] . To account for differing polarization along each axis, a new term known as the depolarization factor, A_α, which represents the different degrees of frequency dependent polarization along each axis of the non-spherical cell, for the axis α, will be defined as the elliptical integral [35],

$$A_{j,\alpha} = \frac{a_j b_j c_j}{2} \int_0^\infty \frac{ds}{(s+i^2_\alpha)R} \quad \text{where} \quad i_x = a, \imath_y = b,\ i_z = c \\ \text{and } R = \sqrt{(s+a^2)+(s+b^2)+(s+c^2)} \tag{2.23}$$

At high and low frequency, the long axis of the cell will always be aligned parallel to the electric field as the dipole moment across the long axis trumps the short axis

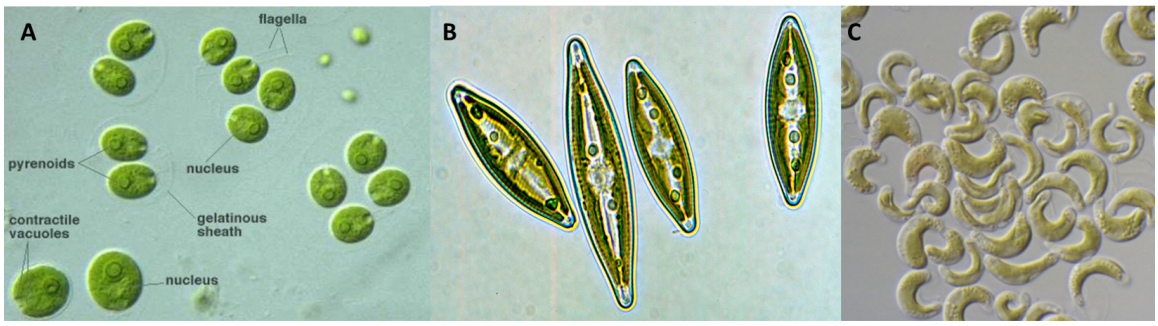

Figure 2.4. Microscopic images of Phytoplankton species. (A) Spherical *Chlamydomonas reinhardtii* algae [107] . (B) *Navicula* boat shaped algae. (C) *Selenastrum Reinsch* algae, cashew nut shaped. Reproduced from [108]

at these two frequency extremes. At intermediate frequencies, however, the cell can sometimes be observed to flip spontaneously to a new orientation as one induced dipole moment becomes dominant over another axis. Hence, the modified CM factor for an ellipsoid, for the axis α will be

$$(f_{\mathrm{cm}})_\alpha = \frac{\epsilon^*_{eff} - \epsilon^*_{mem}}{(\epsilon^*_{eff} - \epsilon^*_m)A_\alpha + \epsilon^*_m} \tag{2.24}$$

where ϵ^*_{eff} this time, is the effective complex permittivity of the cell. As expected, this is also a function of A_α,

$$\epsilon^*_{eff,\alpha} = \epsilon^*_{mem} \frac{\epsilon^*_{mem} + (\epsilon^*_{cyt} - \epsilon^*_{mem})[A_{2\alpha} + v(1 - A_{1\alpha})]}{\epsilon^*_{mem} + (\epsilon^*_{cyt} - \epsilon^*_{mem})[A_{2\alpha} - VA_{1\alpha}]} \tag{2.25}$$

where $v = r^2c/[(r+d)^2(c+d)]$ is the volume ratio of the cell exterior to interior, $A_{1\alpha}$ describes the axial polarization from just inside the membrane to infinity and $A_{0\alpha}$ is the result from evaluating Eq. (2.23) from just outside the membrane edge to infinity.

Typically, most publications involving non-spherical particles often model the frequency dependent DEP force along the major axis only, as the minor axis will often be unstable in alignment due to the much smaller axial length scale and resulting dipole moment. Hence, this model can be further simplified by analyzing the CM factor along the major axis. Figure 2.4, demonstrates the implementation of this model to extract the dielectrophoretic properties of non-spherical cells,indicating the regions wherein sub-cellular phenotypes dominates at different applied frequencies.

Further analysis, implementations, and applications including red blood cells, yeast, cylindrical bacteria, cardiac myocytes, and viruses for this model can be found explicitly in these reviews and book [35, 99, 100, 109–112].

2 Isomotive Dielectrophoresis (isoDEP)

In this section, the status of isoDEP is presented with a highlight on the progress that has been achieved over the past 60 years in various avenues of isoDEP since Pohl

initially described its premise. Since H.A. Pohl introduced the theory of isoDEP, numerous authors have implemented isoDEP as a tool for the manipulation, sorting, separation, and characterization of polarizable particles without the need for biochemical labels or other bioengineered tagging. The growing field of microfluidics and electrokinetics has renewed interest in isoDEP, particularly for analytical characterization or separation of particles based on their trajectories.

As mentioned previously, the dielectric properties of the particles can be measured based on a particle's frequency-dependent response to the applied field. However, one challenge is that the electric field itself typically produces a significantly non-uniform force throughout the observation region, this is particularly true for co-planar electrodes [113]. Thus, particles of the same type but at different locations in the microchannel will be subjected to different DEP forces, which is proportional to the gradient of the field-squared (∇E_{rms}^2). However, if ∇E_{rms}^2 is constant then these particles will be subjected to the same DEP force no matter where they are located in the microchannel. A dielectrophoretic system where ∇E_{rms}^2 is constant is termed isomotive dielectrophoresis and first demonstrated by H.A. Pohl [114]. The following section will show how to derive the solution of an isoDEP field.

2.1 Theory

In reviewing the status of isoDEP theory, it is instructive to examine how to derive a constant gradient of the field-squared (∇E_{rms}^2). Recell that The time-average DEP force (acting on a homogenous spherical particle) is typically expressed as in Eq.(2.18). To generate the isomotive DEP field, *i.e.,* to obtain a constant ∇E_{rms}^2, the electrical potential will take the following form [15, 114] (in cylindrical coordinates)

$$V = Ar^n sin(n\theta) \tag{2.26}$$

where A is a constant. Since $\mathbf{E} = -\nabla V$ we have

$$\mathbf{E}_{\text{rms}} = (\frac{\partial V}{\partial r})\hat{r} + \frac{1}{r}(\frac{\partial V}{\partial \theta})\hat{\theta} \tag{2.27}$$

$$\mathbf{E}_{\text{rms}} = Ar^{n-1}[\sin(n\theta)\hat{r} + \cos(n\theta)\hat{\theta}] \tag{2.28}$$

$$E_{\text{rms}}^2 = \mathbf{E}_{\text{rms}} \cdot \mathbf{E}_{\text{rms}} = n^2 A^2 r^{2n-2} \tag{2.29}$$

$$\nabla E_{\text{rms}}^2 = 2n^2(n-1)A^2 r^{2n-3}\hat{r} \tag{2.30}$$

In order for the gradient of the field-squared to be constant, n = 3/2 such that

$$\nabla E_{\text{rms}}^2 = (\frac{3}{2}A)^2\hat{r} \tag{2.31}$$

A substitution of $k = \frac{3}{2}A$ yields

$$F_{\text{DEP}} = 4\pi\epsilon_m a^3 \,\text{Re}[F_{\text{cm}}(\omega)]k^2\hat{r} \tag{2.32}$$

where the constant DEP force is applied in the radial direction. Hence, the equation describing the surfaces of constant potential in this isomotive field is

$$V = (\frac{2}{3})kr^{3/2}\sin(3\theta/2) \tag{2.33}$$

To avoid multiple mathematical solutions, limits on θ will restrict the defined region to be a function of $\frac{2}{3}2\pi = \frac{4}{3}\pi$ *i.e.,* $120^\circ \leq \theta \leq 240^\circ$ [**?**]. Figure 2a shows graph of the equipotential lines that obeys (Eq. 2.33). By placing metallic electrodes along the indicated equipotential lines (solid lines, Fig. 2.5a) and applying potential difference between them, the desired isomotive field will occur everywhere between the electrodes. Hence, particles traveling along the x-axis will be subjected to the same DEP force (Fig. 2.5b). Contributions due to multipole effects are negligible outside of a region within a few particle radii about the origin [115]. Two-electrode isoDEP systems can be created (Fig. 2.5c) knowing that $V = 0$ along $\theta = 0^\circ$ and 120°. Further, and isoDEP field can be created using the same curvature with insulative features and applying a potential through the channel itself [15].

2.2 Technical Realization Platforms for isoDEP Devices

The isomotive dielectrophoresis field can be produced by either using patterned microelectrodes or insulative microchannels designed with a specific curvature. For either case, a particular isoDEP device is characterized by its characteristic electrode spacing, δ. For the microelectrode version (Fig. 2.5c), the characteristic length is $\delta = r_{60}$ which is the largest gap between the two electrode sidewalls. In the insulative isoDEP device (Fig. 2.5d) $\delta = L$ is the distance from the origin of the system to either of the electrodes. For either case, the value of k can be expressed in terms of δ and the voltage difference across its length scale, $\triangle V$. k^2 can be described with these system parameters by

$$k^2 = \nabla|E_{\text{rms}}|^2 = \frac{9}{4}\frac{(\triangle V)^2}{(\delta)^3} \tag{2.34}$$

For a given particle size, the desired k^2 value can be estimated to provide the relative DEP force, then the $\triangle V$ value can be determined based on the available AC generator maximum output voltage, and δ can be calculated [117]. In some applications, direct contact between the electrodes and the analyte may be undesired, hence, an electrodeless (insulative) version of isoDEP can be considered. In insulative isoDEP the applied electrical potential is in the form [15].

$$V = (\frac{2}{3})kr^{3/2}\cos(3\theta/2) \tag{2.35}$$

The following sections will review existing electrode-based and insulator-based isoDEP platforms that have been used for the separation and/or characterization of particles

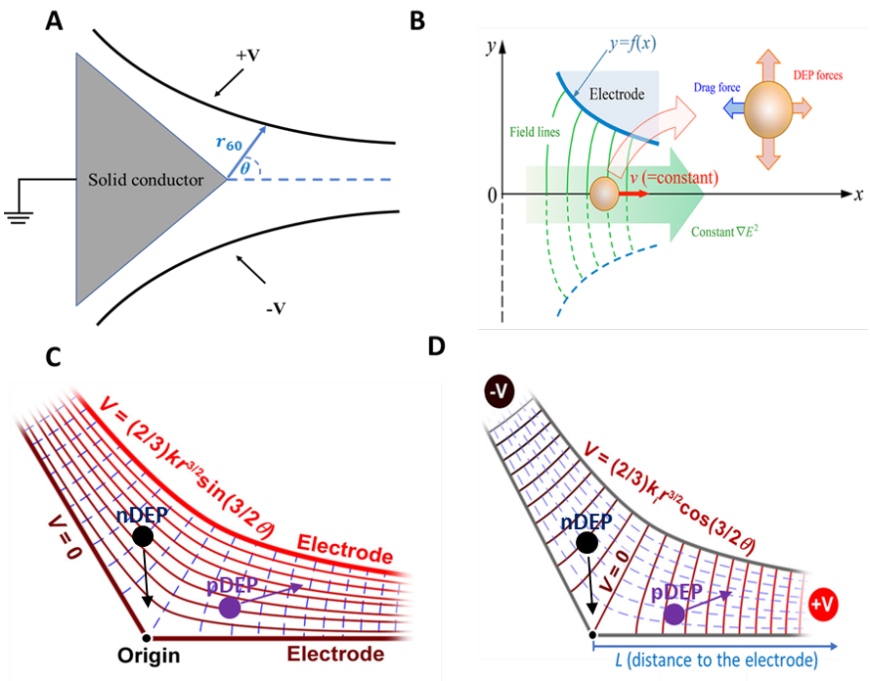

Figure 2.5. A schematic of applicable designs to generate isomotive DEP field. (A) Generated isoDEP field equipotential lines from Eq. 2.34. (B) Schematic illustration of the resultant constant DEP velocity of particles traveling along the symmetrical line. (C) Practical designs of isoDEP field electrode system shown in x-y plane showing the respective equipotential lines (solid lines) and the electric field applied through the sidewalls of the microchannel (dashed lines). (D) An insulative isoDEP system where the electric field is applied (dashed lines) through the ends of the microchannel and its respective equipotential lines (solid lines). (B) is reproduced with permission from [15], (C) & (D) are reproduced from [116].

and cells. However, there exists some practical limitations between these two different approaches. For either case Joule heating and electrothermal flow is possible and could compromise the operation of the isoDEP devices unless design rules are tuned for a given particle size [117]. Additional challenges occur when putting into practice the desired k^2 value; for example, benchtop AC signal amplifiers generally do not provide significant amplification ($>$ 100 V) at large frequencies ($>$ 1 MHz) thus perhaps preventing the implementation of insulative isoDEP platforms where L is large ($>$ 1 mm). Particle separation is more effective with greater fields, hence it is favored to include microelectrodes fabricated inside the channel to enhance the generation of large DEP forces. In traditional electrode-based designs, the microelectrodes are fabricated from indium tin oxide (ITO), copper, or gold [118], and located inside the microchannel in direct contact with the analytes. In some applications, the microelectrodes are coated with a thin insulator to avoid electrode fouling, electrolysis, and electrode-fluid interactions. The most common electrode geometry used in DEP applications are 2D planar electrodes that can be realized including interdigitated,

parallel, and curved electrodes. As discussed previously, planar designs provide a non-uniform DEP force through the microchannel's depth. Several designs have been used to distribute DEP forces more effectively, including placing electrodes on the top and bottom of the channel and 3D extruded electrodes [15, 118–120]. Such 3D electrodes provide more consistent separation and characterization capabilities. The main advantages of the insulative device are mitigating issues related to bubble formation and electrode fouling taking places in the vicinity of the electrodes, especially at low frequencies [118]. Insulative isoDEP devices can be easily fabricated with soft lithography and from biocompatible materials such as glass, polydimethylsiloxane (PDMS), or SU-8 or can be mass produced inexpensively via injection molding or hot embossing [121–123].

Both macroscale and microscale separation schemes have been developed utilizing electrode-based isoDEP configurations. Even though almost all present-day DEP applications are realized by microfabrication, the first time isoDEP was used in 1960 was to separate large non-biological particles ($\sim 100 - 200$ µm) at a time where microfabrication technology was in its infancy and not widely available. Since the introduction of the first isoDEP platform achieved by H.A. Pohl and C.E. Plymale [124], the electrode-based isoDEP device has been utilized to separate or characterize both non-biological particles [124–126] and biological particles [116, 127–130].

In 2011, Weis, et al. [131] introduced the concept of DC insulator-based isoDEP particle characterization utilizing the particle's specific DEP mobility analysis. Since then, and insulator-based isoDEP devices have been used to characterize non-biological [15, 131] and biological particles [132].

Allen, et al. [15], in 2017, proposed the concept of DEP multi-frequency characterization of particles, rather than separation, utilizing microelectrode-based and insulative-based isoDEP microfluidic devices. The group demonstrated nDEP and pDEP of both types of devices with carboxylate modified polystyrene particles ($18-25$ µm in diameter) and silver-coated hallow glass particles ($5 - 30$ µm in diameter), respectively. The microelectrode-based device was fabricated from an extruded silicon wafer (350 µm) using deep reactive ion etching (DRIE) technique (Fig. 2.6a). The insulative-based device was made from PDMS microchannels which were later bonded to a glass substrate and voltages were applied through two metal needles that simultaneously served as inlet/outlet as well (Fig. 2.6b). The voltage applied to the insulative-based device follows Eq. 2.35 (Fig. 2.6c). Particles were injected manually into the device, bulk fluid motion was ceased, and particles were allowed to sediment (1 min) before the AC field was applied. For a given voltage and frequency, videos were acquired for the particle while translating through the microchannel under the exerted DEP force. For the electrode-based isoDEP device, pDEP and nDEP experiments were conducted with a device with $r_{60} = 800$ µm at frequencies of 500 kHz and 100 kHz, respectively, with an applied potential of 34 V Fig. 2.6c, d) which results in $k^2 = 1.5 \times 10^{13}$ V^2/m^3. For the insulative isoDEP device, the applied AC signal was 300 V at 2 kHz; this results in $\mathrm{k}_i^2 = 3.36 \times 10^{11}$ V^2/m^{3}using $V = 150$ V and $L = 2.48$ mm (Fig. 2.6e, f, Fig. 2.5c). Once particles reach their terminal velocity, their motions will be balanced by the drag force ($F_{\mathrm{DEP}} = F_{\mathrm{Drag}}$), which will result in constant DEP velocity (ν_{DEP}) proportional to the dielectrophoretic force. Assuming

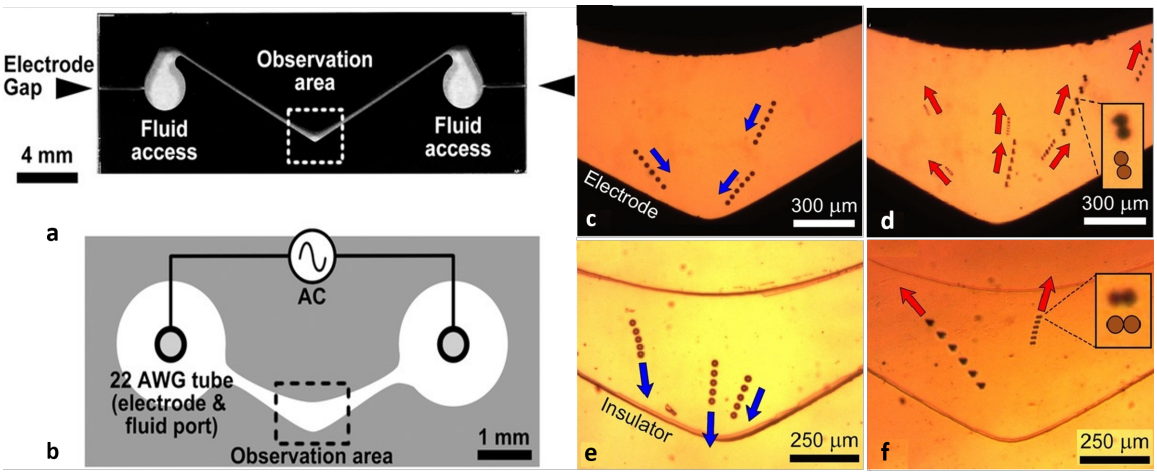

Figure 2.6. (A) A picture of a fabricated microelectrode isoDEP device consisting of two extruded silicon (350 µm thick) electrodes with r_{60}=500 µm sandwiched between anodically bonded borosilicate glass wavers. A gap between the electrodes at the fluid access ports prevented electrical shorting. (B) A schematic of the resulting insulative-based isoDEP device fabricated from PDMS device with r_{60}=800 µm. The experimental observation area is shown as well as how the AC signal was applied. Demonstration of the consistent radial translation of particles for microelectrode-based isoDEP device r_{60}=800 µm. (C) Negative dielectrophoresis was demonstrated using polystyrene particles at 100 kHz, 34 V. (D) Positive dielectrophoresis was demonstrated using silver-coated, hollow glass particles at 500 kHz, 34 V. Demonstration of the consistent radial translation of particles for insulative-based isoDEP device r_{60}=500 µm. (E) Negative DEP at 300 V, 2 kHz. (F) Positive DEP at 300 V, 2 kHz (overlaid particle images are 0.33 s apart). Reproduced with permission from [15]

Stoke's drag (neglecting wall drag), then the

$$\nu_{\mathrm{DEP}} = {}^{F_{\mathrm{DEP}}}\!/_{6\pi\mu a} = {}^{2\pi\epsilon_m a^3 \,\mathrm{Re}[F_{\mathrm{cm}}(\omega)]\nabla E^2_{\mathrm{rms}}}\!/_{6\pi\mu a} \tag{2.36a}$$

$$\mathrm{Re}[F_{\mathrm{cm}}(\omega)] = {}^{3\nu_{\mathrm{DEP}}\mu}\!/_{\pi\epsilon_m a^2 \nabla E^2_{\mathrm{rms}}} \tag{2.36b}$$

with a friction factor of $6\pi\mu a$ where µ in this case is fluid viscosity.

A significant advantage of isoDEP techniques that utilizes the dielectrophoretic velocity of the particle to determine its dielectric properties is that it can allow future DEP device portability. This can be done by substituting big microscopes with smaller sized portable cameras or utilizing the positioning technique that measures the position and throughput of particles passing over equally spaced embedded planar electrodes [133, 134]. An alternate switching between DEP field and sensing field can be used to apply the DEP force, then utilizes buried electrodes to measure the particle velocity, after application of DEP field, without interfering with the electric field.

A custom MATLAB program determined particle velocity and trajectory from particle position data obtained from the acquired videos. Next, the calculated particle velocities from each frame were averaged over the duration of its trajectory for an overall average particle velocity. A scaled velocity (${}^{\nu_{\mathrm{DEP}}}\!/_{a^2}$) was also calculated for

each particle using their respective measured particle diameter ($2a$). Hence, the real part of Clausius-–Mossotti factor ($\mathrm{Re}[F_{\mathrm{cm}}(\omega)]$) can be calculated from the measured scaled velocity with additional assumptions regarding the properties of the fluid and relating $\nabla E^2_{\mathrm{rms}}$ to the k^2 value.

Even though the device was not tested on a bioparticle, the premise of the device verifies the capability of isoDEP as a tool for characterization of cell subpopulations and extracting their dielectric properties at an achievable rate of approximately one to ten particles per second. However, perturbations generated from bulk fluidic motion or tubing instability may exacerbate the device operation. Such problems can be reduced by using rigid tubing, microfluidic resistive features, and proper valving systems. Moreover, analogous to previously discussed issues with isoDEP devices, the electrothermal-driven flow generated from Joule heating as well as AC electroosmotic-driven flow at low frequencies might compromise the DEP-driven particle motion. To avoid such perturbations, certain design rules has to be taken into account during device design and fabrication to provide a maximized DEP force for a given particle size [117].

2.3 Application of IsoDEP Devices

Both macroscale and microscale separation schemes have been developed that use electrode-based isoDEP configurations. Even though almost all present-day DEP applications are realized by microfabrication, the first time isoDEP was used in 1960 was to separate large non-biological particles (100-200 µm) at a time where microfabrication technology was in its infancy and not widely available. Here, isoDEP was used for mineral separation and as a new technique for petroleum refinement.

2.3.1 Electrode-based IsoDEP Device

2.3.1.1 Non-biological Particles

The first isoDEP platform was achieved by H.A. Pohl and C.E. Plymale [135] demonstrating separation of various particles in powder forms suspended in dielectric medium of very low electric conductivity (carbon tetrachloromethane (CCl_4) or cyclohexane or benzene (C_6H_6). The separation was achieved with two different setups implementing either a cylindrical electrode geometry where the force exerted on the particles depends strongly on their radial location from the central electrode ($\propto 1/r^3$), or an isomotive cell geometry where the force exerted on particles was independent of their radial location. Various powders ($94-177$ µm in diameter, see Table 2.1) were fed into the hopper then delivered into a cell consisting of a long narrow tray passing through two electrodes that separated the samples which were subsequently collected at two different ends (Fig. 2.7). Electric fields ranging from 4×10^4 to 7×10^5 V/m were used (Table. 2.1). The size of the system was large compared to today's miniaturized microfluidic devices, but it was suitable for large size particles separations ($\sim 90-150$ µm). The produced electric field still falls within the acceptable range for current DEP biological studies [136, 137]; however, the high voltages used ($\sim$ 11 kV) gives rise to Joule heating ($\propto V^2$) which disrupts DEP-induced motion of particles. This

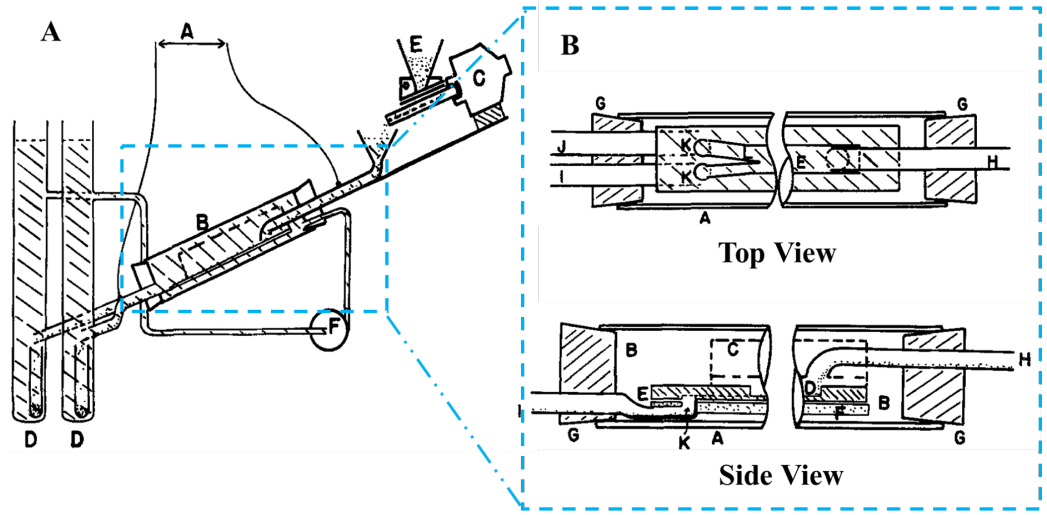

Figure 2.7. A schematic diagram of isomotive cell setup used for continuous separation of particles from mixtures. (A) General setup of the cell with A, AC high voltage source; B, isoDEP cell where separation occurs; C, vibrator; D, separated particle outlet; E, supply hopper as an inlet for powder mixture. (B) Top view and side view of the isoDEP cell showing the separation region where A, outer glass wall of the chamber; B, suspending medium; C, top brass electrode; D, solid particles; E, Teflon plate serving as an insulator; F, bottom brass electrode; G, neoprene stopper; H, feed inlet from copper; I, lower exit tube made from copper; J, upper exit tube; K, exit hole leading to the separate outlets; L, divided separation outlets. Reproduced with permission from [135].

effect can be mitigated by miniaturized electrodes which can achieve the same DEP force at lower applied voltages, thus avoiding thermal and electrolysis effects [138].

After introducing the concept of isoDEP, Pohl and Pethig [140] provided further validation and characterization of the DEP force showing the uniqueness of the isoDEP design. In 1988 C.M. Feeley and F. McGovern [141] used a design similar to Pohl's crude design to determine the dielectric proprieties of insulating liquids throughout the manipulation of suspended nitrogen bubbles. They used a cylindrical electrode configuration to produce the isoDEP field with a characteristic length of $r_{60} \approx 5$ mm. The electrodes were immersed inside three different low conductive liquids ($\sim 10^{-11}$S/m) and aligned so that the motion of nitrogen bubbles rising vertically in the inter-electrode space was opposed by the DEP force. Different applied voltages between 0 and 3 kV (at 50 Hz) were applied and the translation of bubbles were measured by three laser beams. Bubbles were generated every 30 s and at each of the applied voltages one hundred transits were timed, their distribution displayed, and their mean value calculated. The results showed that decreasing the applied voltage decreased the mean velocity of the bubbles. However, near the electrodes edges the motion of the bubbles were unpredictable which were not explained at the time but were likely due to electrohydrodynamics like electrothermal flow.

In 1996 Andres [142] reported a review of techniques for dielectric separation

Table 2.1. Summarized isoDEP applications for cells/particles manipulations in chronological order. Reproduced with permission from [139].

Application [Reference] & Electrode Type	Cells/Particles (Diameter)	**Applied Potential (Electric Field) &** ***Fluid Conductivity*** **[Throughput or/ Flow Rate or/ Particle Velocity or/Not Reported]**
Separation [124]	Polyvinyl chloride Spherical particles (~ 90 µm)	1000 – 2000 Vrms (~ $4 \times 10^5 - 8 \times 10^5$ V/m)
Copper Wire electrodes of 0.74 mm	Powder mixture of dichromate $Na_2Cr_2O_7{\cdot}2H_2O$ and TiO_2 (~ 177 µm)	100 – 1000 Vrms (~ $4 \times 10^4 - 4 \times 10^5$ V/m)
in diameter and spaced 0.241 cm (Electrode-based)	Mixture of rutile mineral (gray-black form of TiO_2) (150-250*m*)*and*polyvinylchloride*spherical*particles(~ 90 µm)	0 – 750 Vrms (~ 3×10^5 V/m)
	Silicon carbide-silicon dioxide particle mixture (~ 127 µm)	0 – 2000 Vrms (~ 8.3×10^5 V/m)
	Silicon carbide and calcium fluoride particle mixture (~ 147 µm)	0 – 1700 Vrms (~ 7×10^5 V/m)
	Zircon and rutile mineral mixture (~ 94 µm)	0 – 1500 Vrms (~ 6×10^5 V/m)
	All powders were suspended in Tetrachloromethane (CCl_4) or Benzene (C_6H_6) organic dielectric liquid	[Not Reported]
Separation [127]	*Chlorella vulgaris* (5 – 10 µm) with *Netrium digitus* (65 – 70 µm in diameter and 216 – 264 µm in length)	40 Vrms at 100 kHz (~ 45 kV/m) *1 mS/m*
electrode geometry with two copper	*Ankistrodesmus falcatus* (2 – 6 µm in diameter and 25 – 100 µm in length) with *Staurastrum gracles*	60 Vrms at 600 kHz (~ 67 kV/m) *0.2 mS/m*
electrodes of 2 mm in diameter surrounding glass capillary	*Saccharomyces cerevisiae* (5 – 10 µm) with *Netrium digitus* (65 – 70 µm in diameter and 216 – 264 µm in length)	100 Vrms at 2 MHz (~ 111 kV/m) *8.3 mS/m*
$r_{90} \approx 1$ mm (Electrode-based)		[Flow Rate: 9.6 µL/min, Cell Velocity: 200 µm/s]
Characterization [125]	Bubbles (~ 500 µm)	0 – 3 kV at 50 Hz (0 – 600 kV/m)
Cylindrical electrode geometry	*Suspended in transformer oil, corn oil, and castor oil*	*Very low conductivity* $\approx 10^{-11} S/m$
$r_{90} \approx 5$ mm (Electrode-based)		[2 bubbles/min]
Separation [126]	Diamond-kimberlite (<1 mm) mixture	100 kV at 50 Hz *Kerosene (Very low conductivity)*
Two electrodes forming isoDEP geometry (Electrode-based)	Quartz particulates (50 µm)	100 kV at 100 kHz (1 MV/m) *Non-purified water* [Not Reported]
Cell Sorting, Fractionation and Characterization [129]	Viable and non-viable canola paut protoplast (20 – 40 µm in diameter)	16 V_{pp} at 1 – 10 kHz (0 – 600 kV/m)
Cylindrical electrode geometry (Electrode-based)		*1-10 mS/m* [Cell Velocity: 100 – 200 µm/s]
Cell Sorting and Fractionation [128]	Viable and non-viable yeast cells (unknown size)	10 V_{pp} at 100 Hz–10 MHz *1.5– 3 mS/m*
Cylindrical electrode geometry (Electrode-based)		[~ 13, 320 particles/min]
Characterization of Particle DEP Mobility [131]	Sulfated polystyrene fluorescent particles (1 µm)	1500 V DC (100 – 200 kV/m) *25 mS/m*
PDMS channel with isoDEP geometry design		[Particle Velocity: ~ 500 – 2500 µm/s, Cross-Sectional Area: 1.92 mm^2]
(electrodes dipped into microchannel) (Insulative-based)		
Characterization[15]	Carboxylate modified polystyrene particles (18 – 25 µm)	34 V_{rms} at 100 kHz (68 kV/m) *0.6 mS/m*
(Electrode-based) (r_{90} = 500 µm)	Silver-coated hollow glass particles (5-30 µm)	300 V_{rms} at 2 kHz (~ 50 kV/m) *0.6 mS/m*
(Insulative- based) (*L*=2.48 mm)		[~ 600 – 6000 particles/min]
Characterization [116]	Human breast epithelial cells (MCF10A) (17.5 µm)	20 V_{pp} at 20 & 40 kHz (~ 45 kV/m) *40 mS/m*
Creek-gap electrode (Electrode-based)		[~60 cells/min]
Characterization [132]	Human breast epithelial cells (MCF10A) (17.5 µm)	34 V_{pp} at 200 kHz & 50 MHz (~ 100 kV/m) *70 mS/m*
Creek-gap design (Insulative-based)		[~85 cells/min]
Separation [130]	Jurkat E6.1 cells (11 µm) from beads (11 µm) mixture	7 V_{pp} at 300 kHz (~ 28 kV/m) *30 mS/m*
(Electrode-based)	MDA-MB-231 cells breast cancer cells (~ 14 µm) from either ~ 14 µm beads or ~ 5 µm mixture	7 V_{pp} at 100 kHz (~ 28 kV/m) *30 mS/m*
	Red blood cells (RBC) (~ 7 µm) from beads (14 µm)	7 V_{pp} (~ 28 kV/m) *30 mS/m*
		[20,000 cells/min]

of minerals, particularly diamond. Their technique depends on the formation of pearl-chained particles within a high non-uniform electric field (800-1000 kV/m). Particles with dielectric permittivity lower than the suspending medium (*i.e.,* medium is more polarizable than the particle, $\epsilon_{p,1} < \epsilon_m$) formed pearl-chained clusters that exhibit nDEP and were repelled to weak-field regions. While particles of dielectric permittivity larger than the suspending medium (*i.e.,* the particle is more polarizable than the medium, $\epsilon_{p,2} > \epsilon_m$) exhibit pDEP and moved towards high electric field regions. Pearl-chains formed with $\epsilon_{p,1}$ will repel those formed with $\epsilon_{p,2}$ while each cluster will simultaneously attract like particles. Chains will only form at a particular field strength, above which horizontal clustering of particles of the same type takes place giving rise to chains and their subsequent clustering in the horizontal direction producing elongated structures with multiparticle links.

Successful separation of diamond-kimberlite mixture was performed. The mixture was loaded into a chamber filled with kerosene medium (Fig. 2.8A) and isoDEP geometry electrodes serving as the top channel constraint (1) and flat electrode serving as ground (2) where a screen separates particles from contacting the electrodes (3).

Upon the application of the 1 MV/m electric field, chains of kimberlite particles were formed in the horizontal channel. The channel containing the liquid dielectric was fixed on the vibrator (4), which generates translational movement of solids from the feed end to the discharge end of the channel along its longitudinal axis. Hence, it facilitates the movement of separated chains where material with $\epsilon_p > \epsilon_m$ is falling through the pipes labeled (7) in Fig. 2.8A, and $\epsilon_p < \epsilon_m$ particles discharged through the central pipe (6). This technique was more efficient with small diamond stone recovery (100% with $55 - 60\%$ of diamond concentration in mixture) and stones with significant surface contamination, which contemporary techniques at that time could not offer such sensitivity of separation. Although di-n-butyl phthalate medium can offer inexpensive and non-toxic medium for mineral separation compared to other

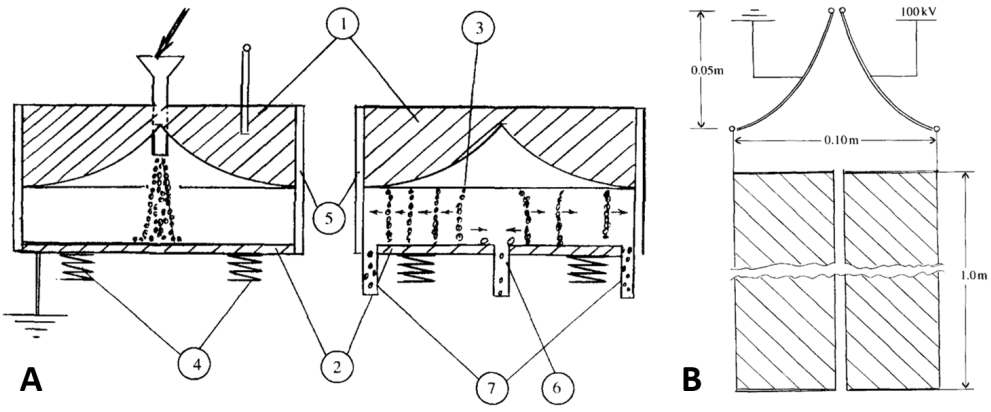

Figure 2.8. (A) A schematic diagram showing the isoDEP device used for separation of diamond-kimberlite mixture showing the loading process (left) and discharging process (right). (B) Diagram of the vertical separator with water medium. Reproduced with permission from [142].

high cost and toxic media such as nitrobenzene, kerosene, and xylol. However, using water as a medium for separation is better because it is less expensive, non-toxic, and more abundant. Andres and O'Reilly proposed a design for separating quartz particulate (50 µm) from mixtures suspending in non-purified water with electric field strength ~ 1 MV/m (without breakdown).

2.3.1.2 Biological Particles

In 1966 Pohl and Hawk [143] followed their first isoDEP-based separation experiment and suggested another electrode-based searation platform which was the first demonstration of DEP-based separation of live/dead yeast cells using pin-plate electrode arrangement with a rounded 0.66 mm stainless steel wire facing a flat steel plate positioned 1 mm away from each other with 30 V_{rms}(45 kV/m) applied at 2.55 MHz. However, they did not demonstrate yeast separation using their isoDEP platform. There was not any further isoDEP separation studies (except for theory development and validation [140, 144, 145]) until two decades later in 1978 when Pohl and Kaler [146] described an isoDEP-based separation of different microorganisms. Using a continuous separator of the form shown in Figure 2.9 they described continuous separation of yeast (*Saccharomyces cerevisiae*) from green algae (*Netrium digitus*), as well as different types of green algae from their mixtures (*Chlorella vulgaris* with *Netrium digitus*; *Ankistrodesmus falcatus* with *Staurastrum gracile*).

The setup was simple using components such as metal wires and thin sheet electrodes to produce non-uniform fields. The setup consisted of two copper wire electrodes (2 mm in diameter) sandwiching a square glass capillary (ID =900 µm, length =50 mm) with inlet and outlet covered with silicon tubing, and both wires and glass chamber were mounted on a microscope glass slide. Yeast and green algae cell mixture were injected to the separation using a pressure pump (providing a flow rate of 9.6 µL/min) reaching an average linear velocity of about 200 µm/s. The cells were subjected to non-uniform electric fields ranging $45 - 111$ kV/m for about $100 - 180$ s in their travel of 20 mm. This field should not affect cell viability [137, 147]; however, the low ionic conductivity of the suspending media used in their experiments (0.2, 1, and 8.3 mS/m) might be tolerated by cells for a short period of time, but for extended exposure the solution may require higher osmolarity and/or higher ionic solutes. Even though having the electrodes lying outside the suspending media prevents electrolysis and electrode fouling, it will hinder the operation of the device for applied frequencies less than 10 kHz. Electrode insulation applies a frequency-dependent impedance that reduces electric potentials at elevated frequencies (>3 kHz). Further complications may occur for characterization of mammalian cells because mammalian cells are smaller compared to the previously studied particles.

Unfortunately, the isoDEP platform was not used (*i.e.,* published) again for biological cells until 2004 when Kaler's group [148] described a versatile DEP cell fractionation system that generated an isomotive field using a discrete array of planar electrodes on the base and a grounded top plate (Fig. 2.10). The resulting constant ∇E_{rms}^2 causes hydrodynamically-focused cells to translate perpendicular to the

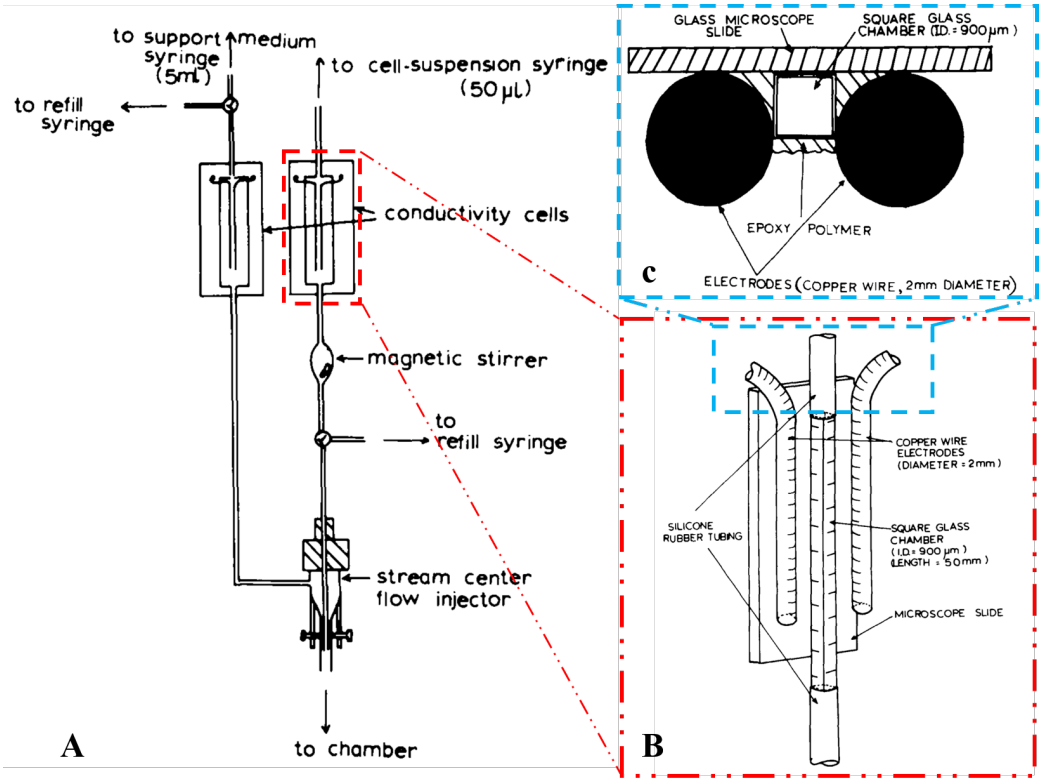

Figure 2.9. A schematic diagram representing of the isoDEP-based yeast-algae separation. (A) Stream-centered flow injection system setup. (B)Close up view of the continuous separation chamber. (C) Cross-sectional view showing the arrangement of the electrodes and flow chamber. Reproduced with permission from [146].

flow direction thus fractionating cells exhibiting different dielectrophoretic responses. They were able to perform continuous cell (plant protoplasts) sorting based on their viability status (dielectric properties) with high throughput over wide range of frequencies (10 Hz−5 kHz). Figure 10A, B shows how their devices was configured. Sheath flow was introduced to achieve a maintained stable laminar flow of the injected cells for subsequent fractionation. The parallel electrode array was realized using patterning of thin gold layer on glass substrate. Each electrode was separated and addressed individually by using a custom-built PCB control unit. A voltage dividing resistive ladder network was used to generate the appropriate voltage applied to the electrode array to produce the desired isomotive electric field.

Separation can be achieved in three different modes. In the first mode (Fig. 2.10D) the chip was positioned horizontally so that the electrode array faces upward. Hence, the particle translating in the channel under the pressure-driven flow parallel to the electrodes will be sorted using the DEP force that deflects them based on their polarizability. Particles will be levitated at an equilibrium height when their respective DEP force component in z-direction are balanced with gravity and buoyancy forces. Particles then can be separated and directed towards left or right across the channel by applying either pDEP or nDEP forces. In the second mode (Fig. 2.10E), the chip

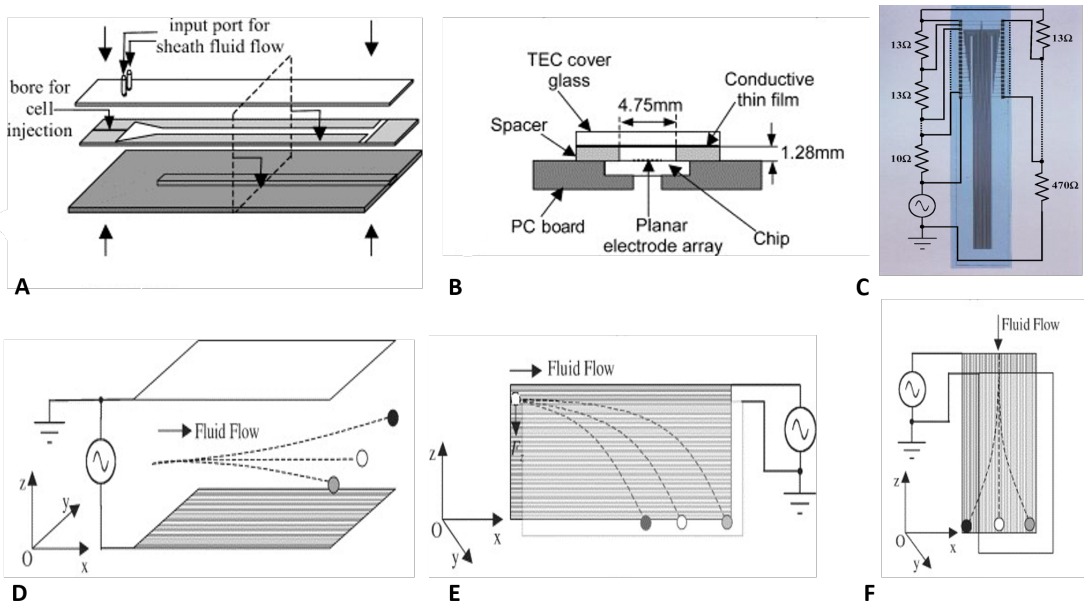

Figure 2.10. (A) A schematic diagram representing of the isoDEP-based cell fractionation system. (B),(C) Solid and cross-sectional view of the three-layer microfluidic chip to accommodate fluidic stream-centered injection and sheath fluid ports, two outlet ports and housing a resistor ladder network and interconnections to the chamber electrodes. (C) Demonstration of biasing resistive ladder values used for facilitating the generation of the desired isoDEP field. Practical realization of separation modes based on the chip positioning; (D) in the horizontal placement. (E) and **f** in a vertical placement. Reproduced with permission from [148].

can be mounted vertically, parallel to the z-direction, while the patterned electrodes are maintained parallel to the $x-y$ plane. Hence, as the particle travels in the fluid along the electrode strips, the net resultant force (F_z) for the particle is determined by a combination of DEP, gravitational, drag, buoyancy, and lifting forces. Therefore, DEP force exerted on the particle, will influence its time required for decent, hence enabling spatial separation. In the third mode (Fig. 2.10F), the chip remains vertical however, the patterned electrodes are maintained perpendicular to the $x-y$ plane. Hence, the gravity is acting on the particles driving them to move along the electrodes' length. Either pDEP or nDEP forces can be used to fractionate particles.

Successful separation of viable canola plant protoplast cells obtained from six to eight weeks old plant tissue subjected to enzymatic digestion and non-viable cells (heated in high power microwave to cause cell death) was achieved. Cell fractionation occurred in a continuous manner utilizing parallel electrode separator (first mode of separation). As the cells were transported in the isomotive DEP field (with cell velocity of $100-200$ µm/s), based on the excess polarizability of the individual particles comprising the cell stream, the cells experienced either positive or negative DEP forces. These forces act to impel the particles in opposite directions and orthogonal to the direction of the cell stream, as illustrated in Fig. 2.10D. Successful

separation requires prior knowledge of cell polarization. The membrane capacitance of the viable canola cells was characterized. A value of $C_m = 5.3$ mF/m^2 for canola protoplasts were estimated using an approximation of the zero-cross frequency from the experimental normalized velocity spectra. The reported value seems to be an acceptable value and similar to what the group reported by utilizing their developed dual-frequency excitation technique that uses feedback-control of a DEP force to levitate particles and to investigate both positive and negative DEP characteristics [149].

The premise of the device offers high continuous separation capability compared to conventional separation techniques [150]. However, utilizing planar electrodes for DEP applications is not ideal due to the lack of consistent DEP force throughout its depth. There are further complications associated with the application of low AC fields (< 1 kHz) including fluid motion induced by electro-osmosis and electrochemical / electrolysis effects [151–153]. These effects are exacerbated when dealing with elevated voltages required to manipulate smaller cells (< 10 µm), hindering isoDEP repeatability and sensitivity.

Kaler, et al. [154] addressed the limitation imposed on the cell size to be used in their previous setup with a miniaturized version allowing on-chip integration of the system. Figure 11a shows device fabrication which contained an array of planar electrodes and SU-8 microchannel features before an ITO slide is adhered to seal the channel. Biasing resistors are then soldered to provide the correct voltage for isoDEP field application. Figure 7b shows the assembled integrated microfluidic device (95 mm $\times$ 26 mm $\times$ 2.3 mm) with two separate outlets for cell sample collection. The width of the focused central cell stream is controlled by the sheath fluid flow rate (Fig. 2.11c) with an acceptable sheath (~ 200 µl/min) to sample flow ratio of 1:1.

Successful separation of viable and non-viable yeast cells was achieved with 10 V_{pp} at 100 Hz $-$ 10 MHz. At low frequency (~ 1 kHz) the non-viable cells experience pDEP and the viable cells will experience nDEP and hence were directed to outlet ports 2 and 1, respectively. In contrast, at high frequencies (~ 2 MHz) the viable cells experience a pDEP and are collected by fluid outlet port 1 while the non-viable cells experience negative DEP and are hence directed towards and collected at fluid outlet port 2. Despite being a continuous separator, the setup was only able to analyze 27% of the introduced cells in the microchannel due to the flow rate being too large. Hence, to achieve greater analytical throughput ($\sim 13,320$ cells/min), flow rate was decreased. unfortunately, caused cell sedimentation. Moreover, like their previous design, the electrodes are in direct contact with the sample, and not insulated, which may compromise analysis at low frequencies as discussed earlier [155].

In 2018 Tada, et al. [156] proposed a newly designed creek-gap electrode isoDEP design, where the electrokinetic behavior of cells was characterized by DEP velocimetry under the exposure of an approximately constant ∇E_{rms}^2 established along the gap of the electrodes. The shape of creek-gap electrode (Fig. 2.8a), y, can be expressed as a function of x as the following

$$y = \frac{V}{2\sqrt{ax+b}} \tag{2.37}$$

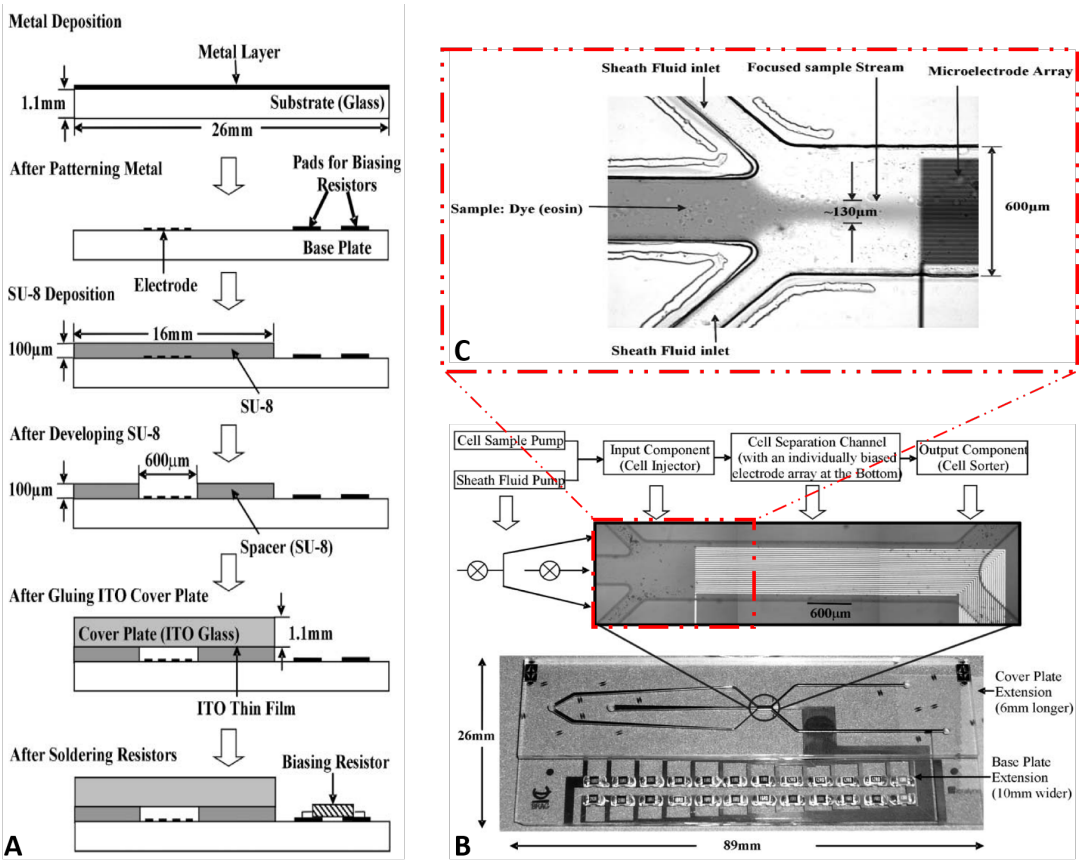

Figure 2.11. (A) A schematic diagram representing the process flow utilized to fabricate the continuous microfluidic isoDEP cell fractionation system. (B) An image of the fabricated isoDEP cell fractionation system showing the microfluidic components, the metal electrode array and on-chip surface mount resistor ladder used to bias the electrodes. (C) Images of the cell injector region, showing the dimension of the separation region and hydrodynamic focusing of the sample (dark color) by the support sheath flow. Reproduced with permission from [154].

where V is the voltage applied, a (V^2/m^3) and b (V^2/m^2) are constants related to the device dimensions, and $2\sqrt{ax+b} = |E|$ is the functional form of the electric field along the x-axis (Fig. 2.12B). In the examination area of the creek-gap electrode, particles traveled straightly along the centerline of the electrode will translate at constant velocity because of the constant ∇E_{rms}^2 (Fig. 2.5B, Fig. 2.12B), making it simple to track their motion.

The group successfully characterized the dielectrophoretic properties of human breast epithelial cells (MCF10A) (17.5 µm) suspended in 40 mS/m media. The analytical steps to calculate $\text{Re}[F_{\text{cm}}(\omega)]$ were determined in a manner similar to what Allen, et al. [15] followed, but with the inclusion of the friction force between cells and

microchannel wall. The dielectrophoretic velocity was calculated from the distance of cell movement and the time required to translate that distance (Fig. 2.8c). The average cell velocities measured under the exposure of an AC voltage of V_{pp} =20 V at two different field frequencies, 20 and 40 kHz were $\sim$ 2.25 and 1.35 µm/s respectively. Hence, calculated Re$[F_{cm}(\omega)]$ at 20 kHz (~ -0.27) was higher than 40 kHz (~ -0.2). Therefore, a relationship for Re$[F_{cm}(\omega)]$ versus frequency can be obtained.

Although this design offers a simpler way of isoDEP fabrication, the rigorous uniformity of the DEP force along the centerline of the electrode might be compromised in the creek-gap electrode due to the geometrical approximation. As reported by the group, the device design and structure is favorable for cells exhibiting negative DEP; however, it cannot be applied to the analysis of positive DEP cells because positive DEP cells are captured at the electrode edges [157]. This can be resolved by adapting an insulative-based isoDEP structure and device design similar to what was reported by Allen, et. al.[15].

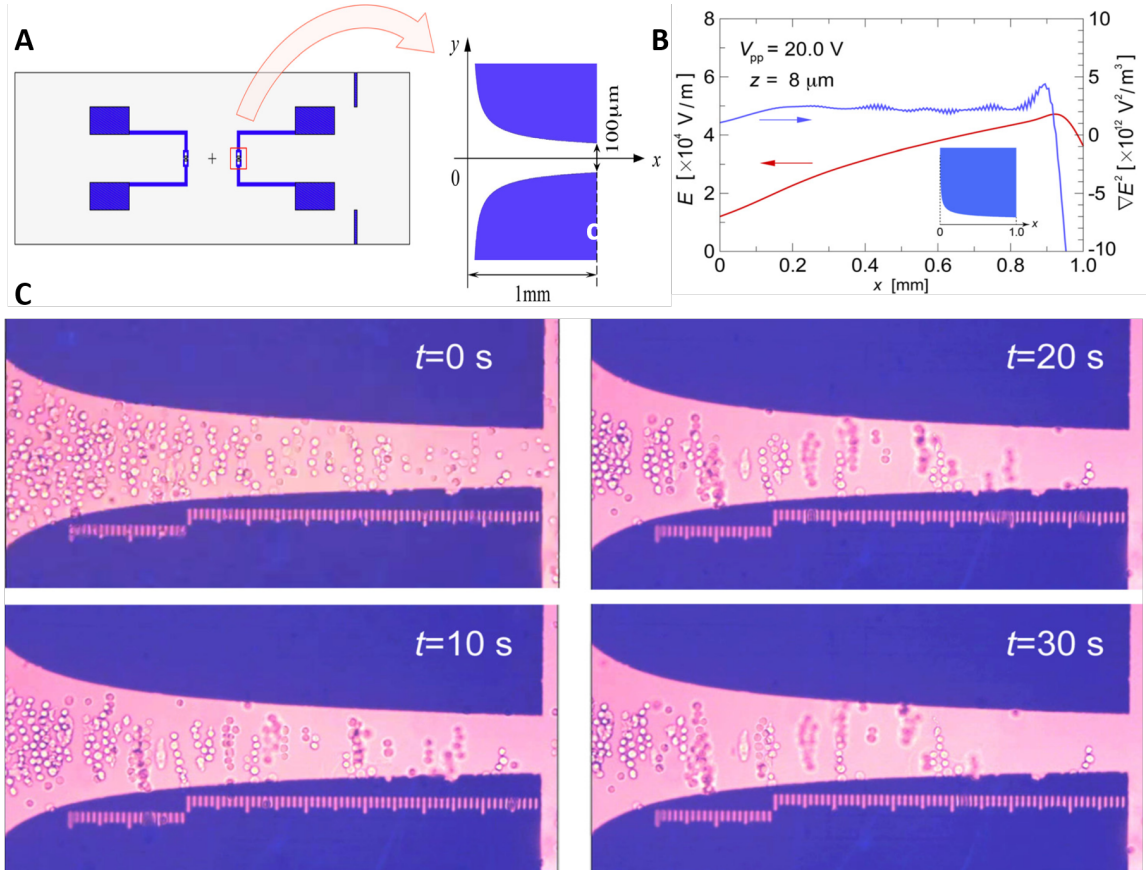

Figure 2.12. (A) The design and specification of the creek-gap electrode. The shape of the creek-gap was specified by Eq. 2.37. (B) A Profiles of the electric field strength, $|E_{rms}|$, and the value of ∇E_{rms}^2 along the centerline (x-axis) of the gap at a height of z = 8 µm. (C) Time-lapse images of cells moving from right to left through the creek-gap at times t=0, 10, 20, and 30 s after the application of 20 V_{pp} at 20 kHz. Reproduced with permission from [156].

Recently, Shkolnikov, et al. [158] developed a novel technique for continuous isoDEP separation of particles from mixtures. The unique geometry allows generation of stagnation flow thanks to the hydrodynamic focusing of particles utilizing sheath flows (Fig. 13A). Particles are then focused onto stagnation streamlines, where isoDEP force can separate particles and direct them into two different outlets based on their DEP response (nDEP or pDEP, Fig. 2.13A). The separation can be achieved in two different modes; centered mode, which was used to separate particle sets that are similar in size (Fig. 2.13B), and directed mode, which was used to separate particle sets that are different in size (Fig. 2.13C). To operate in centered mode, the resistance of the outlet channels was turned, utilizing micro-metering valves, such that the focused particle streamlines were split evenly between the two outlets. To operate in the directed mode, the resistance of the outlet channels was tuned to such that the focused particle streamlines were largely directed into one of the channels then separated the particles experiencing a larger DEP force into the other channel.

Separation dynamics and design parameters (*e.g.,* channel size, flow rate, and electric field) have been described to develop a simple scaling model to predict the range of particle sizes that can be separated as well as the processing rate that can be achieved. They concluded that to increase the range of particle size and sample flow rates the particle focusing had to increase as well (*i.e.,* smaller λ/W where λ is the half width of the focused particle stream and W is the distance of the channel wall from the center of the stream, Fig. 2.13B,C). However, the maximum sample flow rate was limited by the channel depth, particle size, maximum tolerable electric field strength, the inherent geometry of the electrodes, and the inherent properties of the carrier liquid.

The group successfully achieved separation of same size particles using immortalized cancer cells and polystyrene beads performed in centered mode. Two mixtures were used, one containing Jurkat E6.1 cells ($\sim$ 11 µm) and beads ($\sim$ 11 µm), and the other one containing MDA-MB-231 cells ($\sim$ 14 µm) and beads ($\sim$ 14 µm) (Table. 2.1). The separation purity and yield were measured as a function of particle stream direction. At an applied voltage of 7 V_{pp} at 300 kHz, Jurkat cells suspended in 30 mS/m experienced pDEP while the beads experienced nDEP. The purity and yield of cells varied with the direction of particle flow (Fig. 2.13D). However, Jurkat cells exhibited high cell purity at the pDEP but low cell yield. For MDA-MB-231 cells, the separation was achieved at 100 kHz, with cells exhibiting pDEP and achieving highest purity and yield observed when $\sim$ 70% particles are directed to pDEP outlet (Fig. 2.13E). Separation of red blood cells (RBCs) of ($\sim$7µm) from 14 µm beads was achieved under the same condition achieving highest yield and purity when $\sim$ 80% of particles are directed into pDEP outlet.

The device offers a novel technique for continuous, high throughput, particle separation ($\sim 20,000$ cells/min) as well as detailed model that relates design parameters to the desired particle sizes. Even though the achieved yield and purity was good, the device did not achieve separation of two different cell types with similar size nor same cell type versus a modified cell property (*e.g.,* live vs dead cells) which would have greater significance for biomedical applications. This can be achieved by extensive DEP characterization of cells and modified cells to obtain their real Clausius–Mossotti

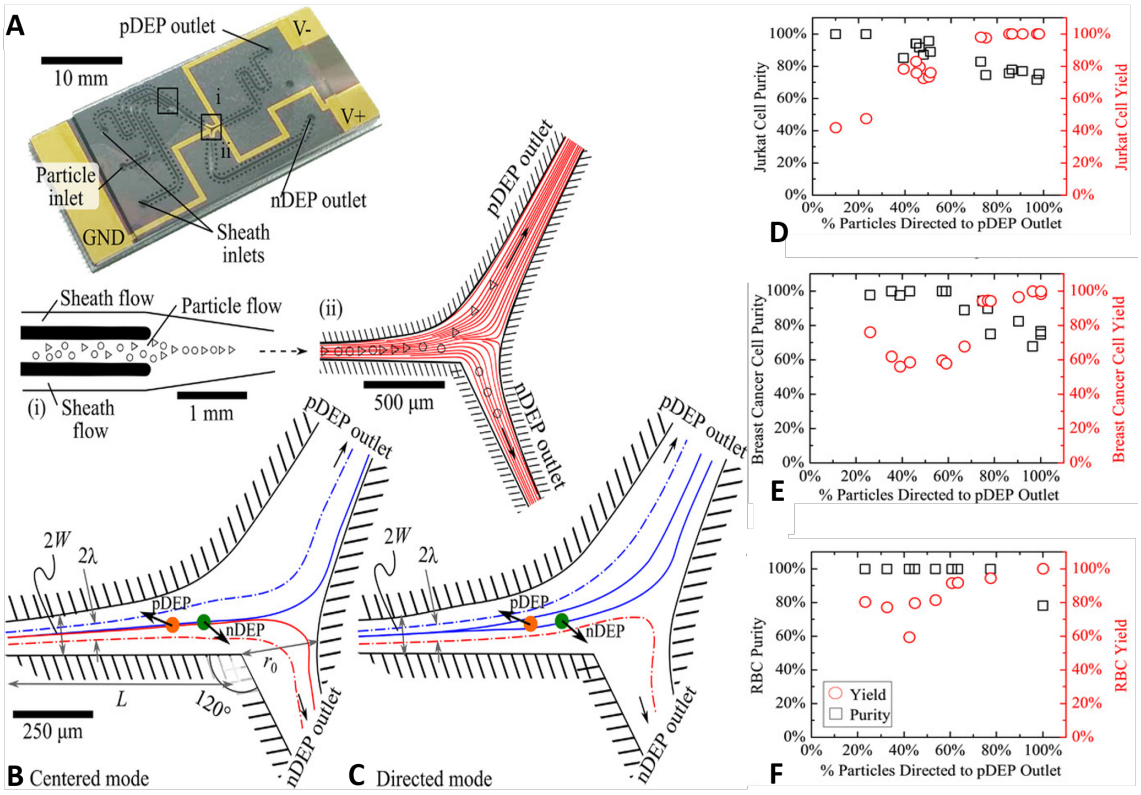

Figure 2.13. (A) Image of the final assembled device showing the relative locations. Schematic of the focused isoDEP separation device (i) hydrodynamic focusing of particles using two sheath flows, (ii) isoDEP separation region. Illustration of separation modes of the device where DEP force guides particle stream towards two different outlets (B) Centered mode where the focused stream is directed such that the flow splits evenly between the two outlets. (C) Directed mode where the focused stream is directed such that the flow in one outlet is larger than the other. The solid lines represent the center (stagnation) streamlines of the focused stream, while the dash-dot lines represent the outer streamline of the focused stream. Yield and purity of mixtures as different percentages of particle mixtures are directed into pDEP outlet (D) Jurkat cells ($\sim$ 11 µm) and 11 µm beads (not shown) exhibit inverse trends as different percentages of total particle mixture is directed into pDEP outlet achieving highest yield when $\sim$ 50% of the cells are directed to the pDEP outlet. (E) MDA-MB-231 cells (14 µm) and 14 µm beads (not shown) exhibit similar inverse trends. Here, highest yield of cells occurs when $\sim$ 70% of the cells are directed to the pDEP outlet. **f** Red blood cells ($\sim$ 7 µm) and 14 µm beads exhibit inverse trends and are highest when $\sim$ 80% of particle stream is directed into pDEP outlet. Reproduced with permission from [158].

factor values instead of assuming these values (unity), which would provide higher purity and yield of cell separations.

2.3.2 Insulative-based IsoDEP Device

2.3.2.1 Non-biological Particles

In 2011, Weiss, et al. [159] introduced the concept of DC insulator-based isoDEP for particle separation and characterization. The group characterized particles within an isoDEP field through monitoring their dielectrophoretic mobility. Moreover, the insulative microchannel itself can incorporate obstructions, serpentine features, and sawtooth features (Fig. 2.14A-C) [11] which are suitable for DEP trapping applications. DEP mobility for a particle will be dependent on the device-specific structures and the magnitude of the applied electric field. The incorporation of insulative isoDEP can characterize the specific mobility of the particle which can be attributed to the intrinsic particle phenotype independently from the electric field properties and only depends on a particle's size and Clausius–Mossotti factor.

The electrokinetic and electrophoretic mobilities of 1 µm polystyrene particles were determined simultaneously from the spatial velocity profile of the particles generated from streak-based velocimetry analysis. Particles ($\sim 5\times10^6$ particles/mL) are introduced into the channel (made from 10 µm thick PDMS) by pressure difference made between two reservoirs. 1500 V DC is applied through platinum electrodes at either end of the channel. Images were then captured while particles traveled through the channel for a given voltage. Images were then are analyzed and particles were tracked. The electric field is mostly uniform in Region 1 (Fig. 2.14D, E), hence the electrokinetic mobility (μ_{EK}) can be initially determined with negligible DEP forces. The velocity of the particle along the x-direction ($V_{p,x}$) can be related to the electrokinetic mobility and intrinsic particle DEP mobility (μ_{DEP}) with

$$V_{p,x} = E(\mu_{\mathrm{EK}} + \mu_{\mathrm{DEP}}\frac{\partial E}{\partial x}) \tag{2.38}$$

where μ_{EK} can be calculated by measuring the x-component of the particle velocity along the channel centerline ($V_{p,x}(x)$). Positive μ_{DEP} is defined as movement towards high field strength and positive μ_{EK} is defined as movement towards the negative electrode. Hence, ($V_{p,x}(x)$) will be:

$$V_{p,x}(x) = (\gamma^2k^2\mu_{\mathrm{DEP}} + \gamma k\mu_{\mathrm{EK}})x + \gamma^2k^2\mu_{\mathrm{DEP}} + \gamma k\mu_{\mathrm{EK}} \tag{2.39}$$

where $\gamma = \frac{i\rho}{w_1 h}$, ρ is the charge density, w_1 is the width of Region 1, h is the height of the channel, and k is the rate at which the channel tapers in Region 2 (cross-sectional area of 1.92 mm^2). Therefore, according to Eq. 2.39 the velocity slope of the particle ($\sim 500-2500$ µm) will be steeper in the case of pDEP and shallower in the case of nDEP compared to that predicted if there is no DEP force (Fig. 2.14F).

The streak-based velocity estimations were used to characterize 1 µm polystyrene particles. The electrokinetic mobility was estimated to be 3.5×10^{-4}cm^2/(V.s), which is dominated by electroosmotic flow and similar to other reported values [160, 161].

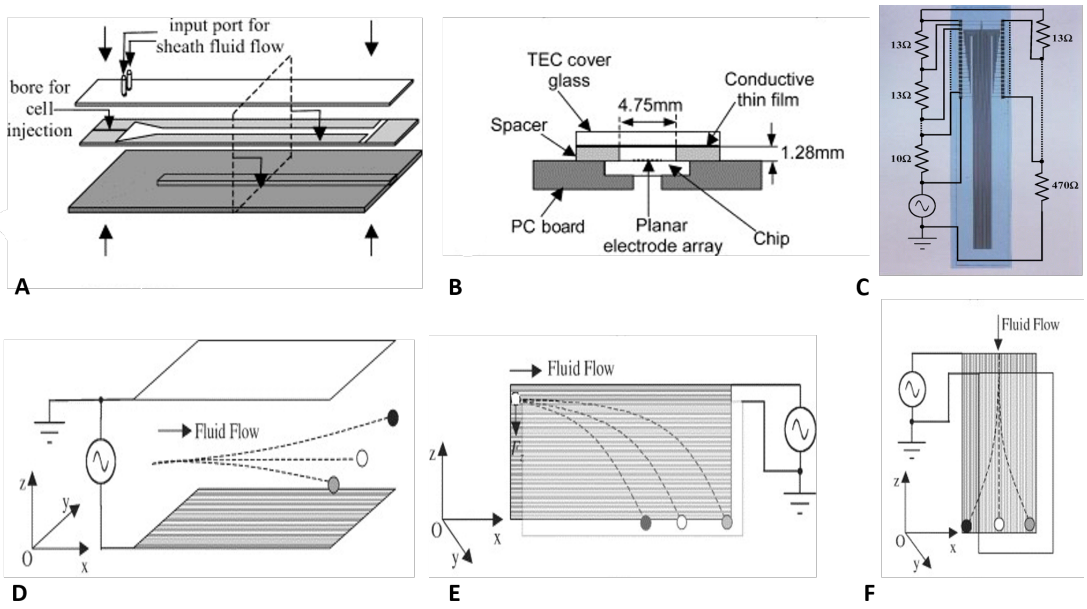

Figure 2.14. A schematic diagram illustrating the common types of insulative DEP applications where the insulating material (dark gray) perturbs the electric field (dashed lines) while traveling through the suspending media (light gray).(A) Array of insulators where the DEP trapping occurs between the insulators. (B) Obstructed channel where the DEP force maxima occur around the edges of the obstacle. (C) converging-diverging (saw-tooth) structure. (D) Diagram and dimensions of the insulative isoDEP device consisting of a wide uniform electric field segment (Region 1), taper segment where the electric field has a constant gradient (Region 2), and narrow uniform electric field segment (Region 3). (E) COMSOL simulation of the electric field of the insulative isoDEP device. (F) Theoretical velocity profile based on Eq. (2.39). Reproduced with permission from [159].

The estimated dielectrophoretic mobility was found to be $-2 \pm 0.4 \times 10^{-8}$ cm^2/(V^2.s) where the negative sign is due to the nDEP expressed by the polystyrene particles at such conditions.

The setup shows a good premise and capability for isoDEP as a tool to characterize the intrinsic dielectrophoretic mobility of particles; however, for bioparticles the medium conductivity (25 mS/m) and such high electric field magnitude ($100 - 200$ kV/m) would potentially be harmful for cells. This is because cells' viability decrease dramatically when using DC-based voltages [147]. Moreover, the electrodes in direct contact with the liquid medium which my induce electrolysis and/or induce significant Joule heating thus compromising DEP mobility measurements.

2.3.2.2 Biological Particles

Tada et. al [162] developed an insulative-based version of the creek-gap device. In their insulative creek device the fan-shaped microchannel was formed from a pair of planar insulators with a tapper gap of 50 µm (Fig. 2.15A,B), compared to 100

μm in the electrode-based device. The surface of the device was coated with 0.5% w/v ethanol solution of 2−methacryloyloxyethyl phosphorylcholine polymer, which is known to increase surface hydrophobicity and suppress cell adhesion.

Operation of the device was demonstrated using human breast epithelial cells (MCF10A) by applying an AC voltage of 34 V_{pp} at frequencies of 200 kHz and 50 MHz to the device. The electric field applied was higher than in the electrode-based creek-gap device (compare Fig. 2.12B to Fig. 2.15C). Unlike the electrode-based design, cells were able to exhibit both pDEP (at 200 kHz, Fig. 2.15D) and nDEP (at 50 MHz, Fig. 2.15E). The characterization of cells' Re$[F_{cm}(\omega)]$ was made in similar

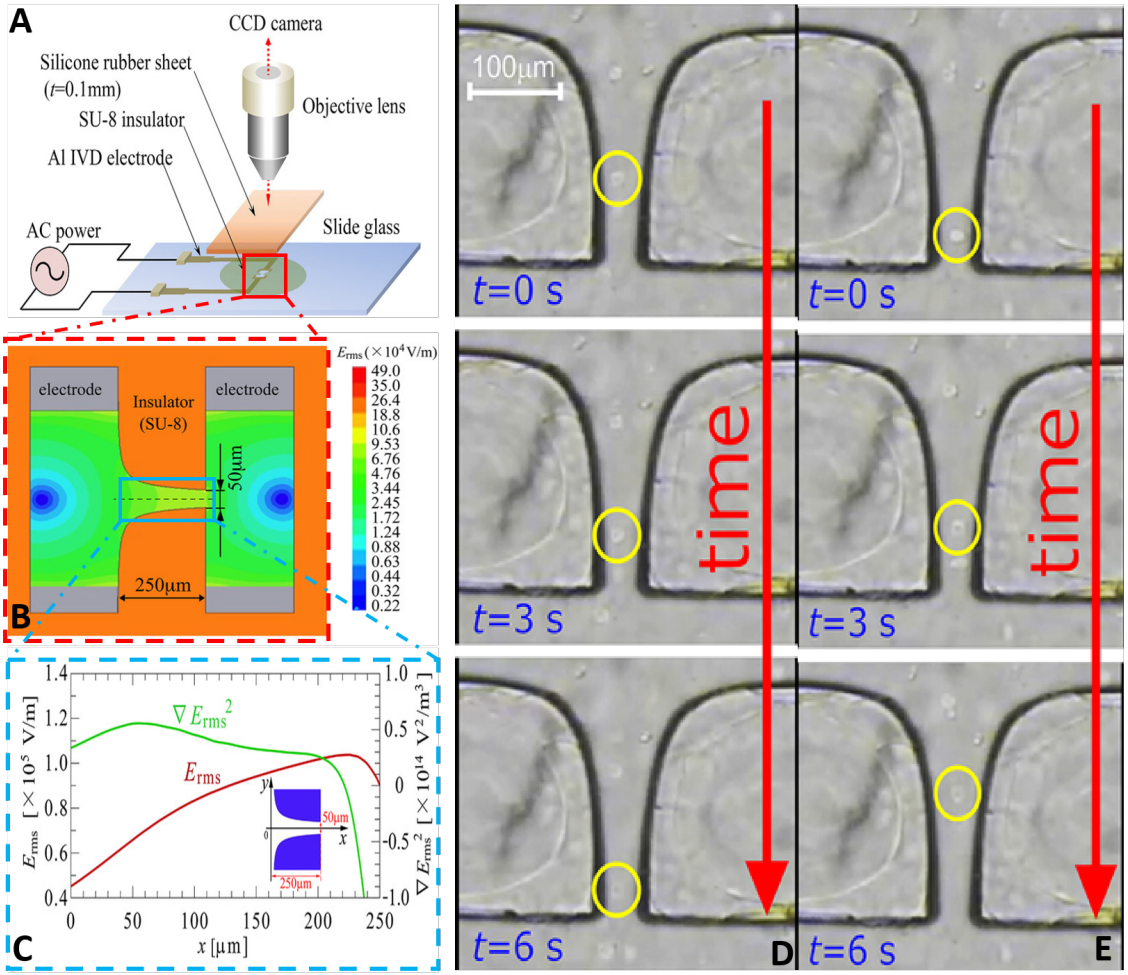

Figure 2.15. (A) The experimental setup of the insulative creek-gap insulative device. The shape and geometry of the creek-gap. (B) Geometry and dimensions of the primal part of the creek-gap device. (C) simulated profile of the electric field and gradient of field-squared along the centerline. Time-lapse images of the cells translating through the microchannel after application of 34 V_{pp} at (D) 200 kHz, causing cells to exhibit pDEP. (E) 50 MHz, causing cells to exhibit nDEP. Reproduced with permission from [162]

manner to what was followed in the electrode-based design. The values of $\mathrm{Re}[F_{\mathrm{cm}}(\omega)]$ were calculated to be 0.14 ± 0.01 for the frequency of 200 kHz and -0.12 ± 0.01 for 50 MHz.

A common issue in insulative-based devices is the necessity for high electric field to sustain the desired DEP force, especially for smaller cell sizes, which might compromise the viability of cells being studied. As example of such compromise is the decreased cell cytoplasm of MCF10A cells reported by the group as a result of high electric field magnitude (~ 100 kV/m). However, demonstrated results of $\mathrm{Re}[F_{\mathrm{cm}}(\omega)]$ of cells for both the p- and n-DEP effects could be evaluated with an accuracy required for practical application to biomedical engineering. Therefore, the demonstrated data suggest that the proposed creek-gap device shows a great potential to be used in the analysis of cell DEP properties.

Applications and description of the various configurations of generating an isomotive force are presented in Table. 2.1 which provides applications of isoDEP utilizing both electrode-based and insulative-based designs in chronological order. Recent work has demonstrated that isoDEP can address some unmet needs for biomedical applications including single-cell analysis; however, advances in throughput as well as combining characterization and separation simultaneously will add significant value to isoDEP. Further review on advances and applications of isoDEP for particle analysis can be found here[139].

CHAPTER III

DESIGN METHODS TO MITIGATE ELECTROHYDRODYNAMICS IN ISODEP MICROFLUIDIC DEVICE

This chapter discusses the advances in both design and fabrication of isoDEP to mitigate the undesired forces that act simultaneously on tested particles. This chapter contains content from published work (section 3.3) [117] but, additional information has been provided throughout the chapter.

The dielectrophoretic response of bio-particles are a function of their dielectric properties, which is influenced by their structural, morphological, and chemical characteristics. Therefore, each bio-particle has its own dielectric signature which has been demonstrated for a variety of cells [163]. DEP has been extensively used for selective separation and concentration of bio-particles and, since DEP depends on the bio-particles' intrinsic electrical properties, electrokinetic manipulation techniques do not require any labeling. DEP has trapped, manipulated, or sorted nanoparticles [164, 165], proteins [166], DNA [82, 167], viruses [165], and enabled particle patterning [168, 169] which has paved the way to other electrokinetic patterning techniques [170].

For any DEP device to function, it must have a mean of generating non-uniform electric field which can either be generated by means of (i) insulator structures or (ii) microelectrodes [171, 172]. As mentioned previously, the importance of DEP lies in its analytical capabilities. However, straightforward analytical application of DEP is nontrivial using traditional coplanar microelectrode designs and fabrication techniques. This is because the electric field within DEP systems is inherently, and purposefully, non-uniform whose force is proportional to the gradient of the field-squared (∇E_{rms}^2). In traditional DEP systems the force exerted on a particle is spatially non-uniform, typically by orders of magnitude over relatively short distances. For example, using coplanar electrodes the DEP force is greatest close to the surface of the electrodes but exponentially decreases with height above the electrode plane. Consider a 25 µm gap between two coplanar electrodes, the magnitude of the DEP force is approximately 100 times less for a particle 10 µm above the electrode edge compared to a distance of 1 µm [13]. Hence, an analytical DEP system is nontrivial because particles at different locations will be subjected to different DEP forces. To simplify analysis ∇E_{rms}^2 must be constant within the region of interest. The primary advantage of isoDEP is that the response of a particle is uniform throughout the analytical space can be obtained via particle tracking; this concept is analogous to how particle rotation is used to measure particle dielectric properties through measuring their rotational speed [120, 173]. Other designs have followed the premise of the

isoDEP design and have been used successfully for single-cell analysis applications [156, 162].

In addition to DEP, the applied AC field will also induce other electrokinetic phenomena such as: (i) Joule heating [19, 174–176]; (ii) AC electro-osmosis (ACEO) where the induced flow is generated by the action of an electric field on induced diffuse charges near a polarizable surface [177, 178]; and (iii) AC electrothermal hydrodynamics which occurs when the field interacts with fluid temperature gradients [17]. Such forces generate non-desirable fluid motion that impacts of the desired performance of isoDEP devices. Unwanted electrokinetics can be reduced through analysis of device dimensions, material properties, media properties, and the magnitude of the applied AC field. The goal of this study is to determine their impact on particle translation relative to particle translation caused by DEP forces within an isoDEP device, thereby enhancing its analytical capabilities.

IsoDEP produces a uniform DEP force using two different configurations: an electrode-based and an insulator-based arrangement In Allen, et al.'s work [15], the electric field required to induce the DEP effect was approximately 68 kV/m and 50 kV/m for the electrode-based and insulator-based versions, respectively. In general, the insulative-based design might require higher applied voltages to achieve the same DEP effect. This is due to the larger distance between the electrodes (on the order of millimeters) which requires higher voltages to achieve the same field strength compared to the electrode-based design. At these large fields ($>$ 50 kV/m) cell death may occur if cells are exposed for several minutes or at low frequencies [137, 179, 180]; however, this is not the case for isoDEP where the field is applied to an individual cell for less than a minute. In addition, high electric fields cause Joule heating which, in turn, causes the local temperature-induced variations in the conductivity (σ_m) and permittivity (e_m) of the suspending medium causing electrothermal forces [13, 76]. Jaeger, et al.[181] found that the electric field induced temperature rise is proportional to conductivity of the medium, which impacts studies with biological cells as they require suspension in conductive media (typically larger than 0.1 S/m). Although reducing the conductivity of the suspending media can mitigate Joule heating, it's not the ideal solution when considering cell viability [19]. 3D extruded electrode designs have been proposed to reduce Joule heating 8–10 times lower than planar electrode designs, because it requires lower electric fields to obtain same DEP effect along the channel's depth [182].

Design and Fabrication Methods of isoDEP Platform

In this work, various isoDEP design have been attempted to achieve a reliable, inexpensive, and operating devices either in electrode-based or insulative-based designs. The main goal of those designs is to mitigate the complications in the devices that leads to undesired operation. Also, to achieve an off-cleanroom fabrication technique that can be achieved in labs without the need for expensive fabrication tools.

1 Insulative-based IsoDEP Design Methods

The most common way to achieve an inexpensive microfluidic device is through molding multiple devices from a master mold which reduces the cost per chip. In our case, we used SU-8 master mold to produce PDMS isoDEP devices. After that, the PDMS microchannel is aligned manually and bonded, with the help of a plasma wand pretreatment, to either a patterned ITO glass coated electrodes Or, a patterned gold electrodes that have been deposited onto a glass wafer.

An isoDEP master mold has been fabricated from SU-8 as the following: First, the wafer has to be dehydrated on a hotplate at 110°C for 2 min. Then, some drops of MCC Primer 80/20 (MicroChem Corp., MA, USA) have to be dropped and after waiting 10 s it can be spun at speed of (4000 rpm for 30 s with an acceleration of 1000 rpm/s^2). After that, it will be baked on the hotplate at 110°C for 2 min. Then, a layer of SU-8 2150 (MicroChem Corp., MA, USA) is spun over the substrate in two phases so as to achieve a thickness of 200 µm:

- First phase for 5 s at low rotation speed (500 rpm) with acceleration of 100 rpm/s^2 which works to distribute the resist over the whole surface
- Second phase which longer and with higher rpm (30 s at 2820 rpm and acceleration of 500 rpm/s^2) is designed to obtain the desired and uniform thickness of 200 µm.

Then, the substrate is prebaked for 6 mins at 65 °C onto a hot plate then the temperature elevated to 95 °C and left there for 40 min after which the hot plate is switched off and left to cool down to room temperature. It's strictly advised to check the planarity of all the working surfaces and equipment used in the process, since the resist has a relatively good reflow capability also helped by the long bake and relaxation steps required, so as to avoid final non-uniform thicknesses of the mold. As the master mold will be fabricated using SU-8 and hence this mold will be used to create new replica, so the problems due to the adhesion of PDMS and the SU-8 must be minimized to allow an easy peeling-off process of the PDMS casted into the mold. This is achieved by plasma polymerization of C4F8 passivation layer deposited onto the SU-8 layer which is necessary to allow for ease of de-molding PDMS [183]. Fluorine containing plasma is known to decrease surface energy and increase the hydrophobic behavior of surfaces [184]. The microchannels were achieved with a gap of 500, 400, 300, 200 µm at ($\theta = 60°$) ($r_{60,1}$= 77 µm and $r_{60,2}$= 577 µm for the 500 µm gap device). The centers of the inlet and outlet wells (2 mm in diameter) were 3.0 mm from the device origin.

For creating PDMS replicas, PDMS casing, Sylgard 184 elastomer and curing agent (10:1wt.%) are mixed and poured onto the mold configuration and then cured for 30 mins at 80°C. Figure 3.1 shows the final PDMS device that's obtained after de-molding process as well as, after bonding to patterned ITO glass substrate.

For an off-cleanroom fabrication process, one can go with PDMS replicas bonded to patterned ITO electrodes. However, during the operation of the device, leakage of the sample was always observed due to the pressure of the fluid from the inlet which

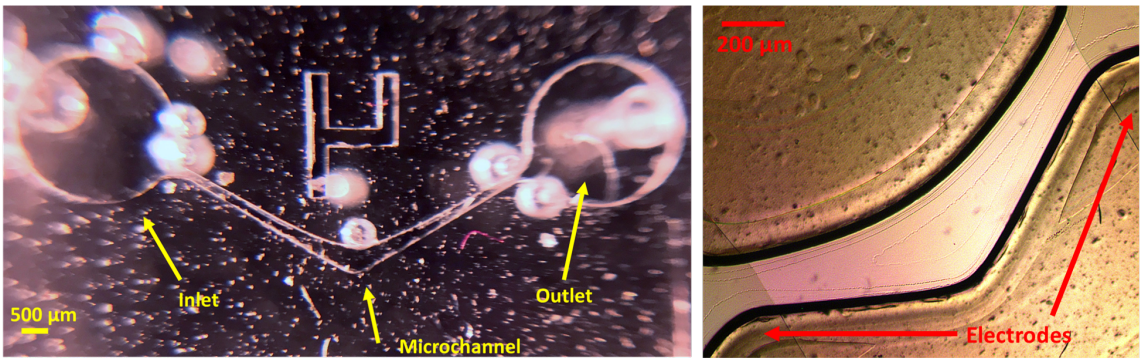

Figure 3.1. Realization of PDMS isoDEP device (Left) Microscopic image for the finished isoDEP PDMS replica. (Right) PDMS device bonded to a patterned ITO electrode.

compromised the operation of the device. Hence, other techniques were pursued to obtain an inexpensive and reliable device.

Dry film photoresist can be considered a cheap and fast alternative to SU-8. The buried microfluidic device will be formed by fabrication of two active parts, A dry resist based microfluidic chip fabricated over a glass substrate, and an ITO -over glass- patterned electrode buried under it. Multiple (three/four) dry resist layers can be laminated (Ordyl SY300/550), achieving the desired buried microchannel thickness (150-160) µm, will be bonded at relatively low temperatures without the use of extra adhesives. A postbake transfers the resist into a rigid structure. The resist is qualified in terms of resolution, biocompatibility, and fluidic sealing. Fabrication in both a fully equipped clean room setting as well as a minimally equipped laboratory can be possible. A negative dry film photoresist Ordyl SY550 (50 µm thick resist, Elga Europe) is used. It consists of a resist layer protected on one side by a polyester (PET) layer and on the other side by a polyethylene (PE) layer. The PE layer is peeled off and the photoresist is applied on a previously selected pre-processed glass substrate. Substrates were previously cleaned ultrasonically in a 2% detergent solution, rinsed for 10 min in DI water and dehydrated for 1 hour at 120°C in an oven. Before lamination, complete glass substrates were placed on a piece of cleanroom paper. Ordyl was cut such that it covers the wafer completely but did not exceed the borders of the cleanroom paper, so that laminator rolls were protected. The top of the resist sheet was attached to the cleanroom paper with scotch tape, before removing the protective PE layer. To prevent bubbles or trapping, it was important that the resist was not in contact with the substrate until lamination.

After manual application of the first layer of resist using a hard rubber roller, the substrates are put through a hot-roll laminator (GBC 13 Pro, speed 3 setting, 176 °F/ 80 °C. In order to increase the resist thickness, the protective PET layer had to be removed from the already laminated layer of resist and the lamination procedure repeated, the lamination procedure repeated with the same setting mentioned above. It's noted that after the first step lamination, high temperature is used to allow easy peeling of the PET layer which will stick to the cleanroom paper. After the last

lamination step (which is performed with 150 °F/ 65.5 °C speed 5, the protective PET should remain on top to prevent the resist surface from oxidation. The resist is exposed with 150 400 mJ/cm^2 UV light using a custom-built UV lamp mask of 401 nm wavelength. For the exposure of resist on glass substrates, a sheet of Riston R anti-reflective foil is placed under the substrate with a droplet of water in between the Riston film and the glass. This prevents unwanted exposure effects due to reflection and non-perfectly parallel exposure. As seen in Table 3.1 four different samples have been treated separately to figure out which parameter setting can lead to final best device fabrication, as long post baking times will lead to hard and longer developing process as well as, short exposure time will lead to thinner void (microchannel) formation. The resist is then developed for 30-60 min in homemade developer (90% Xylenes and 10% Isopropanol (IPA) (Thermo Fisher Scientific), using a nitrogen spray and paddle development. After that, the sample is rinsed for 30 s in BMR rinse (Elga Europe) once again by using a paddle rinsing followed by a 5 min spray rinse. The samples are dried at room temperature for half an hour followed by the double bonding of the second sub- strate. The sample is put into an oven (Yamato DX-300) at 70-95 °C under a pressure of 650kPa. The pressure is applied using two parallel metal plates on which the required amount of weights can be placed. After half an hour temperature is ramped up in steps of 20 °C per 20 minutes to 150 °C followed by a 2-hour post-bake at 150 °C. For full wafer double bonding, a heated press is used (Carver No3969 CE press). The same temperature and pressure settings as for the oven are used.

Table 3.1. Experiment setting for dry film photoresist-based prototypes. Note: (') stands for minutes, (") for seconds

Process Sequence	**Sample A**	**Sample B**	**Sample C**	**Sample D**
Exporue Time (@ 2.94 mW/cm^2.s UV Energy Dosage	20 s	25 s	30 s	35s
Post Exposure Bake (PEB)	2' 15" @ 55 °C	2' @ 85 °C	2' 15" @ 55 °C	2' @ 85 °C

Electrodes are patterned to achieve both the -ve and +ve field. ITO on glass (25 X 75 mm) (Thermo Fisher Scientific) were first cleaned with Acetone and IPA prior to the patterning process, then rinsed in DI water. The substrates are then patterned with 150-400 mJ/cm2 UV light using a mask aligner (Karl Suss MA6/BA6). After that, they are developed using HCl solution in wet bench chemical etch process. For an off-clean room process, the electrodes were masked using a cutter plotter (Roland GS-24, Roland DGA Corporation) generated Vinyl mask. In this case, there is no need for mask aligner which will reduce the cost of fabrication. However, the resolution of this process is defined by the resolution of the cutter plotter used.

Figure 3.2 shows the results of the final isoDEP chip with two different microchannel widths that are suited for different particle sizes.

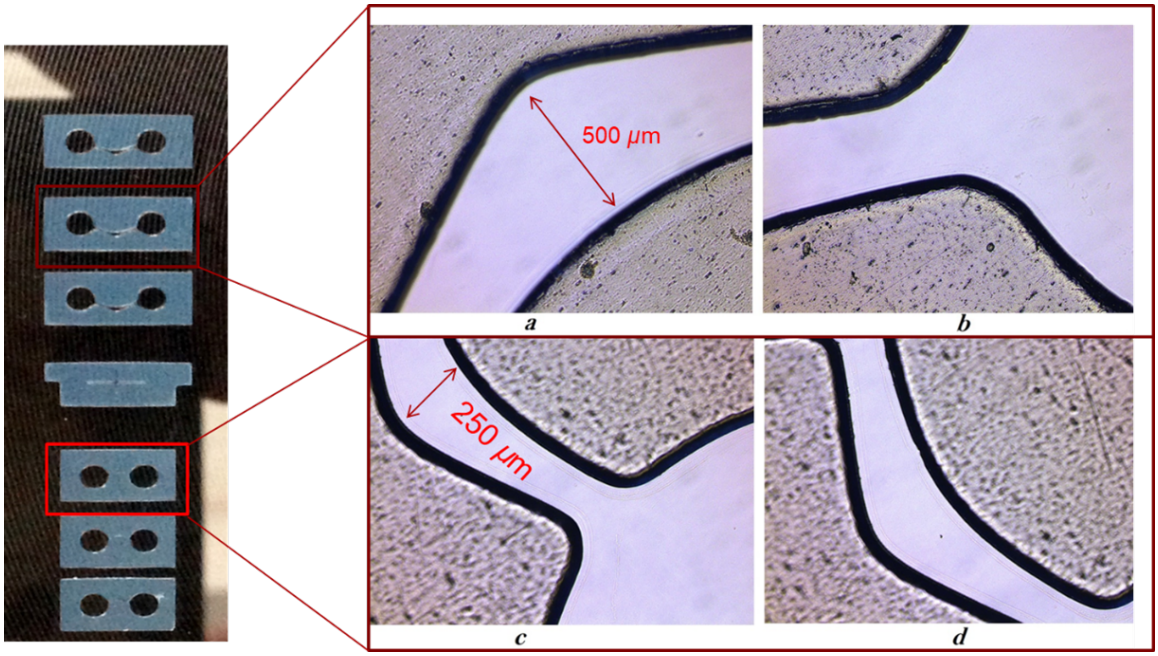

Figure 3.2. Dry film resist isoDEP microchannel on patterned ITO coated glass substrate. Two different microchannel widths are attempted for different particle size and electric field applications. On the right, a microscopic image of both microchannels is shown indicating fine sidewalls and microchannel contours.

The only disadvantage of such unsealed isoDEP devices is the need to use glass coverslip on the top of the microchannel. However, such non-monolithic structure is the instability of the liquid beneath the coverslip which in turns generates undesired medium motion as well as the tested particles which compromise the operation of the device.

For an inexpensive sealed device, a PDMS conductive electrodes are used to be bonded to a PDMS microchannel. First, PDMS replicas, PDMS casing, Sylgard 184 elastomer and curing agent (10:1wt.%) are mixed and poured onto a glass substrate ($4'' \times 4''$) and left to cured at 80 °C for 45 min then de-molded from the glass substrate. Then, a Vinyl adhesive mask which configure the electrodes, designed with cutter plotter (Roland GS-24, Roland DGA Corporation), is then attached to the PDMS (Fig. 3.3A). An inexpensive conductive paint (MG Chemicals. USA) with surface resistance @ 50 μm: 100 Ω/sq is then coated upon the surface of the PDMS masked layer and then left to cure for 24h (Fig. 3.3B). After that, the Vinyl adhesive mask is peeled off and the final coated electrodes are obtained. Another electrode design is proposed to achieve easy chip dicing/cutting to obtain separate isoDEP device (Fig. 3.3D). Using the prepared PDMS isoDEP microchannels following same process utilized to realize the device in Fig. 3.1, is then aligned manually and bonded to the PDMS coated electrodes (Fig. 3.3E). However, when the device is tested, high electric field was required to operate the device. After two trials, electrode damage and erosion were noticed (Fig. 3.3F) which in turns compromised the operation of the device. Also, due to the low conductivity of the coated electrodes, high frequencies

signals were not propagated well through the electrodes which showed no effect for the tested particles when actuated with high frequency signals.

As the electrodes are buried under the channels which require high electric field magnitude to operate the device. A common issue in insulative devices is the necessity for high electric fields to sustain the desired DEP force, especially for smaller cell sizes, which might compromise the viability of cells being studied. This is usually one of the disadvantages of the insulative-based isoDEP devices. As the device was intended to characterize phytoplankton cells, there will be a need for high electric field magnitudes at higher frequencies ($\sim 40-80$ MHz) needed [150]. High frequency benchtop amplifiers are usually very costly, hence, in this work, a custom-built inexpensive amplifier is attempted to assist with the operation of the isoDEP device testing.

1.1 Design of Power Amplifier

Apex PA94 power amplifier (Apex Microtechnology, USA) (900V, 700V/µs) is a very high-power operational amplifier designed as a low-cost solution for driving continuous output currents up to 100mA and pulse currents up to 200mA in high-voltage applications. PA94 has been assembled according to the manufacturer guidelines (Fig. 3.4A). The final PCB assembled circuit has been tested at high frequency (30 MHz) and showed a gain of 5.5 (V/V) of the input signals as expected from gain Vs frequency curve. However, for higher gain at MHz range, T16 RF transformers (mini-circuits, USA) can be used. However, an advanced PCB circuit is required to multiplex between low frequency and high frequency amplifiers.

Observed electrohydrodynamics

In this work, several fabrication and device designs have been made to obtain a better DEP analysis microfluidic device that was used to investigate the properties of Phytoplankton cells. It was concluded that devices fabricated by full depth etching using DRIE to create the microchannel resulted in a good DEP response at lower voltages compared to devices made from PDMS microchannel bonded to patterned ITO coated glass electrodes. However, rough wall surface containing etched silicon spikes (Fig. 3.5) generates high localized electric field that generates localized heating which in turns generates electrothermal vortices that compromises the operation of the device. Also, the heat generated is enough to melt polystyrene particles and infuse them irreversibly to the glass substrate which in turns compromise the area of vision of the isoDEP chip over time. Hence, isoDEP microchannel made from insulative PDMS insulative can minimize this electrothermal hydrodynamics (ETH) effect by making electrodes in far sites from the analyzing window. In addition, it can be easily tailored to the desired cell size and microchannel height, but it requires

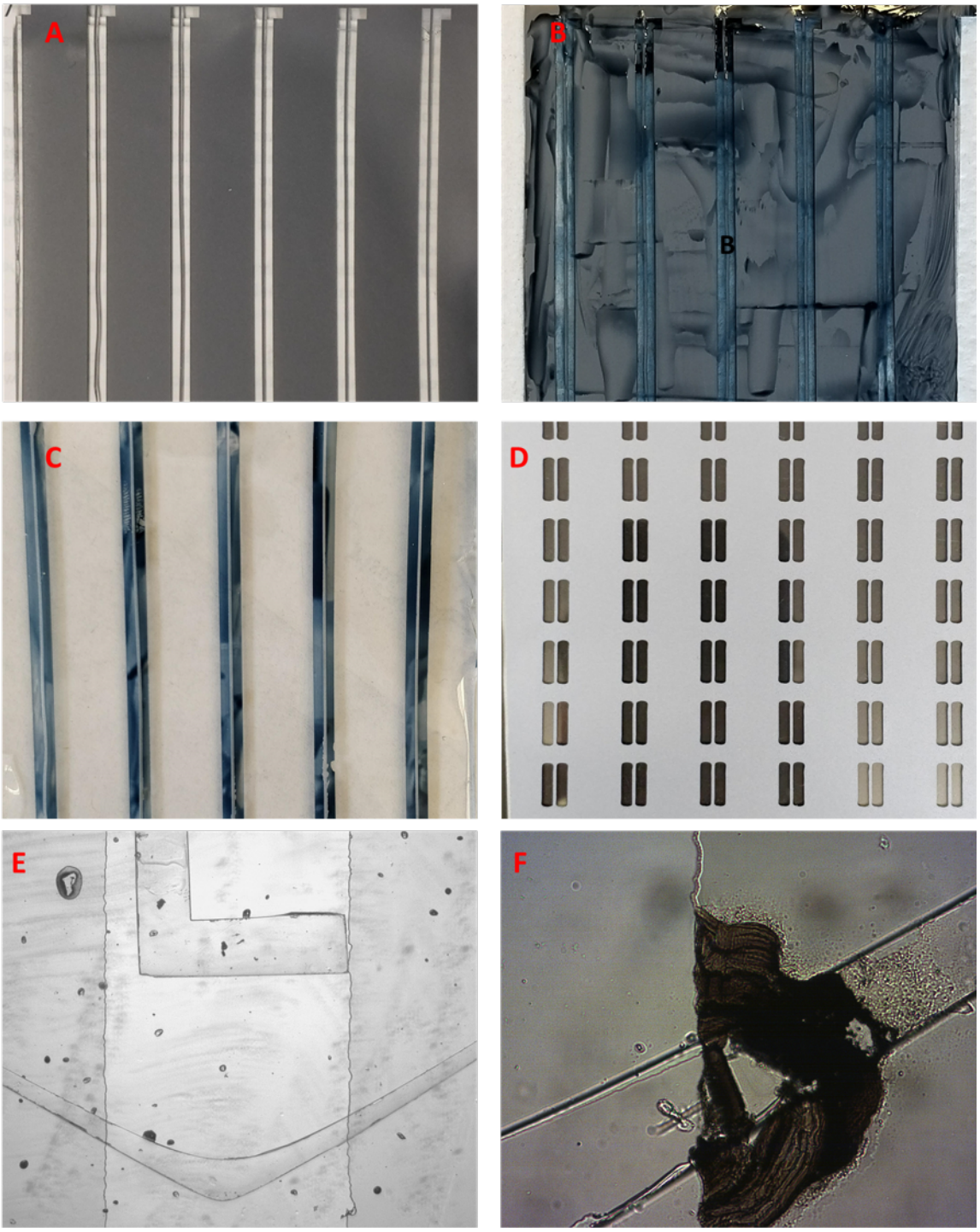

Figure 3.3. (A) Vinyl masked PDMS. (B) Conductive paint poured onto the masked PDMS to define electrodes. (C) Final conductive pained electrodes onto PDMS. (D) Different electrode design to achieve easy chip dicing. (E) Final isoDEP device made from bonding PDMS microchannel to PDMS conductive coated electrodes

a higher AC voltage amplitude which requires expensive amplifiers to provide high

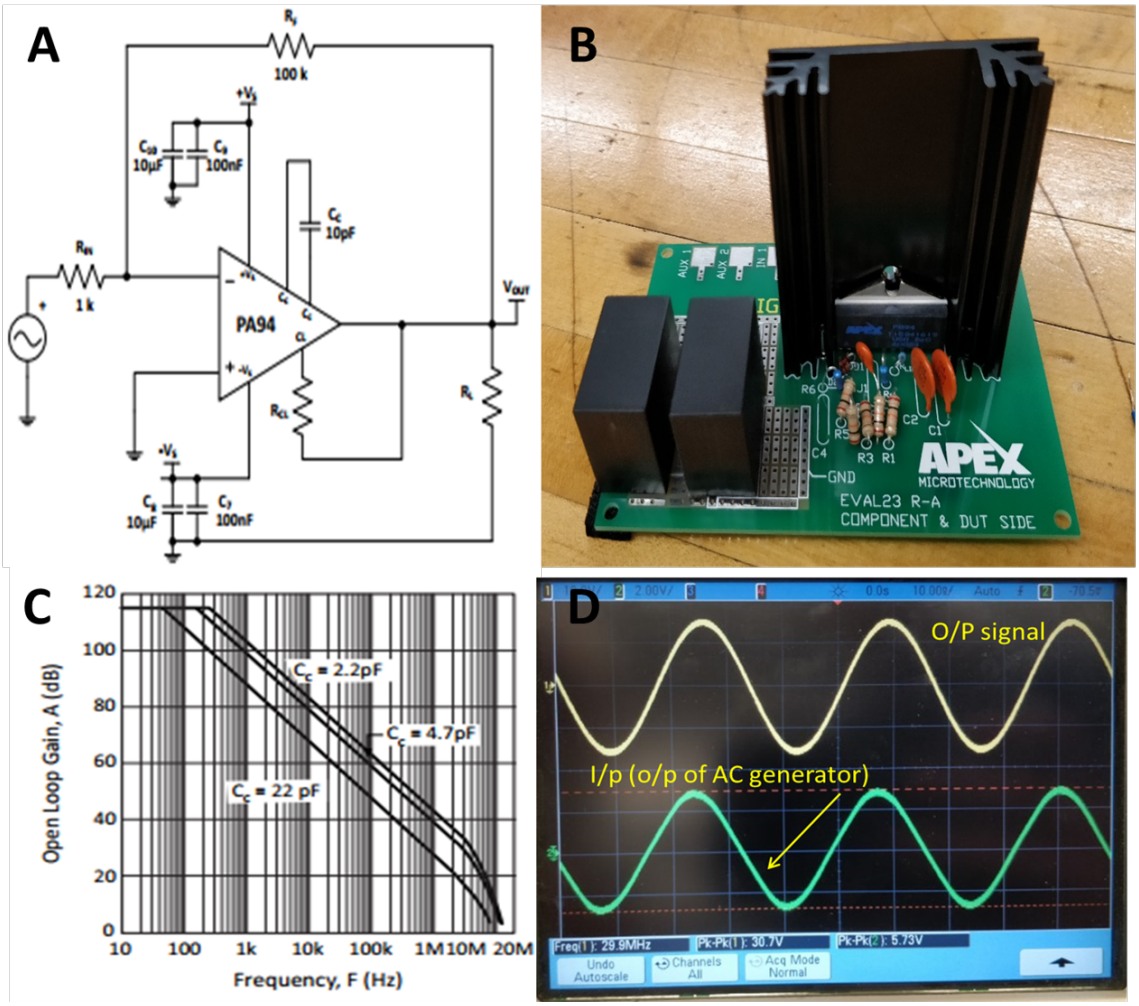

Figure 3.4. (A) Schematic diagram of the circuit design for the amplifier. (B) Final assembled amplifier circuit. (C) Gain Vs Frequency curve showing the low gain at high frequencies. (D) Oscilloscope image of the measured gain at 30 MHz.

amplification at high frequency.

To visualize the rule of ETH forces in an isoDEP device, further analysis has been made to conducted. Figure 3.6A shows COMSOL®simulation analysis for the fluid flow velocity inside an insulative-based isoDEP device with r_{60} = 0.05 mm, h (microchannel height) =5 µm showing. The analysis clearly shows the effect of the ETH induced force onto the fluid which generate induced vortices which in turns compromise the operation of the device. Experiments have been conducted to visualize such ETH force effect. 2 µm fluorescent particles submerged into 1 mS/m suspending medium is then pipetted inside an insulative isoDEP device. A video has been captured and then analyzed with PIVlab MATLAB®tool to produce the streamline vector analysis of the fluid flow velocity. An application of of 110 V at 500 kHz was enough to induce high fluid flow velocity magnitude that induced vortices within the microchannel (Fig. 3.6B). Figure 3.6C, D show a confocal image (Ixon

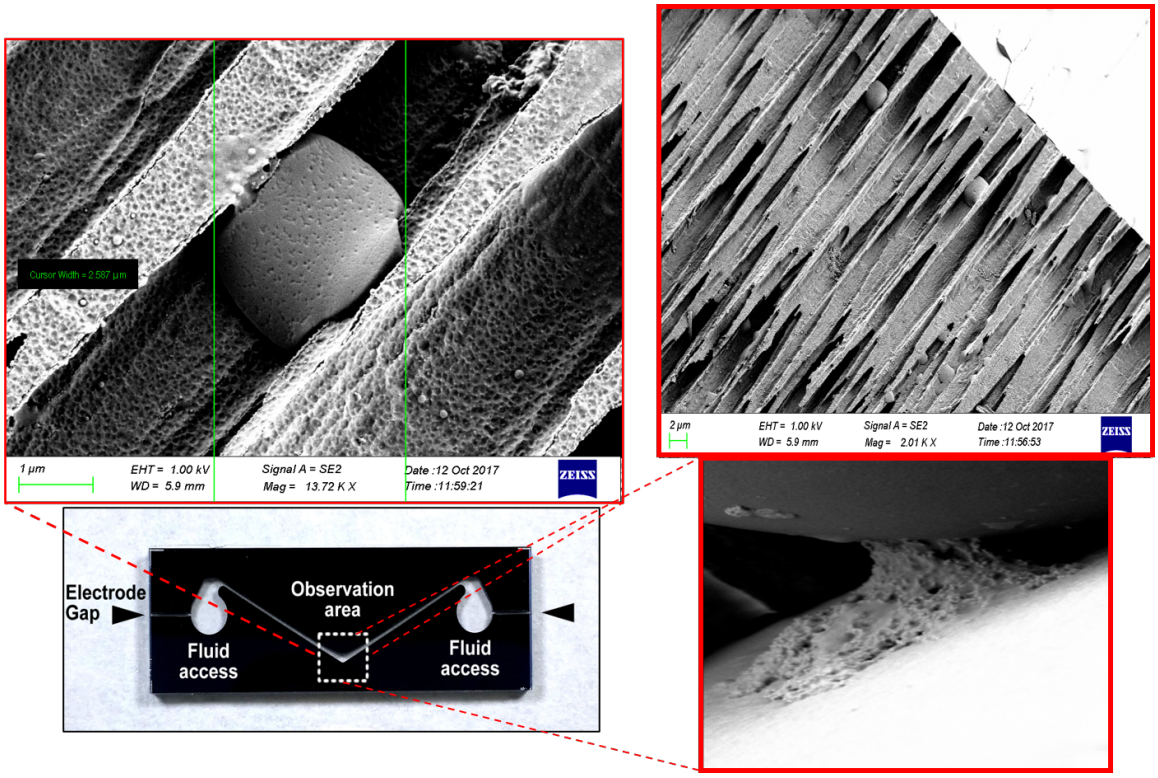

Figure 3.5. SEM images showing a close-up view of the DRIE sidewalls. On the top left, a polystyrene particle (1 µm) melted and infused inside the spikes of the silicon wafer due to the localized generated heat from the applied electric field. On the bottom right, a polystyrene particle is melted to the bottom glass substrate.

Ultra, Nikon Eclipse TI-U) of a DRIE microelectrode-based isoDEP device for 2 µm fluorescent particles submerged into 1 mS/m medium. 50 V at 500 kHz was applied to the sample and a video was captured in stack mode, which emphasize the effect of the ETH induced motion of the fluorescent particles' trajectories and vortices and bubbles along the depth of the microchannel which caused a separation of the fluid layers within the fluid.

Electrohydrodynamic motion was observed at larger applied potentials ($>$ 50V for microelectrode isoDEP, $>$ 400 V for insulator isoDEP); a more comprehensive investigation is needed to be conducted in to determine the impact of such fluid motion on particle trajectory. Electrohydrodynamic motion, in general, is either AC electro-osmosis (ACEO) and/or electrothermal (ET) flow [185, 186] which will be mainly discussed and studied during this work to minimize the unwanted electrokinetic phenomenon that could interfere with the isoDEP operation. ACEO occurs when the electric field acts upon the charges accumulated on the surface of a polarized electrode, inducing hydrodynamic slip [187]. It is expected that this isoDEP device will produce negligible ACEO flow as the tangential component of the electric field at the electrode surface is significantly weaker compared to other studied ACEO microelectrode geometries like interdigitated electrodes [188]. Therefore, it is hypothesized that ET flow is the cause of the observed electrohydrodynamic motion. In ET

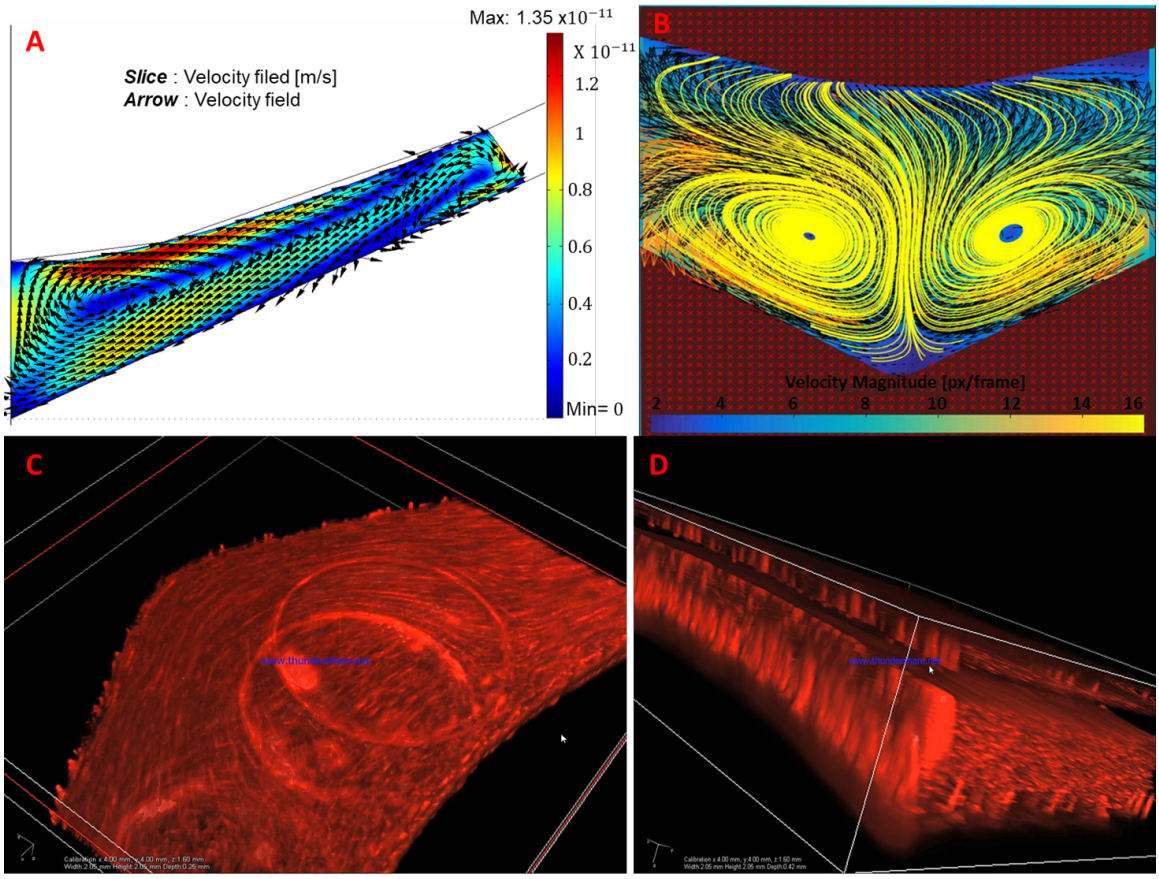

Figure 3.6. : Demonstration of electrothermal heating effect in isoDEP device (A) COMSOL®simulation of the flow field for an insulator isoDEP device at its mid-plane with r_{60} = 0.05 mm, h (microchannel height) =5 µm showing how ETH can affect the desired DEP force acted on particles. (B) PIVlab experimental results showing fluid flow streamlines for insulative isoDEP (r_{60} = 0.05 mm, σ = 0.001 S/m). Video was captured with 10x magnification and, 0.465 µm/px, 300 ms Frames). (C, D) confocal microscopic images for DRIE microelectrode-based isoDEP device showing formation of bubbles and fluid layer separation. (A) Credits for Dr. S. Williams.

flow the electric field acts upon dielectric gradients (permittivity, conductivity) in the fluid caused by Joule heating [189]. The silicon in the microelectrode isoDEP device may serve as a heat sink as well as provide more efficient heat transfer (compared to the glass boundaries) and, thus, propagate temperature gradients in the same direction as the applied field. Insulative-based isoDEP systems are likely more favorable from a heat transfer perspective as temperature gradients are more orthogonal to the field direction relative to the silicon-based devices, thereby reducing the effects of electrothermal flow [190]. Hence, one of the aims of this work to study the heat transfer and resulting electrohydrodynamics of isoDEP devices, and conduct scaling law analysis to minimize unwanted ET flow as well as maximize the DEP force inside the microchannel.

ACEO is generated from the movement of ions in the electric double layer at the

interface between electrode and media. ACEO can be prominent at lower frequencies (typically below 10 kHz) due to the frequency depenent polarization of the electrode double layer which disperses at higher frequencies [176]. Fortunately, ACEO can be considered negligible in isoDEP as the tangential component of the electric field at the electrode surface is significantly weaker due to the inherent geometrical configuration of isoDEP, especially compared to other microelectrode geometries like interdigitated electrodes [15, 191]. The most significant undesired electrohydrodynamic force that occurs in an isoDEP device is derived from electrothermal hydrodynamics [16–18]. Therefore, there is an extreme need to develop design rules for the geometrical configuration of an isoDEP system and develop scaling laws [19] to minimize ET flow relative to isoDEP-induced particle translation for both microelectrode and insulative platforms. These design rules are based on analytical predictions, putting into account how the DEP and ET velocity scale with electrode size, applied voltage, fluid conductivity, and the size of the particles. This approach can be applied to other DEP systems that want to reduce unwanted ET flow.

Scaling Law Analysis of Electrohydrodynamics and Dielectrophoresis for IsoDEP Device

In this section the electrokinetic and heat transfer equations will be developed [192], with some simplifying assumptions, and apply them to isoDEP device geometry. First, we will derive particle translation due to isoDEP in terms of particle diameters per second for a given device length scale and applied potential. Second, for a given particle translational velocity we determined the resultant Joule heating due to the applied field for a given device configuration and channel length scale using analytical conduction relationships based on the device geometry. Last, electrothermal hydrodynamics was estimated from calculated temperature gradients. ET motion is presented relative to isoDEP translation for a range of microchannel geometries.

IsoDEP devices have two general configurations. First is a microelectrode-based isoDEP device where the microchannel wall itself serves as the electrode; one method of fabricating this type of device is to perform DRIE of doped silicon bonded between two glass substrates [15, 156]. The second configuration is an insulative-based device where the microchannel walls are formed from electrically insulative materials (ex: SU8, PDMS, or glass [171, 193]) and the electric field is applied through the channel itself. The curvature of the isoDEP microchannel walls needs to follow the curvature illustrated in Figure 3.7A. The largest channel width occurs at $\theta = 60°$and is defined as the characteristic width, r_{60} (Fig. 3.7A). For the insulative device L refers to the distance between the device origin and the downstream electrode (Fig. 3.7A) [15, 144]. The insulative isoDEP device is less expensive due to more simplistic fabrication methods (ex: soft lithography) compared to extruded microelectrode-based platforms; however, a significantly higher voltage is required from the insulative platforms for comparable DEP performance due to the longer distance between the electrodes.

Several geometric parameters were defined for the proceeding analysis. The mi-

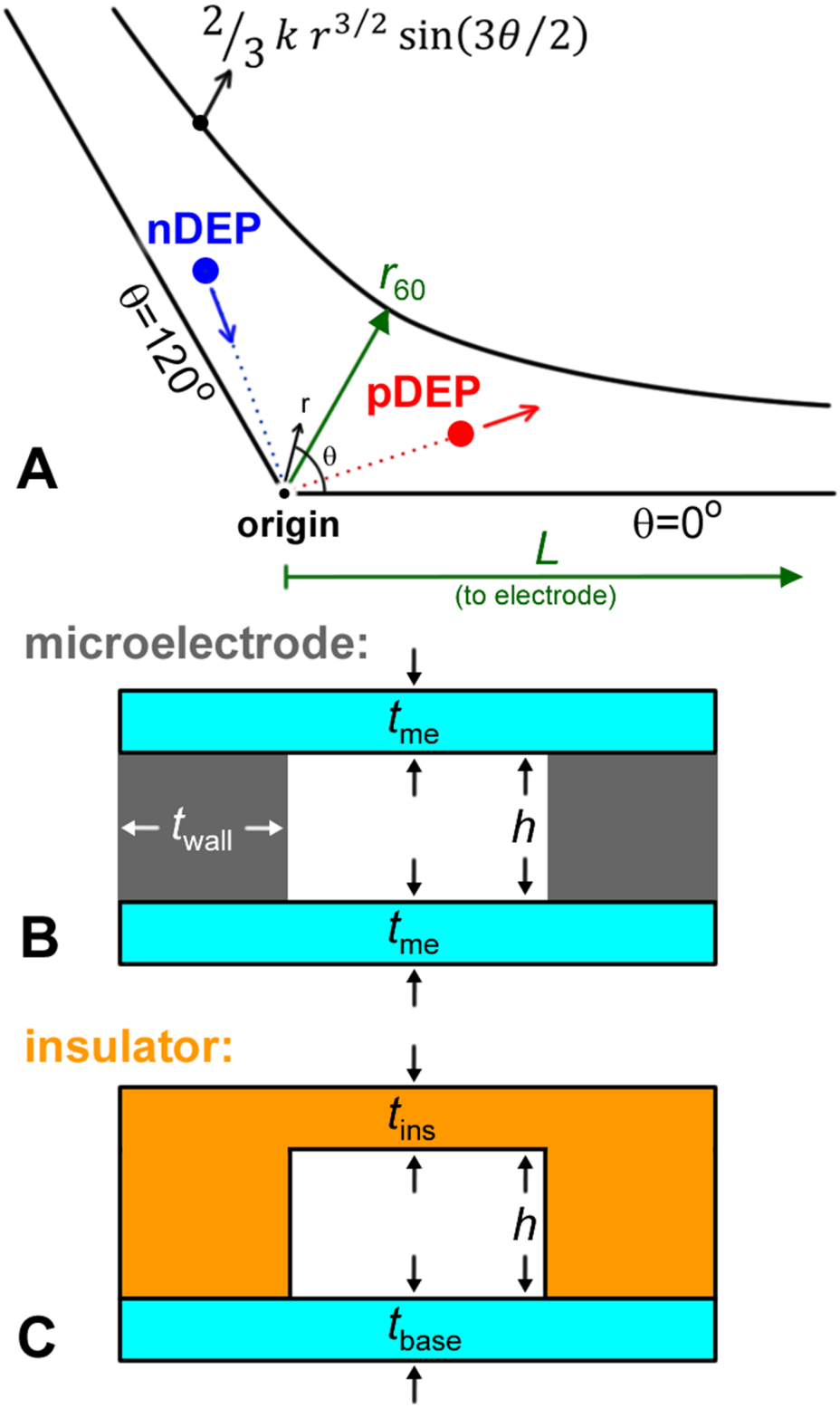

Figure 3.7. (A) Illustration of the isoDEP microchannel geometry which can be demonstrated with (B) vertical microelectrodes serving as the walls or (C) an insulative structure with potential applied through the channel. Variables for the analysis herein are labeled

croelectrode device (Fig. 3.7B) has a microchannel height h, a lid and base thickness of t_{me}, and an electrode wall thickness of t_{wall}. The insulative device (Fig. 3.7C) has a microchannel height h, top insulative thickness t_{ins}, and a substrate thickness t_{base}. If the channel configuration follows that of Figure 3.7A the applied electric potential will yield a constant ∇E_{rms}^2 (refer to [15] for derivation). The potential will be in one of the following forms (in cylindrical coordinates)

$$V = (\frac{2}{3})kr^{3/2}\sin(3\theta/2) \quad \text{For electrode-based} \tag{3.1}$$

$$V = (\frac{2}{3})kr^{3/2}\cos(3\theta/2) \quad \text{For insulative-based} \tag{3.2}$$

where $k^2 = \nabla\left(|E|^2\right) = \frac{9(\triangle)^2}{4(\delta)^3}$ and δ=r_{60} is the characteristic electrode spacing (for microelectrode-based and δ=L for insulative-based devices), and $\triangle$V is the potential difference between the origin and δ. The length scale guides overall electrokinetic behavior and, thus, should be selected based the performance of desired particle translation. First, the magnitude of gradient field-squared k^2 2will determine the field strength required to translate a particle of radius, a, with a velocity,$v = (2a)n$, expressed as an increment of n particle diameters per second. Assuming Stokes drag and that the particle has reached terminal velocity, the particle's dielectrophoretic velocity is related to n with

$$v_{\text{DEP}} = \frac{F_{\text{DEP}}}{6\pi\mu a} = \frac{2\pi\varepsilon_m a^3 Re\left[f_{CM}\right](k^2)}{6\pi\mu a} = (2a)\,n. \tag{3.3}$$

These relationships were used to correlate k^2 with particle size, particle translation, device length scale, and the applied potential. Next, the required k^2 is found for a desired isoDEP particle translation and device geometry. Then temperature gradients were estimated from the input field strength (which is a function of k^2) and the heat transfer properties of the device. Heat conduction was assumed to be the dominant mode of heat transfer due to the nature of Joule heating being accompanied with a low Nusselt number [175, 177, 194]. The heat conduction model was used to find the temperature at the microchannel walls and the maximum temperature in the center of the channel; hence, the temperature gradient within the channel itself can be subsequently calculated.

For simplification of the heat transfer model, a rectangular channel geometry of a fixed width, w, is used. The outside wall temperature, T_{wall}, is assumed to be the same around the device perimeter (isothermal). The heat transfer model herein combines two approaches: (i) heat transfer resistance models for calculations through the solid material and (ii) analytical estimations for the relationship of the channel wall temperature and the maximum temperature. The resistance models are illustrated in figure. 3.8. The lid material is attributed with a thermal resistance, R_{lid}, which is in parallel with the resistance attributed to the base material, R_{base}. Resistance is related to conduction shape factor, S, with $R = \frac{1}{SK}$ where K is the material thermal conductivity. The shape factor of the lid and base assumes the microfluidic channel

as an isothermal rectangular parallelepiped buried in semi-infinite medium having an isothermal surface; for this case the conduction shape factor will be [195, 196].

$$S = 1.685\ L_c \left[log\left(1 + \frac{t_s}{w}\right)\right]^{-0.59} (t_s/h\ )^{-0.078} \tag{3.4}$$

where L_c is microchannel length and t_s is the substrate thickness (either t_{me}, t_{base}, or t_{ins}). The electrode-based version included another resistance element that takes into account heat transfer through the conductive wall features, $R_{\text{wall}} = t_{\text{wall}}/(K\ h\ L_c)$. The equivalent resistance network, R_{eq}, is related to the heat generated inside of the microchannel, q, with $q = (T_{\text{wall}} - T_o)/R_{\text{eq}}$ where To is the outside ambient temperature. For simplicity, To is set to zero such that subsequent temperature calculations will reflect those above ambient conditions. The wall temperature can be related to device parameters from

$$T_{\text{wall}} = \ R_{\text{eq}}\ q = R_{\text{eq}} \left(\sigma_m E^2\right) (\delta\ h\ L_c) = R_{\text{eq}} \left(\sigma_m\ k^2 r\right) (\delta\ h\ L_c) \tag{3.5}$$

where σ_m is fluid conductivity, $|E|^2 = k^2 r$, and $\delta = r_{60}$ or L for an electrode-based or insulative-based device, respectively. Both insulative and electrode-based maximum temperatures are linearly proportional to r. The wall temperature will be independent of channel length, L_c, as this term in Eq. 3.5 will cancel with itself from R_{eq}. The maximum temperature at the center of the microchannel at a given radial location is calculated using a 2D solution from J.H. VanSant [197] where the temperature, T, inside of a rectangular isothermal perimeter (T_{wall}) with volumetric heating, q‴, heated, is a function of its position (using Cartesian coordinates, x,y)

$$\frac{(T - T_{\text{wall}})K}{q'''\ (h/2)^2} = \ \frac{1}{2}\left(1 - Y^2\right) - 2 \times \sum_{n=0}^{\infty} \frac{(-1)^n \cosh\left[(2n+1)\frac{\pi}{2}X\right] \cos\left[(2n+1)\frac{\pi}{2}Y\right]}{\left[(2n+1)\frac{\pi}{2}\right]^3 \cosh\left[(2n+1)\frac{\pi}{2}B\right]} \tag{3.6}$$

where, $Y = \frac{y}{h/2}$, $X = \frac{x}{h/2}$, $B = \frac{w}{h}$. This expression simplifies for the temperature at the center of the channel, $T_{\max}$ at $x = 0$ and $y = 0$, with

$$\frac{(T_{\max} - T_{\text{wall}})K}{q'''\ h/2^2} = \ \frac{1}{2} - 2 \times \sum_{n=0}^{\infty} \frac{(-1)^n}{\left[(2n+1)\frac{\pi}{2}\right]^3 \cosh\left[(2n+1)\frac{\pi}{2}B\right]} \tag{3.7}$$

where volumetric heating (*i.e.,* Joule heating) is $q''' = \sigma_m E \cdot E$. Hence, after $T_{\max}$ is calculated, the temperature gradient can be calculated between the center of the channel and the wall (described in sections 3.1 and 3.2); only the temperature gradients along the direction of the electric field were considered for ET flow (Fig. 3.9) since it is proportional to $\nabla T \cdot E$ (see section 2.3).

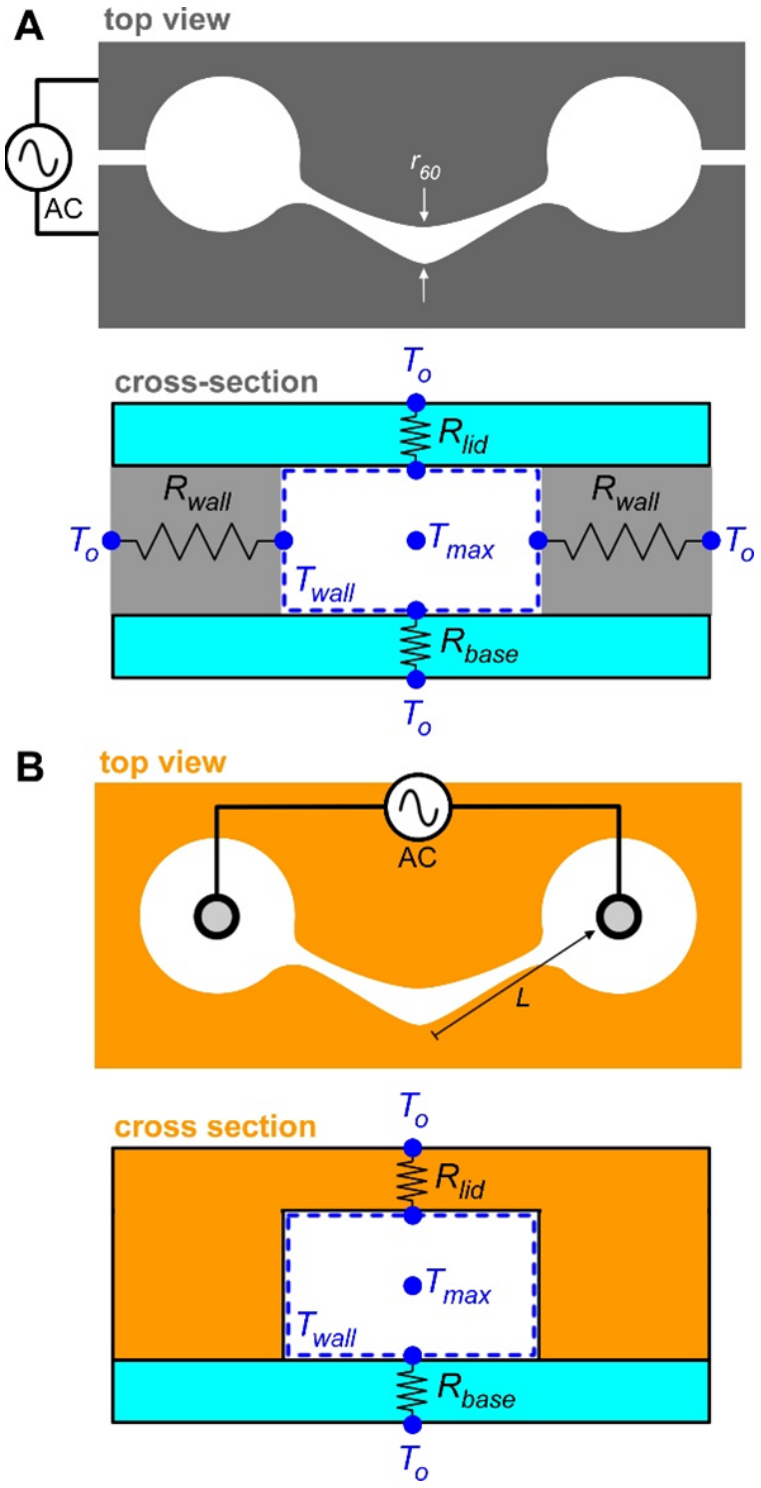

Figure 3.8. Schematic diagram of heat transfer resistance model for (A) the microelectrode-based device where the silicon is serving as electrodes separated by a gap and (B) insulative based device where the electrodes are a distance L from the origin.

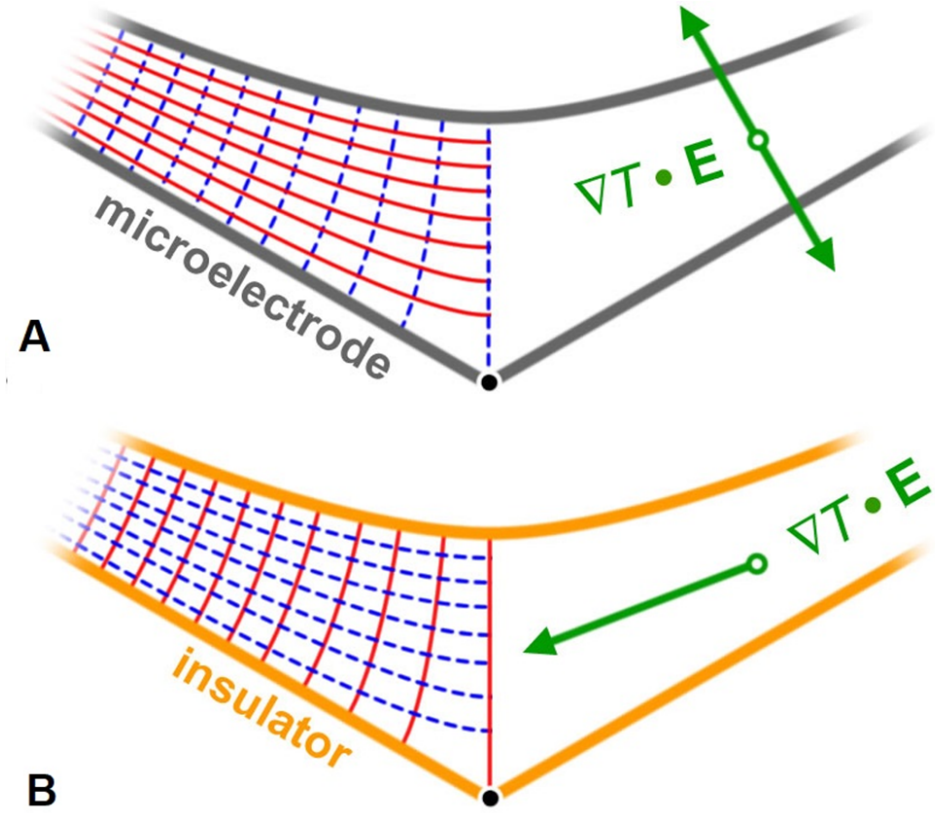

Figure 3.9. The electric potential (solid red) and resultant electric field (dashed blue) for the (A) microelectrode and (B) insulative isoDEP systems. The primary direction of their respective electrothermal body force component is shown

1 Insulative-based Device Temperature Gradient

The temperature gradient (∇ T) along the direction of the channel is needed for the insulative-based design (Fig. 3.8B); this can be estimated by taking the derivative of T_{wall} in Eq 3.5 with respect to the radial direction, resulting in

$$\frac{\partial T_{\text{wall}}}{\partial r} = R_{\text{eq}} \left(\sigma \; k^2\right) \left(LhL_c\right) \tag{3.8}$$

which includes the substitution of $\delta = L$. In insulative isoDEP device $R_{\text{eq}}$is the equivalent heat resistance of R_{lid} and R_{base} in parallel (Fig. 3.9), i.e., $R_{\text{eq}} = \left(\frac{R_{\text{base}} \times R_{lid}}{R_{\text{base}} + R_{lid}}\right)$. The gradient of Tmax, $\frac{\partial T_{\text{max}}}{\partial r}$, can be similarly calculated The representative temperature gradient of the insulative platform, ∇T_{I}, is taken as the average of these

$$\nabla T_I = \frac{\partial T_{\text{wall}}}{\partial r} + \frac{1}{3}\left(\frac{\partial T_{\text{max}}}{\partial r} - \frac{\partial T_{\text{wall}}}{\partial r}\right) \tag{3.9}$$

Heating is proportional to radial position, $q''' = \sigma_m \left|E\right|^2 = \sigma_m \;\; k^2 \; r$. For ET flow analysis heating will be evaluated at $r = L$. Since $\nabla T_{\text{I}} \cdot E$ acts in equal and opposite

directions on either side of the origin (Fig. 3.9B), the net effect will be

$$\left(\nabla T_{\mathrm{I}}\ E^2\right)_{\mathrm{net}} = 2\nabla T_{\mathrm{I}}\ k^2\,(L)\sin 30 = \nabla T_{\mathrm{I}}\ k^2\ L \tag{3.10}$$

2 Electrode-based Device Temperature Gradient

The wall temperature for the electrode-based device is determined by substituting $\delta = r_{60}$ into Eq. 3.5 with $R_{\mathrm{eq}} = \left(\frac{R_{\mathrm{wall}}\ \times R_{\mathrm{base}} \times R_{lid}}{R_{\mathrm{wall}}\ (R_{\mathrm{base}}+R_{lid})+2R_{\mathrm{base}}\times R_{lid}}\right)$ (Fig. 3.8A) and choosing r_{60}. Next, $T_{\max}$ is calculated from (Eq. 3.7) also at r_{60}. The temperature gradient for the microelectrode system in the, ∇T_{E}, is calculated using with

$$\nabla T_{\mathrm{E}} = (T_{\max} - T_{\mathrm{wall}}) \,/\, \left(\frac{1}{2}\ r_{60}\right) \tag{3.11}$$

similiarly, $\nabla T_{\mathrm{E}}\ E^2$ was at $r = r_{60}$ with $E^2 = k^2\ r_{60}$ leading to

$$\nabla T_{\mathrm{E}}\ E^2 = \nabla T_{\mathrm{E}}\ k^2\ r_{60} \tag{3.12}$$

3 Electrothermal Flow Analysis

The non-uniform electric field driving the DEP force will also act on both bound and free charges inside the suspending media which respond differently to the field, resulting in a non-zero body force on the media

$$f_{\mathrm{ET}} = \ \rho_m E - \frac{1}{2}|E|^2 \nabla \varepsilon_m \tag{3.13}$$

where ρ_m and ε_m are the suspending media's volume charge density and the permittivity, respectively. The first and second terms on the right-hand side express the Coulomb force on the free and bound charges, respectively. The free charges relate to the conductivity of the media and represent the conduction force, while the bound charges relate to the permittivity and represent the dielectric force. Following the analysis from Castellanos, et al. 2003 [19], the non-zero time-averaged electrothermal force will be

$$\left\langle f_{\mathrm{ET}} \right\rangle = \frac{1}{2} Re\left(\frac{\sigma_m \varepsilon_m\,(\alpha - \beta)}{\sigma_m + i\omega\varepsilon_m}\right)(\nabla \mathrm{T} \cdot E)\,E^* - \frac{1}{4} Re\left(\varepsilon_m \alpha\,|E|^2\,\nabla \mathrm{T}\right) \tag{3.14}$$

where $\alpha = \frac{\partial \varepsilon_m}{\varepsilon_m \partial T}$, and $\beta = \frac{\partial \sigma_m}{\sigma_m \partial T}$. The dot product $\nabla T \cdot E$ in (3.13) shows that only the component of the temperature gradient that is parallel to the applied field will contribute to the ET force in the Coulombic term. The first term dominates at low AC frequencies whereas the dielectric term has a relatively minor contribution to the generated force [18]. In our analysis we consider only the first part in Eq. 3.14 because relative variations in conductivity $\triangle\sigma/\sigma$ are usually much greater than relative variations in permittivity $\triangle\epsilon/\epsilon$ [19]. Figure 3.9 shows the direction of the applied electric and the temperature gradients for each isoDEP configuration. For microelectrode systems (Fig. 3.9A), the relevant temperature gradient is generated along

the width of the microchannel as the electric field is applied in the same direction; in insulative-based devices (Fig. 3.9B) the relevant ET force is generated along the microchannel length in the direction of the applied field. After the gradient of the temperature is calculated, the ET fluid body force is calculated with

$$f_{\mathrm{ET}} \approx \frac{M\ \nabla \mathrm{T}\ \varepsilon\ E^2}{T} \tag{3.15}$$

where T = 300K and M, a dimensionless factor that predicts the variation of the ET hydrodynamics body force with frequency, ≈ 6.6 when $^{\varepsilon\omega}/_{\sigma} \gg 1$, [19]. The quantity $\nabla\ \mathrm{T}E^2$ is determined from the previous temperature gradient calculations. Finally, the electrothermal fluid velocity is calculated with

$$v_{\mathrm{ETH}} \approx \frac{f_{\mathrm{ET}} D_{\mathrm{h}}^2}{32\mu} \tag{3.16}$$

where the hydraulic diameter is $D_h = \frac{2\ r_{60}\ h}{r_{60}+h}$.

A MATLAB®program (Appendix B) was used to calculate v_{DEP} and v_{ETH} for a range of system inputs. The suspending media conductivity (σ_m) was set to 10 mS/m. The channel height and width were varied from two particle diameters to 200 particle diameters. Calculations were conducted for a σ_m particle traveling at n = 1 particle diameters per second. It will be later shown that the results can be scaled for different particle sizes, DEP velocities, and media conductivity. For the electrode-based device, the lid and base were composed of the same material and thickness (0.5 mm glass). However, the conductive wall was assumed to be silicon with a thickness of 5 mm and thermal conductivity of 150 W/(m·K).

For the insulative-based device, the base was assumed to be either 0.2, 0.5-, or 1-mm thick glass or 0.5 mm silicon. The lid was either a glass coverslip (0.2 or 1 mm) or PDMS (1 mm). Glass and PDMS were considered to have the same thermal conductivity (1 W/(m·K)) in our model, while water has 0.6 W/(m·K). The thickness of both the base and lid were varied to investigate whether it significantly influences minimizing ET effects. In addition, device parameters such as base material type (either silicon or glass) and lid material type were varied while fixing the microchannel heights, width ($w = 3h$), $k^2(10^{14}\ {}^{V^2}/_{m^3})$, and σ_m (10 mS/m).

4 Design Rules for IsoDEP Device

Figure 3.10 shows the relationship between k^2, particle size, the desired translation velocity (n), system length scale (δ), and applied voltage. For example, if a particle of a size 1 µm needs to translate at a speed of 10 µm/s under the applied DEP force, will requires k^2 value of $1.51 \times 10^{15}\ {}^{V^2}/_{m^3}$ (Fig. 3.10A). Hence, by using a 20 V_{rms}source, the characteristic length scale of the device will be 84 µm (*i.e.,* L≈ 84 µm for an insulative-based device or $r_{60} \approx 84$µm for an electrode-based device).

The impact of microchannel dimensions is shown in Figure 5. In general, microelectrode devices perform better than insulative devices for similar microchannel dimensions (Fig. 3.11A, B). Further, smaller microchannel dimensions (w and/or h ¡

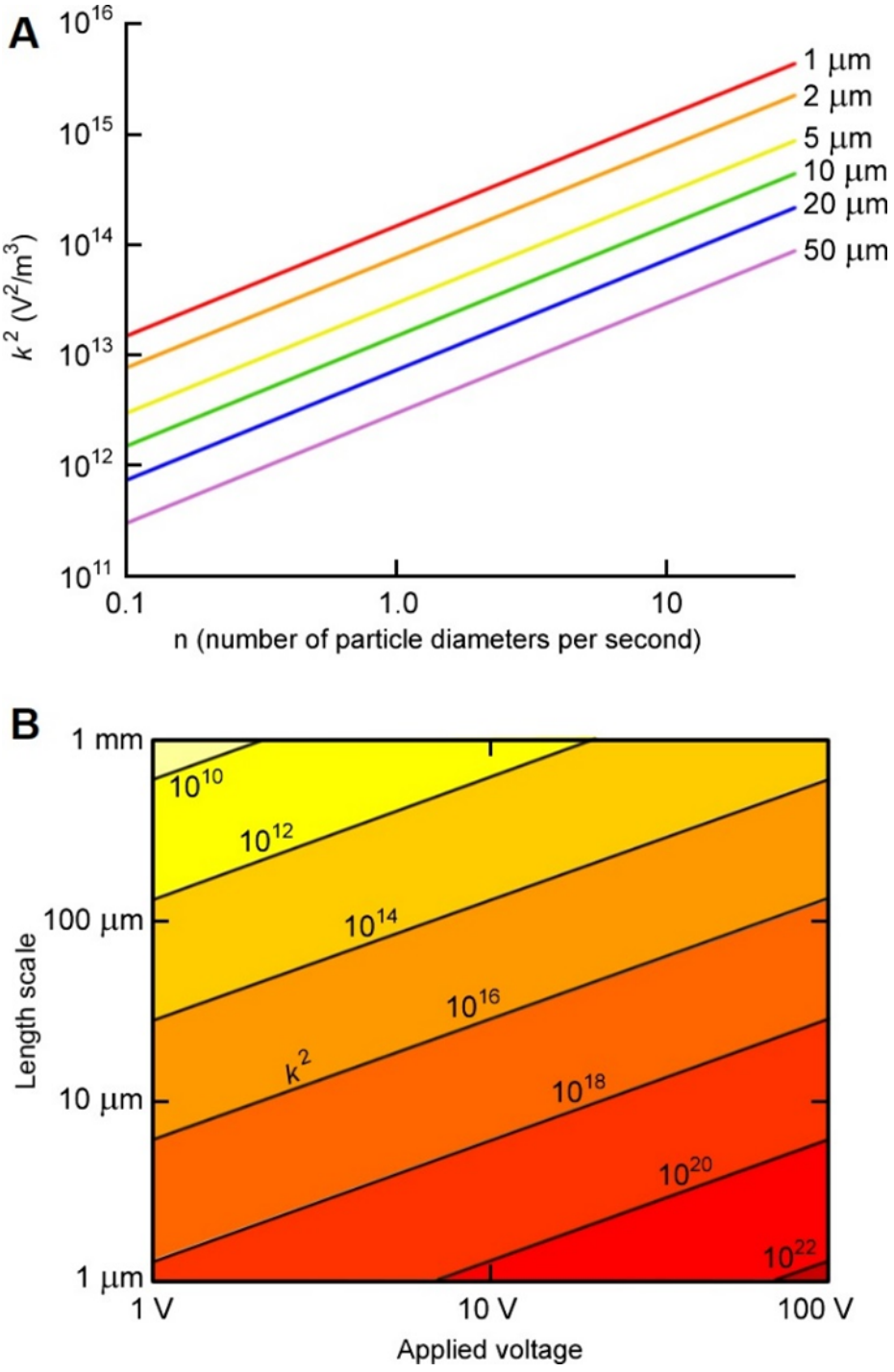

Figure 3.10. (A) Graph of the required gradient of field-squared, k^2, for the isoDEP system to have a particle translate at n particle diameters per second. (B) Contour plot of k^2 for a given system length scale and applied voltage.

10 particle diameters) will yield a more favorable performance, i.e., v_{DEP}/ν_{ETH} . For insulative isoDEP devices (Fig. 3.10B, C) the electrode length scale may be relatively large ($L > 100\sigma_m$) such that a small microchannel height becomes critically important. Coplanar electrodes could perhaps be integrated into the insulative-based device to reduce the distance between the electrodes and the origin (resulting in a smaller L) thus reducing unwanted ET flow. Increasing the lid thickness from 0.21 mm to 1 mm and base thickness from 0.5 mm to 1 mm in insulative isoDEP device decreased the v_{ETH}/ν_{DEP} ratio by approximately 3.7% and 7% respectively. In addition, the ratio of velocities v_{ETH}/ν_{DEP} was approximately 10 times less using a silicon substrate (Fig. 3.11C) compared to a glass substrate ((Fig. 3.11B) for insulative isoDEP devices. Further, Figure . 3.11 results are scalable. If particle speed is increased to $n = 10$, the ratio of velocities should be multiplied by 10. If fluid conductivity is increased by 10, multiply the results by 10. If the particle size is increased by 10, multiply the results by 100.

Deep reactive ion etching (DRIE) of highly doped silicon wafers to fabricate the electrode-based isoDEP device for microchannel heights greater than 20 µm can be challenging due to extended etching times and sidewall roughness generated during the etching process. However, some post-DRIE processing techniques suitable for $\sim$ 10 µm etching depths, [198] might be used to smooth the scalloping effect. Electroplating of metals can be adapted for microchannel heights below 20 µm; however, achieving the desired vertically straight and parallel microchannel sidewalls required for isoDEP field is challenging. Insulative-based devices offer a low-cost fabrication alternative (soft lithography, hot embossing, etc.) but the distance between the electrodes are relatively larger compared to electrodes-based devices, hence requiring greater applied voltages. High voltage gain amplifiers can be used but typically cannot reach high frequencies (limits typically less than 10 MHz) which is a disadvantage because some cells phenotypes, such as cytoplasm properties and lipid formation, can only be investigated at higher frequencies ∼40-80 MHz [150].

Intuitively, the key design parameters to reduce ET flow is to facilitate heat transfer normal to the electric field direction and reduce heat transfer in the direction of the field. Moreover, heat transfer is connected to the volumetric heat flux (q''') which is constrained by the microchannel height and width. Hence, for a given k^2, ET flow reduction can be achieved by either having a material of a high thermal conduction (K) or decreasing the height (h), wall thickness (t_{wall}), width of the microchannel, and the base thickness. Further, v_{ETH}/ν_{DEP} is reduced for smaller particles moving at the same relative speed n. The use of smaller particles will decrease the size of the microchannel and electrode spacing thereby reducing volumetric heating.

Updated Fabrication Methods for IsoDEP Device

After following the derived analysis and design rules for the isoDEP device. The fabrication of new devices was attempted to obtain an ETH force induced fluid motions. The thickness of the microchannel was chosen to be 10x the tested particle diameter.

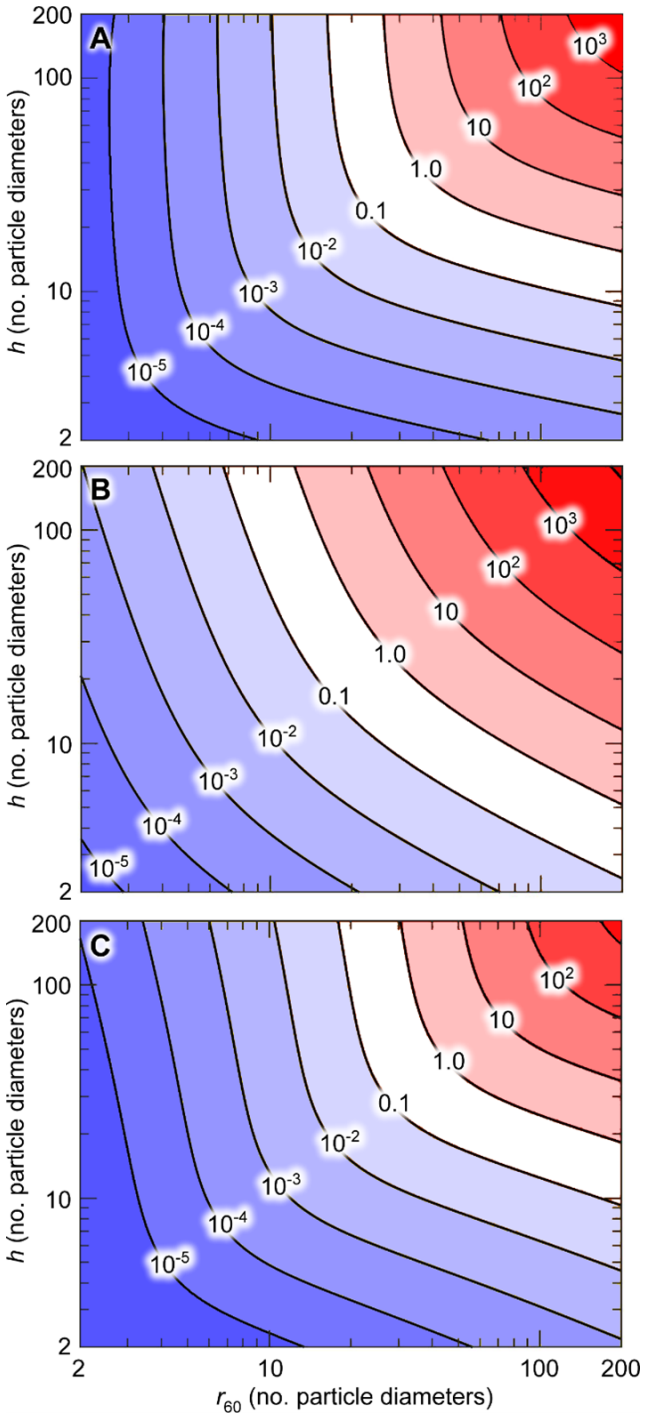

Figure 3.11. Contour plots of the resulting v_{ETH}/ν_{DEP} for different isoDEP systems: (A) microelectrode, (B) insulator, and (C) insulator with silicon base. Results are for a 1 µm particle traveling at $n = 1$ diameters per second. Axis scaling is with respect to particle diameter. Note: These results are scalable for different particle speeds, particle sizes, and fluid conductivity; refer to manuscript for more information.

First, a glass wafer was cleaned with IPA and Acetone, then rinsed in DI water, and the wafer was then put into a 115 °C hotplate to dehydrate for 3 min. After that, first photomask is used to define the electrical connection, pads, and device layer. Next, Electron Beam Evaporation (E-beam) (Lesker) evaporation was used to deposit thin metals (200 A° titanium and 1000A gold). Then, a thin layer of SU-8 25 (Microchem Inc, MA) was spun on the silicon wafer at 2420 rpm for 30 s, yielding a thickness of 20 µm. The wafer was soft baked on a 65 °C hotplate for 2.5 min then elevated to 95 °C and left there for another 6 mins. After that, it has been left to cool down to room temperature. A $170 - 200$ mJ/cm^2 UV exposure dosage with a Karl-Suss MJB3 mask aligner was carried out to crosslink the thin SU-8 layer, followed by a hard bake in an oven at 65 °C for 1 min then elevated to 95 °C and left for 2.5 min which achieved well levelling.

The final device is shown in Figure. 3.12 indicating smaller channel size and electrode distancing. Although the advantage of such design is that the microchannel is sealed, the thickness of the microchannel (∼20 µm) makes it very hard to form inlet/outlet connections for sample handling. It has been extremely difficult to inject the sample inside the microchannel, moreover, it will not be a good candidate for an automized platform for sample handling. Also, the channel width is very small which causes clogging of the injected sample with high particle densities which produces a lot of fluid instability and compromise the operation of the device.

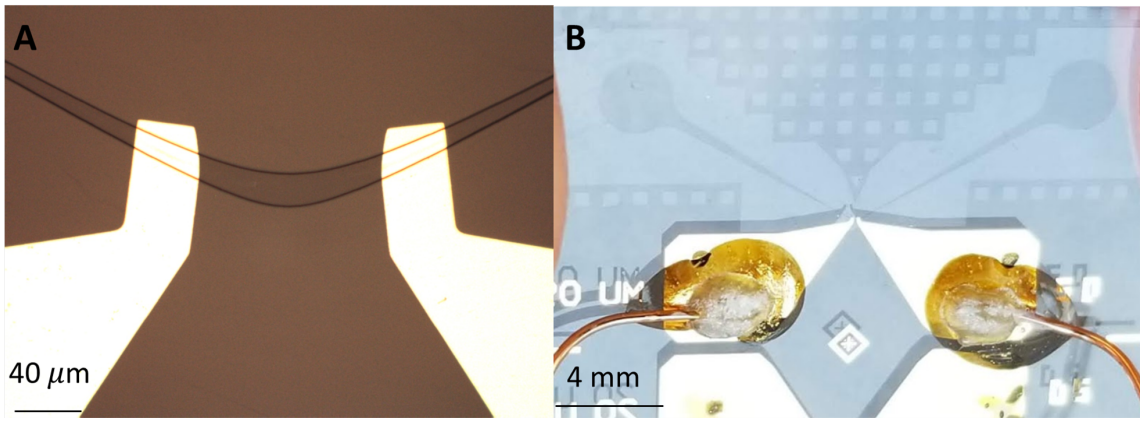

Figure 3.12. (A) Microscopic image for the finished isoDEP SU-8 device with buried electrode. (B) Device ready for testing showing wired connection to the electrodes.

As deduced from the design rules, using a Si base was favored for facilitating heat transfer which will reduce the ETH induced motions. Hence, the DRIE microelectrode-based isoDEP will be repeated with a silicon-on-insulator SOI wafer instead of fully extruded Si wafer. The P-type doped SOI wafer (University Wafer Inc) was 100 mm with handle thickness of 300 µm, device thickness of 35 µm, and oxide thickness of 20 µm. The wafer is then cleaned and patterned to define the microchannel prior to the DRIE process. The DRIE achieved on the device showed a better sidewall finishing results (Fig. 3.13) compared to the one obtained for a fully etched silicon wafer (Fig. 3.5). This was expected as the depth of the etching is almost 10x less than the fully etched device.

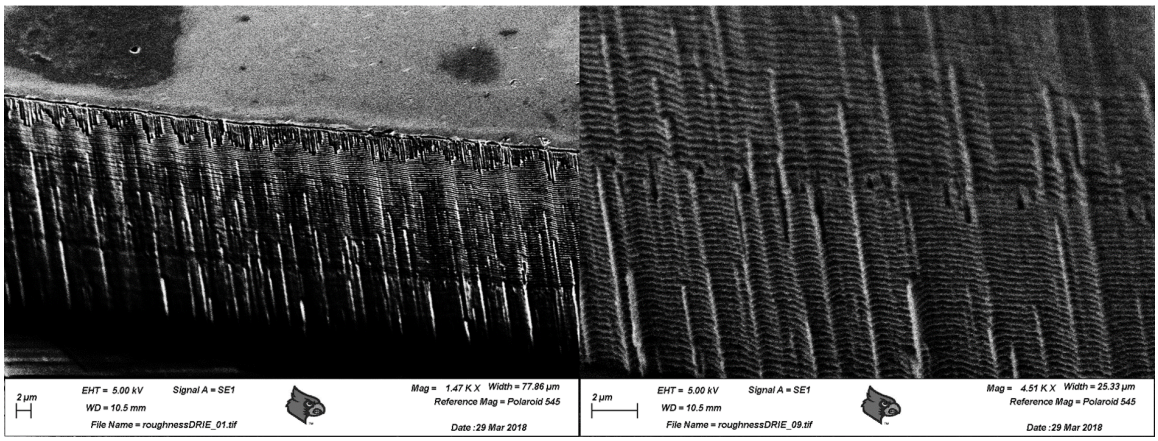

Figure 3.13. SEM images showing a close-up view of the DRIE sidewalls of an isoDEP device realized on SOI wafer.

Unlike the fully etched Si wafer microelectrode-based device (r_{60}=500 µm), the microchannel of the SOI-based device was not transparent. Hence, an inverted microscope cannot be used. However, once the device was prepared for testing, it was observed that the electric signal was not actuating the sample filled within the microchannel. Hence, the capacitance between the device layers was simulated using COVENTOR®. It was concluded that the impedance between the electrodes is higher than between each electrode and the substrate. Hence, the electric signal will not be passing through the microchannel (Fig. 3.14) and therefore, cannot operate the isoDEP device.

An alternative design was proposed to achieve 3D monolithic electrode-based design. For a fully controlled microchannel length, thickness, and width, electroplating will be the best candidate for an inexpensive fabrication. Electroplating has been used extensively for fine side wall 3D structures [199]. First, a silicon wafer was cleaned by standard RCA cleaning at 70 °C, and the wafer was then put into a 115 °C hotplate to dehydrate for 15 min. After that, first photomask is used to define the electrical connection, pads, and device layer. Next, Electron Beam Evaporation (E-beam) evaporation was used to deposit thin metals (200 A° titanium and 1000 A° gold). Then, A thin layer of SU-8 25 (Microchem Inc, MA) was spun on the silicon wafer at 2420 rpm for 30 s, yielding a thickness of 20 µm. The wafer was soft baked on a 65 °C hotplate for 2.5 min then elevated to 95 °C and left there for another 6 mins. After that, it has been left to cool down to room temperature. The second photomask is then patterned to define the holes for the electroplating process. A flood UV exposure with a Karl-Suss mask aligner was carried out to crosslink the thin SU-8 layer, followed by a hard bake in an oven at 65 °C for 1 min then elevated to 95 °C and left for 2.5 min which achieved well levelling.

A homemade beaker electroplating station was used and the device was submerged into a copper electroplating solution to plate copper electrodes with well controlled stir rates and current density to obtain uniform plating. The SU-8 layer was then removed by submerging the substrate in acetone to strip the SU-8 and thickness of

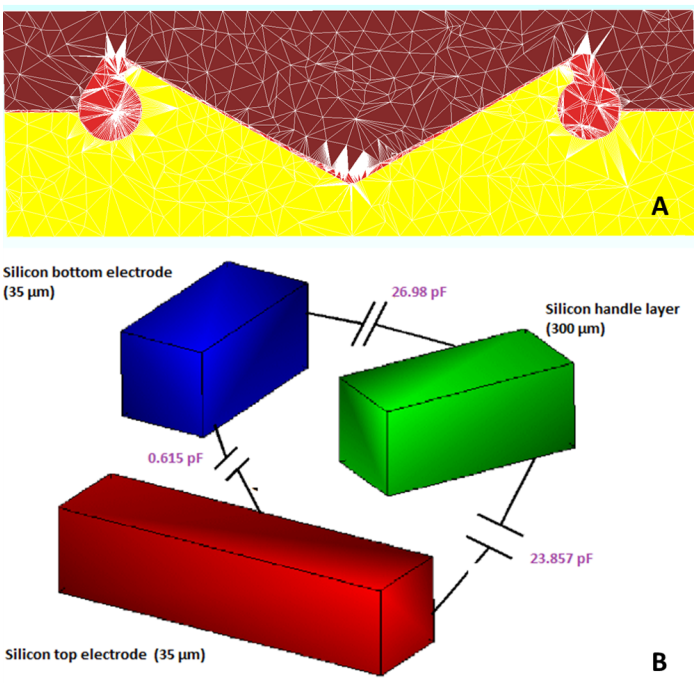

Figure 3.14. Schematic diagram of the (A) Meshed isoDEP device (r_{60} = 500 µm) used for analysis. (B) Calculated device layer capacitances simulated with COVENTOR®indicating that low impedance path is preferred between each electrode and the substrate rather than across the microchannel.

the electroplated device metal layer was measured and verified using the profilometer Dektak (Bruker, USA). The final device (Fig. 3.15) showed smooth sidewalls however, the device layers were not very uniform across the surface. Also, the channel contour was not very well defined to the designed mask. Undefined microchannel contour (Eq. 2.33) would not yield a constant ∇E^2_{rms} upon the application of the electric field. Hence, the device was not used for testing however, this technique is inexpensive and promising. Further improvements can be investigated to achieve better electroplating uniformity achieved at very low deposition rate.

An alternative technique has been proposed to achieve smooth and monolithic sidewall for electrode-based isoDEP device. Carbonized SU-8 has been extensively used recently to produce 3D electrodes arrays and pillars [200–202]. SU8 pyrolysis carbon structures are fabricated as the following: First, a silicon wafer was cleaned by standard RCA cleaning at 70 °C, and the wafer was then put into a 115 °C hotplate to dehydrate for 15 min. Then, A thin layer of SU-8 25 (Microchem Inc, MA) was spun on the silicon wafer at 2420 rpm for 30 s, yielding a thickness of 20 µm. The wafer was soft baked on a 65 °C hotplate for 2.5 min then elevated to 95 °C and left there for another 6 mins. After that, it has been left to cool down to room temperature. The second photomask is then patterned to define the holes for the electroplating process. A $170 - 200 mJ/Cm^2$ UV exposure with a Karl-Suss mask aligner was carried out to crosslink the thin SU-8 layer, followed by a hard bake in an oven at 65 °C for 1 min then elevated to 95 °C and left for 2.5 min which achieved well levelling. Then,

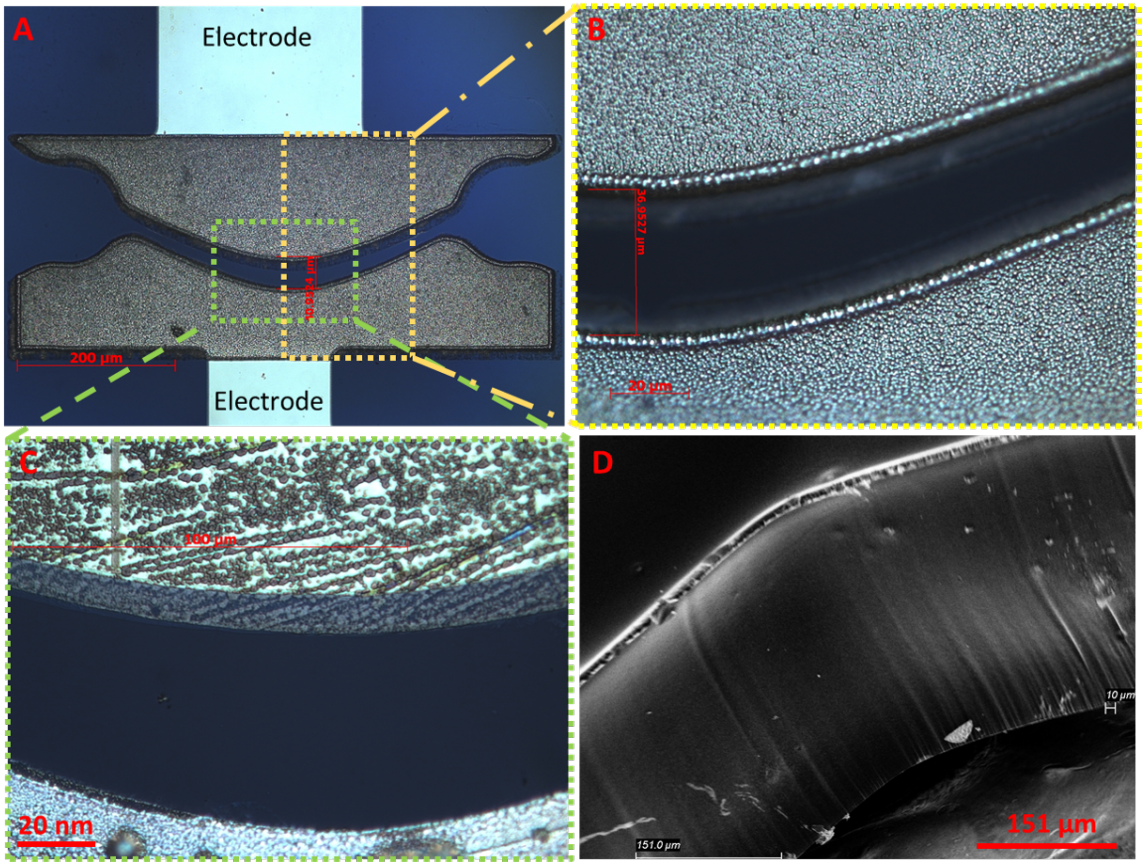

Figure 3.15. (A, B, C) Microscopic image of the final electroplated isoDEP device with a zoomed-in view for the microchannel. (D) SEM image of a carbonized SU-8 device showing smooth side wall with undefined microchannel contour.

development process occurs for 3-4 mins after which the device is baked to ensure dry surface.

After defining the SU-8-based isoDEP device layer. The different SU-8 films were pyrolysed in a YES POLYIMIDE OVEN (YES-550PB6/8/12-2P-CP) in nitrogen atmosphere. The pyrolysis protocol was achieved in two stages: (i) a temperature ramp from room temperature to 200 °CC followed by a 30 min dwell time at 200 °C to allow for any residual oxygen to be evacuated from the chamber and prevent combustion of the SU-8 polymers as the temperature is increased further; and (ii) a temperature ramp from 200 to 900 °C with 1 h dwell time at 900 °C to complete the carbonization process. The samples were heated and cooled down to room temperature at a ramp of 2 °C/min

The device achieved had a very smooth side wall (Fig. 3.15). The problems associated with DRIE sidewall surface can be easily mitigated using such technique. However, similar to reported in literature, the whole SU-8 polymer device layer is shrunk due to the pyrolysis process [203, 204]. As expected, the shrinkage in the device layer will influence the contour of the microchannel. Hence, the contour will not be following the right design (Eq. 2.33) which in turns would not yield a constant

∇E_{rms}^2 upon the application of the electric field.

Concluding Remarks

The premise of isoDEP device is to analyze cell subpopulations relying on DEP particle translation; however, due to unwanted electrokinetic motion, particularly ET flow, the operation of isoDEP can be compromised. In this work developed scaling law analysis was developed to obtain design rules to maximize DEP-induced particle motion relative to ET flow. The Results recommend that in order to reduce the effects of ET flow, for both electrode-based and insulative based devices, the height and width of the microchannel should be less than 10 particle diameters. In addition, designs that facilitate heat transfer normal to the field direction is beneficial; for example, using a silicon base enhances the performance of insulative-based isoDEP devices. Further fabrication and designs were attempted to obtain a reliable isoDEP device. However, due to other unexpected complications, the operation of the device was compromised which require further investigation and analysis to produce a reliable isoDEP device aimable to test small particles/cells while being integrated onto an automized platform. Meanwhile, investigation of bioparticles with other techniques such as electrochemical sensing has been made to produce enough data for phytoplankton cells in order to verify such data with the data produced from the isoDEP device.

CHAPTER IV

CHARACTERIZATION OF CELLS IN SUSPENSION UTILIZING IMPEDANCE SPECTROSCOPY AND SINGLE CELLS UTILIZING ELECTROROTATION

This chapter describes two applications using alternative electrokinetic cell characterization methods other than isoDEP. First, phytoplankton cells in suspension from different species were characterized based on their dielectric properties using impedance spectroscopy. An attempt to differentiate between same species with different nitrogen abundant environment is attempted. Second, electrorotation-based electrokinetic technique is also used to characterize single cells (T-lymphocytes, Hela, and M17 cells).Later in this chapter, these techniques are compared with isoDEP. Some content of this chapter is adapted from published work [120, 205].

Impedance Spectroscopy Based Characterization of Phytoplankton Suspensions

Phytoplankton are photosynthetic micro-organisms that play an indispensable role as indicators of the health and possible changes in most marine ecosystems. As autotrophs they form the basis of most aquatic food chains, and changes in their population health and productivity can have far reaching impacts [206, 207]. Due to their small size and fast metabolism, phytoplankton are the first to respond to environmental changes and can be used to predict how those changes, such as nutrient concentrations, dissolved oxygen, toxin presence, and even weather changes [207] will affect the wider ecosystem. As a result, they are often used as biosensors of a wide range of pollutants, including herbicides, pesticides, and toxic metals [208].

As the primary producers of most marine ecosystems, phytoplankton populations are a food source for a variety of marine life, from microscopic zooplankton to multiton whales [207]. Additionally, small fish and invertebrates feed on phytoplankton, and are then eaten by larger predators. As a result, phytoplankton abundance directly affects the abundance of other food sources in each ecosystem, thereby affecting the migration and population health of most marine life. Phytoplankton population changes can also affect other marine life through "blooms", or periods of explosive phytoplankton population growth [207]. Certain species of phytoplankton produce biotoxins and can cause toxin blooms which can kill marine life and contaminate seafood. Even non-toxic blooms can be harmful, as the rapid growth and subsequent death depletes nutrients and oxygen, resulting in dead zones [207].

Microalgae have several advantages including but limited to, fixing CO_2 through photosynthesis [209], and are diverse and abundant enough that optimal species can

be found in almost any environment [210], including non-arable land [211]. Microalgae are also a source of renewable biofuel and high-value chemical feedstocks [212]. When stressed, some phytoplankton species produce lipids, which can then be extracted and converted into a renewable source of biofuel and other high-value chemicals [212].

Electrochemical impedance spectroscopy (EIS) is a nondestructive tool that detects cellular response to the application of an AC signal over a frequency range [213]. The purpose of analyzing the EIS data is to derive and characterize a load's (*i.e.,* cell suspension) electrical parameters and, although it doesn't directly measure physical phenomena, it is a reliable and sensitive technique [213]. To interpret impedance spectroscopy, a physio-chemical or measurement model must be used. Measurement modeling involves using mathematical functions to explain the experimental impedance using a best fit method. This method involves using good biological knowledge for cells in suspension in order to model their experimental data using equivalent circuit elements, such as resistors, capacitors, and inductors. The equivalent circuit method is simple and straightforward, but lacks high accuracy, which can cause inconsistency and degeneracy. Physio-chemical modeling links the measured impedance and the measurement model to physio-chemical parameters of the process which provides higher accuracy than simply using an equivalent circuit, but obtaining the modeling parameters is highly complex and can lead to over-parameterization. Once the circuit model is established, it can then be used to track changes in electrical properties of a sample under test which indicate physiological changes inside the sample [214].

In these experiments, phytoplankton suspended in a medium are modeled as colloidal particles in suspension. To measure the dielectric properties of conductivity and permittivity, the behavior of cells is described using Maxwell's mixture theory [215, 216]. This relates the complex permittivity of the particle to the complex permittivity of the suspension. Phytoplankton are commonly modelled using a spherical shell model, which describes each phytoplankton cell as a perfect sphere with a conductive outer shell and membrane, and a resistive interior [217]. This model is adequate for cells that are spherical with cell walls, such as *Chlamydomonas rheinhardtii*, but fail to accurately reflect the dielectric characteristics of phytoplankton without cell walls, or with other biologic configurations [217]. These phytoplankton were chosen due to their availability, abundance in local lake waters and ease of culturing in laboratories.

1 Theory and methods

1.1 Theoretical concepts

The basic principle of impedance is based on Ohm's law, where an electric potential, $V(j\omega)$, is measured by applying an electric current through a material or vice versa where $\omega = 2\pi f$ is the angular frequency, and $j^2 = -1$. Conventionally, small AC voltages are used over range of frequencies as an excitation signal. In such case, the applied electric current, $I(j\omega)$, is being opposed by group of cells in suspension generating what is defined as impedance $\widetilde{Z}(j\omega)$, with recorded impedance at different

frequencies:

$$\widetilde{Z}(j\omega) = V(j\omega)/I(j\omega) = \widetilde{Z}_{RE} + j\widetilde{Z}_{IM} \tag{4.1}$$

where $\widetilde{Z}_{RE}$, resistance, and $\widetilde{Z}_{IM}$, reactance, are the real and imaginary parts of the complex impedance, respectively. Moreover, the complex impedance is a function of complex permittivity, $\widetilde{\epsilon}$, of the cell's cytoplasm and membrane. For diluted cells in suspension, the total impedance of the system is described by Maxwell's mixture theory [218]. The equivalent complex permittivity of the mixture is related to the total impedance of the mixture by [215].

$$\widetilde{Z}_{\text{mix}} = \frac{1}{j\omega\widetilde{\epsilon}G} \tag{4.2}$$

where G is the electrode's geometric constant, which is the ratio of the electrode area to the gap between the electrodes used for the experiment, and

$$\widetilde{\epsilon}_{\text{mix}} = \widetilde{\epsilon}_{\text{m}}\frac{1 + 2\phi\widetilde{f}_{\text{cm}}}{1 - \phi\widetilde{f}_{\text{cm}}} \tag{4.3}$$

where ϕ is the volume fraction (ratio of the particle volume to the suspending medium volume), and $\widetilde{f}_{\text{cm}}$ is the complex Clausius-Mossotti, given by

$$\widetilde{f}_{\text{cm}} = \frac{\widetilde{\epsilon}_{\text{p}} - \widetilde{\epsilon}_{\text{m}}}{\widetilde{\epsilon}_{\text{p}} + 2\widetilde{\epsilon}_{\text{m}}} \tag{4.4}$$

where $\widetilde{\epsilon}_{\text{p}}$ and $\widetilde{\epsilon}_{\text{m}}$ are the complex permittivity of the particle/cell and medium, given by

$$\widetilde{\epsilon} = \epsilon - j\frac{\sigma}{\omega} \tag{4.5}$$

where ϵ is the permittivity and σ is the conductivity.
It is noted that Maxwell mixture theory is valid for low volume fractions ($\phi < 10\%$) *i.e.,* the volume of the cells suspended in the media is below $< 10\%$ of the total mixture volume.

$$1 - \phi = \big(\frac{\widetilde{\epsilon}_{\text{mix}} - \widetilde{\epsilon}_{\text{p}}}{\widetilde{\epsilon}_{\text{m}} - \widetilde{\epsilon}_{\text{p}}}\big)\big(\frac{\widetilde{\epsilon}_{\text{m}}}{\widetilde{\epsilon}_{\text{mix}}}\big)^{1/3} \tag{4.6}$$

In impedance spectroscopy-based analysis, dielectric properties of the single cell (*e.g.,* cytoplasm conductivity, σ_{cyt}, membrane conductance, σ_{mem}, and specific membrane capacitance, C_{mem}, are extracted from suspension by utilizing the single shell model and Maxwell mixture theory [216].

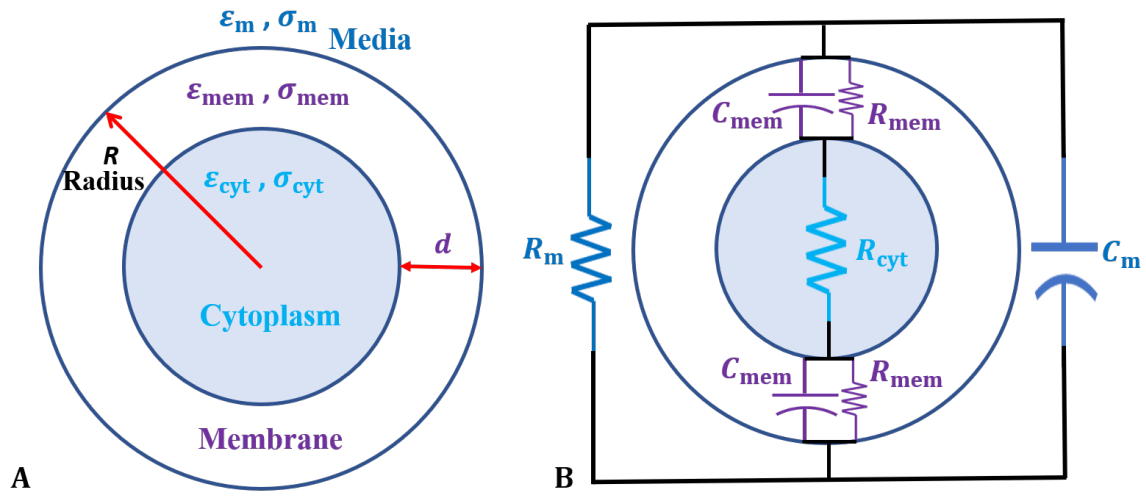

Figure 4.1. Schematic diagram of (A) single-shell model of cells in suspension, (B) simplified equivalent electrical circuit model (ECM) of single cells in suspension neglecting the electric double layer components.

In single shell model (Fig. 4.1a), the complex permittivity of the cell is given by [215, 216]

$$\widetilde{\epsilon}_p = \widetilde{\epsilon}_{mem} \frac{\gamma^3 + 2\frac{\widetilde{\epsilon}_{cyt}-\widetilde{\epsilon}_{mem}}{\widetilde{\epsilon}_{cyt}+2\widetilde{\epsilon}_{mem}}}{\gamma^3 - \frac{\widetilde{\epsilon}_{cyt}-\widetilde{\epsilon}_{mem}}{\widetilde{\epsilon}_{cyt}+2\widetilde{\epsilon}_{mem}}} \tag{4.7}$$

where $\gamma = R/(R-d)$, R is the radius of the cell, d is the thickness of the cell membrane (Fig. 4.1a) and $\widetilde{\epsilon}_{cyt}$, $\widetilde{\epsilon}_{mem}$ are the complex permittivities of the cytoplasm and membrane, respectively.

The equivalent electrical model of cells suspended in aqueous media is used to simplify the mathematical expressions used to extract the single cell properties from the measured complex impedance. By stating that $\widetilde{\epsilon}_{cyt} = -j\sigma_{cyt}/\omega$ and $\widetilde{\epsilon}_{mem} = \epsilon$, then Eq. 4.7 can be simplified to [206]

$$\widetilde{\epsilon}_p = \epsilon \frac{\gamma^3 + 2\frac{-j\sigma_{cyt}/\omega-\epsilon}{2\epsilon-j\sigma_{cyt}/\omega}}{\gamma^3 - \frac{-j\sigma_{cyt}/\omega-\epsilon}{2\epsilon-j\sigma_{cyt}/\omega}} \left(\frac{\mathrm{Re}[\widetilde{\epsilon}_p] + j\,\mathrm{Im}(\widetilde{\epsilon}_p)}{\epsilon} \right) \tag{4.8}$$

which can be further simplified to

$$\widetilde{\epsilon}_p = \epsilon \left(\frac{2b\epsilon^2 + a(\sigma_{cyt}/\omega)^2}{b^2\epsilon^2 + (\sigma_{cyt}/\omega)^2} \right) + j \left(\frac{\epsilon\sigma_{cyt}/\omega(2-ab)}{b^2\epsilon^2 + (\sigma_{cyt}/\omega)^2} \right) \tag{4.9}$$

where $a = \left[\frac{\gamma^3+2}{\gamma^3-1}\right]$ and $b = \left[\frac{2\gamma^3+1}{\gamma^3-1}\right]$.

A quadratic equation can be obtained by dividing the real and imaginary parts by $\widetilde{\epsilon}_p$ in Eq. (4.9):

$$a/\omega(\sigma_{cyt}/\epsilon)^2 - k(2-ab)(\sigma_{cyt}/\epsilon) + 2b\omega = 0 \tag{4.10}$$

Table 4.1. Culturing conditions for phytoplankton cells

Taxon	Source	Cell Size	Culturing Conditions			
		Diameter (µm)	Temperature (℃)	Light/Dark (hours)	Growth media	Incubator
Chlamydomonas sp.	CBS	10-12	22	12hr/12hr 5-6 watts	Alga-Gro, BBM, Soil Extract + Spring water	Percival
Selenastrum sp.	CBS	5 – 7	22	12hr/12hr 5-6 watts	Alga-Gro, BBM	Percival

where $k = \left[\frac{\mathrm{Re}[\widetilde{\epsilon}_\mathrm{p}]}{\mathrm{Im}[\widetilde{\epsilon}_\mathrm{p}]}\right]$. By assuming that $L = \sigma_{\mathrm{cyt}}/\omega$ and equating the imaginary part of Eq. (4.9), the extracted permittivity of a single cell from the complex becomes

$$\epsilon = \left(\frac{b^2 + (L/\omega)^2}{(L/\omega)(2-ab)}\right) \mathrm{Im}[\widetilde{\epsilon}_\mathrm{p}] \tag{4.11}$$

From (Eq. 4.10), L can be calculated and can be used to calculate ϵ; after that σ_{cyt} can be calculated.

As shown in Fig. 4.1b, the total impedance of the mixture consists of the impedance of the medium represented by the parallel resistance and capacitance of the aqueous media, and the impedance of the single cells. The impedance of single cell is simplified to include the resistance of the cytoplasm in series with the membrane impedance represented as resistance and capacitance which acts as a dielectric material which can be measured at higher frequencies where it plays a major role in determining the impedance of cells [219]. Hence, the values of the frequency dependent cell parameters such as specific membrane capacitance can be determined by the volume fraction, conductive and dielectric properties of both cell and medium, as well as the cell size and geometric constant of the electrodes used for measurements [215, 216]:

$$C_{\mathrm{mem}}(\omega) = \frac{9\phi R\epsilon}{4d} G \tag{4.12}$$

1.2 Phytoplankton culturing methods for experiments

Two genera of phytoplankton, *Selenastrum sp.* and *Chlamydomonas sp.*, were selected for these experiments based on their cell configurations and characteristics and ease of culturing under stressed and non-stressed conditions (Carolina Biological Supply (CBS), Burlington, NC). Table 4.1 summarizes the culturing conditions and physical dimensions [220, 221] for each of the taxa.

The two phytoplankton genera used in this study are in the Chlorophyceae group of green algae. The layered cell wall of Chlamydomonas is rigid and composed of hydroxyproline-rich polymers that are linked by glycoproteins containing the sugars galactose, arabinose, mannose, and glucose [222]. The cells in culture were ovoid, singular, not aggregated, and most were flagellated during the experiments. *Selenastrum*, is a crescent-shaped cell and slightly smaller in size than *Chlamydomonas*

in culture. The cell wall of *Selenastrum* is less well-described; however, because *Selenastrum* has been included within the same taxonomic group of green algae as *Chlamydomonas*, we assumed similar cell envelope structure.

Chlamydomonas sp. and *Selenastrum sp.* were initially cultured in Alga-Gro (AG) or soil extract-spring water (SoilXSW) media. After acclimation to culture conditions in the lab using AG or SoilXSW, cells of each taxon were transferred to Bold's Basal Medium (BBM) [220] and cultured for several days to weeks prior to stress manipulations in preparation for experimentation. Cells of both *Chlamydomonas* and *Selenastrum* were always singular, free-floating, and uniform in culture and during the experimental procedures.

After cells had stabilized at known densities in culture (*e.g.,* approximately 10^9 cells m/L), they were transferred to either nitrogen-rich BBM (N^+) or nitrogen-poor BBM (N^-) approximately five days before conducting the experiments. The time frame allowed for development and confirmation of lipid storage bodies in the N^-stressed cells.

The N^- stressed cells were monitored for lipid production by staining with $5-10$ µL of Bodipy 5/515 stock solution (Invitrogen, Grand Island, NY) dissolved in dimethyl sulfoxide at 0.5 mg m/L. Cells were allowed to stain for 30 min (Hadady et al. 2014) then examined at 400X magnification to confirm the presence of lipid bodies using a fluorescence Zeiss Axioplan microscope (Excitation: 470/40X, dichromatic mirror: 495, Emission: 525/50m). Cells grown in the non-N stressed medium were also stained to confirm non-lipid production.

On the morning of the experiments, each culture was concentrated by centrifugation (Epindorf microcentrifuge) at 1500 rpm (relative centrifugal force = 170 g) and rinsed several times in selected low conductivity medium. Media with conductivity of 10 ± 2 µS/cm were initially created with potassium chloride in deionized water. Glucose was added to the three media (85 g/L) to raise the osmotic pressure without affecting its external conductivity as implemented in literature [221]. Portions of the N^+ and N^- cultures were separately pelleted and then rinsed with the test media several times prior to performing each experiment to achieve selected low conductivities. Cell densities were adjusted to 10^5 or 10^6 cells m/L depending on the experimental use to ensure low volume fraction of cells suspended in the aqueous test media.

1.3 Electrical impedance spectroscopy

The bioimpedance measurement of the phytoplankton in suspension was performed by using commercially-available electrodes integrated into an eight-well plate (ECIS-8W20idf, Fig. 4.2). These wells were independently addressable using a custom-built PCB holder that facilitated the selection of the desired wells to the impedance analyzer. First, wells were cleaned with DI water and dried prior to the experiment, then a background (*i.e.,* no-load or "dry well") impedance measurements were acquired to determine hardware system impedance. After that, a 100 µL of cells suspended in 10 µS/cm were filled inside the well and complex impedance measurement was taken. The impedance magnitude and phase angle were recorded each time using Agilent precision impedance analyzer 4294-A with 201 data point covering a frequency range

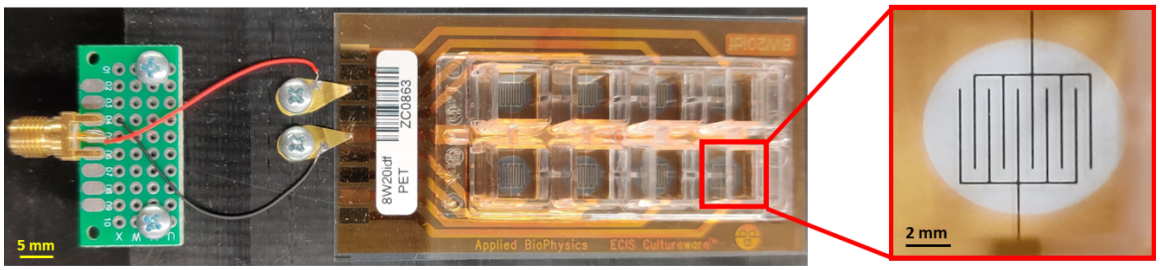

Figure 4.2. An image of the ECIS cultureware® electrodes with a magnified electrode geometry.

of 3 Hz to 10 MHz for an excitation voltage of 10 mV. The recorded measurements were then analyzed using Maxwell's mixture theory and the equivalent circuit model (Fig.4.1) to extract the dielectric properties of phytoplankton cells. It is noted that, prior to measurements, the impedance system was compensated using the provided manufacturer's fixtures to cancel out the probes'(lead) impedance.

2 Results and discussion

Fig. 4.3 shows the impedance magnitude and phase of media only (without cells), and with *Chlamydomonas* and *Selenastrum* cells. The plotted data represents the phytoplankton cells of the same density and suspended in the same medium conductivity. The impedance magnitude of media decreases with increasing the frequency, which represents the transition from the capacitive behavior that dominates at lower frequencies to resistive behavior that dominates at higher frequencies. The effects of adding the phytoplankton cells can be seen in the increased impedance values. However, the impedance curves start to converge at $\sim$ 200 kHz due to the presence of a very thin coating on the electrodes that form a very small capacitance ($\sim$ nF range) that dominates the high frequency zone [206]. Such low capacitance, in parallel with the solution resistance, form a RC circuit that inhibits the effect of the other electrical components inside the solution, as well as the limitation imposed due to the chip metal connections; this leads to the observed coincidence of all curves at the high frequency which does not change when different excitation voltages are used. Low excitation voltage (10 mV) was used because higher voltages might influence the permittivity and conductivity of the cells' cytoplasm due to the extra ion channels opened through the membrane which might influence the total complex impedance [223, 224]. These measurements (Fig. 4.3) indicate that it is possible to differentiate between different cell types at intermediate frequencies ($\sim$ 300 Hz to 40 kHz).

A custom MATLAB code (Appendix B) was used to implement Maxwell's mixture theory. The radius (R) of the *Chlamydomonas* was $\sim$ 5.5 µm, and *Selenastrum* was $\sim$ -3 µm. This corresponding volume fraction ($\phi = 4/3\pi R^3/10^{-6}$) of 1 million phytoplankton cells suspended in a total volume of 100 µL were $\sim$0.001 which shows that Maxwell's mixture theory can be applied in such analysis (where $\phi << 0.1$).

Figure 4.4 shows the extracted phytoplankton single cell electrical properties versus frequency. Table 4.2 shows the averaged values for each cell parameters over

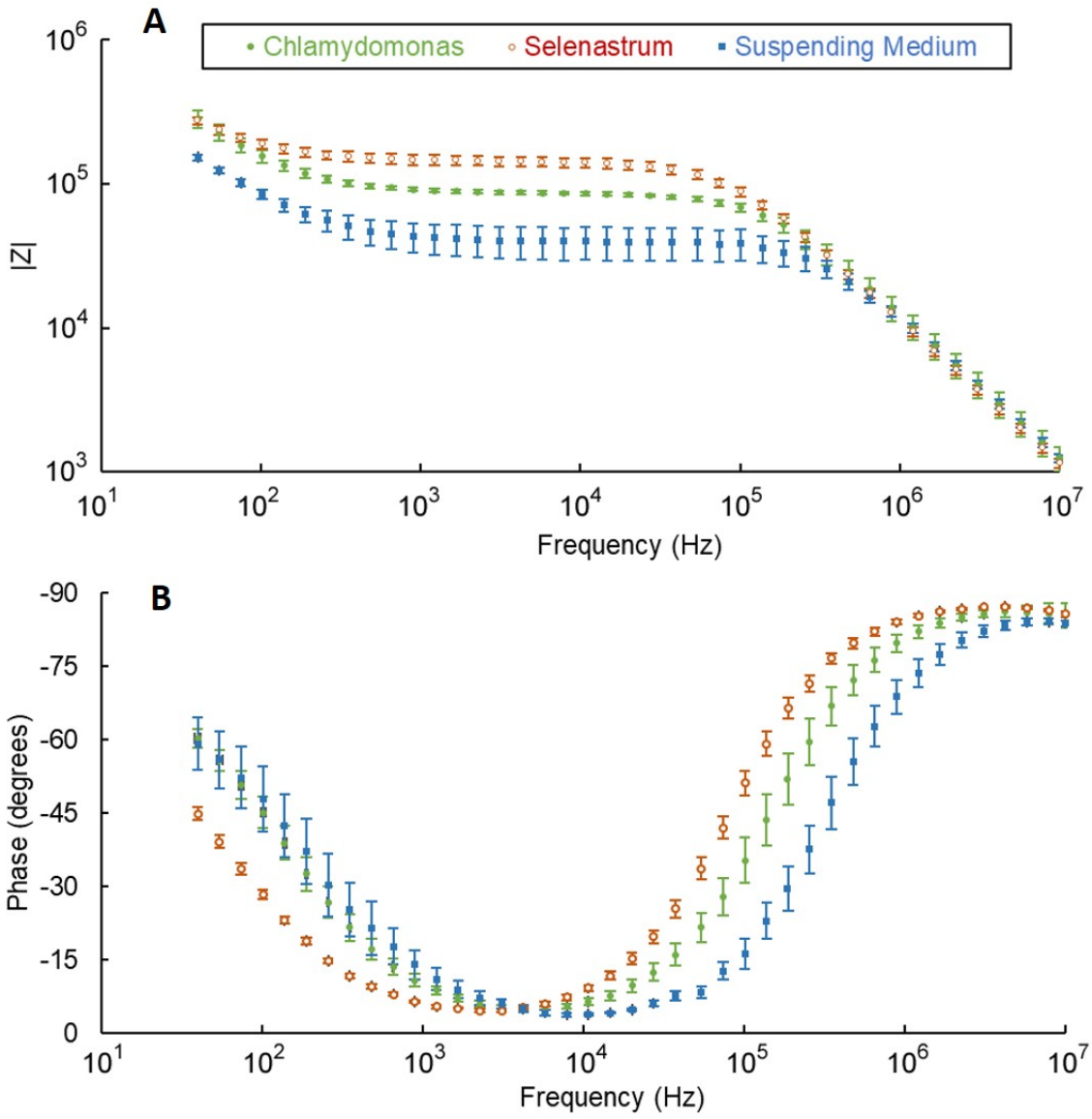

Figure 4.3. (A) Impedance magnitude, and (B) phase angle for *Chlamydomonas* ($n = 17$), *Selenastrum* ($n = 7$) cells, and suspending media (without cells) ($n = 6$).

the frequency range (3 kHz−10 MHz) to avoid the low frequency noise. There was no significant difference in the extracted cytoplasm conductivity (∼14.4 mS/m of all cell types (4.4C). However, there was significant difference in the specific membrane capacitance (membrane capacitance per unit area) between *Chlamydomonas* and *Selenastrum* cells.

Table 4.2. Extracted cell parameters for phytoplankton cells utilizing EIS-based characterization

Cell Type	Cell Size Diameter (µm)	Specific Membrane Capacitance ($mF//m^2$)	Cytoplasm Conductivity (mS/m)
Chlamydomonas sp. N^+	10-12	15.5 ±3.6 (*n=30*)	14.4 ± 0.9 (*n=30*)
Chlamydomonas sp. N^-	10-12	13.2 ± 2.3 (*n=44*)	14.1 ± 0.4 (*n=44*)
Selenastrum sp. N^+	5-7	40.6 ± 12.6 (*n=28*)	14.4 ± 0.5 (*n=28*)

Unlike membrane capacitance, which is usually investigated at low frequencies (< 1 MHz), differentiation based on cytoplasm conductivity of cells can only be achieved by utilizing high frequency AC generators ($\sim 40 - 80$ MHz) which requires complicated PCB and/or electrode setup to accommodate such high frequency generators and avoid any interference from the surrounding environments which can falsify the measured data [225]. Nitrogen limited cells were expected to exhibit high content of lipids which will correspond to lower the cytoplasmic conductivity of cells (decreases by $\sim 60\%$) [221]. However, in this study, this was not achievable due to the system's limitation at high frequencies, where all curves are coinciding above ∼200 kHz, and no further information regarding cytoplasm conductivity can be retrieved from the cells in suspension.

The specific membrane capacitance decreases with increasing frequency as shown in Figure 4.4c. *Chlamydomonas* values dropped from ~ 600 to 15.5 mF/m^2, where it becomes stable in the β-dispersion range (> 100 kHz). Similarly, the measured values for *Selenastrum* cells range from ~ 1500 to a ∼41 mF/m^2. The specific membrane capacitance values for *Chlamydomonas* values closely match reported data using dielectrophoresis [217]. Similarly, as shown in figure 4.4D, the relative permittivity (ϵ/ϵ_0) for single cell which decays with increasing frequency. The values dropped for *Chlamydomonas* cells from ~ 450 to 37 ± 3, while it dropped from ~ 1300 to a stable value of $\sim 98 \pm 14$ for *Selenastrum* cells.

Previously-reported cytoplasm conductivity varies from 0.008 to 0.5 S/m [208, 221, 226–228]; however, this vast range of values corresponds to different techniques used to characterize phytoplankton cells as well as different cell circuit models used for analyses. When cells are being trapped or manipulated for extended periods of time, their cytoplasm conductivity will be compromised due to the formation of lipids in response to induced stress. The purpose of this study was to assess a straightforward impedance measurement method to differentiate different types of phytoplankton cells. Modifications to the electrodes and system hardware could be made to enhance measurements in order to differentiate between same cell types under nitrogen-limited or toxicant environment.

Although it is known that under nutrient limitation, the cell envelope of *Chlamydomonas* changes [229], we did not monitor this change (using scanning electron

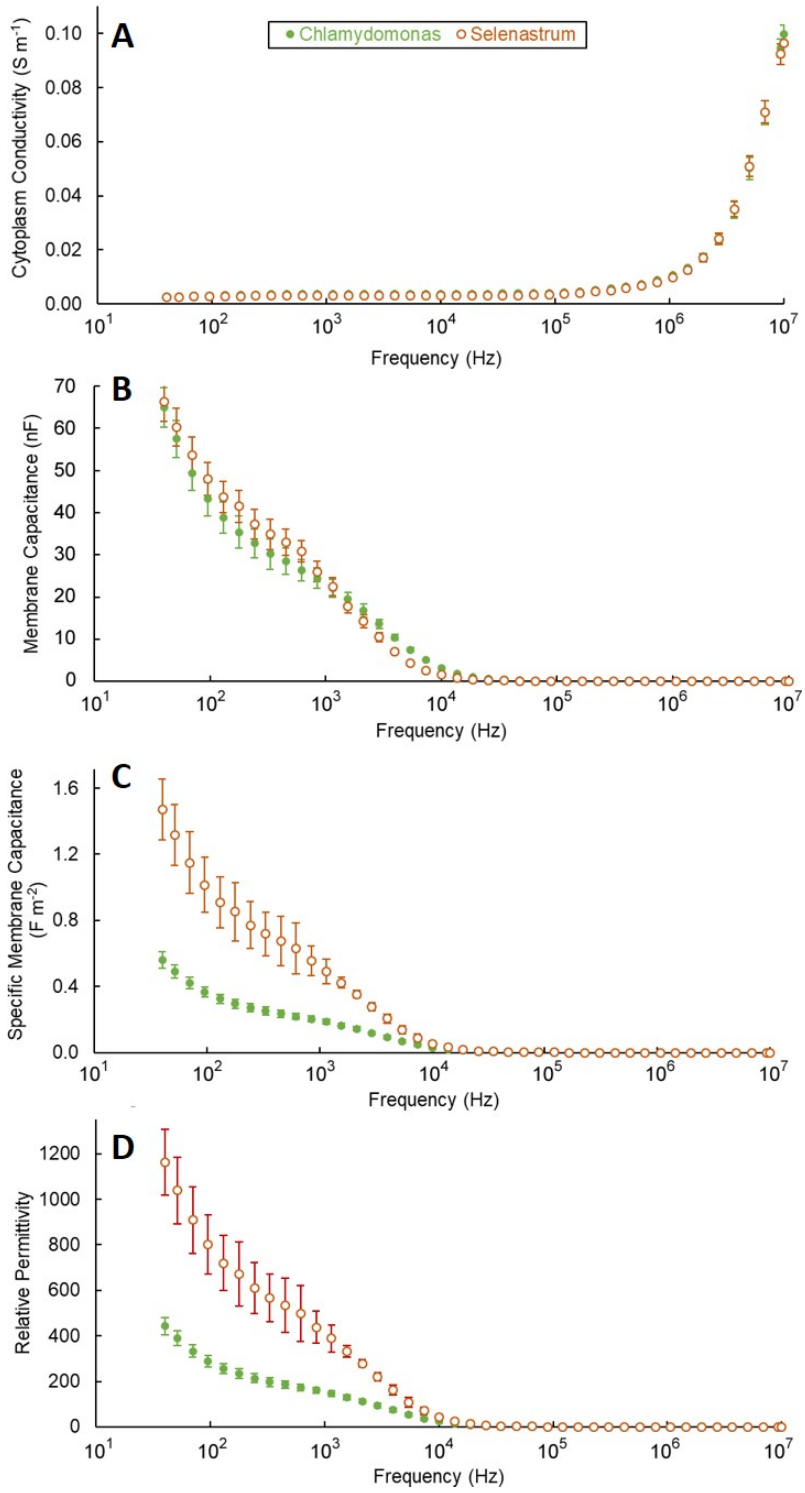

Figure 4.4. Extracted electrical properties of *Chlamydomonas* ($n = 30$) and *Selenastrum* ($n = 28$) cells in suspension (A) cytoplasm conductivity, (B) membrane capacitance, (C) specific membrane capacitance, (D) relative permittivity of single cell with respect to frequency. (ϵ/ϵ_0).

micrography or any other method) prior to or during the experiments. Increases in cell volume and cell wall thickness in nutrient-limited cells may occur because of photosynthetic byproduct accumulation or delays in cell division. Future work should monitor cell size before and after to support the size assumptions used in the fit code to provide more insights into the extracted cell parameters. However, when we implemented the literature values for cell radius ($\sim 7-7.8$ µm) [230] in our analysis, there were no significant differences in the extracted dielectric cell parameters between N^- and N^+ *Chlamydomonas* cells (not reported).

3 Concluding Remarks

The ability to differentiate between suspended phytoplankton cells demonstrates that impedance spectroscopy can be used to perform in-the-field analyses without the need for complex microfluidic handling or preparation that might induce stress. The portability of the system can be improved by designing a custom-built electronic system that operates at specific frequencies, including very high frequencies ($\sim 40-80$ MHz), with lock-in amplifiers that would enhance measurements. Non-spherical multicell cell models [208, 231, 232] could also be implemented to further improve measurements. Although the research presented here has limited ecological application, further research into phytoplankton cell responses to variations in instrument capabilities and under various ecological conditions would contribute to a "proof-of-concept" use of the technology within an ecological context.

Electrorotation-based Single Cell Characterization

This section discusses the electrorotation technique as a tool for a method for label-free single-cell biophysical analysis of multiple cells trapped in suspension by electrokinetic forces. Brief introduction to electrorotation is presented and the experimental setup is discussed. Some content of the this section is reproduced with permission from [120].

Electrorotation (ROT) is a label-free analysis technique, that uses the imaginary part of the Clausius-Mossotti factor where the field and dipole components are out of phase [145, 233]. The rate of rotation for cells is dependent on the applied frequency and electric field magnitude. In this case, the cross over frequency (COF) is the frequency at which the rotation changes its direction. To extract cell dielectric properties, the relationship between cell rotation and applied frequency is fit to the single-shell model (section 2.1). ROT is extensively used in many biomedical application, including but not limited to, to differentiate between cell lines [234], investigate membrane changes of cells [235] and/or investigate the cytoplasm properties of cells [236]. Despite being very efficient single cell characterization tool, it lacks the high throughput as no simultaneous of rotation analysis of parallel cells has been presented except work demonstrating 3 octopoles were presented by Fuher et al. [237] where a single cell was trapped and analyzed.

Applying the 3D vertical electrodes approach [238–240], it's possible to achieve multiple trapping and rotation analysis arrays that can be used to actuate multiple single cell(s) simultaneously. The microcages are addressed independently to allow independent operation of each single microcage therefore, each trapped single cell can be easily manipulated and forced to be hold against the flow motion (Fig. 4.5). Selective trapping/release as well as rotation analysis is possible through the operator control. The dielectrophoretic microcages consist of two arrays of 40 3D electrodes integrated within a microfluidic channel which, at the end, leads to a total amount of 39 arrays. The height of the electrodes and of the surrounding microfluidic channel is 50 µm. The diameter of the electrodes and of the inter electrode distance varies between 20, 40, and 80 µm in order to accommodate different cell sizes since DEP force is proportional to the cubic of the particle diameter. Further detailed fabrication process can be found [120, 238].

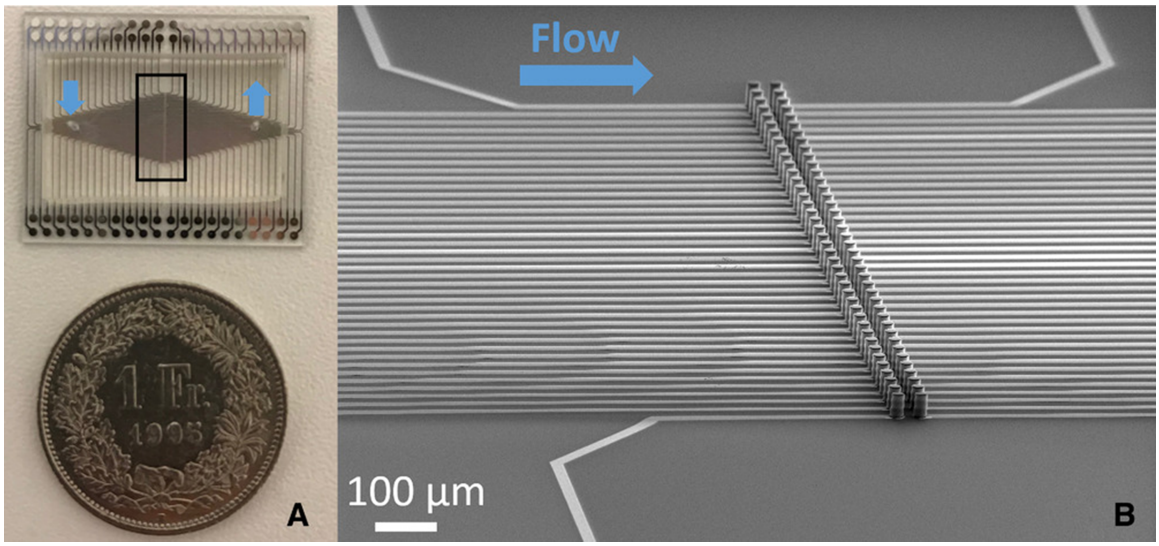

Figure 4.5. (A) An image of the bonded chip with a width of the microfluidic channel of 6.4 mm and with both electrode diameter and interelectrode distance of 80 µm. (B) SEM micrograph of two arrays of metal covered SU-8 electrodes, which are separately connected by an underlying, insulated metal wire. The electrode´s diameters and interelectrode distance is 20 µm. Reproduced with permission from [120].

The advantage of such 3D electrode microcage over the conventional 2D electrode design is employing full use of the microchannel depth which allows further control on tested cells using electric field. In 2D electrode arrays, the DEP force is not effective throughout the whole depth of the microchannel and only effective close the electrode edges. Hence, 3D electrodes structure can be useful to maximize the DEP force needed to apply negative DEP force to trap the cells flowing throughout the channel [151, 241]. nDEP is used to trap cells of interest within the quadrupole in order to investigate the cells with rotation field. Unlike optical tweezers [237], DEP force does not require very extensive manual operation to keep the cells in position.

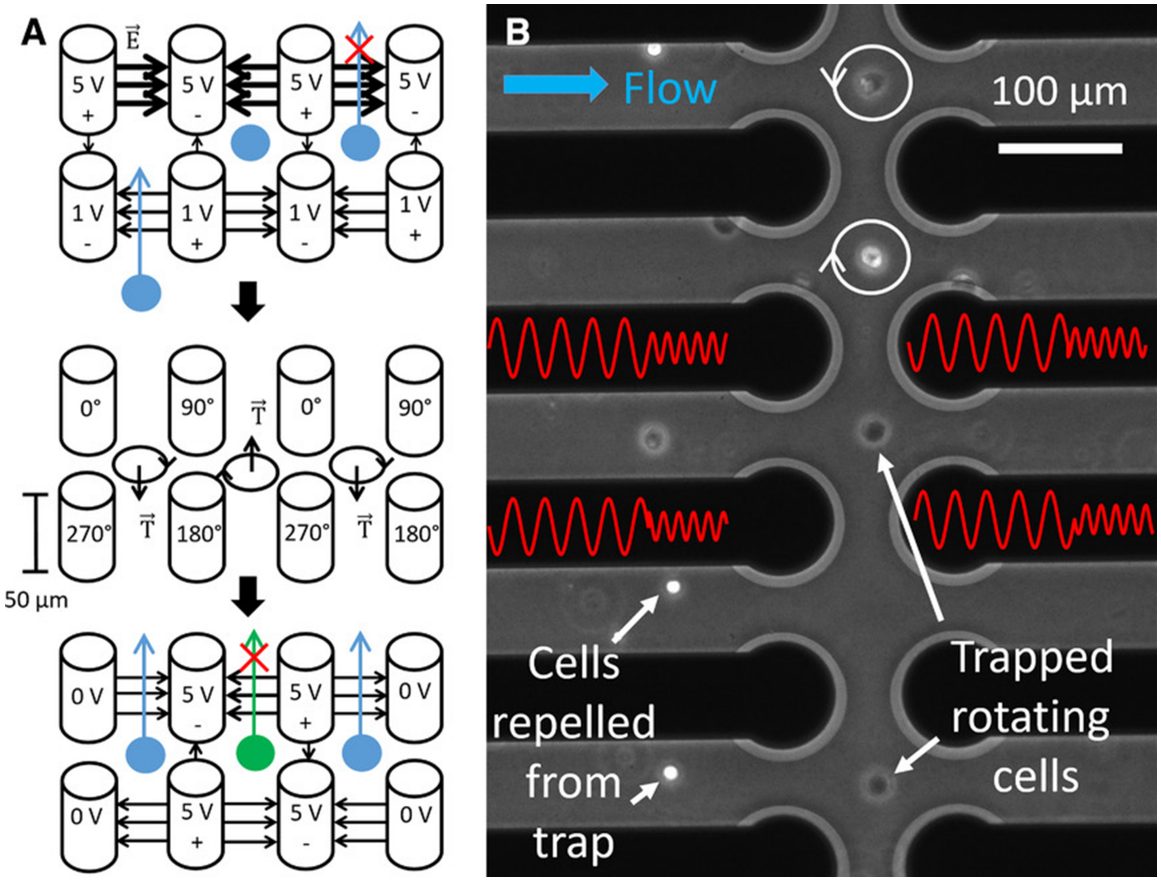

Figure 4.6. (A) Schematic demonstrating the working principle of the microcage array. First, single cell(s) are trapped, then analyzed by electrorotation after that, they are selectively released. (B) Microscope image of rotating cells simultaneously trapped within the microcage array by alternating DEP and ROT signals. The first DEP signal has a phase shift of 180° between neighboring electrodes and exerts a trapping force. The second ROT signal has a phase shift of 90° between neighboring electrodes (the electric signals on the electrodes are illustrated in red) and exerts a torque on the cells making them rotate. Cells outside the cages are repelled and this cannot enter due to the presence of a dielectrophoretic barrier. Reproduced with permission from [120].

Continuous trapping and position in the microcage are achieved by applying the trapping nDEP signal for fraction of seconds (≈ 100 ms) then the electrorotation signal is applied [242] with a phase shift of 90 ° between the sinusoidal signal applied at the neighboring electrodes (Fig. 4.6) to achieve the parallel trapping at different microcages simultaneously.

1 Theory of ELectrorotation

Recall from Eq 2.18, the DEP force acting on a homogeneous particle is:

$$\langle f_{\mathrm{DEP}} \rangle = 2\pi\varepsilon_0\epsilon_m R^3 Re[f_{\mathrm{cm}}]\nabla|E|^2 \tag{4.13}$$

with ϵ_m is the permittivity of the medium,ε_0 is the permittivity of the vaccum, R, is the cell radius and $Re[f_{\mathrm{cm}}]$ is the real part of the Clausius-Mossotti factor, which depends on the dielectric properties of the cell and the surrounding medium. $]\nabla|E|^2$ is the gradient of the peak electric field. The speed of rotation for electrorotation can be related to the imaginary CM factor from [153]

$$\Omega = -\frac{\varepsilon_0\varepsilon_m}{2\eta} Im[f_{\mathrm{cm}}]E^2 \tag{4.14}$$

with the medium viscosity η and Im$[f_{\mathrm{cm}}]$ the imaginary part of the Clausius-Mossotti factor. The Clausius-Mossotti factor's expression depends on the model used for the cell and is given by [243]

$$f_{\mathrm{cm}} = \left(\frac{\epsilon_p^* - \epsilon_m^*}{\epsilon_p^* + 2\epsilon_m^*}\right); \quad \epsilon_p^* = C_{\mathrm{mem}}^* \frac{3R\epsilon_{\mathrm{cyto}}^*}{3\epsilon_{\mathrm{cyto}}^* + 3RC_{\mathrm{mem}}^*} \tag{4.15}$$

where ϵ_p^*, ϵ_m^*, and $\epsilon_{\mathrm{cyto}}^*$ are the complex permittivity of the particle, the suspending medium and the cytoplasm respectively and C_{mem}^* is the complex membrane capacitance defined as $C^* = C - iG/\omega$ with G being the membrane conductance.

2 Cell Preparation

Microchips fabrication was achieved in CMi (EPFL, Switzerland), experiments and cell preparation were conducted in CLSE lab (EPFL, Switzerland).

HeLa, HEK 293 and BE (2)-M17 human neuroblastoma cells are cultured in DMEM (Dulbecco's Modified Eagle's Medium), human immortalized T lymphocytes are grown in suspension in RPMI (Roswell Park Memorial Institute) Medium. In both media, 10% FBS (Fetal bovine serum) and antibiotics are added. Before the experiments, the adherent HeLa, HEK 293 and M17 cells are detached from the surface of the culture flask using 1X *Trypsin* and all cells are resuspended in an isotonic solution (8.6% dextrose and 0.3% sucrose) with an adapted conductivity of 100 mS/m using 1X PBS (phosphor-buffered saline). The cell concentration was about 200,000 cells per milliliter.

To allow bubble-free flow before the experiments, the testing chips are flushed with 2 ml of the corresponding culture medium (including FBS) and subsequently with 2 ml of the 100 mS/m solution, in which the cells are suspended. From reported literature values, electrorotation experiments are performed at a medium conductivity of 56 mS/m, which is found to be the conductivity at which the cytoplasm conductivity of cells can be investigated [233, 236]. However, to obtain nDEP at frequencies high enough to avoid electrolysis at the electrodes, 100 mS/m conductive media was used.

Based on the cell size (diameter), the proper microchip electrode diameter (20, 40, or 80 µm) will be selected to satisfy the right magnitude of the electric field required to actuate the cells. HeLa, HEK 293, and M17 neuroblastoma cells are injected in chips with an electrode diameter of 40 and 80 µm as their diameter are $\sim 10 - 18$ µm. Hence, they are not injected in chips with an interelectrode distance of 20 µm, since they occasionally cause clogging due to their size, especially if cell clusters are formed. On the other hand, T-lymphocytes can be injected in chips featuring any of the three designs with different electrode diameter however, they would require higher voltage application when injected inside the large electrode size chips.

The cells in suspension are driven through the device by a flowrate between 200 and 1 µL/min. With no electric field applied, they simply pass by the upstream (entrance) electrodes first and then the downstream (exit) electrodes. For the trapping of cells, the arbitrary waveform generator (TTi TGA12104) creates four signals. Two signals of 5 V_{pp} amplitude and a phase shift of 180° and two signals of 1 V amplitude and a phase shift of 180°. Applying an alternating current (100 kHz) electric voltage signal of 1 V amplitude at the entrance and of 5 V amplitude at the exit electrodes creates a lower dielectrophoretic barrier at the entrance and a higher barrier at the exit of the array. Due to the drag force of the fluid flow, the cells can pass the lower entrance barrier, but cannot overcome the higher barrier at the exit electrodes which forces the cells to be trapped within the selected microcage (Fig. 4.6A).

Once the cell is trapped in within the addressed single cell microcage, the voltage at the two upstream electrodes is raised to 5 V amplitude preventing additional cells to enter the trap (the voltage is changed by means of selection of a custom-built PCB controlled by a LABVIEW program. Meanwhile, the other traps are kept open, with an entrance voltage of 1 V amplitude. Adjacent quadrupoles now have one entrance electrode with an applied voltage of 1 V amplitude and one with 5 V_{pp} amplitude, however, the dielectrophoretic barrier is still low enough to allow incoming cells to enter the trap. Upon successful passage of sufficient amount of cells inside parallel microcages, all traps are closed by raisin the voltage again to 5 V_{pp} and the actuating electric signal which contains a superposition between a DEP trapping (5 V_{pp} amplitude, 100 kHz, and a phase shift of 180° between neighboring electrodes) and a ROT signal (2.5 V_{pp} amplitude, a swept frequency and 90° phase shift between neighboring electrodes) as illustrated in Fig. 4.6B. The torque induced by the ROT signal generates on the cells causes them to rotate (Fig. 4.6A). Figure 4.6 shows a microscope image of the measurement in which four single cells are rotating within the array and another four cells are prevented from entering the trap Further supporting trapping/releasing and rotation videos can be found from supporting information published here [120] . The frequency of the rotating electric field is swept between 10 kHz and 10 MHz in 25 logarithmic steps. Multiple single cells are rotating simultaneously in individual neighboring microcages. Videos of the cells rotation are captured with a frame rate between 5 and 25 Hz using a microscope camera (Andor Neo sCMOS) for 3 s for each electric signal frequency. Then, the rotation speed of the cell rotation captured in the videos were extracted by an automatic pattern matching

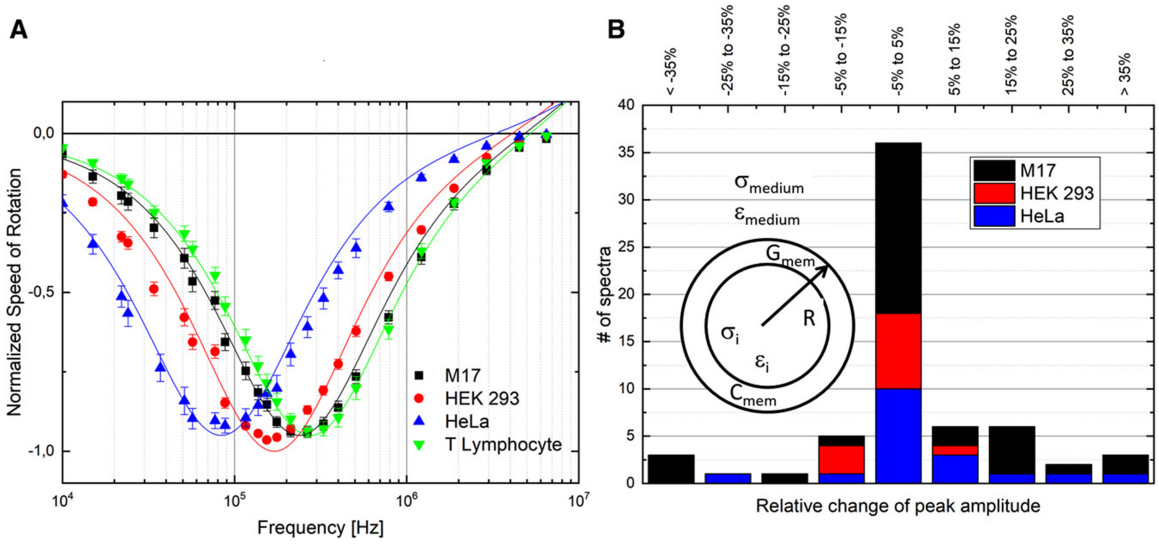

Figure 4.7. (A) Averaged and normalized electrorotation spectra and standard error of M17 neuroblastoma cells (black), HEK 293 (red) cells, HeLa (blue) cells, and human immortalized T lymphocytes (green) and their corresponding theoretical curves based on the extracted cell parameters. (B) Evaluation of the relative change of the absolute peak amplitude before and after the exposure to the rotating electric field for 5 min. Reproduced with permission from [120].

algorithm implemented in custom-built LabVIEW Vi. Since T lymphocytes could not get held against the flow by cages of 40 and 80 µm interelectrode distance, the flow was stopped as soon as the T-lymphocytes were within the microcage array. Hence, the nDEP force was sufficient to center them and their electrorotation spectra could be acquired (Fig. 4.7A).

After the acquisition of the ROT spectra, the cells can be selectively released by turning off the electric signal at one of the exit electrodes. The exit barrier is thus reduced, and the cell is carried away by the flow as illustrated at the bottom of Fig. 4.6A. It has been noted that HeLa, HEK 293 cells, and M17 neuroblastoma are getting trapped in arrays with 40 µm and 80 µm inter electrode distance, while human immortalized T lymphocytes are not due to their small cell size ($\sim 5-7$ µm in diameter) which requires higher electric field magnitude to sustain the same similar DEP force exerted on the other cells. Even though the platform can provide voltages as high as 20 V, therefore electric field, higher magnitudes were not applied to ensure the viability of the trapped cells.

Over 125 spectra were acquired, including repeated measurements on the same cell to verify the stability and repeatability of the system. The averaged electrorotation spectra and its standard error of each population are shown in Fig. 4.7A. By dividing each spectrum by dividing the relevant speed of rotation, the correspondent peak speed of rotation of each spectrum. The extracted parameters are traced as a continuous line in the Fig 4.7A. The first acquired electrorotation spectrum of each cell was fitted to the single shell model discussed in section 2.2 & 4.2.1, depicted in Fig. 4.7B, using a least square method. The cell radii were measured by the microscope in order

to be used in the fitting model. Since our measurements were performed below a frequency of 10 MHz, the cytoplasm parameters hardly influence the electrorotation spectrum [243], therefore cells' cytoplasm conductivity and permittivity values were adapted to those reported in literature for fitting purposes. Hence, the value for T lymphocytes [234, 244, 245] and HEK 293 cells [246–248] a cytoplasm conductivity of 0.5 S/m and a cytoplasm permittivity of $78\varepsilon_0$ (same as water) is adapted. Moreover, M17 neuroblastoma are fitted with these cytoplasm parameters too, since these are values commonly used for several cell lines. For HeLa cells, a cytoplasm conductivity of 0.84 S/m is the average literature value and a cytoplasm permittivity of $60\varepsilon_0$was assumed [249]. The membrane conductance was fixed to a value of 100 S/m2 for T lymphocytes [8] and 0.95 S/m2 for HeLa cells [249]. However, for HEK 293 cells and M17 neuroblastoma the membrane conductance value was kept floating in the fitting program.

To verify the repeatability and the effect of the ROT platform on the cells being studied, acquisition of consecutive spectrum for the same trapped cells were achieved for 30 mins with 5 min interval time. It was observed that the peak frequency, at which the highest rotation speed occurs, deviated $\pm 10\%$ from the original starting time however, this value is lower than reported over similar time period when using other techniques such as laser tweezers (approx. 50% in 40 min) [237] . In order to investigate the stability of the acquired spectra over time, electrorotation of 63 cells was performed before and after 5 min exposure to nDEP trapping and rotation within the array. The relative change of the peak amplitude is illustrated in Fig. 4.7B. About 57% cells experience a variation of less than $\pm 5\%$, the other vary more. Such variation of the peak amplitude could be that the cells are observed in flow and possibly particulates in the solution or fluctuations within the solution might impact the rotation. However, the different contributions to this variation, on one side the sources of noise derived by the imprecise definition of the cell position and, on the other side, the actual changes of the rotation speed over time can be further investigated.Figure 4.8 shows the extracted dielectric properties for cells studied using the ROT platform. The extracted values are mostly in agreement with the literature values. However, the specific membrane capacitance of M17 neuroblastoma, 7.49 ± 0.39 mF/m2 , was reported for the first time [120].

The throughput of the platform is limited to the field of view of the used camera. Hence, with the current setting, the 20X magnification has a field of view of 690 µm X 582 µm. Therefore, 10 quadrupoles, with 40 µm electrode design, can be observed at once and the electrorotation spectra of the parallel cells trapped within can be acquired. Using the same analogy, by using 20 µm electrode design, 39 traps can be visualized at once. On the other hand, giving that the flow rate used for the experiments was 1 µL/min with 2×10^5 cells/ml, a new cell can be trapped within a cage in 12 s. Hence, the time needed to fill the whole batch of traps around 90 s. Using statistical probability analysis for determining the possibility of a trap to be filled or not, the total throughput of the device can be 600 cells/h which is very high compared to other single cell techniques combined with laser tweezer where a throughput of $12 - 20$ cells/h can be achieved [250].

Once cells have been trapped and analyzed, they can be addressed separately

Cell Type	Radius (μm)	Cytoplasm conductivity σ_i (S/m)	σ_i reported in literature (S/m)	Cytoplasm permittivity ε_i	ε_i reported in literature	Membrane Conductance G_{mem} (S/m^2)	G_{mem} reported in literature (S/m^2)	Specific Membrane Capacitance C_{mem} (mF/m^2)	C_{mem} reported in literature (mF/m^2)
Human T-lymphocyte ($n = 7$)	4.25 ± 0.05	0.5	0.5	78	78	100	10 −1000	9.61 ± 2.39 (0.97)	13.49 ± 4.72
			0.53 ± 0.1		100		–		7.01 ± 0.91
			0.65 ± 0.15		103.9 ± 24.5		–		10.5 ± 3.1
			1.06 ± 0.14		74.0 ± 5.3		100		12.1 ± 1.4
			0.3 − 1		85		–		11±1.1
HEK293 ($n = 33$)	6.75 ± 0.5	0.5	0.175 ± 0.014	78	85 ± 15	3×10^{-14}	~ 0	9.81 ± 2.24 (0.39)	7.5 ± 0.3
			-		–		–		11.1 ± 0.8
			0.5		60		7 X 10^-14		-
			0.408 ± 0.019		85 ± 4		~ 0		7.94 ± 0.4
Hela ($n = 14$)	8.74 ± 1.33	0.84	–	60	47	0.95	0.95 − 1.2	17.51 ± 2.72 (0.75)	18.5 ± 2.6
			0.435 − 1.25		35 − 60		–		19
M17 ($n = 29$)	6.30 ± 1.29	0.2	–	78	–	3.5×10^{-14}	–	5.35 ± 1.37 (0.26)	–
		0.5				5.7×10^{-13}		7.49 ± 2.07 (0.39)	

Figure 4.8. The extracted dielectric parameters and their standard error compared to the values found in literature. The values indicated with * were fixed. The cell radii were measured by optical observation of the cells in suspension. Reproduced with permission from [120].

to be released (Fig. 4.9E) thanks to the separate electrodes design and connections that can be controlled by the operator. This design allows further manipulation, if needed, for selective cells to go further analysis or to be released to a discharge reservoir (Fig. 4.9).

Concluding Remarks

The aim of this chapter was to describe other electrokinetic characterization techniques for cell analysis. In general, the main advantages of DEP- based microfluidic devices are the ability to trap, manipulate, separate, sort and catheterize analytes. Unlike separation applications, throughputs achieved from characterization devices cannot be achieved that high. Because of the high sensitivity required to analyze cells/particles which in turns requires low flow rates, high throughput characterization techniques are not trivial. EIS-based characterization can provide dielectric properties of cells as an average of dielectric properties of bulk of cells in suspension hence, it cannot provide reliable data compared to ROT or isoDEP. Electrorotation is a DEP-based technique which is mainly used for single cell characterization. ROT was the widely used DEP-based technique to precisely extract cells' phenotypes [8, 120, 246] with throughput of ~ 10 cells/min using parallel cages design. Despite it is nontrivial to position individual cells within an electrode region (microcage) due to the physics of laminar flow, it still can offer reliable data. Also, the electrode geometry needs to be scaled to accommodate different cell sizes. Hence, ROT can be the best candidate when reliable single cell characterization is urgent without the need for high throughput analysis. The platform reported by Allen, et al. [15] utilizing isoDEP-based design can characterize the dielectric properties of particles with a throughput

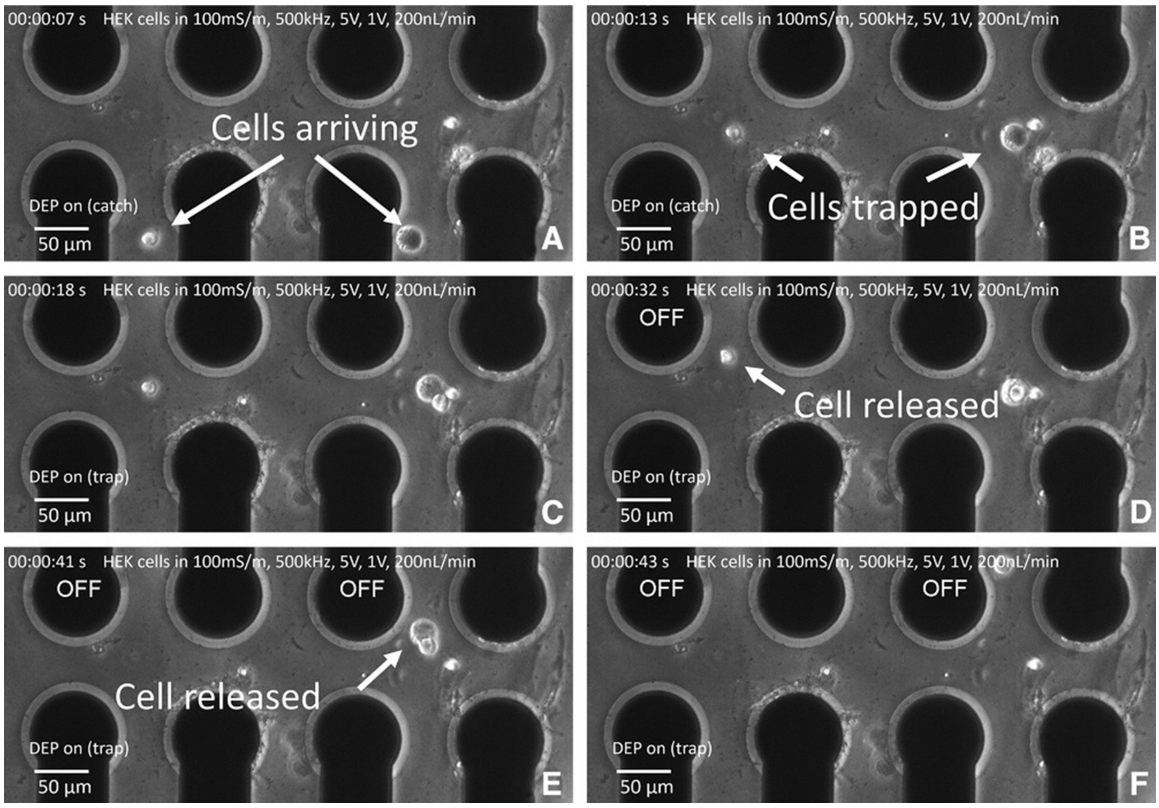

Figure 4.9. Image series of the selective trapping/release mechanism. (A–C) two HEK 293 cells are trapped simultaneously in the microcage array. (E) Switching off the electric signal on the very left electrode to release the left cell. (F), (G) Controlling the signal on the electrode bordering the cell on the right releases it. Reproduced with permission from [120].

of $\sim 600 - 6000$ particles/min which is one or two magnitude higher than ROT and static electrical impedance spectroscopy based characterization (∼60/min) [251] while maintaining the same level of analytical sensitivity. Even though such throughput is one or two magnitudes lower than flow cytometry based characterization techniques ($\sim 60,000$ cells/min) [252], or dynamic EIS characterization ($\sim 1000 - 60,000$ cells/min) [251, 253].However, for high throughput EIS analysis, cells are characterized with one or two frequencies, and not with range of frequencies like ROT or isoDEP, hence, It cannot provide comprehensive frequency analysis. Moreover, EIS-based technique's sensitivity is not as high as ROT or isoDEP but, it can be the best candidate for characterization of cells in suspension without the need for high electric field magnitudes, required for cell trapping, which ensures the cell viability and stress-free environment for the cells. However, to achieve higher sensitivity, static EIS systems are required, in this case, the throughput will be minimized. Also, single cell EIS platforms requires impedance analyzers which makes the portability of such systems nontrivial. Hence, ROT and EIS-based characterization platforms are expensive and their portability for in-the-field applications is not easily realized. However, the common advantage of ROT and isoDEP is that both require camera system to

characterize the particles, such imaging system can provide further insights into the particles analyzed such as size and shape. Additionally, ROT and isoDEP devices can be incorporated simultaneously with fluorescence analysis. On the other hand, the most distinct advantage is that the cost of IsoDEP device fabrication and operation will be significantly lower than the other techniques, especially when utilizing the insulative-based isoDEP design which can be made disposable and be fabricated in parallel manner to achieve higher throughput.

On the other hand, isoDEP not only can be used as a characterization tool but also as particle separator. Such advantage is lacked in ROT or EIS applications. By utilizing isoDEP-based electrode design, achieved by Pohl and Hawk [143] were able to achieve separation of large-size particles with high flow rates ($\sim$9.6 µL/min) which is comparable to the throughput achieved by traditional DEP-based separators. Kaler, et al. [154] achieved separation throughput of $\sim$13,320 cells/min which was limited by the purity of the separation yield. In the same manner, Shkolnikov, et al. [158] achieved the highest isoDEP-based separation throughput ($\sim$20,000 particles/min) and efficiency ($\sim 70 - 80\%$). Although such throughputs still fall behind the one achieved from traditional DEP-based commercialized separators, however, thanks to the uniqueness of isoDEP geometry, parallelizing active separation regions can be achieved without fabrication complexities to obtain higher throughput.

CHAPTER V

DIELECTROPHORESIS-BASED CHARACTERIZATION OF LEA PROTEINS

This chapter describes an application for dielectrophoresis-based platform that's utilized to characterize LEA proteins and their role in desiccation tolerance. The content of this chapter is adapted from published work [254].

The ability to enter and exit anhydrobiosis relies on an array of molecular mechanisms designed to repair and protect various cellular structures and macromolecules (e.g. DNA, RNA, proteins, membranes, etc.). Common anhydrobiotic strategies observed in animals include the accumulation of protective osmolytes, particularly trehalose, as well as the expression of a variety of ARID proteins including late embryogenesis abundant (LEA) proteins [255, 256] and tardigrade-specific intrinsically disordered proteins (TDPs). LEA proteins were originally discovered in plants, and predominantly occur in the late embryogenesis stage of orthodox seeds, but were later also found in other plant tissues and in anhydrobiotic animals [257]. Several sequence-based grouping methods for LEA proteins have been described and this work will adapt the grouping scheme proposed by Tunnacliffe and Wise as a means to classify and organize groups of LEA proteins [258].

This study focuses on two different LEA proteins from *A. franciscana*, *Afr*LEA3m and *Afr*LEA6, a group 3 and 6 LEA protein, respectively. While *Afr*LEA3m is a mitochondrial-targeted protein, it was shown to protect artificial membranes with a similar composition to the inner leaflet (*i.e.,* inner side) of the plasma membrane with the same efficacy as it protected artificial membranes with lipid composition mimicking the inner mitochondrial membrane [259–261]. Since the vast majority of mitochondrial proteins, including *Afr*LEA3m, are synthesized in the cytoplasm of the cell, it seems plausible that *Afr*LEA3m before its transport into the mitochondrial matrix could aid in protecting the plasma membrane during desiccation. While bioinformatic data suggests that *Afr*LEA3m can form amphipathic α-helices during water stress to integrate into membranes, it remains experimentally undetermined if *Afr*LEA3m can directly or indirectly interact with membranes during water stress [262]. In contrast, *Afr*LEA6 localizes to the cytoplasm as judged by bioinformatics and confirmed by ectopic expression in Kc167 cells (data not shown) [263]. While group 3 LEA proteins are commonly found in anhydrobiotic animals, *A. franciscana* is the only known anhydrobiotic animal to express a group 6 LEA protein, making it an interesting target for further study. Furthermore, bioinformatics does not suggest that *Afr*LEA6 can fold into amphipathic α-helices during water stress, making it a good candidate for comparison to *Afr*LEA3m.

AC-electrokinetic based techniques such as dielectrophoresis [264–269], electrorotation (ROT) [270–273], and electrochemical impedance spectroscopy (EIS) [274–277]

have been used to investigate and analyze properties of biological systems. DEP measures electrical properties by applying a non-unifrom electric field to a liquid media of a known conductivity containing suspension of cells [278–281]. The non-uniform electrical field will induce a dipole within each cell; the induced translation of each cell in the electrical field depends on their phenotype *i.e.,* permittivity and conductance properties of the membrane and cytoplasm as well as the conductivity of the solution. In this study, dielectrophoresis was used to gain insights into the molecular mechanisms of cellular protection during water stress conferred by *Afr*LEA3m and *Afr*LEA6, two LEA proteins from the anhydrobiotic brine shrimp, *Artemia franciscana*. Extracted DEP-based characterization data in this study demonstrates that expression of LEA proteins from *A. franciscana* in desiccation sensitive cells from the fruit fly *D. melanogaster* have pronounced impact on cytoplasmic conductivity and membrane capacitance. These results show that DEP can offer a novel approach to gain insights into the molecular mechanisms of protections this elusive class of proteins offers during anhyrdobiosis.

Methods

1 Cells, Culture and Transfections

Kc167 cells were purchased from the Drosophila Genomics Research Center (DGRC; Bloomington, IN). Cells were cultured on 100 or 60 mm cell culture-treated dishes (Corning Incorporated, Corning NY) in Schneider's media (Caisson, USA) supplemented with 10 % heat-inactivated fetal bovine serum (FBS) (Atlanta Biologicals, Lawrenceville, GA). Transfections were performed as previously described with the exception that Schneider's media was used in place of M3+BPYE medium, and that 2.0 mg/mL G418 (ultrapure; VWR International) was used to select transfected cells to generate and maintain stable cell lines [261]. The *pAc5-STABLE2-neo* vector was acquired from Addgene (Cambridge, MA). For additional information on the *pAc5-STABLE2-neo* vector, please see the discussion and reference [282]. Immunoblotting with primary antibodies (Aves Labs Inc, Tigard, OR) raised against *Afr*LEA6 or *Afr*LEA3m was performed on all cell lines to confirm transgenic protein expression [263, 283] (Fig. 5.1).

SDS-PAGE and Western blot analyses were performed as previously described [261]. However, primary polyclonal antibodies raised against purified *Afr*LEA6 and *Afr*LEA3m (Aves Labs Inc., Tigard, OR; 1:5000 dilution) and HRP-linked goat anti-hen secondary antibodies (Aves Labs Inc, Tigard, OR; 1:5000 dilution) were used for detection.

2 SEM Imaging

Kc167 cells were plated onto an aluminum SEM stage at a concentration of 2×10^6 cells/mL. The cells were allowed to attach to the stage for 1h in a humidified chamber at 25 °C. Culture media was removed, and cells were then dried overnight at 10 % relative humidity. The dried samples were sputter coated with an 18 nm film of gold

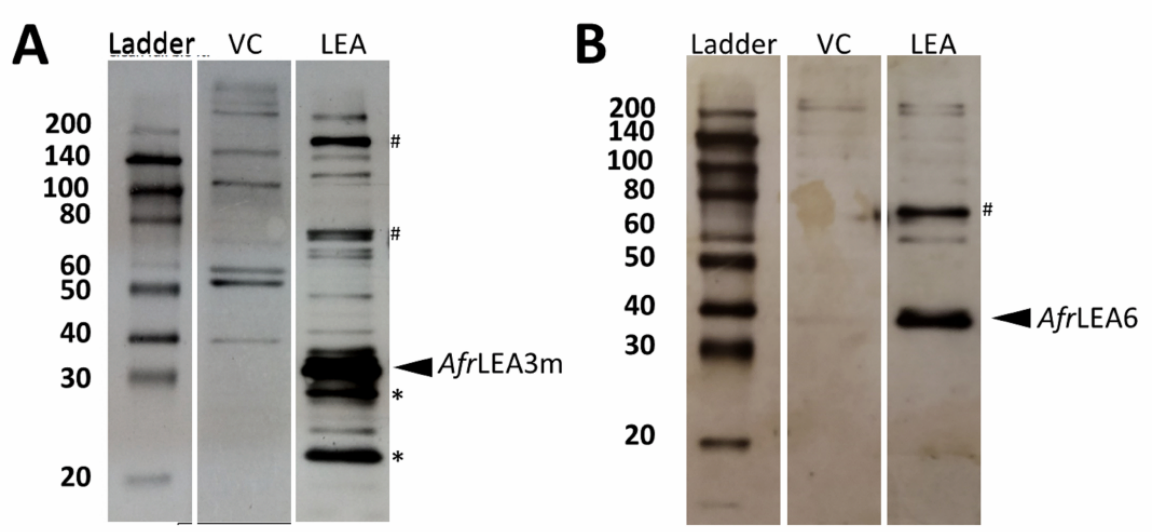

Figure 5.1. Immunoblots confirming expression of (A) *Afr*LEA3m ($\sim$ 31 kDa [260]) in Kc167 cells. Several possible higher-order structures were also identified (#) as well as breakdown products ($*$). Blotting results for vector control cells (VC) stably transfected with the expression vector but lacking inserted LEA proteins are shown for comparison. (B) *Afr*LEA6 expression in Kc167 cells. The apparent Mw was about 8 kDa larger than expected ($\sim$ 27 kDa [263]). The increased apparent Mw might be related to post-translational modification and the known behavior of some LEA proteins to migrate slower during SDS-PAGE than most non-LEA proteins. One higher-order structure was also identified (#).

and palladium, and examined using a Zeiss Supra 35 VP scanning electron microscope with an electron high tension voltage of 15-20 kV.

3 DEP Characterization

To collect cells and remove cell culture medium, Kc167 cells were centrifuged at 400 g for 2 min at room temperature. The cellular pellets were resuspended in 10 mL of medium consisting of 85 g/L sucrose plus 3 g/L glucose, 11 mg/L $CaCl_2$, and 24 mg/L $MgCl_2$, $\sim$360 mOsmol/kg. In experiments using hypertonic media, the osmolarity was brought to $\sim$560 mOsmol/kg and $\sim$760 mOsmol/kg with an additional 200 mM and 400 mM sucrose, respectively. To ensure complete removal of cell culture medium, Kc167 cells were pelleted again and the final resuspension volume was approximately 1 mL. The final conductivity of the medium was adjusted to 5 mS/m using Phosphate Buffered Saline (PBS) and the desired conductivity was verified with a conductivity meter (HORIBA Ltd, Koyoto, Japan). The number of cells was enumerated using a hemocytometer and adjusted to approximately $5 - 8 \times 10^6$ cells/mL ($\pm$10 %) for the DEP measurement. In general, one sample of 5 mL of cells, n_{bio}, in suspension can provide, on average, approximately $10 - 12$ technical repeats, n_{tec}, of data sets with total number of trials, $n = n_{bio} \times n_{tec}$. The 3DEP (Deptech, Ringmer, UK)

platform was used to study the electrical properties of the cell. The experimental set up and electrode arrangement were used as described by Labeed and colleagues [284]. To operate the instrument, cells are injected inside a microchip containing 20 micro wells (3DEP 806), consisting of layers of embedded electrodes. Next, the chip is mounted on a camera setup where a light beam is directed from the top of the chip. An AC signal of 10 V_{pp} and frequencies between 3 kHz and 40 MHz (at 5 frequencies per decade) are applied to all microwells simultaneously and the intensity of light passing through the microwells is then recorded concurrently. The intensity of light changes depending on the movement of the cells by the DEP force, F_{DEP}, exerted on them is:

$$F_{DEP} = 2\pi\epsilon_s r^3 \,\mathrm{Re}[F_{cm}(\omega)]\nabla E^2 \tag{5.1}$$

F_{DEP} is the force exerted on a particle of radius r in a medium of permittivity ϵ_s within an electric field, E. The dielectric proprieties of the cell governs its movement within the non-uniform electric field. A single shell model was used which approximates cells as spheres of cytoplasm of conductivity, σ_c, and permittivity, ϵ_c, surrounded by a membrane of conductivity, σ_{mem}, and permittivity, ϵ_{mem}, suspended in a medium of conductivity, σ_s, and permittivity, ϵ_s. This simplified model offers a solvable number of parameters for a DEP spectrum which is related to the data output of the 3DEP platform. This is represented by Clausius-Mossotti factor, $F_{cm}(\omega)$, which is a function of frequency, conductance and permittivities of cell cytoplasm, membrane and suspending media, thus:

$$F_{cm}(\omega) = \left(\frac{\epsilon^*_{cell} - \epsilon^*_s}{\epsilon^*_{cell} + 2\epsilon^*_s}\right) \tag{5.2}$$

$$\epsilon^*_{cell} = \epsilon^*_s \frac{\left(\frac{r}{r-d}\right)^2 + 2\frac{\epsilon^*_c - \epsilon^*_{\mathrm{mem}}}{\epsilon^*_c + 2\epsilon^*_{\mathrm{mem}}}}{\left(\frac{r}{r-d}\right)^3 - \frac{\epsilon^*_c - \epsilon^*_{\mathrm{mem}}}{\epsilon^*_c + 2\epsilon^*_{\mathrm{mem}}}} \tag{5.3}$$

where ϵ^*_{cell} is the effective complex permittivity of the cell with r and d are the radius of the cell and membrane thickness (d=10 nm) respectively. $\epsilon^* = \epsilon - j\sigma/\omega$ represents the complex permittivity and is a function of the permittivity ϵ, conductivity σ, angular frequency of the electric field ω. Hence, based on the sign of $\mathrm{Re}[F_{cm}(\omega)]$, cells will experience either a negative dielectrophoresis (nDEP), or a positive (pDEP) force. Cells experiencing an nDEP force will be centered in the middle of the micro well where they will be blocking the light (*i.e.,* repelled to field minima). Conversely, the cells experiencing a pDEP force will be attracted towards the perimeter of the micro well, and more light will pass through the center of the micro wells (*i.e.,* attracted to field maxima).

Light intensity, in each micro well, was measured for 30 seconds sweeping a frequency range from 3 kHz to 40 MHz. The light intensity vs frequency spectrum generated was next fitted by an iterative least square method [284] to Eqs.1, 2 and 3 to yield individual values of membrane and cytoplasmic conductivity as well as specific membrane capacitance, $c = \epsilon_{\mathrm{mem}}/d$. 3DEP light intensity bands from 4 to 9, from the platform spectrum output, were only selected for each experiment to be

fitted, resulting in a better DEP spectrum fitting correlation coefficient $R > 0.97$ (Fig. 5.2). Cells were measured immediately (¡17 min) after being suspended into the DEP media to minimize artefacts due to cell stress by the non-physiological ion composition of the medium. The time to collect and characterize approximately 10-13 samples using the 3DEP platform takes only 15 to 17 min. To investigate the effect of the DEP buffer on cell viability and potentially changes in the measured parameters we studied Kc167 cells' viability in isotonic and hyperosmotic DEP media for up to 1 h. No significant changes in cell viability were found for up to 30 min and all other experiments were completed in under 20 min (±SD; $P > 0.05$; One-way ANOVA, Fig. 5.3). Furthermore, no significant changes in the resultant DEP spectrum of Kc167 cells characterized within 30 min was observed (±SD; $P > 0.05$; One-way ANOVA, Fig. 5.3).

Results and Discussions

In this study a detailed characterization of the electrical properties of Kc167 cells from *D. melanogaster* and the changes that occur in these properties in response to acute osmotic stresses has been achieved. Using ectopic protein-expression models, modulations in the osmotic-stress response could be correlated to molecular mechanisms of cellular protection conferred by two LEA proteins that ameliorate water-stress damage in the anhydrobiotic embryos of *A. franciscana*[285]. Previous studies conducted with artificial liposomes have indicated that *Afr*LEA3m can directly interact with phospholipid bilayers during severe water stress[259]. Based on theses data it was hypothesized that the specific membrane capacitance of Kc167 cells expressing *Afr*LEA3m will increase during water stress, and that the specific membrane conductance be unaltered if *Afr*LEA3m was indeed interacting directly with the plasma membrane during moderate osmotic stress (∼760 mOsmol/kg). To test this hypothesis, a dielectrophoresis-based platform was used to characterize the cytoplasmic conductivity, the specific membrane capacitance, and the specific membrane conductance of cells in isotonic sucrose medium (∼360 mOsmos/kg) with a low ionic strength (¡ 6.5 S/m), and hypertonic media of either 560 or 760 mOsmol/kg adjusted by addition of sucrose to reach the desired osmolarity, to mimic water stress (Table 5.1). The low ionic strength of the media was required to create a significant difference between media conductivity and that of the cytoplasm and membrane, thereby increasing the resolution of DEP measurements (Eq. 5.2), hence, achieving better resolution. Conversely, relatively high media conductivity (∼100 mS/m) will compromise the reliability of the DEP measurements by introducing other electrokinetic effects (e.g. Joule heating [113]). However, these DEP-compatible media may negatively impact cell viability over time, since the cells are deprived of several important components normally found in insect cell-culture media (e.g. monovalent ions, sugars, and amino acids). Not surprisingly, a significant decrease in the values of all three fitted parameters (cytoplasmic conductivity, the specific membrane capacitance, and the specific membrane conductance) was observed for control cells incubated in isotonic sucrose media for $\sim$ 16 h, where 100% of cells showed a collapse in membrane integrity

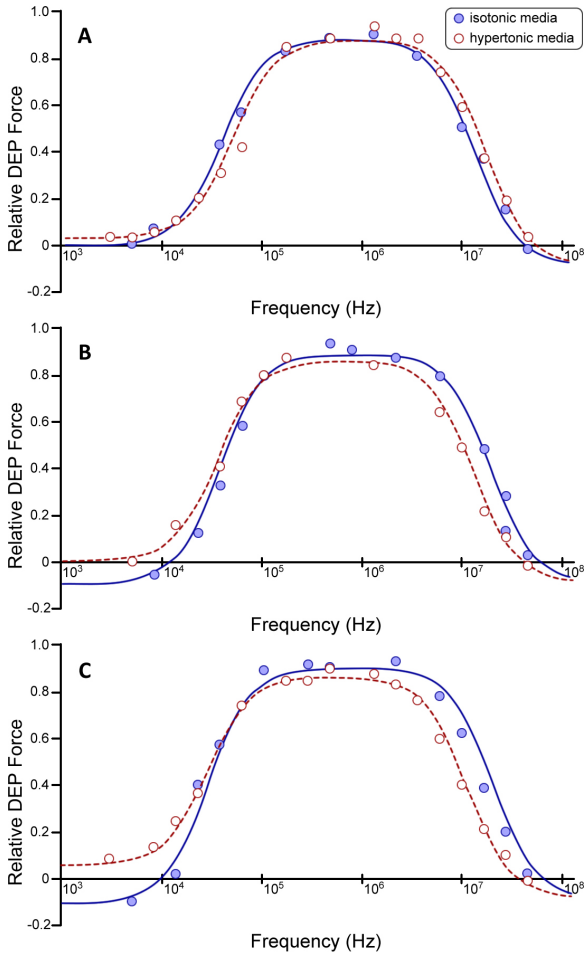

Figure 5.2. Dielectrophoretic proprieties of Kc167 cells. Comparison of DEP spectra produced from suspending cells in isotonic media (∼360 mOsmol/kg; blue), and hypertonic media (∼760 mOsmol/kg; red) for (A) Kc167 vector control (VC) cells averaged DEP spectra ($n = 68$ and $n = 61$). (B) Kc167 cells expressing the *Afr*LEA3m protein averaged DEP spectra ($n = 72$ and $n = 58$). (C) Kc167 cells expressing the *Afr*LEA6 protein averaged DEP spectra ($n = 72$ and $n = 57$). The solid line curves are fits of Eqs. 5.1, 5.2, and 5.3, see Methods. The y-axis relative polarizability is a function of the $[F_{cm}(\omega)]$ factor with positive values equivalent to pDEP and negative values equivalent to nDEP. The respective correlation coefficient, R, values for all fitted curves were $R > 0.97$.

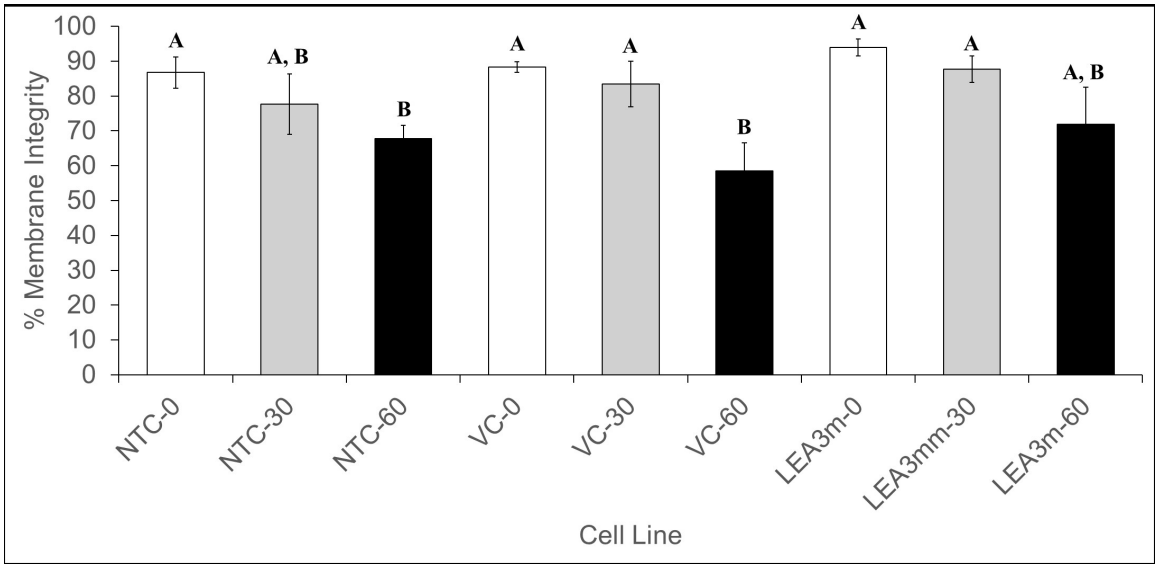

Figure 5.3. Viability of Kc167 cells is significantly reduced when incubated for up to 60 min in low ionic strength ($<$ 6.5 S/m) isotonic sucrose medium ($\sim$ 360 mOsmol/kg). White bars represent 0 min incubation, grey bars represent 30 min incubation, and black bars represent 60 min incubation. Letters denote significance (*i.e.,* "A" and "B" are significantly different from one another, but neither are significantly different from "A,B") ($\pm$SD; $p < 0.05$; One-way ANOVA).

(Table 5.1, VC-Dead). Furthermore, the viability of cells in isotonic sucrose media was also significantly reduced after only 60 min of incubation for non-transfected control and vector control cells, indicating the time-sensitivity of the measurements (Fig. 5.3). However, there was no significant reduction in viability for up to 30 min of incubation for any cell line in all DEP media employed. Based on these data, all other measurements were completed within ¡ 18 min to avoid artifacts caused by cell death. There was no significant difference observed in any fitted values between non-transfected control cells and vector control cells demonstrating that expression of transgenic genes such as the aminoglycoside 3′-phosphotransferase to confer G418 resistance, does not *per se* change the electrical properties of cells (Table 5.1).

Interestingly, there was an $\sim$41 % and $\sim$51 % increase in the cytoplasmic conductivity of cells expressing *Afr*LEA3m and *Afr*LEA6, respectively, over vector controls under isotonic media conditions. The impact on cytoplasmic conductivity was surprising, given that the concentration of cytoplasmic ions is much higher than the concentrations of ectopically expressed proteins. Cytoplasmic conductivity is assumed to be primarily affected by the intracellular [K^+] and, to a lesser amount [Cl^-], given their relatively high concentrations compared to other ions, charged molecules, and macromolecules. The specific membrane capacitance (*i.e.,* the capacitance of the membrane normalized to the unit cell cross section and membrane area), is defined here as the ability of a membrane to hold an electric charge. By treating the membrane as a dielectric slab, with a relative permittivity (ϵ_r), that is flanked by two parallel plate electrodes that are distance (d) apart, each with an area (A), and a

Table 5.1. Extracted cellular electrical constants (cyotplasm conductivity, S/m, Specific membrane capacitance, mF/m^2 and conductance, S/m^2) of Kc167 cells.

	Isotonic sucrose/glucose medium + $CaCl_2$ and $MgCl_2$ (360 mOsmol/kg)	Hypertonic sucrose/glucose medium (+200 mM sucrose) (560 mOsmol/kg)	Hypertonic sucrose/glucose medium (+400 mM sucrose) (760 mOsmol/kg)
Cytoplasm conductivity (S/m)			
Kc167 Vector control (VC)	0.152 ± 0.016 (*n=68*)	0.192 ± 0.009[1] (*n=62*)	0.189 ± 0.012[a] (*n=61*)
Non-transfected control	0.162 ± 0.014 (*n=18*)		
VC-Dead	0.032 ± 0.002[b] (*n=7*)		
*Afr*LEA3m	0.215 ± 0.018[2] (*n=72*)	0.172 ± 0.007[a,b] (*n=63*)	0.139 ± 0.014[a,b] (*n=58*)
*Afr*LEA6	0.23 ± 0.0186[b] (*n=72*)	0.188 ± 0.0163[a] (*n=61*)	0.126 ± 0.015[a,b] (*n=57*)
Specific membrane capacitance (mF/m^2)			
Kc167 Vector control (VC)	10 ± 1.6 (*n=68*)	11.4 ± 1.18 (*n=62*)	12.6 ± 1.3 (*n=61*)
Non-transfected control	10.5 ± 1.6 (*n=18*)		
VC-Dead	2.7 ± 0.06[b] (*n=7*)		
*Afr*LEA3m	9.8 ± 1.2 (*n=72*)	14.7 ± 1.6 [a,b] (*n=63*)	14.2 ± 0.8[a,b] (*n=58*)
*Afr*LEA6	11.8 ± 1.8 (*n=72*)	12.4 ± 1.53 (*n=61*)	15.0 ± 3.0 (*n=57*)
Specific membrane conductance (S/m^2)			
Kc167 Vector control (VC)	793 ± 63 (*n=68*)	1114 ± 80[a] (*n=62*)	1129 ± 132[a] (*n=61*)
Non-transfected control	812 ± 38 (*n=18*)		
VC-Dead	503 ± 43[b] (*n=7*)		
*Afr*LEA3m	758 ± 75 (*n=72*)	878±73 [b] (*n=63*)	915 ± 73[a,b] (*n=58*)
*Afr*LEA6	710 ±42 (*n=72*)	956 ± 62[a,b] (*n=61*)	1050 ± 110[a] (*n=57*)
Cell diameter (µm)	10 ± 0.23 (*n=7*)	9.2 ± 0.31 (*n=10*)	8.9 ± 0.21 (*n=10*)

dielectric constant (ϵ_0), giving rise to the equation $C_{\text{mem}} = (\epsilon_r)(\epsilon_0)/(d)$ (Farad per unit area). In reference to the cell, changes in the specific membrane capacitance can be affected by the dielectric constant, ϵ_{mem} (determined by the composition of the membrane), the area of the membrane (*i.e.,* morphology), and the thickness of the plasma membrane (particularly within the insulating hydrophobic tail region) [286]. The specific membrane conductivity is simply the ability of a electric current to pass through the membrane and was generally thought to be primarily impacted by membrane thickness, gating state of ion channels, and area [287]. However, recent data has shown that an increase in ion efflux or influx can increase the specific membrane conductivity and concurrently decrease cytoplasmic conductivity, while both membrane thickness and area remain unchanged [288]. In absence of ion-channel involvement, any increase in membrane thickness should decrease both, the membrane conductance and capacitance, while an increase in membrane area should increase both values [278]. It was hypothesized that *Afr*LEA3m would interact with the inner leaflet of the plasma membrane during acute osmotic stress. Bioinformatic analysis predicts that *Afr*LEA3m folds into amphipathic α-helices during water stress, whereas *Afr*LEA6 does not [262]. Amphipathic α-helices are often associated with membrane interactions (*i.e.,* a protein would be able to interact with charged phospholipid head groups, as well as their hydrophobic tail region). This may cause a change in its dielectric constant, ϵ_{mem}, while not significantly impacting the membrane thickness and area (*i.e.,* the specific membrane capacitance increases, while the specific membrane conductance would remain constant). In contrast, *Afr*LEA6 was hypothesized to not interact with the inner leaflet of the plasma membrane, and thereby any change (positive or negative) observed in the specific membrane conductance may lead to changes in the specific membrane capacitance.

Data in Table 5.1 shows that the specific membrane conductance and capacitance

were unaffected by the ectopic expression of either *Afr*LEA3m or *AfrLEA6*. The effect of both proteins on cytoplasmic conductivity could be mediated by direct or indirect interactions with ion channels causing an influx of monovalent ions (*i.e.,* increasing the concentration of a simple electrolyte such as K^+ or Na^+ will theoretically increase the cytoplasmic conductivity). In the case of red blood cells, however, the specific membrane conductivity and cytoplasmic conductivity move in antiphase with rhythmic efflux of K^+ ions [288]. The lack of K^+ and Na^+ in the employed DEP-media and presence of only minor amounts of divalent ions make a mechanism based on ion influx highly unlikely.

An alternative mechanism might be that, due to the highly hydrophilic and charged nature of *Afr*LEA3m and *Afr*LEA6, the mobility of monovalent ions surrounding *Afr*LEA3m and *Afr*LEA6 is effectively higher than VC cells, without actually changing ion concentration. This may increase the molar conductivity of the cytoplasm. Molar conductivity (Λ_m) is defined as the relationship between electrolyte concentration (c), and conductivity (κ). In the equation $(\Lambda_m) = (\kappa)/(c)$, any increase in electrolyte concentration will decrease molar conductivity [286]. This is due an increasing drag force being placed on a given diffusing ion as the concentration of ions of an opposite charge increase (*i.e.,* Debye-Huckel theory). If the equation is written instead as $\kappa = (\Lambda_m)(c)$, then it becomes clear that an increase in molar conductivity at a constant ion concentration will increase cytoplasmic conductivity. This alternative mechanism is supported by molecular dynamics simulations of polyelectrolytes (highly charged polymers) and simple electrolytes, where increasing the concentration of polyelectrolytes increased the dispersion of ions around the polymers and thereby increased the molar conductivity of the ions [286]. In addition, the cytoplasmic conductivity of cells expressing *Afr*LEA3m or *Afr*LEA6 progressively decreases as the cells were exposed to hypertonic solutions (Table 5.1). This is in stark contrast to vector control cells, which displayed a cytoplasmic conductivity that progressively increased when exposed to increasingly hypertonic solutions. In the case where the electrolyte concentrations are increasing, as would be the case when osmotically active water is being pulled out of the cell due to hypertonic stress, conductivity should decrease if molar conductivity decreases. However, the equation $\kappa = (\Lambda_m)(c)$ does demonstrate that increasing ion concentrations in a cell should increase the conductivity of the cytoplasm. However, this assumes that the decrease in molar conductivity is sufficiently outweighed by the increase in electrolyte concentrations. This can be observed in vector control cells under osmotic stress, where a decrease in cell volume leads to a subsequent increase in intracellular ion concentrations and cytoplasmic conductivity. In case of cells expressing *Afr*LEA3m and *Afr*LEA6, the observed decrease in cytoplasmic conductivity during hyperosmotic stress may be a result of a decrease in molar conductivity out-weighing the increase in electrolyte concentration, leading to a net loss in cytoplasmic conductivity (*i.e.,* in $\kappa = (\Lambda_m)(c)$, the decrease in (Λ) outweighs the increase in (c) and leads to a reduction in (κ). This data suggest that, under isotonic conditions, LEA proteins are unentangled and increase the cytoplasmic conductivity by behaving as typical polyelectrolytes, thereby increasing cytoplasmic ion diffusivity [289]. During osmotic stress, the decrease in cellular volume may be sufficient to concentrate LEA proteins enough to shift their dynamics from a semi-

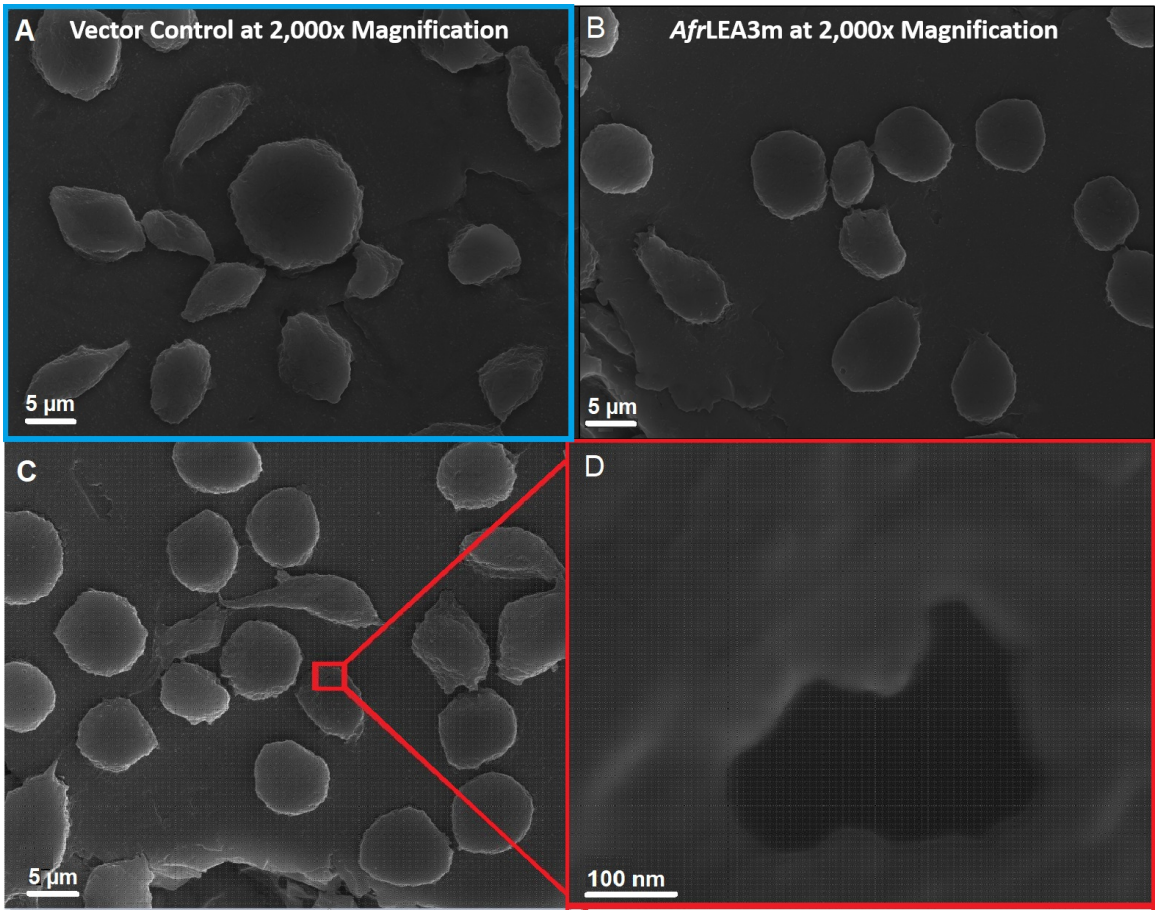

Figure 5.4. SEM images demonstrating that cells expressing *Afr*LEA3m retain a more circular shape after complete desiccation and have pore-like formations in their plasma membranes. Vector control (VC) cells (A) and cells expressing *Afr*LEA3m (B and C) were completely desiccated prior to imaging. (D) Pores were observed exclusively in intact, desiccated *Afr*LEA3m cells. Scale bars for A-C represent 5 µm, while the scale bar for D represents 100 nm.

dilute, unentangled regime to an entangled regime. Under entangled conditions the effect of LEA proteins on ion diffusivity may be negated [289, 290].

When Kc167 cells were challenged with hyperosmotic stress (∼570 and 760 mOsmol/kg), cells expressing *Afr*LEA3m experienced a sharp increase in in specific membrane capacitance (∼ 56 %). However, specific membrane conductance did not significantly change when cells expressing *Afr*LEA3m were challenged with a moderate hypertonic stress of 570 mOsmol/kg. In the case of the osmotically stressed cells, the radius decreases by approximately (∼ 11 %) and, in turn, should increase the specific membrane capacitance by (∼ 11 %). However, this increase does not sufficiently explain the observed (∼ 56 %) increase in specific membrane capacitance. No apparent differences in cell morphology (aside from reported changes in cell diameter; Table 1) were observed when cells were subjected to severe osmotic stress (∼760 mOsmol/kg) and imaged with confocal microscopy (data not shown).

Further analysis of the data relies on two assumptions; first, the effective area of the membrane surface is changing, hence changing the capacitance of the membrane ($C_{\text{mem}} = \phi\epsilon_0\epsilon_r/d$), where ϕ membrane topography parameter that represents the ratio of the actual membrane area of the cell to the membrane area ($4\pi R^2$) that would form a perfectly smooth and spherical covering of the cytoplasm and it is proportional to the 'roughness' of the membrane surface. Furthermore, cells subjected to the hypertonic media would shrink them causing the membrane to wrinkle leading to an increase in ϕ (≈ 1.5) and therefore C_m [278, 291]. Similar results were observed for salivary gland cells (*Drosophila, Chironomids and Sciarids*), where ϕ ranged from 160 to 830 [292]. Furthermore, the change in membrane effective area is further proved by the data reporting a decrease in membrane capacitance of cells suspended in hypotonic media due to cell swelling and the opposite effect when suspended in hypertonic media [291, 293–295]. However, it's also noted that this increase in C_{mem}, for Kc167 cells expressing either *Afr*LEA3m or *Afr*LEA6 suspended in 760 mOsmol/kg, does not mean the formation of blebs or shriveling of the membrane, as there was no indication of apoptosis or necrosis of the cells [296, 297]. These data were supplemented with SEM imaging. After complete desiccation for 18-24 h, cells expressing *Afr*LEA3m retained a more circular morphology than vector control cells, which displayed a variety of shapes and sizes (Fig. 5.4, A and B). In addition, cells expressing *Afr*LEA3m often displayed relatively large pore-like structures that were never observed in vector control cells (Fig. 5.4, C and D). These pore-like structures may be stress points where the membrane begun ripping apart but complete lysis was stopped due to the presence of *Afr*LEA3m. Indeed, vector control cells can often be seen with large tears that allows for cytoplasm to leak out while desiccation is still occurring. Data in Table 5.1 shows no significant difference of the membrane conductance of Kc167 cells expressing *Afr*LEA3m indicating that the cell membrane is intact, and cells did not exhibit either necrosis or apoptosis. Moreover, this increase in the membrane conductance (~ 16 %) for osmotically stressed *Afr*LEA3m can be attributed to the effective area of the membrane surface ($G_{\text{mem}} = \phi G_0$ where $\phi \approx 1.2$) which is close to the actual increase in G_{mem} (≈ 1.5). However, the increase in membrane conductance of the Kc167 vector control could be attributed to degradation of the plasma membrane [297].

The second assumption states that the relative dielectric constant, ϵ_r, and thickness, d, of the membrane are changing due to the expression of LEA proteins as well as osmotic stress imposed from the hypertonic media, with the relative dielectric constant, ϵ_r, surprisingly increasing due to the expression of the LEA proteins. The presence of organelles, structures, or polypepetides such as LEA proteins will contribute to the internal dielectric properties of the cell. Several studies reported changes in the dielectric constant which in turns have an influence on the membrane capacitance [298–300]. Gentet et al. [301] showed minor decrease in the membrane capacitance ($\sim 6\%$) due to expressing glycine receptors and other membrane proteins in embryonic kidney cells (HEK-293). Similarly, Stoneman et al. [302] also reported a decrease in the membrane capacitance of yeast cells (~ 7 %) overexpressing a G protein coupled receptor (Ste2p protein). In contrast to our work, these two experiments did not induce any osmotic stress on the cells being studied. The C_{mem} value mostly

reflects the properties of the hydrophobic layer of the membrane, which is populated by the hydrocarbon tails of the phospholipids and hydrophobic segments of integral membrane proteins [303]. Considering that *Afr*LEA3m is expected to only fold into its native structure in response to water stress, the observed increase in membrane capacitance under osmotic stress is not surprising. Therefore, Kc167 cells expressing *Afr*LEA3m will yield different membrane capacitance (C_{mem}) and conductance (G_{mem}) values when subjected to hyperosmotic stress. It should be noted that the pore-like formations in the SEM images (Fig. 5.4. C,D) only form in the completely dried state. In case of pore-like formations occurring during osmotic stress of ∼760 mOsmol/kg, then the relative dielectric constant of the membrane would decrease by a factor of approximately one fourth [278]. This is in contrast to the observed increase in specific membrane capacitance in cells expressing *Afr*LEA3m. Formation of $\sim 200-300$ nm large pores would result in a loss of membrane integrity, but this was not observed during preparation of cells for hyperosmotic stress experiments (data not shown). Furthermore, our data suggest that *Afr*LEA3m is integrating, at least to some capacity, into the plasma membrane which agrees with previously published results that suggests *Afr*LEA3m protects membranes during water stress [259].

Lacking any apparent propensity to form amphipathic α-helices, *Afr*LEA6 is an ideal protein to compare to *Afr*LEA3m [262]. In comparison with *Afr*LEA3m, cells expressing *Afr*LEA6 experienced a significant increase in membrane conductance, but not specific membrane capacitance, when challenged with moderate hyperosmotic stress (∼570 mOsmol/kg). Furthermore, specific membrane capacitance for cells expressing *Afr*LEA6 was not significantly different than what was observed for vector control cells under all conditions. The observed increase in specific membrane conductance for cells expressing *Afr*LEA6, as well as vector control cells, is thought to be due to an efflux of monovalent ions (likely by gated ion channels) that is ameliorated when *Afr*LEA3m integrates into the membrane as well as the change in the effective area of the membrane surface (*i.e.,* ϕ) which influences both C_{mem} and G_{mem}.

Concluding Remarks

In summary, a dielectrophoresis-based platform was used to characterize the electrical proprieties of Kc167 cells from *D. melanogaster* expressing late embryogenesis abundant proteins from the anhydrobiotic embryos of *A. franciscana*. The increase in cytoplasmic conductivity observed in Kc167 vector control cells under osmotic stress is related to the reduction in cell volume and the increase in ion concentration. We hypothesis, that the increase in cytoplasmic conductivity, for cells ectopically expressing *Afr*LEA3m or *Afr*LEA6, under isotonic conditions, is related to both LEA proteins behaving as typical polyelectrolytes increasing the diffusivity of cytoplasmic ions. Under osmotic stress conditions, the protein dynamics shift from an unentangled regime to a concentrated regime which leads to a decrease in cytoplasmic conductivity. In case of *Afr*LEA3m being activated during osmotic stress then the increases in the specific membrane capacitance during hyperosmotic stress may be due its direct interactions with the plasma membrane. The increase in specific membrane

conductance observed in Kc167 vector control cells was related to changes in plasma membrane morphology during hyperosmotic stress. In contrast, for cells ectopically expressing LEA proteins, the increase in specific membrane conductance is driven by a change in the effective area of their membrane surfaces in addition to any changes in membrane morphology that may occur during hyperosmotic stress. Altogether, these data support the utility of cellular DEP-based characterization as a powerful tool to identify protein-membrane interactions *in vivo* when direct observations are challenging.

CHAPTER VI

OBSERVATION AND CONCLUSION

A topic search using Web of Science (April 2021) showed over 5,530 publications for "dielectrophoresis" compared to eleven results searching "isomotive dielectrophoresis", most of the latter published within the past decade. Various microfluidic applications have successfully demonstrated DEP as a method for the separation, concentration, and trapping of bio-particles. However, utilizing DEP for multi-frequency quantitative characterization has not been intensively studied. Besides isoDEP, the only viable multi-frequency analysis techniques are ROT and 3DEP. Thus, isoDEP could be considered as a robust characterization tool due to its ability to generate the constant gradient of the field-squared (∇E^2_{rms}) thereby creating a uniform applied force. However, further development of isoDEP is needed to demonstrate its reliability and efficiency for characterization, continuous separation, and purification of particles with high throughput.

The specific objective of this project entailed: (1) design/optimization, fabrication, and characterization of an isoDEP platform. (2) assess electrohydrodynamic forces and design rules to mitigate their effect in isoDEP device (3) comparing the isoDEP platform with alternative characterization techniques such as electrical impedance spectroscopy and electrorotation as well as, demonstrating the application of microfluidic DEP-based platform for cells analysis.

Design/optimization, Fabrication, and Characterization of an IsoDEP platform

The design of the isoDEP microfluidic chip incorporated microchannels either in electrode-based or insulative-based designs. The electrode-based design encompassed mainly extruded silicon wafer to form the microchannel while the insulative-based design had glass substrate and photoresist polymers as the main device layers. Different microchannels were designed based on the δ, the characteristic electrode spacing ($\delta = r_{60}$ for electrode-based and $\delta = L$ for insulative-based devices). Various electrode spaces (δ) of 20, 40, 100, 200, 300, 400, and 500 µm) was fabricated and tested for particle analysis. Despite that the initial experiments demonstrated that electrode-based designs are more efficient and reliable more than insulative-based designs, they suffered from significant disturbances from undesired electrohydrodynamic forces although they did not require as large of voltages.

For an inexpensive microchip fabrication, PDMS replicas were obtained from a master mold which made it possible to test multiple chips without the need for continuous cleanroom visits. Although bonding between PDMS and ITO coated glass

substrates was enhanced by oxygen plasma (using a plasma wand), the PDMS/ITO device (Fig. 3.1) was prone to detachment due to fluid injection. On the other hand, SU-8 based microchannels were not complex to make though, the need to cover the microchannel with a cover slip caused some undesired fluid motion. The only way to inject the sample through the SU-8 based devices was to fill the sample then place the coverslip on top. There was additional complexity with drilling inlet/outlet ports in the coverslip and finding coverslips that would adapt to the design. Future SU-8 designs could incorporate alternative sealing substrates (instead of coverslips) as well as use a thin film of SU-8 as a bonding layer.

On the other hand, dry film photoresist based devices (Fig. 3.2) offer a straightforward and inexpensive method of device fabrication. The device offers a promising quick testing prototypes as well as, a monolithic isoDEP device can be made to achieve a covered top microchannel which can eliminate issues faced with the SU-8 based devices. Fabricating electrodes on PDMS through conductive paint (Fig. 3.3) offered a good solution for PDMS/PDMS bonding which can minimize the issues regarding detachment of the microchannel when high-pressure fluid flow is injected. However, the high resistances of the coated electrodes make the application of high frequency signal nontrivial. Also, damage to the electrodes has been easily occurring when high electric field has been applied.

Throughout the project, there were efforts to incorporate automated fluid handing with isoDEP for cell analysis. Microfluidic flow control system (Fluigent MFCS-EZ) was used to control the inlet fluid flow to avoid undesired fluid motions due to tubing or manual handling. A 2-way microvalve was used as intermediate control unit (Labsmith AV201 3-port Microfluidic selector valve) before the flow was injected to the microchannel. This valve ensured the full stoppage of the fluid flow during the analysis of the particles. An acrylic substrate was design using laser cutting tools to work as the handle of the isoDEP chip with access to inlet/outlet ports to ensure the rigidity of the tubing and reduce undesired motion and vibration. The fluid flow rate was controlled by the operator through the vendor's software. On the other hand, the main challenge to the isoDEP device testing was the amplifiers used to obtain high electric field application at higher frequencies. Hence, a custom-built amplifier was achieved to ensure the application of high electric field at $\sim$ 3 kHz-30 MHz also, to ensure portability of the platform.

Most of the devices fabricated have been tested with phytoplankton cells. However due to the lack of repeatability of the experiments, the results were not included in this dissertation. In addition, the phytoplankton cells contain flagella that keeps them in motion when suspended in aqueous media. Recalling that isoDEP devices require the flow to be undisturbed during the analysis, makes it not a strong candidate for analyzing mobile cells such as phytoplankton. However, successful nDEP and pDEP force demonstration was achieved with suspended phytoplankton cells, but the high electric field used ($\sim 10^6$ V/m) might cause cells stress which could compromise the measured dielectric cell properties.

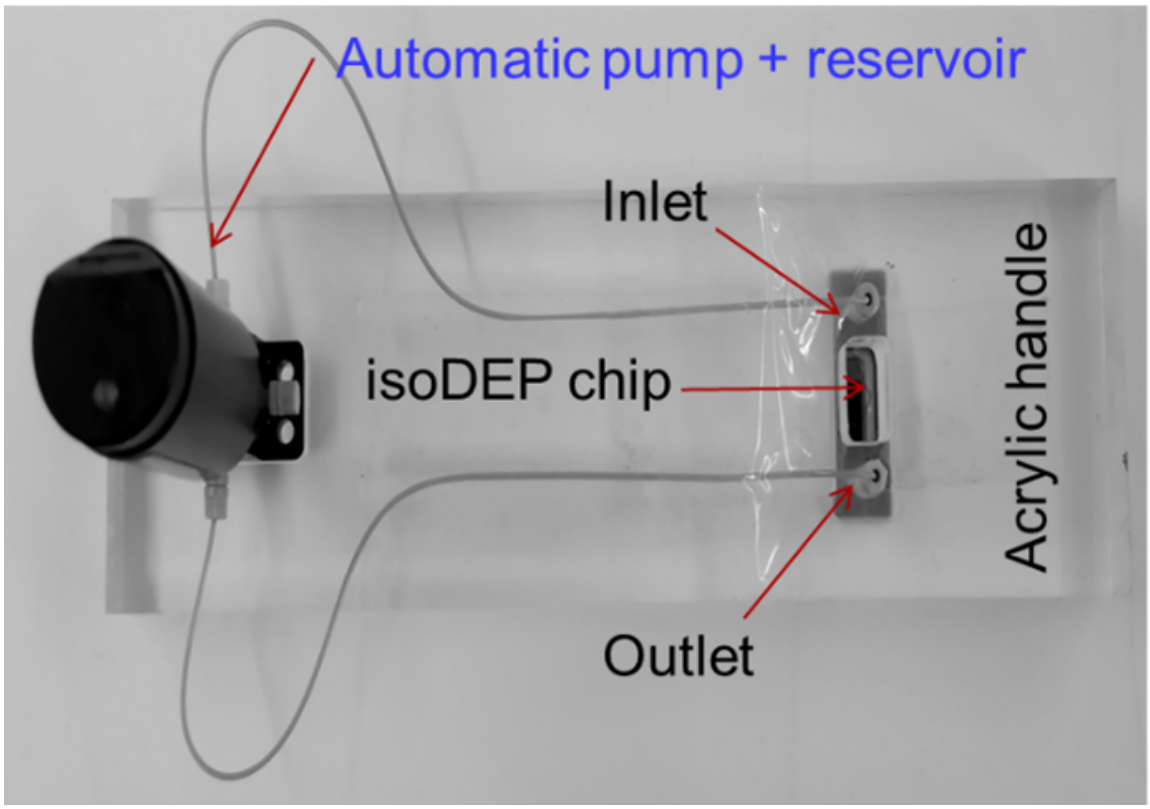

Figure 6.1. An image of the isoDEP platform

Design Rules to Mitigate Electrohydrodynamic Effects in IsoDEP Device

Several fabrication and device designs have been made to obtain a better DEP analysis microfluidic device that was used to investigate the properties of phytoplankton cells. It was concluded that devices fabricated by full depth etching using DRIE to create the microchannel resulted in a good DEP response at lower voltages compared to devices made from PDMS microchannel bonded to patterned ITO coated glass electrodes. However, rough wall surface containing etched silicon spikes generates high localized electric field that generates localized heating which generated electrothermal vortices that compromised the operation of the device. Therefore, isoDEP microchannel made from insulative PDMS can minimize this ETH effect by placing electrodes far from the analyzing region. In addition, it can be easily tailored to the desired cell size and microchannel height, but it requires a higher AC voltage amplitude which requires expensive amplifiers to provide high amplification ($>$ 100 V) at high frequency ($>$ 1 MHz).

Despite the efforts to redesign the isoDEP chips, all device fabricated suffered from high electrohydrodynamic effects whenever tested (Fig. 3.6). Electrohydrodynamic motion was observed at larger applied potentials ($>$ 50 V for microelectrode isoDEP and, ¿ 120 V for insulator isoDEP). Subsequent scaling law analysis was de-

rived to understand the heat transfer inside an isoDEP device and the sources of the undesired forces in order to minimize them with respect to the dielectrophoresis force. AC electroosmosis was expected to be negligible inside an isoDEP device as the tangential component of the electric field at the electrode surface is significantly weaker compared to other studied ACEO micro-electrode geometries like interdigitated electrodes. Hence, the electrothermal forces are mainly the cause for the undesired motion of particles when high electric field magnitudes are applied.

Intuitively, the key design parameters to reduce ET flow is to facilitate heat transfer normal to the electric field direction and reduce heat transfer in the direction of the field. Insulative-based devices were expected to have a better heat transfer perspective as the temperature gradients are orthogonal to the direction of the electric field (Fig. 3.9), which makes them favorable devices to maximize the heat transfer. On the other hand, the electrode-based device benefit from the conductive microchannel which serves as a heat sink compared to a glass substrate -based device. However, in both cases, it was concluded that the microchannel dimensions impact of the isoDEP device performance (Fig. 3.11). Having a material of high thermal conduction coefficient can enhance the heat transfer. Using a silicon-based substrate reduced the ET-induced fluid motion to the DEP induced one ($v_{\mathrm{ETH}}/v_{\mathrm{DEP}}$) 10 times compared to glass substrate. In addition, having the microchannel thickness (height) and width to be below10x the diameter of the particle being studied, minimize the effect of the ET-driven flow is reduced by ~ 500 times.

Further device fabrications were further attempted to design an isoDEP device with maximized DEP force operation. The SU-8 based devices were easily tailored to the new smaller microchannel thickness. However, due to the small channel height ($\sim 20 - 40$ µm) made fluid handling nontrivial (Fig. 3.12).

Despite having rough sidewalls in the DRIE silicon-based isoDEP devices (Fig. 3.1), the sidewall quality improved due to the smaller etching depth (~ 35 µm, Fig. 3.13). The silicon wafer would also improve heat transfer and reduce ET flow. Hence, a silicon on insulator wafer was used to simultaneously provide both small electrode layer as well as a high thermally conductive handle layer. However, the impedance between the isoDEP electrodes was higher than between the electrodes and handle substrate, leading to a weaker electric field applied to the sample (Fig . 3.14). Hence, another microchannel thickness and r_{60} parameters can be attempted and simulated to predict the feasibility of the design prior to the fabrication. Electroplating and pyrolyzed SU-8 (Fig. 3.15) structures offered a very smooth sidewalls and controlled channel thickness. However, the nonuniformity of the electroplating process made the application of $\nabla E_{\mathrm{rms}}^2$ nontrivial. Also, the nonuniform shrinkage in the pyrolyzed SU-8 structures affected the microchannel contour, channel thickness, and width which in turns compromised the application of the proper electric field signal.

Characterization of Cells utilizing impedance Spectroscopy, Electrorotation, and DEP-based Platform

The isoDEP platform can be compared to other cell characterization techniques such as electrochemical-based impedance spectroscopy, electrorotation, and an existing DEP-based commercial platform (3DEP Deptech). In the future, such studies can be used to verify the operation of isoDEP. As mentioned previously, phytoplankton have flagella which enable them to swim. Despite applied DEP forces, reliable isoDEP characterization of mobile cells is nontrivial. The same issue occurred for the 3DEP platform; hence, reliable extraction of cell's dielectric properties was not possible with that platform (data not reported). Hence, EIS-based technique was the best candidate to provide extraction of single cell phenotype from cells in suspension. This approach does not require the swimming phytoplankton to be trapped or stressed due to the experiment. Additionally, low applied voltages (max 1 V) ensured the cells were not compromised by the applied field. The impedance measurement was acquired for multiple wells with buried, isolated electrodes at the bottom of each wells. A custom-built PCB ensured the addressing of each well separately and provided the connection to the impedance analyzer. Despite of the goal of the study was to differentiate between healthy and non-healthy phytoplankton cells, the concluded data showed no significant difference between cells cultured in nitrogen abundant and deficient media. However, successful differentiation between phytoplankton species was achieved based on the specific membrane capacitance of the cells.

Electrorotation was investigated for label-free multiple single cells analysis. The 3D electrode design ensured the application of the electric signal across the depth of the microchannel ensuring the uniformity of the applied DEP force. Also, 3D ROT allows the trapping of the cells regardless of their position inside the flow compared to the conventional 2D electrode design where the DEP force is maximum near the planar electrodes and decreases drastically far from the electrode surface [13]. The parallel and separate electrodes connections enabled independent addressing of the microcages. Different microcage sizes (electrode spacing of 20, 40, and 80 µm) were fabricated based on the size of the studied cells. Negative DEP trapping was utilized to hold the cells, against the flow, within the center of the quadrupoles, then the electrorotation signal is applied alternatively. The cells within the cages can be from different populations, and the ROT spectra of each cell is acquired regardless of the cell type. The extracted membrane capacitance for HeLa, HEK 293, and human immortalized T lymphocytes are in agreement with the literature. Moreover, the dielectric properties of M17 neuroblastoma cells were characterized and reported for the first time by using electrokinetic based technique. The throughput of the device could be around 600 cells/h which demonstrates one of the highest reported throughputs of single cell characterization technique.

3DEP (DEPTech Ltd) platform was used characterize the mechanism of different LEA proteins from the brine shrimp Artemia franciscana (a primitive arthropod that lives in saline water [304]) in the Drosophila melanogaster cell lines Kc167 ($12 - 15$ µm in diameter). Three different Kc167 cell lines have been prepared to study their

DEP measurements and spectra. (i) Kc167 cells is used as a control line, while (ii) Kc167 containing *Afr*LEA1.1, a group 1 LEA protein which resides in the cytoplasm with a total of 182 amino acids[305], as well as (iii) Kc167 containing *Afr*LEA3m, a group 3 LEA protein which resides in the mitochondria with a total of 307 amino acids. DEP spectra of three different Kc167 cell lines were obtained, showing minor differences between the membrane's properties of control line cells and cells containing any of the LEA proteins in isotonic media. However, at higher frequencies in the DEP spectra the cytoplasm properties of the cells were found to be significant, especially with the cells containing *Afr*LEA3m protein, indicating its activity is majored inside the cytoplasm more than in the membrane. Cells expressing LEA proteins showed preservation in membrane integrity when conferring stress (hypertonic media), while control cells' membrane were compromised due to the osmotic stress. This work demonstrates the strength of DEP as a tool for cell characterization.

Further investigation of LEA proteins and their roles in desiccation tolerance can be achieved through studying different proteins from different groups. Currently, trehalose which is an excellent lyoprotectant found in anhydrobiotic organisms has similar role in dessication tolerance. Trehalose has been loaded into red blood cells using sonoporation microfluidic device which demonstratd the potential of sonoporation-mediated trehalose loading to increase recovery of viable red blood cells (RBCs) when dried for preservation and then rehydrated [306]. 3DEP (DEPtech) platform can be utilized to investigate and characterize the effect of sonoporation of loaded trehalose to preserve the RBCs in a similar procedure to the work presented here regarding LEA proteins. The results regarding the dielectric properties of RBCs can provide insights regarding the mechanism of trehalose sugar in protecting the cell membrane which in turns opens the avenues for further biological application for dry preservations of cells. Moreover, the data obtained from 3DEP platform can also be used to verify the operation of the isoDEP device and its resolution for characterization the cell membrane changes.

Comparing the potential of isoDEP against other electrokinetic techniques shows that the isoDEP can offer high sensitivity characterization similar to ROT while potentially achieving a higher throughput ($\sim 10 - 100$ particles per second). The expected isoDEP throughput is lower than traditional flow cytometry and dynamic EIS platforms, but it is label-free and enables comprehensive multi-frequency analysis. Further, isoDEP could be coupled with imaging flow cytometry [**?**] for more comprehensive analysis. The fabrication of isoDEP chips is not as complicated as the fabrication of EIS or ROT platforms, especially for insulative-based devices. In addition, the isoDEP requires less electronic hardware to operate compared to costly waveforms for ROT (four-channel waveform generators are needed) or EIS (where an impedance analyzer is required for highly sensitive impedance measurements), thus making isoDEP a better candidate for in-the-field dielectric characterization tool for biological applications and environmental monitoring. Existing platforms such the 3DEP platform are not cheap and cannot provide reliable characterization for moving cells (e.g., phytoplankton cells). Moreover, population-based characterization techniques, such as 3DEP platform, which derive the dielectric properties of single cell from cells in suspension is nontrivial and cannot provide reliable data due to the

change in cell population diameters which is an important fitting parameter for single-shell model. Additionally, by considering the relationship between light intensity and DEP properties of the cells which is unreliable when compared to the relationship between the cell velocity and its Clausius-Mossotti factor which is well defined and governed by equations (Eq. 2.35).

Unlike EIS or ROT, isoDEP platform can be used as a particle separator with the incorporation of hydrodynamic focusing and the incorporation of multiple outlets. Traditional DEP-based separation techniques such as DEP field-flow fractionation (DEP-FFF) [307–309] and traveling wave DEP (TwDEP) [310, 311] offer continuous flow particle sorting and separation, which is suitable for sub-micron analytes. Other techniques such as techniques utilizing gravitational force combined with nDEP barrier can offer higher throughput ($\sim 17,000$ cells/min) compared to traditional DEP devices while maintaining descent high separation efficiencies ($\sim 95\%$) and yield [312, 313].On the other hand, isoDEP platforms can achieve high throughput separation (from 13,320 to 20,000 particles/min) [154, 158] while maintaining high flow rates which is comparable to the throughput achieved by traditional DEP-based separators.

Future Work

The initial finding of this work provided a solid foundation for future improvement and applications of the isoDEP platform. Possible improvement can be the redesign and fabrication of the isoDEP electrode-based devices using electroplating techniques. Further investigation can be made to take into account the effect of slow metal plating time to provide a uniform final metal device layer. Following the isoDEP design rules, channel thickness and width of about 40 µm can provide a better aspect ratio and can be achieved with controlled plating settings.

Moving forward, to provide a full portability of the isoDEP device, further investigations are required using square waves signals instead of AC signals or the use of discrete AC frequencies (for example, 3DEP applies twenty fixed AC frequencies) would minimize the need for an AC generator. A PCB that can provide multiplexer/switching between various RF transformers where each RF transformer can provide a discrete AC signal with high amplification at a specific frequency range. Hence, it can eliminate the need for bench-top and bulky amplifiers.

Additional challenges for isoDEP is better fluid handling and reducing unwanted electrohydrodynamics. This includes reducing electrothermal forces, limiting tubing movement and vibrations, and developing methods for effective and rapid intermittent stopping of fluid flow. However, isoDEP analysis using a continuous flow platform is possible. This approach analyses the streamlines of particles while passing through the device.Once the DEP force is applied, the particle's velocity will change. By tracking such change, the related DEP induced velocity can be calculated over a range of frequencies hence, a comprehensive characterization for particle in flow can be obtained. By integrating the RF transformers, discrete application of selective frequencies can be applied to study the response of the particle fur to the applied DEP force. The DEP force would be applied intermittently at different frequencies

while the velocity of each particle is simultaneously trapped. Hence, particles can be characterized while they are passing through the channel, this approach also increase the throughput of the isoDEP device.

Perhaps, the most important task in the future will be more comprehensive verification of the isoDEP devices through testing of biological particle. It would be advised to test non-swimmer cells (e.g., yeast, mammalian cells) instead of phytoplankton cells which can provide reliable data and ensure the stress-free environment for the cells being studied because high electric field magnitudes are required to to be applied to overcome the motion of the swimmer cells. By following the design rules, fabrication of isoDEP chips with minimized electrothermal effects can be achieved. Therefore, electric field magnitudes can be reduced to ensure the viability of cells being characterized.

In conclusion, the next generation of DEP devices should incorporate additional analytical capabilities and/or manipulation tasks. For example, comprehensive electrokinetic platforms should trap bio-particles, characterize their DEP spectra, and finally separate them without affecting their viability. Hence, isoDEP may be the best candidate for these multipurpose platforms because the isoDEP field can perform both separation and characterization simultaneously. IsoDEP theory and operation has been well-established, emerging microfabrication procedures coupled with innovative applications of the isoDEP geometry will continue to improve its performance thus providing future researchers with a versatile electrokinetic platform for the dielectric characterization and separation of individual cells.

REFERENCES

[1] T. Xu, M. Lizarralde, W. E. Nemer, B. L. Pioufle, and O. Français, "Monitoring biological cell flow within a mimicking capillary device with impedance measurement," in "Multidisciplinary Digital Publishing Institute Proceedings," , vol. 1 (2017), vol. 1, p. 517.

[2] R. Pethig, "Dielectrophoresis: Status of the theory, technology, and applications," Biomicrofluidics **4**, 022811 (2010).

[3] A. Kuzyk, "Dielectrophoresis at the nanoscale," electrophoresis **32**, 2307–2313 (2011).

[4] B. H. Lapizco-Encinas, B. A. Simmons, E. B. Cummings, and Y. Fintschenko, "Dielectrophoretic concentration and separation of live and dead bacteria in an array of insulators," Analytical chemistry **76**, 1571–1579 (2004).

[5] R. C. Gallo-Villanueva, N. M. Jesús-Pérez, J. I. Martínez-López, A. Pacheco, and B. H. Lapizco-Encinas, "Assessment of microalgae viability employing insulator-based dielectrophoresis," Microfluidics and Nanofluidics **10**, 1305–1315 (2011).

[6] H. M. Coley, F. H. Labeed, H. Thomas, and M. P. Hughes, "Biophysical characterization of mdr breast cancer cell lines reveals the cytoplasm is critical in determining drug sensitivity," Biochimica et Biophysica Acta (BBA)-General Subjects **1770**, 601–608 (2007).

[7] E. A. Henslee, M. B. Sano, E. M. Schmelz, and R. V. Davalos, "Isolation of human breast cancer cells by metastatic stage using contactless dielectrophoresis," in "Summer Bioengineering Conference," , vol. 44038 (American Society of Mechanical Engineers, 2010), vol. 44038, pp. 93–94.

[8] J. Yang, Y. Huang, X. Wang, X.-B. Wang, F. F. Becker, and P. R. Gascoyne, "Dielectric properties of human leukocyte subpopulations determined by electrorotation as a cell separation criterion," Biophysical journal **76**, 3307–3314 (1999).

[9] S. K. Srivastava, P. R. Daggolu, S. C. Burgess, and A. R. Minerick, "Dielectrophoretic characterization of erythrocytes: Positive abo blood types," Electrophoresis **29**, 5033–5046 (2008).

[10] L. Liu, K. Chen, N. Xiang, and Z. Ni, "Dielectrophoretic manipulation of nanomaterials: A review," Electrophoresis **40**, 873–889 (2019).

[11] B. H. Lapizco-Encinas, "On the recent developments of insulator-based dielectrophoresis: A review," Electrophoresis **40**, 358–375 (2019).

[12] H. Shafiee, J. L. Caldwell, M. B. Sano, and R. V. Davalos, "Contactless dielectrophoresis: a new technique for cell manipulation," Biomedical microdevices **11**, 997–1006 (2009).

[13] A. Ramos, H. Morgan, N. G. Green, and A. Castellanos, "Ac electrokinetics: a review of forces in microelectrode structures," Journal of Physics D: Applied Physics **31**, 2338 (1998).

[14] H. A. Pohl, "Dielectrophoresis," The behavior of neutral matter in nonuniform electric fields (1978).

[15] D. J. Allen, R. P. Accolla, and S. J. Williams, "Isomotive dielectrophoresis for parallel analysis of individual particles," Electrophoresis **38**, 1441–1449 (2017).

[16] N. G. Green, A. Ramos, A. Gonzalez, A. Castellanos, and H. Morgan, "Electrothermally induced fluid flow on microelectrodes," Journal of Electrostatics **53**, 71–87 (2001).

[17] B. G. Hawkins and B. J. Kirby, "Electrothermal flow effects in insulating (electrodeless) dielectrophoresis systems," Electrophoresis **31**, 3622–3633 (2010).

[18] F. M. White and I. Corfield, *Viscous fluid flow*, vol. 3 (McGraw-Hill New York, 2006).

[19] A. Castellanos, A. Ramos, A. Gonzalez, N. G. Green, and H. Morgan, "Electrohydrodynamics and dielectrophoresis in microsystems: scaling laws," Journal of Physics D: Applied Physics **36**, 2584 (2003).

[20] R. Lindsey, M. Scott, and R. Simmon, "What are phytoplankton," NASA's Earth Observatory. Available on http://earthobservatory. nasa. gov/Librar y/-phytoplankton (2010).

[21] D. Das, F. A. Kamil, K. Biswas, and S. Das, "Evaluation of single cell electrical parameters from bioimpedance of a cell suspension," RSC Advances **4**, 18178–18185 (2014).

[22] C. Siebman, O. D. Velev, and V. I. Slaveykova, "Alternating current-dielectrophoresis collection and chaining of phytoplankton on chip: Comparison of individual species and artificial communities," Biosensors **7**, 4 (2017).

[23] A. Lasia, "Definition of impedance and impedance of electrical circuits," in "Electrochemical Impedance Spectroscopy and its applications," (Springer, 2014), pp. 7–66.

[24] H. Morgan, T. Sun, D. Holmes, S. Gawad, and N. G. Green, "Single cell dielectric spectroscopy," Journal of Physics D: Applied Physics **40**, 61 (2006).

[25] Q. Hassan, S. Ahmadi, and K. Kerman, "Recent advances in monitoring cell behavior using cell-based impedance spectroscopy," Micromachines **11**, 590 (2020).

[26] M. A. Zabara and B. Ulgut, "Electrochemical impedance spectroscopy based voltage modeling of lithium thionyl chloride (li\ socl2) primary battery at arbitrary discharge," Electrochimica Acta **334**, 135584 (2020).

[27] B. Janis, C. Belott, and M. A. Menze, "Role of intrinsic disorder in animal desiccation tolerance," Proteomics **18**, 1800067 (2018).

[28] F. A. Hoekstra, E. A. Golovina, and J. Buitink, "Mechanisms of plant desiccation tolerance," Trends in plant science **6**, 431–438 (2001).

[29] S. C. Hand, M. A. Menze, M. Toner, L. Boswell, and D. Moore, "Lea proteins during water stress: not just for plants anymore," Annual review of physiology **73**, 115–134 (2011).

[30] M. J. Wise and A. Tunnacliffe, "Popp the question: what do lea proteins do?" Trends in plant science **9**, 13–17 (2004).

[31] M. Z. Rashed and S. J. Williams, "Advances and applications of isomotive dielectrophoresis for cell analysis," Analytical and bioanalytical chemistry **412**, 3813–3833 (2020).

[32] H. Helvajian and S. Janson, "Microengineering space systems," Microengineering aerospace systems p. 29 (1999).

[33] G. Karniadakis, A. Beskok, and M. Gad-el Hak, "Micro flows: fundamentals and simulation," Applied Mechanics Reviews **55**, B76 (2002).

[34] H. Morgan, N. G. Green, M. Hughes, W. Monaghan, and T. Tan, "Large-area travelling-wave dielectrophoresis particle separator," Journal of Micromechanics and Microengineering **7**, 65 (1997).

[35] H. Morgan and N. G. Green, "Dielectrophoretic manipulation of rod-shaped viral particles," Journal of Electrostatics **42**, 279–293 (1997).

[36] S. J. Williams, A. Kumar, and S. T. Wereley, "Electrokinetic patterning of colloidal particles with optical landscapes," Lab on a Chip **8**, 1879–1882 (2008).

[37] X. Chen, D. Cui, and L. Zhang, "Isolation of plasma from whole blood using a microfludic chip in a continuous cross-flow," Chinese Science Bulletin **54**, 324–327 (2009).

[38] P. Sethu, A. Sin, and M. Toner, "Microfluidic diffusive filter for apheresis (leukapheresis)," Lab on a Chip **6**, 83–89 (2006).

[39] S. Zheng, H. Lin, J.-Q. Liu, M. Balic, R. Datar, R. J. Cote, and Y.-C. Tai, "Membrane microfilter device for selective capture, electrolysis and genomic analysis of human circulating tumor cells," Journal of chromatography A **1162**, 154–161 (2007).

[40] H. Mohamed, J. N. Turner, and M. Caggana, "Biochip for separating fetal cells from maternal circulation," Journal of Chromatography A **1162**, 187–192 (2007).

[41] P. Wilding, L. J. Kricka, J. Cheng, G. Hvichia, M. A. Shoffner, and P. Fortina, "Integrated cell isolation and polymerase chain reaction analysis using silicon microfilter chambers," Analytical biochemistry **257**, 95–100 (1998).

[42] L. Yang, P. P. Banada, M. R. Chatni, K. S. Lim, A. K. Bhunia, M. Ladisch, and R. Bashir, "A multifunctional micro-fluidic system for dielectrophoretic concentration coupled with immuno-capture of low numbers of listeria monocytogenes," Lab on a Chip **6**, 896–905 (2006).

[43] J. J. Hawkes and W. T. Coakley, "Force field particle filter, combining ultrasound standing waves and laminar flow," Sensors and Actuators B: Chemical **75**, 213–222 (2001).

[44] S. Kapishnikov, V. Kantsler, and V. Steinberg, "Continuous particle size separation and size sorting using ultrasound in a microchannel," Journal of statistical mechanics: theory and experiment **2006**, P01012 (2006).

[45] M. Evander and J. Nilsson, "Acoustofluidics 20: applications in acoustic trapping," Lab on a Chip **12**, 4667–4676 (2012).

[46] A. Lenshof, C. Magnusson, and T. Laurell, "Acoustofluidics 8: Applications of acoustophoresis in continuous flow microsystems," Lab on a Chip **12**, 1210–1223 (2012).

[47] T. Leong, L. Johansson, P. Juliano, S. L. McArthur, and R. Manasseh, "Ultrasonic separation of particulate fluids in small and large scale systems: a review," Industrial & Engineering Chemistry Research **52**, 16555–16576 (2013).

[48] F. Petersson, A. Nilsson, C. Holm, H. Jönsson, and T. Laurell, "Separation of lipids from blood utilizing ultrasonic standing waves in microfluidic channels," Analyst **129**, 938–943 (2004).

[49] F. Arai, C. Ng, H. Maruyama, A. Ichikawa, H. El-Shimy, and T. Fukuda, "On chip single-cell separation and immobilization using optical tweezers and thermosensitive hydrogel," Lab on a Chip **5**, 1399–1403 (2005).

[50] D. Erickson, X. Serey, Y.-F. Chen, and S. Mandal, "Nanomanipulation using near field photonics," Lab on a Chip **11**, 995–1009 (2011).

[51] N. J. Halas, S. Lal, W.-S. Chang, S. Link, and P. Nordlander, "Plasmons in strongly coupled metallic nanostructures," Chemical reviews **111**, 3913–3961 (2011).

[52] H. Zhang and K.-K. Liu, "Optical tweezers for single cells," Journal of The Royal Society Interface **5**, 671–690 (2008).

[53] S. Choi, S. Song, C. Choi, and J.-K. Park, "Microfluidic self-sorting of mammalian cells to achieve cell cycle synchrony by hydrophoresis," Analytical chemistry **81**, 1964–1968 (2009).

[54] D. Di Carlo, "Inertial microfluidics," Lab on a Chip **9**, 3038–3046 (2009).

[55] J. V. Green, M. Radisic, and S. K. Murthy, "Deterministic lateral displacement as a means to enrich large cells for tissue engineering," Analytical chemistry **81**, 9178–9182 (2009).

[56] T. M. Squires and S. R. Quake, "Microfluidics: Fluid physics at the nanoliter scale," Reviews of modern physics **77**, 977 (2005).

[57] M. Tanyeri, M. Ranka, N. Sittipolkul, and C. M. Schroeder, "A microfluidic-based hydrodynamic trap: design and implementation," Lab on a Chip **11**, 1786–1794 (2011).

[58] X. Xuan, J. Zhu, and C. Church, "Particle focusing in microfluidic devices," Microfluidics and nanofluidics **9**, 1–16 (2010).

[59] J. D. Adams, U. Kim, and H. T. Soh, "Multitarget magnetic activated cell sorter," Proceedings of the National Academy of Sciences **105**, 18165–18170 (2008).

[60] L. Borlido, A. Azevedo, A. Roque, and M. Aires-Barros, "Magnetic separations in biotechnology," Biotechnology advances **31**, 1374–1385 (2013).

[61] T. P. Forbes and S. P. Forry, "Microfluidic magnetophoretic separations of immunomagnetically labeled rare mammalian cells," Lab on a Chip **12**, 1471–1479 (2012).

[62] N. Pamme and A. Manz, "On-chip free-flow magnetophoresis: continuous flow separation of magnetic particles and agglomerates," Analytical chemistry **76**, 7250–7256 (2004).

[63] S. A. Peyman, E. Y. Kwan, O. Margarson, A. Iles, and N. Pamme, "Diamagnetic repulsion—a versatile tool for label-free particle handling in microfluidic devices," Journal of Chromatography A **1216**, 9055–9062 (2009).

[64] A. I. Rodríguez-Villarreal, M. D. Tarn, L. A. Madden, J. B. Lutz, J. Greenman, J. Samitier, and N. Pamme, "Flow focussing of particles and cells based on their intrinsic properties using a simple diamagnetic repulsion setup," Lab on a Chip **11**, 1240–1248 (2011).

[65] M. Suwa and H. Watarai, "Magnetoanalysis of micro/nanoparticles: A review," Analytica chimica acta **690**, 137–147 (2011).

[66] B. Gaš, "Theory of electrophoresis: Fate of one equation," Electrophoresis **30** (2009).

[67] M. Jaeger, T. Mueller, and T. Schnelle, "Thermometry in dielectrophoresis chips for contact-free cell handling," Journal of Physics D: Applied Physics **40**, 95 (2006).

[68] K. Klepárník and P. Boček, "Electrophoresis today and tomorrow: Helping biologists' dreams come true," Bioessays **32**, 218–226 (2010).

[69] J. Minden, "Comparative proteomics and difference gel electrophoresis," Biotechniques **43**, 739–745 (2007).

[70] H. A. Pohl, "Dielectrophoresis-the behavior of neutral matter in nonuniform electric fields," Cambridge Monographs on Physics pp. Chapter1–3 (1978).

[71] J. Voldman, "Electrical forces for microscale cell manipulation," Annu. Rev. Biomed. Eng. **8**, 425–454 (2006).

[72] F. F. Becker, X.-B. Wang, Y. Huang, R. Pethig, J. Vykoukal, and P. Gascoyne, "Separation of human breast cancer cells from blood by differential dielectric affinity," Proceedings of the National Academy of Sciences **92**, 860–864 (1995).

[73] J. Yang, Y. Huang, X.-B. Wang, F. F. Becker, and P. R. Gascoyne, "Cell separation on microfabricated electrodes using dielectrophoretic/gravitational field-flow fractionation," Analytical Chemistry **71**, 911–918 (1999).

[74] P. R. Gascoyne, X.-B. Wang, Y. Huang, and F. F. Becker, "Dielectrophoretic separation of cancer cells from blood," IEEE transactions on industry applications **33**, 670–678 (1997).

[75] G. H. Markx, P. A. Dyda, and R. Pethig, "Dielectrophoretic separation of bacteria using a conductivity gradient," Journal of biotechnology **51**, 175–180 (1996).

[76] N. G. Green, A. Ramos, A. González, H. Morgan, and A. Castellanos, "Fluid flow induced by nonuniform ac electric fields in electrolytes on microelectrodes. i. experimental measurements," Physical review E **61**, 4011 (2000).

[77] N. G. Green and H. Morgan, "Dielectrophoresis of submicrometer latex spheres. 1. experimental results," The Journal of Physical Chemistry B **103**, 41–50 (1999).

[78] N. G. Green, H. Morgan, and J. J. Milner, "Manipulation and trapping of sub-micron bioparticles using dielectrophoresis," Journal of Biochemical and Biophysical Methods **35**, 89–102 (1997).

[79] Q. Chen and Y. J. Yuan, "A review of polystyrene bead manipulation by dielectrophoresis," RSC advances **9**, 4963–4981 (2019).

[80] M. Washizu, S. Suzuki, O. Kurosawa, T. Nishizaka, and T. Shinohara, "Molecular dielectrophoresis of biopolymers," IEEE Transactions on Industry Applications **30**, 835–843 (1994).

[81] M. Washizu and O. Kurosawa, "Electrostatic manipulation of dna in microfabricated structures," IEEE Transactions on industry applications **26**, 1165–1172 (1990).

[82] C. L. Asbury and G. Van Den Engh, "Trapping of dna in nonuniform oscillating electric fields," Biophysical Journal **74**, 1024–1030 (1998).

[83] M. Talary, K. I. Mills, T. Hoy, A. K. Burnett, and R. Pethig, "Dielectrophoretic separation and enrichment of cd34+ cell subpopulation from bone marrow and peripheral blood stem cells," Medical and Biological Engineering and Computing **33**, 235–237 (1995).

[84] L. A. Flanagan, J. Lu, L. Wang, S. A. Marchenko, N. L. Jeon, A. P. Lee, and E. S. Monuki, "Unique dielectric properties distinguish stem cells and their differentiated progeny," Stem cells **26**, 656–665 (2008).

[85] F. F. Becker, X.-B. Wang, Y. Huang, R. Pethig, J. Vykoukal, and P. Gascoyne, "Separation of human breast cancer cells from blood by differential dielectric affinity," Proceedings of the National Academy of Sciences **92**, 860–864 (1995).

[86] R. Krupke, F. Hennrich, H. v. Löhneysen, and M. M. Kappes, "Separation of metallic from semiconducting single-walled carbon nanotubes," Science **301**, 344–347 (2003).

[87] R. Krupke, S. Linden, M. Rapp, and F. Hennrich, "Thin films of metallic carbon nanotubes prepared by dielectrophoresis," Advanced materials **18**, 1468–1470 (2006).

[88] Z.-B. Zhang, X.-J. Liu, E. E. Campbell, and S.-L. Zhang, "Alternating current dielectrophoresis of carbon nanotubes," (2005).

[89] F. E. Tay, L. Yu, and C. Iliescu, "Particle manipulation by miniaturised dielectrophoretic devices," Defence Science Journal **59**, 595 (2009).

[90] S. Fiedler, S. G. Shirley, T. Schnelle, and G. Fuhr, "Dielectrophoretic sorting of particles and cells in a microsystem," Analytical chemistry **70**, 1909–1915 (1998).

[91] C. Zhang, K. Khoshmanesh, A. Mitchell, and K. Kalantar-zadeh, "Dielectrophoresis for manipulation of micro/nano particles in microfluidic systems," Analytical and bioanalytical chemistry **396**, 401–420 (2010).

[92] B. Çetin and D. Li, "Dielectrophoresis in microfluidics technology," Electrophoresis **32**, 2410–2427 (2011).

[93] R. Pethig, "Dielectrophoresis: Status of the theory, technology, and applications," Biomicrofluidics **4**, 022811 (2010).

[94] K. Khoshmanesh, S. Nahavandi, S. Baratchi, A. Mitchell, and K. Kalantar-zadeh, "Dielectrophoretic platforms for bio-microfluidic systems," Biosensors and Bioelectronics **26**, 1800–1814 (2011).

[95] Z. R. Gagnon, "Cellular dielectrophoresis: applications to the characterization, manipulation, separation and patterning of cells," Electrophoresis **32**, 2466–2487 (2011).

[96] J. Voldman, "Electrical forces for microscale cell manipulation," Annu. Rev. Biomed. Eng. **8**, 425–454 (2006).

[97] R. Martinez-Duarte, "Microfabrication technologies in dielectrophoresis applications—a review," Electrophoresis **33**, 3110–3132 (2012).

[98] J. Regtmeier, R. Eichhorn, M. Viefhues, L. Bogunovic, and D. Anselmetti, "Electrodeless dielectrophoresis for bioanalysis: Theory, devices and applications," Electrophoresis **32**, 2253–2273 (2011).

[99] T. Jones, "Electromechanics of particlescambridge univ," Press, Cambridge (1995).

[100] Z. R. Gagnon, "Cellular dielectrophoresis: applications to the characterization, manipulation, separation and patterning of cells," Electrophoresis **32**, 2466–2487 (2011).

[101] M. Washizu and T. Jones, "Multipolar dielectrophoretic force calculation," Journal of Electrostatics **33**, 187–198 (1994).

[102] R. E. Fernandez, A. Rohani, V. Farmehini, and N. S. Swami, "Microbial analysis in dielectrophoretic microfluidic systems," Analytica chimica acta **966**, 11–33 (2017).

[103] A. Irimajiri, T. Hanai, and A. Inouye, "A dielectric theory of "multi-stratified shell" model with its application to a lymphoma cell," Journal of theoretical biology **78**, 251–269 (1979).

[104] Y. Huang, X.-B. Wang, J. Tame, and R. Pethig, "Electrokinetic behaviour of colloidal particles in travelling electric fields: studies using yeast cells," Journal of Physics D: Applied Physics **26**, 1528 (1993).

[105] Y. Huang, X.-B. Wang, J. Tame, and R. Pethig, "Electrokinetic behaviour of colloidal particles in travelling electric fields: studies using yeast cells," Journal of Physics D: Applied Physics **26**, 1528 (1993).

[106] J. Griffin and R. Stowell, "Orientation of euglena by radio-frequency fields," Experimental cell research **44**, 684–688 (1966).

[107] T. Nakada, H. Shinkawa, T. Ito, and M. Tomita, "Recharacterization of chlamydomonas reinhardtii and its relatives with new isolates from japan," Journal of plant research **123**, 67 (2010).

[108] https://www.xn-krinfo wxa.hu/en/node/4193, "Phytoplankton images," .

[109] P. Gascoyne, R. Pethig, J. Satayavivad, F. F. Becker, and M. Ruchirawat, "Dielectrophoretic detection of changes in erythrocyte membranes following malarial infection," Biochimica et Biophysica Acta (BBA)-Biomembranes **1323**, 240–252 (1997).

[110] Z. Gagnon, J. Gordon, S. Sengupta, and H.-C. Chang, "Bovine red blood cell starvation age discrimination through a glutaraldehyde-amplified dielectrophoretic approach with buffer selection and membrane cross-linking," Electrophoresis **29**, 2272–2279 (2008).

[111] M. Castellarnau, A. Errachid, C. Madrid, A. Juarez, and J. Samitier, "Dielectrophoresis as a tool to characterize and differentiate isogenic mutants of escherichia coli," Biophysical journal **91**, 3937–3945 (2006).

[112] Z. Gagnon, J. Mazur, and H.-C. Chang, "Glutaraldehyde enhanced dielectrophoretic yeast cell separation," Biomicrofluidics **3**, 044108 (2009).

[113] A. Ramos, H. Morgan, N. G. Green, and A. Castellanos, "Ac electrokinetics: a review of forces in microelectrode structures," Journal of Physics D: Applied Physics **31**, 2338 (1998).

[114] H. A. Pohl, *Dielectrophoresis: The behavior of neutral matter in nonuniform electric fields (Cambridge Monographs on physics)* (Cambridge/New York: Cambridge University Press, 1978).

[115] R. Adamson and K. Kaler, "Multipole effects on the dielectrophoretic force in an 'isomotive'field," Journal of Biological Physics **13**, 95–98 (1985).

[116] S. Tada, Y. Omi, and M. Eguchi, "Analysis of the dielectrophoretic properties of cells using the isomotive ac electric field," Biomicrofluidics **12**, 044103 (2018).

[117] M. Z. Rashed, N. G. Green, and S. J. Williams, "Scaling law analysis of electrohydrodynamics and dielectrophoresis for isomotive dielectrophoresis microfluidic devices," Electrophoresis (2019).

[118] R. Martinez-Duarte, "Microfabrication technologies in dielectrophoresis applications—a review," Electrophoresis **33**, 3110–3132 (2012).

[119] J. Voldman, M. L. Gray, M. Toner, and M. A. Schmidt, "A microfabrication-based dynamic array cytometer," Analytical chemistry **74**, 3984–3990 (2002).

[120] K. Keim, M. Z. Rashed, S. C. Kilchenmann, A. Delattre, A. F. Gonçalves, P. Éry, and C. Guiducci, "On-chip technology for single-cell arraying, electrorotation-based analysis and selective release," Electrophoresis **40**, 1830–1838 (2019).

[121] B. A. Simmons, G. J. McGraw, R. V. Davalos, G. J. Fiechtner, Y. Fintschenko, and E. B. Cummings, "The development of polymeric devices as dielectrophoretic separators and concentrators," MRS bulletin **31**, 120–124 (2006).

[122] S. K. Srivastava, A. Gencoglu, and A. R. Minerick, "Dc insulator dielectrophoretic applications in microdevice technology: a review," Analytical and bioanalytical chemistry **399**, 301–321 (2011).

[123] J. Regtmeier, R. Eichhorn, M. Viefhues, L. Bogunovic, and D. Anselmetti, "Electrodeless dielectrophoresis for bioanalysis: Theory, devices and applications," Electrophoresis **32**, 2253–2273 (2011).

[124] H. A. Pohl and C. E. Plymale, "Continuous separations of suspensions by nonuniform electric fields in liquid dielectrics," Journal of The Electrochemical Society **107**, 390 (1960).

[125] C. Feeley and F. McGovern, "Dielectrophoresis of bubbles in isomotive electric fields," Journal of Physics D: Applied Physics **21**, 1251 (1988).

[126] U. Andres, "Dielectric separation of minerals," Journal of electrostatics **37**, 227–248 (1996).

[127] H. Pohl and K. Kaler, "Continuous dielectrophoretic separation of cell mixtures," Cell biophysics **1**, 15–28 (1979).

[128] Y. Li, C. Dalton, H. J. Crabtree, G. Nilsson, and K. V. Kaler, "Continuous dielectrophoretic cell separation microfluidic device," Lab on a Chip **7**, 239–248 (2007).

[129] Y. Li and K. V. Kaler, "Dielectrophoretic fluidic cell fractionation system," Analytica Chimica Acta **507**, 151–161 (2004).

[130] V. Shkolnikov, D. Xin, and C.-H. Chen, "Continuous dielectrophoretic particle separation via isomotive dielectrophoresis with bifurcating stagnation flow," Electrophoresis **40**, 2988–2995 (2019).

[131] N. G. Weiss, P. V. Jones, P. Mahanti, K. P. Chen, T. J. Taylor, and M. A. Hayes, "Dielectrophoretic mobility determination in dc insulator-based dielectrophoresis," Electrophoresis **32**, 2292–2297 (2011).

[132] S. Tada, M. Eguchi, and K. Okano, "Insulator-based dielectrophoresis combined with the isomotive ac electric field and applied to single cell analysis," Electrophoresis **40**, 1494–1497 (2019).

[133] R. Reale, A. De Ninno, L. Businaro, P. Bisegna, and F. Caselli, "Electrical measurement of cross-sectional position of particles flowing through a microchannel," Microfluidics and Nanofluidics **22**, 1–13 (2018).

[134] R. Reale, A. De Ninno, L. Businaro, P. Bisegna, and F. Caselli, "High-throughput electrical position detection of single flowing particles/cells with non-spherical shape," Lab on a Chip **19**, 1818–1827 (2019).

[135] H. A. Pohl and C. E. Plymale, "Continuous separations of suspensions by nonuniform electric fields in liquid dielectrics," Journal of the Electrochemical Society **107**, 390 (1960).

[136] L. Yang, P. P. Banada, A. K. Bhunia, and R. Bashir, "Effects of dielectrophoresis on growth, viability and immuno-reactivity of listeria monocytogenes," Journal of biological engineering **2**, 1–14 (2008).

[137] C. Qian, H. Huang, L. Chen, X. Li, Z. Ge, T. Chen, Z. Yang, and L. Sun, "Dielectrophoresis for bioparticle manipulation," International journal of molecular sciences **15**, 18281–18309 (2014).

[138] J. A. Price, J. P. Burt, and R. Pethig, "Applications of a new optical technique for measuring the dielectrophoretic behaviour of micro-organisms," Biochimica et Biophysica Acta (BBA)-General Subjects **964**, 221–230 (1988).

[139] M. Rashed and S. Williams, "Advances and applications of isomotive dielectrophoresis for cell analysis." Analytical and Bioanalytical Chemistry (2020).

[140] H. Pohl and R. Pethig, "Dielectric measurements using non-uniform electric field (dielectrophoretic) effects," Journal of Physics E: Scientific Instruments **10**, 190 (1977).

[141] C. Feeley and F. McGovern, "Dielectrophoresis of bubbles in isomotive electric fields," Journal of Physics D: Applied Physics **21**, 1251 (1988).

[142] U. Andres, "Dielectric separation of minerals," Journal of electrostatics **37**, 227–248 (1996).

[143] H. A. Pohl and I. Hawk, "Separation of living and dead cells by dielectrophoresis," Science **152**, 647–649 (1966).

[144] H. A. Pohl, "Dielectrophoresis," The behavior of neutral matter in nonuniform electric fields (1978).

[145] H. Pohl, K. Pollock, and J. Crane, "Dielectrophoretic force: A comparison of theory and experiment," Journal of Biological Physics **6**, 133–160 (1978).

[146] .

[147] M. Hakoda and Y. Hirota, "Correlation between dielectric property by dielectrophoretic levitation and growth activity of cells exposed to electric field," Bioprocess and biosystems engineering **36**, 1219–1227 (2013).

[148] Y. Li and K. V. Kaler, "Dielectrophoretic fluidic cell fractionation system," Analytica Chimica Acta **507**, 151–161 (2004).

[149] K. Kaler and T. Jones, "Dielectrophoretic spectra of single cells determined by feedback-controlled levitation," Biophysical journal **57**, 173–182 (1990).

[150] H. Hadady, J. J. Wong, S. R. Hiibel, D. Redelman, and E. J. Geiger, "High frequency dielectrophoretic response of microalgae over time," Electrophoresis **35**, 3533–3540 (2014).

[151] R. Martinez-Duarte, "Microfabrication technologies in dielectrophoresis applications—a review," Electrophoresis **33**, 3110–3132 (2012).

[152] A. Ramos, H. Morgan, N. G. Green, and A. Castellanos, "Ac electrokinetics: a review of forces in microelectrode structures," Journal of Physics D: Applied Physics **31**, 2338 (1998).

[153] R. R. Pethig, *Dielectrophoresis: Theory, methodology and biological applications* (John Wiley & Sons, 2017).

[154] Y. Li, C. Dalton, H. J. Crabtree, G. Nilsson, and K. V. Kaler, "Continuous dielectrophoretic cell separation microfluidic device," Lab on a Chip **7**, 239–248 (2007).

[155] N. Lewpiriyawong, C. Yang, and Y. C. Lam, "Electrokinetically driven concentration of particles and cells by dielectrophoresis with dc-offset ac electric field," Microfluidics and nanofluidics **12**, 723–733 (2012).

[156] S. Tada, Y. Omi, and M. Eguchi, "Analysis of the dielectrophoretic properties of cells using the isomotive ac electric field," Biomicrofluidics **12**, 044103 (2018).

[157] Y.-H. Su, M. Tsegaye, W. Varhue, K.-T. Liao, L. S. Abebe, J. A. Smith, R. L. Guerrant, and N. S. Swami, "Quantitative dielectrophoretic tracking for characterization and separation of persistent subpopulations of cryptosporidium parvum," Analyst **139**, 66–73 (2014).

[158] V. Shkolnikov, D. Xin, and C.-H. Chen, "Continuous dielectrophoretic particle separation via isomotive dielectrophoresis with bifurcating stagnation flow," Electrophoresis **40**, 2988–2995 (2019).

[159] N. G. Weiss, P. V. Jones, P. Mahanti, K. P. Chen, T. J. Taylor, and M. A. Hayes, "Dielectrophoretic mobility determination in dc insulator-based dielectrophoresis," Electrophoresis **32**, 2292–2297 (2011).

[160] J. I. Martínez-López, H. Moncada-Hernández, J. L. Baylon-Cardiel, S. O. Martínez-Chapa, M. Rito-Palomares, and B. H. Lapizco-Encinas, "Characterization of electrokinetic mobility of microparticles in order to improve dielectrophoretic concentration," Analytical and bioanalytical chemistry **394**, 293–302 (2009).

[161] M. Y. Badal, M. Wong, N. Chiem, H. Salimi-Moosavi, and D. J. Harrison, "Protein separation and surfactant control of electroosmotic flow in poly (dimethylsiloxane)-coated capillaries and microchips," Journal of chromatography A **947**, 277–286 (2002).

[162] S. Tada, M. Eguchi, and K. Okano, "Insulator-based dielectrophoresis combined with the isomotive ac electric field and applied to single cell analysis," Electrophoresis **40**, 1494–1497 (2019).

[163] J. Voldman, "Electrical forces for microscale cell manipulation," Annu. Rev. Biomed. Eng. **8**, 425–454 (2006).

[164] N. G. Green and H. Morgan, "Dielectrophoresis of submicrometer latex spheres. 1. experimental results," The Journal of Physical Chemistry B **103**, 41–50 (1999).

[165] N. G. Green, H. Morgan, and J. J. Milner, "Manipulation and trapping of sub-micron bioparticles using dielectrophoresis," Journal of Biochemical and Biophysical Methods **35**, 89–102 (1997).

[166] M. Washizu, S. Suzuki, O. Kurosawa, T. Nishizaka, and T. Shinohara, "Molecular dielectrophoresis of biopolymers," IEEE Transactions on Industry Applications **30**, 835–843 (1994).

[167] M. Washizu and O. Kurosawa, "Electrostatic manipulation of dna in microfabricated structures," IEEE Transactions on industry applications **26**, 1165–1172 (1990).

[168] R. Pethig, Y. Huang, X.-B. Wang, and J. P. Burt, "Positive and negative dielectrophoretic collection of colloidal particles using interdigitated castellated microelectrodes," Journal of Physics D: Applied Physics **25**, 881 (1992).

[169] P. Y. Chiou, A. T. Ohta, and M. C. Wu, "Massively parallel manipulation of single cells and microparticles using optical images," Nature **436**, 370–372 (2005).

[170] M. Z. Rashed, V. Velasco, and S. J. Williams, "Advances and applications of rapid electrokinetic patterning," Journal of the Indian Institute of Science **98**, 85–101 (2018).

[171] M. Li, W. Li, J. Zhang, G. Alici, and W. Wen, "A review of microfabrication techniques and dielectrophoretic microdevices for particle manipulation and separation," Journal of Physics D: Applied Physics **47**, 063001 (2014).

[172] R. Martinez-Duarte, "Microfabrication technologies in dielectrophoresis applications—a review," Electrophoresis **33**, 3110–3132 (2012).

[173] L. Huang, P. Zhao, and W. Wang, "3d cell electrorotation and imaging for measuring multiple cellular biophysical properties," Lab on a Chip **18**, 2359–2368 (2018).

[174] X. Xuan, "Joule heating in electrokinetic flow," Electrophoresis **29**, 33–43 (2008).

[175] A. Sadeghi, Y. Kazemi, and M. H. Saidi, "Joule heating effects in electrokinetically driven flow through rectangular microchannels: an analytical approach," Nanoscale and Microscale Thermophysical Engineering **17**, 173–193 (2013).

[176] N. G. Green, A. Ramos, A. Gonzalez, H. Morgan, and A. Castellanos, "Fluid flow induced by nonuniform ac electric fields in electrolytes on microelectrodes. iii. observation of streamlines and numerical simulation," Physical review E **66**, 026305 (2002).

[177] K. Horiuchi and P. Dutta, "Joule heating effects in electroosmotically driven microchannel flows," International journal of heat and mass transfer **47**, 3085–3095 (2004).

[178] M. Lian, N. Islam, and J. Wu, "Ac electrothermal manipulation of conductive fluids and particles for lab-chip applications," Iet Nanobiotechnology **1**, 36–43 (2007).

[179] Y. Kang, D. Li, S. A. Kalams, and J. E. Eid, "Dc-dielectrophoretic separation of biological cells by size," Biomedical microdevices **10**, 243–249 (2008).

[180] D. S. Gray, J. L. Tan, J. Voldman, and C. S. Chen, "Dielectrophoretic registration of living cells to a microelectrode array," Biosensors and Bioelectronics **19**, 1765–1774 (2004).

[181] M. Jaeger, T. Mueller, and T. Schnelle, "Thermometry in dielectrophoresis chips for contact-free cell handling," Journal of Physics D: Applied Physics **40**, 95 (2006).

[182] F. E. Tay, L. Yu, A. J. Pang, and C. Iliescu, "Electrical and thermal characterization of a dielectrophoretic chip with 3d electrodes for cells manipulation," Electrochimica acta **52**, 2862–2868 (2007).

[183] J. Gao, L. Yeo, M. Chan-Park, J. Miao, Y. Yan, J. Sun, Y. Lam, and C. Yue, "Antistick postpassivation of high-aspect ratio silicon molds fabricated by deep-reactive ion etching," Journal of Microelectromechanical systems **15**, 84–93 (2006).

[184] C.-M. Chan, L.-T. Weng, and Y.-T. R. Lau, "Polymer surface structures determined using tof-sims," Reviews in Analytical Chemistry **33**, 11–30 (2014).

[185] H.-C. Chang and L. Y. Yeo, "Electrokinetically driven microfluidics and nanofluidics," (2010).

[186] A. Ramos, *Electrokinetics and electrohydrodynamics in microsystems*, vol. 530 (Springer Science & Business Media, 2011).

[187] A. Ramos, H. Morgan, N. G. Green, and A. Castellanos, "Ac electrokinetics: a review of forces in microelectrode structures," Journal of Physics D: Applied Physics **31**, 2338 (1998).

[188] A. Ajdari, "Pumping liquids using asymmetric electrode arrays," Physical Review E **61**, R45 (2000).

[189] N. G. Green, A. Ramos, A. Gonzalez, A. Castellanos, and H. Morgan, "Electrothermally induced fluid flow on microelectrodes," Journal of Electrostatics **53**, 71–87 (2001).

[190] A. González, A. Ramos, H. Morgan, N. G. Green, and A. Castellanos, "Electrothermal flows generated by alternating and rotating electric fields in microsystems," Journal of Fluid Mechanics **564**, 415–433 (2006).

[191] A. Ajdari, "Pumping liquids using asymmetric electrode arrays," Physical Review E **61**, R45 (2000).

[192] M. Z. Rashed, N. G. Green, and S. J. Williams, "Scaling law analysis of electrohydrodynamics and dielectrophoresis for isomotive dielectrophoresis microfluidic devices," Electrophoresis **41**, 148–155 (2020).

[193] C. Iliescu, H. Taylor, M. Avram, J. Miao, and S. Franssila, "A practical guide for the fabrication of microfluidic devices using glass and silicon," Biomicrofluidics **6**, 016505 (2012).

[194] D. Burgreen and F. Nakache, "Electrokinetic flow in ultrafine capillary slits1," The Journal of Physical Chemistry **68**, 1084–1091 (1964).

[195] J. E. Sunderland and K. R. Johnson, "Shape factors for heat conduction through bodies with isothermal or convective boundary conditions," in "ASHRAE 71st Annual Meeting, Cleveland," (1964).

[196] J. P. Hartnett and M. Kostic, "Heat transfer to newtonian and non-newtonian fluids in rectangular ducts," in "Advances in heat transfer," , vol. 19 (Elsevier, 1989), pp. 247–356.

[197] J. H. VanSant, "Conduction heat transfer solutions," Tech. rep., Lawrence Livermore National Lab., CA (USA) (1983).

[198] Z. A. S. Mohammed, M. Olimpo, D. Poenar, and S. Aditya, "Smoothening of scalloped drie trench walls," Materials Science in Semiconductor Processing **63**, 83–89 (2017).

[199] L. Wang, L. Flanagan, and A. P. Lee, "Side-wall vertical electrodes for lateral field microfluidic applications," Journal of microelectromechanical systems **16**, 454–461 (2007).

[200] L. Amato, A. Heiskanen, R. Hansen, L. Gammelgaard, T. Rindzevicius, M. Tenje, J. Emnéus, and S. S. Keller, "Dense high-aspect ratio 3d carbon pillars on interdigitated microelectrode arrays," Carbon **94**, 792–803 (2015).

[201] R. M. Duarte, *Label-free cell sorting using carbon-electrode dielectrophoresis and centrifugal microfluidics* (University of California, Irvine, 2010).

[202] S. Hemanth, C. Caviglia, Y. M. Hassan, T. A. Anhøj, J. Emnéus, and S. S. Keller, "Fabrication and characterization of 3d pyrolytic carbon microelectrodes for electrochemistry," in "42nd International conference on Micro and Nano Engineering," (2016).

[203] R. Natu, M. Islam, J. Gilmore, and R. Martinez-Duarte, "Shrinkage of su-8 microstructures during carbonization," Journal of analytical and applied pyrolysis **131**, 17–27 (2018).

[204] P. Ginestra, M. Madou, and E. Ceretti, "Production of carbonized micropatterns by photolithography and pyrolysis," Precision Engineering **55**, 137–143 (2019).

[205] M. R. Jett, M. Z. Rashed, S. P. Hendricks, and S. J. Williams, "Electrical characterization of phytoplankton suspensions using impedance spectroscopy," Journal of Applied Phycology pp. 1–8 (2021).

[206] D. Das, F. A. Kamil, K. Biswas, and S. Das, "Evaluation of single cell electrical parameters from bioimpedance of a cell suspension," RSC Adv. **4**, 18178–18185 (2014).

[207] R. Lindsey and M. Scott (2010).

[208] C. Siebman, O. Velev, and V. Slaveykova, "Alternating Current-Dielectrophoresis Collection and Chaining of Phytoplankton on Chip: Comparison of Individual Species and Artificial Communities," Biosensors **7**, 4–4 (2017).

[209] B. Wang, Y. Li, N. Wu, and C. Q. Lan, "CO2 bio-mitigation using microalgae," Applied Microbiology and Biotechnology **79**, 707–718 (2008).

[210] T. M. Mata, A. A. Martins, and N. S. Caetano, "Microalgae for biodiesel production and other applications: A review," (2010).

[211] T. Searchinger, R. Heimlich, R. A. Houghton, F. Dong, A. Elobeid, J. Fabiosa, S. Tokgoz, D. Hayes, and T. H. Yu, "Use of U.S. Croplands for Biofuels Increases Greenhouse Gases Through Emissions from Land-Use Change," (2008).

[212] L. Zhu, "Biorefinery as a promising approach to promote microalgae industry: An innovative framework," Renewable and Sustainable Energy Reviews **41**, 1376–1384 (2015).

[213] A. Lasia, *Electrochemical impedance spectroscopy and its applications. 1 edn* (Springer-Verlag, New York, 2014).

[214] M. A. Zabara and B. Ulgut, "Electrochemical Impedance Spectroscopy based voltage modeling of lithium Thionyl Chloride (Li\SOCl2) primary battery at arbitrary discharge," Electrochimica Acta **334**, 135584–135584 (2020).

[215] T. Sun and H. Morgan, "Single-cell microfluidic impedance cytometry: a review," (2010).

[216] H. Morgan, T. Sun, D. Holmes, S. Gawad, and N. G. Green, "Single cell dielectric spectroscopy," Journal of Physics D: Applied Physics **40**, 61–70 (2007).

[217] P. Wanichapichart, S. Bunthawin, A. Kaewpaiboon, and K. Kanchanapoom, "Determination of cell dielectric properties using dielectrophoretic technique," ScienceAsia **28**, 113–119 (2001).

[218] J. Maxwell, *Treatise on Electricity and Magnetism, 2 vols* (Dover, New York, 1954).

[219] K. Foster and H. Schwan, "Dielectric properties of tissues and biological materials: A critical review," CRC Biomed Eng **17**, 25–104 (1989).

[220] R. A. Andersen, *Algal culturing techniques* (Elsevier, 2005).

[221] H. Hadady, J. J. Wong, S. R. Hiibel, D. Redelman, and E. J. Geiger, "High frequency dielectrophoretic response of microalgae over time," ELECTROPHORESIS **35**, 3533–3540 (2014).

[222] L. Graham and L. Wilcox, "Algae prentice hall," Upper Saddle River, New Jersey (2000).

[223] L. S. Jang and M. H. Wang, "Microfluidic device for cell capture and impedance measurement," Biomed Microdevices **9**, 737–743 (2007).

[224] J. C. Weaver and Y. A. Chizmadzhev, "Theory of electroporation: A review," Bioelectrochemistry and Bioenergetics **41**, 135–160 (1996).

[225] C. Petchakup, K. H. H. Li, and H. W. Hou, "Advances in single cell impedance cytometry for biomedical applications," Micromachines **8**, 87 (2017).

[226] V. Abt, F. Gringel, A. Han, P. Neubauer, and M. Birkholz, "Separation, Characterization, and Handling of Microalgae by Dielectrophoresis," (2020).

[227] Y. L. Deng, C. J.-S. Juang, and Y. J, "Separation of microalgae with different lipid contents by dielectrophoresis," Bioresour Technol **135**, 137–141 (2013).

[228] R. T. K. Kumar, P. Kanchustambham, D. Kinnamon, and S. Prasad, "2D dielectrophoretic signature of Coscinodiscus wailesii algae in non-uniform electric fields," Algal Research **27**, 109–114 (2017).

[229] D. S. Domozych, M. Ciancia, J. U. Fangel, M. D. Mikkelsen, P. Ulvskov, and W. G. T. Willats, "The cell walls of green algae," Frontiers in Plant Science (2012).

[230] E. V. Donk, M. Lürling, D. Hessen, and G. Lokhorst, "Altered cell wall morphology in nutrient-deficient phytoplankton and its impact on grazers," Limnology and Oceanography **42**, 357–364 (1997).

[231] H. Morgan and N. G. Green, "Dielectrophoretic manipulation of rod-shaped viral particles," Journal of Electrostatics **42**, 279–293 (1997).

[232] M. Sancho, G. Mart´ınez, and C. Mart´ın, "Accurate dielectric modelling of shelled particles and cells," Journal of Electrostatics **57**, 143–156 (2003).

[233] H. A. Pohl and J. S. Crane, "Dielectrophoresis of cells," Biophysical journal **11**, 711–727 (1971).

[234] S.-I. Han, Y.-D. Joo, and K.-H. Han, "An electrorotation technique for measuring the dielectric properties of cells with simultaneous use of negative quadrupolar dielectrophoresis and electrorotation," Analyst **138**, 1529–1537 (2013).

[235] X. Wang, F. F. Becker, and P. R. Gascoyne, "Membrane dielectric changes indicate induced apoptosis in hl-60 cells more sensitively than surface phosphatidylserine expression or dna fragmentation," Biochimica et Biophysica Acta (BBA)-Biomembranes **1564**, 412–420 (2002).

[236] Y. Huang, X.-B. Wang, R. Holzel, F. Becker, and P. Gascoyne, "Electrorotational studies of the cytoplasmic dielectric properties of friend murine erythroleukaemia cells," Physics in Medicine & Biology **40**, 1789 (1995).

[237] C. Reichle, T. Schnelle, T. Müller, T. Leya, and G. Fuhr, "A new microsystem for automated electrorotation measurements using laser tweezers," Biochimica et Biophysica Acta (BBA)-Bioenergetics **1459**, 218–229 (2000).

[238] S. C. Kilchenmann, E. Rollo, P. Maoddi, and C. Guiducci, "Metal-coated su-8 structures for high-density 3-d microelectrode arrays," Journal of Microelectromechanical Systems **25**, 425–431 (2016).

[239] E. Rollo, E. Tenaglia, R. Genolet, E. Bianchi, A. Harari, G. Coukos, and C. Guiducci, "Label-free identification of activated t lymphocytes through tridimensional microsensors on chip," Biosensors and Bioelectronics **94**, 193–199 (2017).

[240] C. K. Harnett, J. Templeton, K. A. Dunphy-Guzman, Y. M. Senousy, and M. P. Kanouff, "Model based design of a microfluidic mixer driven by induced charge electroosmosis," Lab on a Chip **8**, 565–572 (2008).

[241] J. Voldman, M. L. Gray, M. Toner, and M. A. Schmidt, "A microfabrication-based dynamic array cytometer," Analytical chemistry **74**, 3984–3990 (2002).

[242] A. Rohani, W. Varhue, Y.-H. Su, and N. S. Swami, "Electrical tweezer for highly parallelized electrorotation measurements over a wide frequency bandwidth," Electrophoresis **35**, 1795–1802 (2014).

[243] P. R. Gascoyne, R. Pethig, J. P. Burt, and F. F. Becker, "Membrane changes accompanying the induced differentiation of friend murine erythroleukemia cells studied by dielectrophoresis," Biochimica et Biophysica Acta (BBA)-Biomembranes **1149**, 119–126 (1993).

[244] Y. Huang, X.-B. Wang, P. R. Gascoyne, and F. F. Becker, "Membrane dielectric responses of human t-lymphocytes following mitogenic stimulation," Biochimica et Biophysica Acta (BBA)-Biomembranes **1417**, 51–62 (1999).

[245] R. Pethig, V. Bressler, C. Carswell-Crumpton, Y. Chen, L. Foster-Haje, M. E. García-Ojeda, R. S. Lee, G. M. Lock, M. S. Talary, and K. M. Tate, "Dielectrophoretic studies of the activation of human t lymphocytes using a newly developed cell profiling system," Electrophoresis **23**, 2057–2063 (2002).

[246] D. Zimmermann, M. Kiesel, U. Terpitz, A. Zhou, R. Reuss, J. Kraus, W. Schenk, E. Bamberg, and V. Sukhorukov, "A combined patch-clamp and electrorotation study of the voltage-and frequency-dependent membrane capacitance caused by structurally dissimilar lipophilic anions," Journal of Membrane Biology **221**, 107–121 (2008).

[247] L. J. Gentet, G. J. Stuart, and J. D. Clements, "Direct measurement of specific membrane capacitance in neurons," Biophysical journal **79**, 314–320 (2000).

[248] R. Soffe, "Discontinuous dielectrophoresis enabled investigation of high shear stress flows on intracellular calcium signalling of non-adherent cells," Ph.D. thesis, PhD Thesis, Royal Melbourne Institute of Technology, Melbourne, 2016.[Google ... (2016).

[249] K. Asami, Y. Takahashi, and S. Takashima, "Frequency domain analysis of membrane capacitance of cultured cells (hela and myeloma) using the micropipette technique," Biophysical journal **58**, 143–148 (1990).

[250] M. Cristofanilli, G. De Gasperis, L. Zhang, M.-C. Hung, P. R. Gascoyne, and G. N. Hortobagyi, "Automated electrorotation to reveal dielectric variations related to her-2/neu overexpression in mcf-7 sublines," Clinical Cancer Research **8**, 615–619 (2002).

[251] S. Gawad, D. Holmes, G. Benazzi, P. Renaud, and H. Morgan, "Impedance spectroscopy and optical analysis of single biological cells and organisms in microsystems," Microengineering in Biotechnology pp. 149–182 (2010).

[252] V. E. Kalodimou, *Basic principles in flow cytometry* (AABB Press, 2013).

[253] D. Malleo, J. T. Nevill, L. P. Lee, and H. Morgan, "Continuous differential impedance spectroscopy of single cells," Microfluidics and nanofluidics **9**, 191–198 (2010).

[254] M. Z. Rashed, C. J. Belott, B. R. Janis, M. A. Menze, and S. J. Williams, "New insights into anhydrobiosis using cellular dielectrophoresis-based characterization," Biomicrofluidics **13**, 064113 (2019).

[255] B. Janis, C. Belott, and M. A. Menze, "Role of intrinsic disorder in animal desiccation tolerance," Proteomics **18**, 1800067 (2018).

[256] F. A. Hoekstra, E. A. Golovina, and J. Buitink, "Mechanisms of plant desiccation tolerance," Trends in plant science **6**, 431–438 (2001).

[257] S. C. Hand, M. A. Menze, M. Toner, L. Boswell, and D. Moore, "Lea proteins during water stress: not just for plants anymore," Annual review of physiology **73**, 115–134 (2011).

[258] M. J. Wise and A. Tunnacliffe, "Popp the question: what do lea proteins do?" Trends in plant science **9**, 13–17 (2004).

[259] D. S. Moore, R. Hansen, and S. C. Hand, "Liposomes with diverse compositions are protected during desiccation by lea proteins from artemia franciscana and trehalose," Biochimica et Biophysica Acta (BBA)-Biomembranes **1858**, 104–115 (2016).

[260] M. A. Menze, L. Boswell, M. Toner, and S. C. Hand, "Occurrence of mitochondria-targeted late embryogenesis abundant (lea) gene in animals increases organelle resistance to water stress," Journal of Biological Chemistry **284**, 10714–10719 (2009).

[261] M. R. Marunde, D. A. Samarajeewa, J. Anderson, S. Li, S. C. Hand, and M. A. Menze, "Improved tolerance to salt and water stress in drosophila melanogaster cells conferred by late embryogenesis abundant protein," Journal of insect physiology **59**, 377–386 (2013).

[262] B. Janis, V. N. Uversky, and M. A. Menze, "Potential functions of lea proteins from the brine shrimp artemia franciscana–anhydrobiosis meets bioinformatics," Journal of Biomolecular Structure and Dynamics **36**, 3291–3309 (2018).

[263] B. M. LeBlanc, M. T. Le, B. Janis, M. A. Menze, and S. C. Hand, "Structural properties and cellular expression of afrlea6, a group 6 late embryogenesis abundant protein from embryos of artemia franciscana," Cell Stress and Chaperones pp. 1–12 (2019).

[264] F. H. Labeed, H. M. Coley, and M. P. Hughes, "Differences in the biophysical properties of membrane and cytoplasm of apoptotic cells revealed using dielectrophoresis," Biochimica et Biophysica Acta (BBA)-General Subjects **1760**, 922–929 (2006).

[265] L. M. Broche, F. H. Labeed, and M. P. Hughes, "Extraction of dielectric properties of multiple populations from dielectrophoretic collection spectrum data," Physics in Medicine & Biology **50**, 2267 (2005).

[266] D. J. Bakewell, M. P. Hughes, J. J. Milner, and H. Morgan, "Dielectrophoretic manipulation of avidin and dna," (IEEE, 1998), vol. 2, pp. 1079–1082.

[267] L. Zheng, J. P. Brody, and P. J. Burke, "Electronic manipulation of dna, proteins, and nanoparticles for potential circuit assembly," Biosensors and Bioelectronics **20**, 606–619 (2004).

[268] M. Washizu, S. Suzuki, O. Kurosawa, T. Nishizaka, and T. Shinohara, "Molecular dielectrophoresis of biopolymers," IEEE Transactions on Industry Applications **30**, 835–843 (1994).

[269] A. Nakano and A. Ros, "Protein dielectrophoresis: advances, challenges, and applications," Electrophoresis **34**, 1085–1096 (2013).

[270] N. K. Ibrahim, N. Desai, S. Legha, P. Soon-Shiong, R. L. Theriault, E. Rivera, B. Esmaeli, S. E. Ring, A. Bedikian, G. N. Hortobagyi *et al.*, "Phase i and pharmacokinetic study of abi-007, a cremophor-free, protein-stabilized, nanoparticle formulation of paclitaxel," Clinical Cancer Research **8**, 1038–1044 (2002).

[271] S.-I. Han, Y.-D. Joo, and K.-H. Han, "An electrorotation technique for measuring the dielectric properties of cells with simultaneous use of negative quadrupolar dielectrophoresis and electrorotation," Analyst **138**, 1529–1537 (2013).

[272] G. Fuhr, R. Glaser, and R. Hagedorn, "Rotation of dielectrics in a rotating electric high-frequency field. model experiments and theoretical explanation of the rotation effect of living cells," Biophysical journal **49**, 395–402 (1986).

[273] J. Engel, "Electrorotation of red-cells after electroporation," Stud. Biophys. pp. 53–62 (1988).

[274] S.-B. Huang, Y. Zhao, D. Chen, H.-C. Lee, Y. Luo, T.-K. Chiu, J. Wang, J. Chen, and M.-H. Wu, "A clogging-free microfluidic platform with an incorporated pneumatically driven membrane-based active valve enabling specific membrane capacitance and cytoplasm conductivity characterization of single cells," Sensors and Actuators B: Chemical **190**, 928–936 (2014).

[275] L.-S. Jang and M.-H. Wang, "Microfluidic device for cell capture and impedance measurement," Biomedical microdevices **9**, 737–743 (2007).

[276] V. Velasco, S. Williams, and R. Keynton, "A microfluidic chip for impedance analysis and characterization of human umbilical vein endothelial cells under fluid shear stress," .

[277] J. Chen, Y. Zheng, Q. Tan, Y. L. Zhang, J. Li, W. R. Geddie, M. A. Jewett, and Y. Sun, "A microfluidic device for simultaneous electrical and mechanical measurements on single cells," Biomicrofluidics **5**, 014113 (2011).

[278] R. R. Pethig, "Dielectrophoresis: Theory, methodology and biological applications," (2017).

[279] S. Williams, "Dielectrophoretic motion of particles and cells," Encyclopedia of Microfluidics and Nanofluidics pp. 357–364 (2008).

[280] T. B. Jones, "Basic theory of dielectrophoresis and electrorotation," IEEE Engineering in medicine and Biology Magazine **22**, 33–42 (2003).

[281] H. A. Pohl, "Dielectrophoresis," The behavior of neutral matter in nonuniform electric fields (1978).

[282] M. González, I. Martín-Ruíz, S. Jiménez, L. Pirone, R. Barrio, and J. D. Sutherland, "Generation of stable drosophila cell lines using multicistronic vectors," Scientific reports **1**, 75 (2011).

[283] L. C. Boswell and S. C. Hand, "Intracellular localization of group 3 lea proteins in embryos of artemia franciscana," Tissue and Cell **46**, 514–519 (2014).

[284] F. H. Labeed, H. M. Coley, H. Thomas, and M. P. Hughes, "Assessment of multidrug resistance reversal using dielectrophoresis and flow cytometry," Biophysical journal **85**, 2028–2034 (2003).

[285] S. C. Hand and M. A. Menze, "Molecular approaches for improving desiccation tolerance: insights from the brine shrimp artemia franciscana," Planta **242**, 379–388 (2015).

[286] W. Liang, Y. Zhao, L. Liu, Y. Wang, W. J. Li, and G.-B. Lee, "Determination of cell membrane capacitance and conductance via optically induced electrokinetics," Biophysical journal **113**, 1531–1539 (2017).

[287] R. Pethig, L. Jakubek, R. Sanger, E. Heart, E. D. Corson, and P. J. Smith, "Electrokinetic measurements of membrane capacitance and conductance for pancreatic β-cells," in "IEE Proceedings-Nanobiotechnology," , vol. 152 (IET, 2005), vol. 152, pp. 189–193.

[288] E. A. Henslee, P. Crosby, S. J. Kitcatt, J. S. Parry, A. Bernardini, R. G. Abdallat, G. Braun, H. O. Fatoyinbo, E. J. Harrison, R. S. Edgar *et al.*, "Rhythmic potassium transport regulates the circadian clock in human red blood cells," Nature communications **8**, 1978 (2017).

[289] H. Li, A. Erbas, J. Zwanikken, and M. Olvera de la Cruz, "Ionic conductivity in polyelectrolyte hydrogels," Macromolecules **49**, 9239–9246 (2016).

[290] F. Bordi, R. H. Colby, C. Cametti, L. De Lorenzo, and T. Gili, "Electrical conductivity of polyelectrolyte solutions in the semidilute and concentrated regime: the role of counterion condensation," The Journal of Physical Chemistry B **106**, 6887–6893 (2002).

[291] K. Asami, "Dielectric properties of microvillous cells simulated by the three-dimensional finite-element method," Bioelectrochemistry **81**, 28–33 (2011).

[292] W. R. Loewenstein and Y. Kanno, "Some electrical properties of the membrane of a cell nucleus," Nature **195**, 462 (1962).

[293] A. Irimajiri, K. Asami, T. Ichinowatari, and Y. Kinoshita, "Passive electrical properties of the membrane and cytoplasm of cultured rat basophil leukemia cells. ii. effects of osmotic perturbation," Biochimica et Biophysica Acta (BBA)-Biomembranes **896**, 214–223 (1987).

[294] V. L. Sukhorukov, W. M. Arnold, and U. Zimmermann, "Hypotonically induced changes in the plasma membrane of cultured mammalian cells," The Journal of membrane biology **132**, 27–40 (1993).

[295] X.-B. Wang, Y. Huang, P. R. Gascoyne, F. F. Becker, R. Hölzel, and R. Pethig, "Changes in friend murine erythroleukaemia cell membranes during induced differentiation determined by electrorotation," Biochimica et Biophysica Acta (BBA)-Biomembranes **1193**, 330–344 (1994).

[296] X.-F. Zhou, G. H. Markx, R. Pethig, and I. M. Eastwood, "Differentiation of viable and non-viable bacterial biofilms using electrorotation," Biochimica et Biophysica Acta (BBA)-General Subjects **1245**, 85–93 (1995).

[297] K. F. Hoettges, J. W. Dale, and M. P. Hughes, "Rapid determination of antibiotic resistance in e. coli using dielectrophoresis," Physics in Medicine & Biology **52**, 6001 (2007).

[298] H. Pauly, "Electrical conductance and dielectric constant of the interior of erythrocytes," Nature **183**, 333 (1959).

[299] H. Schwan, "Alternating current spectroscopy of biological substances," Proceedings of the IRE **47**, 1841–1855 (1959).

[300] R. Pethig and D. B. Kell, "The passive electrical properties of biological systems: their significance in physiology, biophysics and biotechnology," Physics in Medicine & Biology **32**, 933 (1987).

[301] L. J. Gentet, G. J. Stuart, and J. D. Clements, "Direct measurement of specific membrane capacitance in neurons," Biophysical journal **79**, 314–320 (2000).

[302] M. Stoneman, A. Chaturvedi, D. Jansma, M. Kosempa, C. Zeng, and V. Raicu, "Protein influence on the plasma membrane dielectric properties: In vivo study utilizing dielectric spectroscopy and fluorescence microscopy," Bioelectrochemistry **70**, 542–550 (2007).

[303] M. Muratore, V. Srsen, M. Waterfall, A. Downes, and R. Pethig, "Biomarker-free dielectrophoretic sorting of differentiating myoblast multipotent progenitor cells and their membrane analysis by raman spectroscopy," Biomicrofluidics **6**, 034113 (2012).

[304] B. Y. Kim, H. Y. Song, M. Y. Kim, B. H. Lee, K. J. Kim, K. J. Jo, S. W. Kim, S. G. Lee, and B. H. Lee, "Distinctive localization of group 3 late embryogenesis abundant synthesizing cells during brine shrimp development," Archives of insect biochemistry and physiology **89**, 169–180 (2015).

[305] M. A. Sharon, A. Kozarova, J. S. Clegg, P. O. Vacratsis, and A. H. Warner, "Characterization of a group 1 late embryogenesis abundant protein in encysted embryos of the brine shrimp artemia franciscana," Biochemistry and Cell Biology **87**, 415–430 (2009).

[306] B. R. Janis, C. A. Elder, J. S. Smith, M. C. Priddy, J. A. Kopechek, and M. A. Menze, "Sonoporation-mediated trehalose loading for red blood cell stabilization," Cryobiology **97**, 273 (2020).

[307] I.-F. Cheng, V. E. Froude, Y. Zhu, H.-C. Chang, and H.-C. Chang, "A continuous high-throughput bioparticle sorter based on 3d traveling-wave dielectrophoresis," Lab on a Chip **9**, 3193–3201 (2009).

[308] X.-B. Wang, J. Yang, Y. Huang, J. Vykoukal, F. F. Becker, and P. R. Gascoyne, "Cell separation by dielectrophoretic field-flow-fractionation," Analytical chemistry **72**, 832–839 (2000).

[309] N. Lewpiriyawong, C. Yang, and Y. C. Lam, "Continuous sorting and separation of microparticles by size using ac dielectrophoresis in a pdms microfluidic device with 3-d conducting pdms composite electrodes," Electrophoresis **31**, 2622–2631 (2010).

[310] H. Morgan, N. G. Green, M. Hughes, W. Monaghan, and T. Tan, "Large-area travelling-wave dielectrophoresis particle separator," Journal of micromechanics and Microengineering **7**, 65 (1997).

[311] E. Choi, B. Kim, and J. Park, "High-throughput microparticle separation using gradient traveling wave dielectrophoresis," Journal of Micromechanics and Microengineering **19**, 125014 (2009).

[312] Y. Kim, J. Lee, Y. Kim, S.-M. Shin, and B. Kim, "Cantilever-type electrode array-based high-throughput microparticle sorting platform driven by gravitation and negative dielectrophoretic force," Journal of Micromechanics and Microengineering **21**, 015015 (2010).

[313] D. Lee, B. Hwang, Y. Choi, and B. Kim, "Negative dielectrophoretic force based cell sorter with simplified structure for high reliability," International Journal of Precision Engineering and Manufacturing **17**, 247–251 (2016).

APPENDIX

Appendix A.1: Commonly Used Acronyms

COF – Cross-Over Frequency
CM – Clausius-Mossotti Factor
DEP – Dielectrophoresis
DEP-FFF – Dielectrophoretic-Field Flow Fractionation
EP – Electrophoresis
ETH – Electrothermal Hydrodynamics
isoDEP – Isomotive Dielectrophoresis
LOC – Lab-On-a-Chip
μ**TAS** – Micro-total Analysis System
MW– Maxwell-Wagner Polarization
nDEP – Negative Dielectrophoretic force
pDEP – Positive Dielectrophoretic force
REP – Rapid Electrokinetic Patterning
SWNTs – Single Walled Nanotubes
TW-DEP – Traveling Wave Dielectrophoresis

Appendix A.2: Nomenclature

Symbol	**Notes**	**Units**
a	Particle radius	m
$\mathbf{E}$	Electric field	V m^{-1}
$E(r,t)$	Applied electric field	V m^{-1}
f	AC frequency	s^{-1} (Hz)
f_{cm}	Clausius-Mossotti factor	
$\mathbf{F}$	Force	N
I	Electric current	Ampere
ϵ_0	Permittivity of free space	F m^{-1}
ϵ_r	Relative permittivity	
$\mathbf{P}$	Dipole moment	C m
α	Polarizability	F m^2
r or R	Inner or Outer radius	m
σ	Conductivity	S m^{-1}
τ	Relaxation time	s
ω	Angular frequency	rad s^{-1}
Ω	Rotation speed	rpm

Appendix B: Research Specific Aims

Table B.1. Research specific aims with the respective tasks to realize each aim/goal as well as the status of each task.

Aims	Tasks	Status
IsoDEP platform optimization	Provide a comprehensive isoDEP review article	maintained
	Design and fabrication of isoDEP device	maintained
	Assess the electrohydrodynamics	maintained
	Scaling law analysis and isoDEP design rules	maintained
	Custom-built high power amplifier at MHz frequencies	maintained
	Integration of tight valve and controlled pumping system	maintained
Characterization of Phytoplankton cells using isoDEPdevice	Demonstrate nDEP & pDEP for phytoplankton cells	maintained
	Extracting cells' Clausius-Mossotti factor (I.e., dielectric properties)	changed*
	Differentiate between nitrogen abundant and defficient cultured phytoplankton cells	changed**
Compare isoDEP contrast with alternative characterization techniques	Characterize LEA proteins roles in dissication tolerence utilizing 3DEP (DEPtech) platfom	maintined
	Characterize Phytoplankton cells utilizing electrochemical impedance spectroscopy	maintined
	Electrorotation single cell characterization	maintined

Where the task labeled with (*) has been changed due to the limitation of isoDEP device to characterize the phytoplankton cells due to their continuous swimming nature. Recall that, for isoDEP device to characterize cells, the particle/cell has to translate across the microchannel under the influence of the DEP force. However, due to the fact that phytoplankton cells are swimmer cells, it has been difficult to relate their translation velocity to DEP force only. It is noted that the same issue has been faced while using the 3DEP (DEPtech, UK) platform.

On the other hand the task labeled with (**) has changed due to the previously mentioned issue regarding the swimming nature of phytoplankton cells. Hence, differentiation between phytoplankton cells cultured in nitrogen abundant and deficient environment was nontrivial. The same issue has been faced when characterizing the phytoplankton cells using EIS-based system. However, differentiation between different phytoplankton species has been achieved utilizing the EIS-based system.

Appendix C: Model Codes

C.1: MATLAB Code for Scaling Law Analysis of IsoDEP Device

```
% This code will produce graphs for electrothermal flow scaling laws
% This code is a part of "Scaling law analysis of electrohydrodynamics and
% dielectrophoresis for isomotive dielectrophoresis microfluidic
% devices"Mohamed Z. Rashed  Nicolas G. Green  Stuart J. Williams"
%Manuscript. Please cite if used.
clear;

%% INPUT values
dia = (1e-6); % diameter of the particle
n = (10); % desired velocity, diameters per second

% ASSUMED values
a = (dia/2); %radius of particle
cm = 0.1; %real part of CM factor
visc = (8.9e-4); %viscosity of fluid
ep = 80*8.854e-12; %permittivity of fluid
cw = 1; %drag factor due to wall

cond = (10e-3); %medium conductivity
M = 6.6; %maximum ET factor, from literature
T = 300; %temperature

kw = 0.6; %thermal conductivity of water
kglass = 1.0; %thermal conductivity of glass
ksi = 150; %thermal conductivity of silion
kpdms = 1.0; %thermal conductivity of PDMS

tlid = 500e-6; %ELECTRODE - thickness of lid/base (assumed symmetric)
twall = 5e-3; %ELECTRODE - thickness between electrode-channel wall and outside

inslid = 0.21e-3; %INSUL - thickness of lid
klid = kpdms; %INSUL - properties of lid
insbase = 1e-3; %INSUL - thickness of base
kbase = kglass; %INSUL - properties of base
```

```
35
36 % RANGE of varied values
37 hmin = 2*dia; %minimum height of channel
38 hmax = 200*dia; %maximum height of channel
39 hstep = 500; %height step
40 hh = logspace(log10(hmin),log10(hmax),hstep);
41
42 r60min = 2*dia; %minimum length scale of channel
43 r60max = 200*dia; %maximum length scale of channel
44 r60step = 500; %length step
45 rr = logspace(log10(r60min),log10(r60max),r60step);
46 [r60,h] = meshgrid(rr,hh);
47
48 Dh = 2*(r60.*h)./(r60+h); %hydraulic diameter
49
50 %% CALCULATIONS
51
52 % Finding k^2
53 k2 = (n*dia)*(3*visc*cw)/(ep*cm*a*a); %k2, from DEP velocity
54
55 % Heating
56 eheat = cond*k2; % joule heating, [W/m3]
57 eeheat = eheat.*r60.*h; % joule heating, [W] per unit depth
58
59
60 % Thermal Resistivity
61 %   x-direciton is the same as channel
62 %   y-direction is same plane as channel
63 %   z-direciton is up/down direction through substrate
64
65 %% MICROELECTRODE Calculations
66 Ry = 0.5*twall./(ksi.*h); %thermal resisitivty through
       electrode wall
67 Rz = 0.5*1./(ksi.*1.685.*(log10(1+(tlid./r60)).^(-0.59).*(
       tlid./h).^(-0.078))); %thermal resistivity through
       substrate
68 %Rych = 0.5*(r60/2)./(h*kw); %thermal resistivity through the
        water channel
69 %Rzch = 0.5*(h/2)./(r60*kw); %thermal resistivity throught
       the water channel
70 %Ryeq = Ry+Rych; % eq resistance in y direction
71 %Rzeq = Rz+Rzch; % eq resistance in z direction
72
73 Ryeq = Ry;
74 Rzeq = Rz;
```

```
75
76 ReqM = Ryeq.*Rzeq./(Ryeq+Rzeq); % eq resistance overall
77
78 TwallM = eeheat.*ReqM; %maximum center temperature(x) (x-
       gradient, *x)
79
80 %   loop to determine Tmax in middle of channel
81 BB = r60./h; %ratio of channel width to height
82 Bstep = 0; %reset value for loop
83 for i = 0:5
84       Bcalc = ((-1)^i)./(((2*i+1).*(pi/2)).^3.*cosh((2*i+1).*(
             pi/2).*BB));
85       Bstep = Bstep + Bcalc; %sum the loop
86 end
87 DTmaxM = (0.5-2*Bstep).*((h/2).^2).*eheat/kw; %calculates the
       temp difference across the channel
88 TmaxM = DTmaxM + TwallM; % Maximum temperature in channel
       center
89
90
91 % TyM = TmaxM./(((r60/2).^2)./(2*kw.*h.*r60.*Ry)+1); %
       temperature at y-wall(x) (x-gradient, *x)
92 % TzM = TmaxM./(((h/2).^2)./(2*kw.*h.*r60.*Rz)+1); %
       temperature at z-wall(x) (x-gradient, *x)
93 %
94 % %   calculations at r = r60
95 % TmaxM60 = TmaxM.*r60;
96 % TyM60 = TyM.*r60;
97 % TzM60 = TzM.*r60;
98 % TcM60 = TyM60.*TzM60./TmaxM60; %estimated temperature at
       the corner
99 %
100 % TgradM1 = (TmaxM60-TyM60)./(r60/2);
101 % TgradM2 = (TzM60-TcM60)./(r60/2);
102
103 % TgradM = (TgradM1+TgradM2)/2;
104
105 TgradM = ((1/2)*(DTmaxM)).*r60 ./ (r60/2);
106
107 DTE2M = TgradM.*k2.*r60; % product of temperature gradient
       and E^2 at r60
108
109
110 %% INSULATIVE Calculations
111 Rlid = 1./(klid.*1.685.*(log10(1+(inslid./r60)).^(-0.59).*(
```

```
    inslid./h).^(-0.078))); %thermal resistivity through the
    lid
112 Rbase = 1./(kbase.*1.685.*(log10(1+(insbase./r60)).^(-0.59)
    .*(insbase./h).^(-0.078)));; %thermal resistivity through
    the base
113 Req = (Rlid.*Rbase)./(Rlid+Rbase); %equivalent thermal
    resistance
114
115 Twallxins = Req.*eeheat; % x-gradient of temperature along
    wall
116
117 %   loop to determine Tmax in middle of channel
118 BB = r60./h; %ratio of channel width to height
119 Bstep = 0; %reset value for loop
120 for i = 0:5
121     Bcalc = ((-1)^i)./(((2*i+1).*(pi/2)).^3.*cosh((2*i+1).*(
        pi/2).*BB));
122     Bstep = Bstep + Bcalc; %sum the loop
123 end
124 DTmaxxins = (0.5-2*Bstep).*((h/2).^2).*eheat/kw; %calculates
    the temp difference across the channel
125 Tmaxxins = DTmaxxins + Twallxins; % Maximum temperature in
    channel center
126
127 TgradI = ((1/3)*(DTmaxxins)+Twallxins) * (2*sin(30*pi/180));
    % temperature gradient for insulator calculations
128
129 DTE2I = TgradI.*k2.*r60; % product of temperature gradient
    and E^2 at r60
130
131
132 %% MICROELECTRODE - velocity
133 vdepM = (n*dia); % DEP velocity
134 fethM = (-1).*(M*ep).*DTE2M./T; % ET body force
135 vethM = 10*fethM.*(Dh.^2)./(32*visc); % ET velocity
136
137
138 %% INSULATIVE - velocity
139 vdepI = vdepM; % DEP velocity
140 fethI = (-1).*(M*ep).*DTE2I./T; %ET body force
141 vethI = fethI.*(Dh.^2)./(32*visc); % ET velocity
142
143
144 %% RESULTS
145 vratioM = abs(vethM)./abs(vdepM); %ratio of velocities
```

```
146 vratioM(vratioM>1) = 10; % replace all values greater than 1
      with 10
147 vratioM(vratioM<0.001) = 0.0001; %replace all values less
      than 0.001 with 0.0001
148
149 vratioI = abs(vethI)./abs(vdepI); %ratio of velocities
150 vratioI(vratioI>1) = 10; % replace all values greater than 1
      with 10
151 vratioI(vratioI<0.001) = 0.0001; %replace all values less
      than 0.001 with 0.0001
152
153
154 %% PLOTS
155
156 figure(1)
157 contourf ((r60/dia), (h/dia), log10(vratioM),[-4, -3, -2, -1,
      0]);
158 colormap(hot)
159 colormap(flipud(colormap))
160 set(gca,'TickDir','out');
161 set(gca,'xscale','log');
162 set(gca,'yscale','log');
163 xlabel('r60 (# particle diameters)');
164 ylabel('h (# particle diameters)');
165 title ('Microelectrode isoDEP device' )
166 saveas(gcf,'(a-12) MicroElectrode isoDEP device.png')
167
168 %%%%%%%%%%%%%%%%%%%%%%%%%%%%%%%%%%%%%%%%%%%%%%%%%%%%
169 figure(2)
170 contourf((r60/dia), (h/dia), log10(vratioI),[-4, -3, -2, -1,
      0]);
171 colormap(hot)
172 colormap(flipud(colormap))
173 set(gca,'TickDir','out');
174 set(gca,'xscale','log');
175 set(gca,'yscale','log');
176 xlabel('r60 (# particle diameters)');
177 ylabel('h (# particle diameters)');
178 title ('Insulative isoDEP device ')
179 saveas(gcf,'(b-12) Insulative isoDEP device.png')
```

C.2: MATLAB Code for Extracting Phytoplankton Cell Properties from Cells in Suspension

```
%% Electrical characterization of phytoplankton suspensions using impedance spectroscopy %%
% Margaret R. Jett1*, Mohamed Z. Rashed1*, Susan P. Hendricks2, and Stuart J. Williams1

%% This code was made based on the previous studies:
%Sun T, Morgan H (2010) Single-cell microfluidic impedance cytometry: a review Microfluid Nanofluid 8:423-443
%Morgan H, Sun T, Holmes D, Gawad S, Green NG (2006) Single cell dielectric spectroscopy Journal of Physics D: Applied Physics 40:61

%% Entering corresponding pre-experimental cell values %%
M=readmatrix('YourData.TXT'); % Name your Impedance Analyzer Output file
Sigma_m=xx*10^-3; % Enter your Medium Conudctivty (S/m)
R=xx*10^-6; % Enter your Cell Radius (m)
d=xx*10^-9; % Enter your Cell Membrane's Thickness (from 4-7 nm)
Frequency=transpose(M(1:201,1)); % Reading the frequency range from the Impedance File
%Note: Change the 201 value based on the range of frequency values you have
w=2*pi*Frequency; % Angular Frequency

Volume_Fraction=xxe6;% Enter your Cell volume fraction
phi=(Volume_Fraction*(4/3)*pi*R^3)/(10^-6); %Cell Density
Geometric_constant=xx/(yy); %Calculate the Geomtric constant (Electrode Area/Gap)

Zmag=M(1:201,2); % Extracting the Impedance Magnitude (Change "201" based on your data)
Zphase=M(205:405,2); % Extracting the Impedance phase (Change "201" based on your data)

%% Solving for single cell parameters %%
Zmix=transpose(Zmag.*(cos(Zphase*pi/180)+j*sin(Zphase*pi/180)));%convert to rectangular form
emix=1./(j*w.*Zmix*2*Geometric_constant); %Calculating permitivity of the cell mixture (Eq. 2)
em=(80*8.854187817*10^-12)-j*(Sigma_m./w); %Permitivity of the aqueous medium
```

```
28
29 eterm=((1-phi)./((em./emix).^(1/3))); %
30 ep=(emix-eterm.*em)./(1-eterm); % Calculating single cell
       permitivity
31
32 gamma=(R+d)/R;
33 k=real(ep)./imag(ep);
34 a=((gamma^3)+2)/((gamma^3)-1);
35 b=(2*(gamma^3)+1)/((gamma^3)-1);
36
37 eq=[transpose(a./w) transpose(-k.*(2-a.*b)) transpose(2*b.*w)
       ];
38
39 %% Calculating the roots of the single cell permitivity
       equation
40 for n=1:201
41     er=eq(n,1:3);
42 l(1:2,n)=roots(er);
43 end
44
45 %% Calculating Single Cell Dielectric Parameters %%
46 for n=1:2 %% Calculating the roots of the single cell
       permitivity equation
47 %You can select one root by changing this value (for example
       n=1)
48 e(n,:)=((b^2+(l(n,:)./w).^2)./((l(n,:)./w).*(2-a*b))).*imag(
       ep); % Single cell frequency dependent relative
       permittivity (?)
49
50 Sigma_i(n,:)=l(n,:).* e(n,:); % Frequency dependent
       cytosplasm Conductivity (?i) (S/m)
51 Cmem(n,:)=e(n,:)./(d); % Specific Membrane Capacitance (F/m
       ^2)
52 Mem_Cap(n,:)=(9*phi*R.*e(n,:)*Geometric_constant)./(4*d); %
       Membrane Capacitance (F)
53 Ri(n,:)=4*((1/(2*Sigma_m))+(1./Sigma_i(n,:)))/(9*phi*G); %
       Frequency dependent Cytoplasm Resistance (Ohm/
54
55 %% Plotting extracted parameters Vs frequency%%
56
57 semilogx(Frequency, Mem_Cap(n,:),'k.');
58 xlabel('Frequency')
59 ylabel('Membrane Capacitance (Mem_Cap) F')
60 figure()
61 semilogx(Frequency, Cmem(n,:),'k.');
```

```
xlabel('Frequency')
ylabel('Specific Membrane Capacitance (Cmem) F/m^2')
figure
semilogx(Frequency, Sigma_i(n,:),'k.');
xlabel('Frequency')
ylabel('Cytoplasm conductivity (Sigma_i) S/m')
figure
semilogx(Frequency, Ri(n,:),'k.');
xlabel('Frequency')
ylabel('Cytolasm Resistance (Ri) Ohms')
end
%% Printing the average values of cell parameters

R1=mean(Ri(1,70:201)); % Average Cytoplasm Resistance (Change
     the starting & Ending frequency)
% R2=mean(Ri(2,190:201));
C1_F_m2=mean(Cmem(1,70:201));% Average Specific Membrane
    Capacitance (Change the starting & Ending frequency)
% C2_F_m2=mean(Cmem(2,70:201));
Sigma_i1=mean(Sigma_i(1,70:201)); % Average Cytoplasm
    Conductivity (Change the starting & Ending frequency)
%Sigma_i2=mean(Sigma_i(2,70:201));
C1_Farad=mean(Mem_Cap(1,70:201)); % Average Membrane
    Capacitance (Change the starting & Ending frequency)
% C2_Farad=mean(Mem_Cap(2,70:201));

T=table( R1, C1_F_m2,C1_Farad, Sigma_i1) % Printing data
    values

%% saving the extracted data for further analysis %%
Cytoplasm_Conductivity=Sigma_i(n,:) ';
Membrane_Capacitance=Mem_Cap(n,:) ';
Membrane_SpecificCapacitance=Cmem(n,:) ';
Relative_Permitivity=e(n,:) ';
Data=table(Cytoplasm_Conductivity,Membrane_Capacitance,
    Membrane_SpecificCapacitance.Relative_Permitivity);

filename = 'CellDataParameter.xlsx';
writetable(Data,filename,'Sheet',1,'Range','A1')

%% Please Cite this manuscript if this code was helpful %%
```

Appendix D: Permissions

SPRINGER NATURE LICENSE
TERMS AND CONDITIONS

Apr 02, 2021

This Agreement between university of louisville -- Mohamed Zakarya Rashed ("You") and Springer Nature ("Springer Nature") consists of your license details and the terms and conditions provided by Springer Nature and Copyright Clearance Center.

License Number	5041120618935
License date	Apr 02, 2021
Licensed Content Publisher	Springer Nature
Licensed Content Publication	Analytical and Bioanalytical Chemistry
Licensed Content Title	Advances and applications of isomotive dielectrophoresis for cell analysis
Licensed Content Author	Mohamed Z. Rashed et al
Licensed Content Date	Apr 15, 2020
Type of Use	Thesis/Dissertation
Requestor type	non-commercial (non-profit)
Format	print and electronic
Portion	full article/chapter
Will you be translating?	no
Circulation/distribution	500 - 999
Author of this Springer Nature content	yes

Title	Isomotive dielectrophoresis for enhanced analyses of cell subpopulations
Institution name	University of Louisville
Expected presentation date	May 2021
Requestor Location	university of louisville mechanical Engineer Dept Sacket Hall 200 LOUISVILLE, KY 40292 United States Attn: UOFL
Total	0.00 USD

Terms and Conditions

Springer Nature Customer Service Centre GmbH
Terms and Conditions

This agreement sets out the terms and conditions of the licence (the **Licence**) between you and **Springer Nature Customer Service Centre GmbH** (the **Licensor**). By clicking 'accept' and completing the transaction for the material (**Licensed Material**), you also confirm your acceptance of these terms and conditions.

1. Grant of License

1. 1. The Licensor grants you a personal, non-exclusive, non-transferable, world-wide licence to reproduce the Licensed Material for the purpose specified in your order only. Licences are granted for the specific use requested in the order and for no other use, subject to the conditions below.

1. 2. The Licensor warrants that it has, to the best of its knowledge, the rights to license reuse of the Licensed Material. However, you should ensure that the material you are requesting is original to the Licensor and does not carry the copyright of another entity (as credited in the published version).

1. 3. If the credit line on any part of the material you have requested indicates that it was reprinted or adapted with permission from another source, then you should also seek permission from that source to reuse the material.

2. Scope of Licence

2. 1. You may only use the Licensed Content in the manner and to the extent permitted by these Ts&Cs and any applicable laws.

2. 2. A separate licence may be required for any additional use of the Licensed Material, e.g. where a licence has been purchased for print only use, separate permission must be obtained for electronic re-use. Similarly, a licence is only valid in the language selected and does not apply for editions in other languages unless additional translation rights have been granted separately in the licence. Any content

owned by third parties are expressly excluded from the licence.

2. 3. Similarly, rights for additional components such as custom editions and derivatives require additional permission and may be subject to an additional fee. Please apply to Journalpermissions@springernature.com/bookpermissions@springernature.com for these rights.

2. 4. Where permission has been granted **free of charge** for material in print, permission may also be granted for any electronic version of that work, provided that the material is incidental to your work as a whole and that the electronic version is essentially equivalent to, or substitutes for, the print version.

2. 5. An alternative scope of licence may apply to signatories of the STM Permissions Guidelines, as amended from time to time.

3. Duration of Licence

3. 1. A licence for is valid from the date of purchase ('Licence Date') at the end of the relevant period in the below table:

Scope of Licence	Duration of Licence
Post on a website	12 months
Presentations	12 months
Books and journals	Lifetime of the edition in the language purchased

4. Acknowledgement

4. 1. The Licensor's permission must be acknowledged next to the Licenced Material in print. In electronic form, this acknowledgement must be visible at the same time as the figures/tables/illustrations or abstract, and must be hyperlinked to the journal/book's homepage. Our required acknowledgement format is in the Appendix below.

5. Restrictions on use

5. 1. Use of the Licensed Material may be permitted for incidental promotional use and minor editing privileges e.g. minor adaptations of single figures, changes of format, colour and/or style where the adaptation is credited as set out in Appendix 1 below. Any other changes including but not limited to, cropping, adapting, omitting material that affect the meaning, intention or moral rights of the author are strictly prohibited.

5. 2. You must not use any Licensed Material as part of any design or trademark.

5. 3. Licensed Material may be used in Open Access Publications (OAP) before publication by Springer Nature, but any Licensed Material must be removed from OAP sites prior to final publication.

6. Ownership of Rights

6. 1. Licensed Material remains the property of either Licensor or the relevant third party and any rights not explicitly granted herein are expressly reserved.

7. Warranty

IN NO EVENT SHALL LICENSOR BE LIABLE TO YOU OR ANY OTHER PARTY OR ANY OTHER PERSON OR FOR ANY SPECIAL, CONSEQUENTIAL, INCIDENTAL OR INDIRECT DAMAGES, HOWEVER CAUSED, ARISING OUT OF OR IN CONNECTION WITH THE DOWNLOADING, VIEWING OR USE OF THE MATERIALS REGARDLESS OF THE FORM OF ACTION, WHETHER FOR BREACH OF CONTRACT, BREACH OF WARRANTY, TORT, NEGLIGENCE, INFRINGEMENT OR OTHERWISE (INCLUDING, WITHOUT LIMITATION, DAMAGES BASED ON LOSS OF PROFITS, DATA, FILES, USE, BUSINESS OPPORTUNITY OR CLAIMS OF THIRD PARTIES), AND
WHETHER OR NOT THE PARTY HAS BEEN ADVISED OF THE POSSIBILITY OF SUCH DAMAGES. THIS LIMITATION SHALL APPLY NOTWITHSTANDING ANY FAILURE OF ESSENTIAL PURPOSE OF ANY LIMITED REMEDY PROVIDED HEREIN.

8. Limitations

8. 1. ***BOOKS ONLY:*** Where **'reuse in a dissertation/thesis'** has been selected the following terms apply: Print rights of the final author's accepted manuscript (for clarity, NOT the published version) for up to 100 copies, electronic rights for use only on a personal website or institutional repository as defined by the Sherpa guideline (www.sherpa.ac.uk/romeo/).

8. 2. For content reuse requests that qualify for permission under the STM Permissions Guidelines, which may be updated from time to time, the STM Permissions Guidelines supersede the terms and conditions contained in this licence.

9. Termination and Cancellation

9. 1. Licences will expire after the period shown in Clause 3 (above).

9. 2. Licensee reserves the right to terminate the Licence in the event that payment is not received in full or if there has been a breach of this agreement by you.

Appendix 1 — Acknowledgements:

For Journal Content:
Reprinted by permission from [**the Licensor**]: [**Journal Publisher** (e.g. Nature/Springer/Palgrave)] [**JOURNAL NAME**] [**REFERENCE CITATION** (Article name, Author(s) Name), [**COPYRIGHT**] (year of publication)

For **Advance Online Publication papers:**
Reprinted by permission from [**the Licensor**]: [**Journal Publisher** (e.g. Nature/Springer/Palgrave)] [**JOURNAL NAME**] [**REFERENCE CITATION** (Article name, Author(s) Name), [**COPYRIGHT**] (year of publication), advance online publication, day month year (doi: 10.1038/sj.[JOURNAL ACRONYM].)

For Adaptations/Translations:
Adapted/Translated by permission from [**the Licensor**]: [**Journal Publisher** (e.g. Nature/Springer/Palgrave)] [**JOURNAL NAME**] [**REFERENCE CITATION** (Article name, Author(s) Name), [**COPYRIGHT**] (year of publication)

Note: For any republication from the British Journal of Cancer, the following credit line style applies:

Reprinted/adapted/translated by permission from [**the Licensor**]: on behalf of Cancer Research UK: : [**Journal Publisher** (e.g. Nature/Springer/Palgrave)] [**JOURNAL NAME**] [**REFERENCE CITATION** (Article name, Author(s) Name), [**COPYRIGHT]** (year of publication)

For **Advance Online Publication** papers:
Reprinted by permission from The [**the Licensor**]: on behalf of Cancer Research UK: [**Journal Publisher** (e.g. Nature/Springer/Palgrave)] [**JOURNAL NAME**] [**REFERENCE CITATION** (Article name, Author(s) Name), [**COPYRIGHT**] (year of publication), advance online publication, day month year (doi: 10.1038/sj. [JOURNAL ACRONYM])

For Book content:
Reprinted/adapted by permission from [**the Licensor**]: [**Book Publisher** (e.g. Palgrave Macmillan, Springer etc) [**Book Title**] by [**Book author**(s)] [**COPYRIGHT**] (year of publication)

Other Conditions:

Version 1.3

Questions? customercare@copyright.com or +1-855-239-3415 (toll free in the US) or +1-978-646-2777.

JOHN WILEY AND SONS LICENSE
TERMS AND CONDITIONS

Apr 02, 2021

This Agreement between university of louisville -- Mohamed Zakarya Rashed ("You") and John Wiley and Sons ("John Wiley and Sons") consists of your license details and the terms and conditions provided by John Wiley and Sons and Copyright Clearance Center.

License Number	5041120845379
License date	Apr 02, 2021
Licensed Content Publisher	John Wiley and Sons
Licensed Content Publication	Electrophoresis
Licensed Content Title	Scaling law analysis of electrohydrodynamics and dielectrophoresis for isomotive dielectrophoresis microfluidic devices
Licensed Content Author	Stuart J. Williams, Nicolas G. Green, Mohamed Z. Rashed
Licensed Content Date	Nov 11, 2019
Licensed Content Volume	41
Licensed Content Issue	1-2
Licensed Content Pages	8
Type of use	Dissertation/Thesis
Requestor type	Author of this Wiley article

Format	Print and electronic
Portion	Full article
Will you be translating?	No
Title	Isomotive dielectrophoresis for enhanced analyses of cell subpopulations
Institution name	University of Louisville
Expected presentation date	May 2021
Requestor Location	university of louisville mechanical Engineer Dept Sacket Hall 200 LOUISVILLE, KY 40292 United States Attn: UOFL
Publisher Tax ID	EU826007151
Total	0.00 USD

Terms and Conditions

TERMS AND CONDITIONS

This copyrighted material is owned by or exclusively licensed to John Wiley & Sons, Inc. or one of its group companies (each a"Wiley Company") or handled on behalf of a society with which a Wiley Company has exclusive publishing rights in relation to a particular work (collectively "WILEY"). By clicking "accept" in connection with completing this licensing transaction, you agree that the following terms and conditions apply to this transaction (along with the billing and payment terms and conditions established by the Copyright Clearance Center Inc., ("CCC's Billing and Payment terms and conditions"), at the time that you opened your RightsLink account (these are available at any time at http://myaccount.copyright.com).

Terms and Conditions

- The materials you have requested permission to reproduce or reuse (the "Wiley Materials") are protected by copyright.
- You are hereby granted a personal, non-exclusive, non-sub licensable (on a stand-alone basis), non-transferable, worldwide, limited license to reproduce the Wiley Materials for the purpose specified in the licensing process. This license, **and any CONTENT (PDF or image file) purchased as part of your order,** is for a one-time

use only and limited to any maximum distribution number specified in the license. The first instance of republication or reuse granted by this license must be completed within two years of the date of the grant of this license (although copies prepared before the end date may be distributed thereafter). The Wiley Materials shall not be used in any other manner or for any other purpose, beyond what is granted in the license. Permission is granted subject to an appropriate acknowledgement given to the author, title of the material/book/journal and the publisher. You shall also duplicate the copyright notice that appears in the Wiley publication in your use of the Wiley Material. Permission is also granted on the understanding that nowhere in the text is a previously published source acknowledged for all or part of this Wiley Material. Any third party content is expressly excluded from this permission.

- With respect to the Wiley Materials, all rights are reserved. Except as expressly granted by the terms of the license, no part of the Wiley Materials may be copied, modified, adapted (except for minor reformatting required by the new Publication), translated, reproduced, transferred or distributed, in any form or by any means, and no derivative works may be made based on the Wiley Materials without the prior permission of the respective copyright owner.**For STM Signatory Publishers clearing permission under the terms of the STM Permissions Guidelines only, the terms of the license are extended to include subsequent editions and for editions in other languages, provided such editions are for the work as a whole in situ and does not involve the separate exploitation of the permitted figures or extracts,** You may not alter, remove or suppress in any manner any copyright, trademark or other notices displayed by the Wiley Materials. You may not license, rent, sell, loan, lease, pledge, offer as security, transfer or assign the Wiley Materials on a stand-alone basis, or any of the rights granted to you hereunder to any other person.

- The Wiley Materials and all of the intellectual property rights therein shall at all times remain the exclusive property of John Wiley & Sons Inc, the Wiley Companies, or their respective licensors, and your interest therein is only that of having possession of and the right to reproduce the Wiley Materials pursuant to Section 2 herein during the continuance of this Agreement. You agree that you own no right, title or interest in or to the Wiley Materials or any of the intellectual property rights therein. You shall have no rights hereunder other than the license as provided for above in Section 2. No right, license or interest to any trademark, trade name, service mark or other branding ("Marks") of WILEY or its licensors is granted hereunder, and you agree that you shall not assert any such right, license or interest with respect thereto

- NEITHER WILEY NOR ITS LICENSORS MAKES ANY WARRANTY OR REPRESENTATION OF ANY KIND TO YOU OR ANY THIRD PARTY, EXPRESS, IMPLIED OR STATUTORY, WITH RESPECT TO THE MATERIALS OR THE ACCURACY OF ANY INFORMATION CONTAINED IN THE MATERIALS, INCLUDING, WITHOUT LIMITATION, ANY IMPLIED WARRANTY OF MERCHANTABILITY, ACCURACY, SATISFACTORY QUALITY, FITNESS FOR A PARTICULAR PURPOSE, USABILITY, INTEGRATION OR NON-INFRINGEMENT AND ALL SUCH WARRANTIES ARE HEREBY EXCLUDED BY WILEY AND ITS LICENSORS AND WAIVED BY YOU.

- WILEY shall have the right to terminate this Agreement immediately upon breach of this Agreement by you.

- You shall indemnify, defend and hold harmless WILEY, its Licensors and their respective directors, officers, agents and employees, from and against any actual or threatened claims, demands, causes of action or proceedings arising from any breach of this Agreement by you.

- IN NO EVENT SHALL WILEY OR ITS LICENSORS BE LIABLE TO YOU OR ANY OTHER PARTY OR ANY OTHER PERSON OR ENTITY FOR ANY SPECIAL, CONSEQUENTIAL, INCIDENTAL, INDIRECT, EXEMPLARY OR

PUNITIVE DAMAGES, HOWEVER CAUSED, ARISING OUT OF OR IN CONNECTION WITH THE DOWNLOADING, PROVISIONING, VIEWING OR USE OF THE MATERIALS REGARDLESS OF THE FORM OF ACTION, WHETHER FOR BREACH OF CONTRACT, BREACH OF WARRANTY, TORT, NEGLIGENCE, INFRINGEMENT OR OTHERWISE (INCLUDING, WITHOUT LIMITATION, DAMAGES BASED ON LOSS OF PROFITS, DATA, FILES, USE, BUSINESS OPPORTUNITY OR CLAIMS OF THIRD PARTIES), AND WHETHER OR NOT THE PARTY HAS BEEN ADVISED OF THE POSSIBILITY OF SUCH DAMAGES. THIS LIMITATION SHALL APPLY NOTWITHSTANDING ANY FAILURE OF ESSENTIAL PURPOSE OF ANY LIMITED REMEDY PROVIDED HEREIN.

- Should any provision of this Agreement be held by a court of competent jurisdiction to be illegal, invalid, or unenforceable, that provision shall be deemed amended to achieve as nearly as possible the same economic effect as the original provision, and the legality, validity and enforceability of the remaining provisions of this Agreement shall not be affected or impaired thereby.

- The failure of either party to enforce any term or condition of this Agreement shall not constitute a waiver of either party's right to enforce each and every term and condition of this Agreement. No breach under this agreement shall be deemed waived or excused by either party unless such waiver or consent is in writing signed by the party granting such waiver or consent. The waiver by or consent of a party to a breach of any provision of this Agreement shall not operate or be construed as a waiver of or consent to any other or subsequent breach by such other party.

- This Agreement may not be assigned (including by operation of law or otherwise) by you without WILEY's prior written consent.

- Any fee required for this permission shall be non-refundable after thirty (30) days from receipt by the CCC.

- These terms and conditions together with CCC's Billing and Payment terms and conditions (which are incorporated herein) form the entire agreement between you and WILEY concerning this licensing transaction and (in the absence of fraud) supersedes all prior agreements and representations of the parties, oral or written. This Agreement may not be amended except in writing signed by both parties. This Agreement shall be binding upon and inure to the benefit of the parties' successors, legal representatives, and authorized assigns.

- In the event of any conflict between your obligations established by these terms and conditions and those established by CCC's Billing and Payment terms and conditions, these terms and conditions shall prevail.

- WILEY expressly reserves all rights not specifically granted in the combination of (i) the license details provided by you and accepted in the course of this licensing transaction, (ii) these terms and conditions and (iii) CCC's Billing and Payment terms and conditions.

- This Agreement will be void if the Type of Use, Format, Circulation, or Requestor Type was misrepresented during the licensing process.

- This Agreement shall be governed by and construed in accordance with the laws of the State of New York, USA, without regards to such state's conflict of law rules. Any legal action, suit or proceeding arising out of or relating to these Terms and Conditions or the breach thereof shall be instituted in a court of competent jurisdiction in New York County in the State of New York in the United States of America and each party hereby consents and submits to the personal jurisdiction of such court, waives any objection to venue in such court and consents to service of process by registered or

certified mail, return receipt requested, at the last known address of such party.

WILEY OPEN ACCESS TERMS AND CONDITIONS

Wiley Publishes Open Access Articles in fully Open Access Journals and in Subscription journals offering Online Open. Although most of the fully Open Access journals publish open access articles under the terms of the Creative Commons Attribution (CC BY) License only, the subscription journals and a few of the Open Access Journals offer a choice of Creative Commons Licenses. The license type is clearly identified on the article.

The Creative Commons Attribution License

The Creative Commons Attribution License (CC-BY) allows users to copy, distribute and transmit an article, adapt the article and make commercial use of the article. The CC-BY license permits commercial and non-

Creative Commons Attribution Non-Commercial License

The Creative Commons Attribution Non-Commercial (CC-BY-NC)License permits use, distribution and reproduction in any medium, provided the original work is properly cited and is not used for commercial purposes.(see below)

Creative Commons Attribution-Non-Commercial-NoDerivs License

The Creative Commons Attribution Non-Commercial-NoDerivs License (CC-BY-NC-ND) permits use, distribution and reproduction in any medium, provided the original work is properly cited, is not used for commercial purposes and no modifications or adaptations are made. (see below)

Use by commercial "for-profit" organizations

Use of Wiley Open Access articles for commercial, promotional, or marketing purposes requires further explicit permission from Wiley and will be subject to a fee.

Further details can be found on Wiley Online Library
http://olabout.wiley.com/WileyCDA/Section/id-410895.html

Other Terms and Conditions:

v1.10 Last updated September 2015

Questions? customercare@copyright.com or +1-855-239-3415 (toll free in the US) or +1-978-646-2777.

SPRINGER NATURE LICENSE
TERMS AND CONDITIONS

Apr 02, 2021

This Agreement between university of louisville -- Mohamed Zakarya Rashed ("You") and Springer Nature ("Springer Nature") consists of your license details and the terms and conditions provided by Springer Nature and Copyright Clearance Center.

License Number	5041130046195
License date	Apr 02, 2021
Licensed Content Publisher	Springer Nature
Licensed Content Publication	Journal of Applied Phycology
Licensed Content Title	Electrical characterization of phytoplankton suspensions using impedance spectroscopy
Licensed Content Author	Margaret R. Jett et al
Licensed Content Date	Feb 9, 2021
Type of Use	Thesis/Dissertation
Requestor type	academic/university or research institute
Format	print and electronic
Portion	full article/chapter
Will you be translating?	no
Circulation/distribution	20000 - 49999
Author of this Springer Nature content	yes

Title	Isomotive dielectrophoresis for enhanced analyses of cell subpopulations
Institution name	University of Louisville
Expected presentation date	May 2021
Requestor Location	university of louisville mechanical Engineer Dept Sacket Hall 200 LOUISVILLE, KY 40292 United States Attn: UOFL
Total	0.00 USD

Terms and Conditions

Springer Nature Customer Service Centre GmbH
Terms and Conditions

This agreement sets out the terms and conditions of the licence (the **Licence**) between you and **Springer Nature Customer Service Centre GmbH** (the **Licensor**). By clicking 'accept' and completing the transaction for the material (**Licensed Material**), you also confirm your acceptance of these terms and conditions.

1. Grant of License

1. 1. The Licensor grants you a personal, non-exclusive, non-transferable, world-wide licence to reproduce the Licensed Material for the purpose specified in your order only. Licences are granted for the specific use requested in the order and for no other use, subject to the conditions below.

1. 2. The Licensor warrants that it has, to the best of its knowledge, the rights to license reuse of the Licensed Material. However, you should ensure that the material you are requesting is original to the Licensor and does not carry the copyright of another entity (as credited in the published version).

1. 3. If the credit line on any part of the material you have requested indicates that it was reprinted or adapted with permission from another source, then you should also seek permission from that source to reuse the material.

2. Scope of Licence

2. 1. You may only use the Licensed Content in the manner and to the extent permitted by these Ts&Cs and any applicable laws.

2. 2. A separate licence may be required for any additional use of the Licensed Material, e.g. where a licence has been purchased for print only use, separate permission must be obtained for electronic re-use. Similarly, a licence is only valid in the language selected and does not apply for editions in other languages unless additional translation rights have been granted separately in the licence. Any content

owned by third parties are expressly excluded from the licence.

2. 3. Similarly, rights for additional components such as custom editions and derivatives require additional permission and may be subject to an additional fee. Please apply to Journalpermissions@springernature.com/bookpermissions@springernature.com for these rights.

2. 4. Where permission has been granted **free of charge** for material in print, permission may also be granted for any electronic version of that work, provided that the material is incidental to your work as a whole and that the electronic version is essentially equivalent to, or substitutes for, the print version.

2. 5. An alternative scope of licence may apply to signatories of the STM Permissions Guidelines, as amended from time to time.

3. Duration of Licence

3. 1. A licence for is valid from the date of purchase ('Licence Date') at the end of the relevant period in the below table:

Scope of Licence	Duration of Licence
Post on a website	12 months
Presentations	12 months
Books and journals	Lifetime of the edition in the language purchased

4. Acknowledgement

4. 1. The Licensor's permission must be acknowledged next to the Licenced Material in print. In electronic form, this acknowledgement must be visible at the same time as the figures/tables/illustrations or abstract, and must be hyperlinked to the journal/book's homepage. Our required acknowledgement format is in the Appendix below.

5. Restrictions on use

5. 1. Use of the Licensed Material may be permitted for incidental promotional use and minor editing privileges e.g. minor adaptations of single figures, changes of format, colour and/or style where the adaptation is credited as set out in Appendix 1 below. Any other changes including but not limited to, cropping, adapting, omitting material that affect the meaning, intention or moral rights of the author are strictly prohibited.

5. 2. You must not use any Licensed Material as part of any design or trademark.

5. 3. Licensed Material may be used in Open Access Publications (OAP) before publication by Springer Nature, but any Licensed Material must be removed from OAP sites prior to final publication.

6. Ownership of Rights

6. 1. Licensed Material remains the property of either Licensor or the relevant third party and any rights not explicitly granted herein are expressly reserved.

7. Warranty

IN NO EVENT SHALL LICENSOR BE LIABLE TO YOU OR ANY OTHER PARTY OR ANY OTHER PERSON OR FOR ANY SPECIAL, CONSEQUENTIAL, INCIDENTAL OR INDIRECT DAMAGES, HOWEVER CAUSED, ARISING OUT OF OR IN CONNECTION WITH THE DOWNLOADING, VIEWING OR USE OF THE MATERIALS REGARDLESS OF THE FORM OF ACTION, WHETHER FOR BREACH OF CONTRACT, BREACH OF WARRANTY, TORT, NEGLIGENCE, INFRINGEMENT OR OTHERWISE (INCLUDING, WITHOUT LIMITATION, DAMAGES BASED ON LOSS OF PROFITS, DATA, FILES, USE, BUSINESS OPPORTUNITY OR CLAIMS OF THIRD PARTIES), AND
WHETHER OR NOT THE PARTY HAS BEEN ADVISED OF THE POSSIBILITY OF SUCH DAMAGES. THIS LIMITATION SHALL APPLY NOTWITHSTANDING ANY FAILURE OF ESSENTIAL PURPOSE OF ANY LIMITED REMEDY PROVIDED HEREIN.

8. Limitations

8. 1. ***BOOKS ONLY:*** Where **'reuse in a dissertation/thesis'** has been selected the following terms apply: Print rights of the final author's accepted manuscript (for clarity, NOT the published version) for up to 100 copies, electronic rights for use only on a personal website or institutional repository as defined by the Sherpa guideline (www.sherpa.ac.uk/romeo/).

8. 2. For content reuse requests that qualify for permission under the STM Permissions Guidelines, which may be updated from time to time, the STM Permissions Guidelines supersede the terms and conditions contained in this licence.

9. Termination and Cancellation

9. 1. Licences will expire after the period shown in Clause 3 (above).

9. 2. Licensee reserves the right to terminate the Licence in the event that payment is not received in full or if there has been a breach of this agreement by you.

Appendix 1 — Acknowledgements:

For Journal Content:
Reprinted by permission from [**the Licensor**]: [**Journal Publisher** (e.g. Nature/Springer/Palgrave)] [**JOURNAL NAME**] [**REFERENCE CITATION** (Article name, Author(s) Name), [**COPYRIGHT**] (year of publication)

For **Advance Online Publication papers:**
Reprinted by permission from [**the Licensor**]: [**Journal Publisher** (e.g. Nature/Springer/Palgrave)] [**JOURNAL NAME**] [**REFERENCE CITATION** (Article name, Author(s) Name), [**COPYRIGHT**] (year of publication), advance online publication, day month year (doi: 10.1038/sj.[JOURNAL ACRONYM].)

For Adaptations/Translations:
Adapted/Translated by permission from [**the Licensor**]: [**Journal Publisher** (e.g. Nature/Springer/Palgrave)] [**JOURNAL NAME**] [**REFERENCE CITATION** (Article name, Author(s) Name), [**COPYRIGHT**] (year of publication)

Note: For any republication from the British Journal of Cancer, the following credit line style applies:

Reprinted/adapted/translated by permission from [**the Licensor**]: on behalf of Cancer Research UK: : [**Journal Publisher** (e.g. Nature/Springer/Palgrave)] [**JOURNAL NAME**] [**REFERENCE CITATION** (Article name, Author(s) Name), [**COPYRIGHT]** (year of publication)

For **Advance Online Publication** papers:
Reprinted by permission from The [**the Licensor**]: on behalf of Cancer Research UK: [**Journal Publisher** (e.g. Nature/Springer/Palgrave)] [**JOURNAL NAME**] [**REFERENCE CITATION** (Article name, Author(s) Name), [**COPYRIGHT**] (year of publication), advance online publication, day month year (doi: 10.1038/sj. [JOURNAL ACRONYM])

For Book content:
Reprinted/adapted by permission from [**the Licensor**]: [**Book Publisher** (e.g. Palgrave Macmillan, Springer etc) [**Book Title**] by [**Book author**(s)] [**COPYRIGHT**] (year of publication)

Other Conditions:

Version 1.3

Questions? customercare@copyright.com or +1-855-239-3415 (toll free in the US) or +1-978-646-2777.

On-chip technology for single-cell arraying, electrorotation-based analysis and selective release

Author: Kevin Keim, Mohamed Z. Rashed, Samuel C. Kilchenmann, et al

Publication: Electrophoresis

Publisher: John Wiley and Sons

Date: Jun 3, 2019

AIP PUBLISHING LICENSE
TERMS AND CONDITIONS

Apr 02, 2021

This Agreement between university of louisville -- Mohamed Zakarya Rashed ("You") and AIP Publishing ("AIP Publishing") consists of your license details and the terms and conditions provided by AIP Publishing and Copyright Clearance Center.

License Number	5041121135105
License date	Apr 02, 2021
Licensed Content Publisher	AIP Publishing
Licensed Content Publication	Biomicrofluidics
Licensed Content Title	New insights into anhydrobiosis using cellular dielectrophoresis-based characterization
Licensed Content Author	Mohamed Z. Rashed, Clinton J. Belott, Brett R. Janis, et al
Licensed Content Date	Nov 1, 2019
Licensed Content Volume	13
Licensed Content Issue	6
Type of Use	Thesis/Dissertation
Requestor type	Author (original article)
Format	Print and electronic
Portion	Excerpt (> 800 words)

Will you be translating?	No
Title	Isomotive dielectrophoresis for enhanced analyses of cell subpopulations
Institution name	University of Louisville
Expected presentation date	May 2021
Portions	Full article including figures and Tables.
Requestor Location	university of louisville mechanical Engineer Dept Sacket Hall 200 LOUISVILLE, KY 40292 United States Attn: UOFL
Total	0.00 USD

Terms and Conditions

AIP Publishing -- Terms and Conditions: Permissions Uses

AIP Publishing hereby grants to you the non-exclusive right and license to use and/or distribute the Material according to the use specified in your order, on a one-time basis, for the specified term, with a maximum distribution equal to the number that you have ordered. Any links or other content accompanying the Material are not the subject of this license.

1. You agree to include the following copyright and permission notice with the reproduction of the Material:"Reprinted from [FULL CITATION], with the permission of AIP Publishing." For an article, the credit line and permission notice must be printed on the first page of the article or book chapter. For photographs, covers, or tables, the notice may appear with the Material, in a footnote, or in the reference list.
2. If you have licensed reuse of a figure, photograph, cover, or table, it is your responsibility to ensure that the material is original to AIP Publishing and does not contain the copyright of another entity, and that the copyright notice of the figure, photograph, cover, or table does not indicate that it was reprinted by AIP Publishing, with permission, from another source. Under no circumstances does AIP Publishing purport or intend to grant permission to reuse material to which it does not hold appropriate rights.
   You may not alter or modify the Material in any manner. You may translate the Material into another language only if you have licensed translation rights. You may not use the Material for promotional purposes.
3. The foregoing license shall not take effect unless and until AIP Publishing or its agent, Copyright Clearance Center, receives the Payment in accordance with Copyright Clearance Center Billing and Payment Terms and Conditions, which are incorporated herein by reference.

4. AIP Publishing or Copyright Clearance Center may, within two business days of granting this license, revoke the license for any reason whatsoever, with a full refund payable to you. Should you violate the terms of this license at any time, AIP Publishing, or Copyright Clearance Center may revoke the license with no refund to you. Notice of such revocation will be made using the contact information provided by you. Failure to receive such notice will not nullify the revocation.
5. AIP Publishing makes no representations or warranties with respect to the Material. You agree to indemnify and hold harmless AIP Publishing, and their officers, directors, employees or agents from and against any and all claims arising out of your use of the Material other than as specifically authorized herein.
6. The permission granted herein is personal to you and is not transferable or assignable without the prior written permission of AIP Publishing. This license may not be amended except in a writing signed by the party to be charged.
7. If purchase orders, acknowledgments or check endorsements are issued on any forms containing terms and conditions which are inconsistent with these provisions, such inconsistent terms and conditions shall be of no force and effect. This document, including the CCC Billing and Payment Terms and Conditions, shall be the entire agreement between the parties relating to the subject matter hereof.

This Agreement shall be governed by and construed in accordance with the laws of the State of New York. Both parties hereby submit to the jurisdiction of the courts of New York County for purposes of resolving any disputes that may arise hereunder.

V1.2

Questions? customercare@copyright.com or +1-855-239-3415 (toll free in the US) or +1-978-646-2777.

CURRICULUM VITA

Name	Mohamed Zakarya Rashed
Address	Schumaker Research Building, RM 221
	University of Louisville
	2210 S Brook St, Louisville, KY 40208
Birth Place	Egypt

Education

2016–2021	Ph.D. in Electrical and Computer Engineering, University of Louisville, USA.
2012–2014	M.Sc. in Nanotechnologies for ICTs, Politecnico Di Torino, Italy.
2006–2011	B. Sc. in Electronics & Telecommunication Engineering, Mansoura University, Egypt.

Professional Positions

DEC 2018–MAY 2019	Visiting researcher at CLSE Lab, EPFL, Lausanne, Switzerland.
OCT 2011–June 2012 NOV 2014–Dec 2015	Teaching Assistant in electronics engineering Mansoura University, Egypt.
SEP 2015–July 2016	Startup member of the online advertisement platform (Luanco.de). Berlin, Germany.

Honors and Awards

Awarded NSF Innovation Corps Grant
Received Doctoral Dissertation Completion Award , $6,000, Spring 2020
Awarded University Graduate Student Research Fund, $300, Fall 2017 & Spring 2019.
Awarded KY Multiscale fund, $1200, Summer 2019.
Awarded AiChe Society Travel Fund, $550, Fall 2017.

Publications

2021 MR Jett, MZ Rashed, SP Hendricks, SJ Williams,
"Electrical characterization of phytoplankton suspensions using impedance spectroscopy," *Journal of Applied Phycology (DOI:10.1007/s10811-020-02363-2).*

2020 MZ Rashed, JA Kopechek, MC Priddy, KT Hamorsky, KE Palmer, N Mittal, J Valdez, J Flynn, SJ Williams,
"Rapid detection of SARS-CoV-2 antibodies using electrochemical impedance-based detector," *Biosensors and Bioelectronics (doi.org/10.1016/j.bios.2020.112709)*

MZ Rashed and SJ Williams,
"Review: Advances and Applications of isomotive Dielectrophoresis" *Analytical and Bioanalytical Chemistry (DOI: 10.1007/s00216-020-02590-z)*

AD Carrithers, MJ Brown VI, MZ Rashed, S Islam, OD Velev, and SJ Williams,
"Multiscale Self-Assembly of Distinctive Weblike Structures from Evaporated Drops of Dilute American Whiskeys," *ACS Nano (DOI:https://doi.org/10.1021/acsnano.9b08984)*

2019 MZ Rashed, CJ Belott, BR Janis, MA Menze, and SJ Williams,
"New insights into anhydrobiosis using cellular dielectrophoresis-based characterization," *Biomicrofluidics (DOI:10.1063/1.5126810).*

MZ Rashed, NG Green, and SJ Williams, **"Scaling law analysis of electro-hydrodynamics and dielectrophoresis for isomotive dielectrophoresis, microfluidic devices,"** *Electrophoresis, (DOI: 10.1002/elps.201900311).*

K Keim, MZ Rashed, SC Kilchenmann, AG Delattre, A. F Goncalves,

P Ery, and C Guiducci.**"On-chip technology for single-cell arraying, electrorotation-based analysis and selective release."** *Electrophoresis,* 40(14), pp.1830-1838.

2018 MZ Rashed, V Velasco, and SJ Williams,
"Advances and applications of Rapid Electrokinetic Patterning,"
J INDIAN I SCI, 98(2), 85-101.

Full-Length Peer-Reviewed Conference Papers

2020 | MZ Rashed, JA Kopechek, MC Priddy, KT Hamorsky, KE Palmer, N Mittal, J Valdez, J Flynn, SJ Williams, **"Electrochemical impedance-based detector for SARS-CoV-2 antibodies,"** *International Conference on Miniaturized Systems for Chemistry and Life Sciences (μTAS2020),* Virtual Oct. 4-9, 2020.

2019 | K. Keim, M. Rashed, C. Guiducci, **"Resolution on membrane changes and influences on cell viability of a parallelized electrorotation platform,"** *Proc. 23rd International Conference on Miniaturized Systems for Chemistry and Life Sciences (μTAS2019)*, Basel, Switzerland Oct. 27-31, 2019.

K Keim, MZ Rashed, C Guiducci, **"A parallelized in flow electrorotation platform with individual control on the trapping and release of single cells,"** *Proc. 23rd International Conference on Miniaturized Systems for Chemistry and Life Sciences (μTAS2018)*, Kaohsiung, Taiwan, Nov. 11-15, 2018.

2018 | MZ Rashed, CJ Belott, MA Menze, and SJ Williams, **"Dielectrophoresis based characterization of lEA proteins",** *Proc. 22nd International Conference on Miniaturized Systems for Chemistry and Life Sciences (μTAS2017)*,Savannah, GA WA, Oct. 22-26, 2017.

2017 | MZ Rashed, KC Grome, G Gasser, SP Hendricks, and SJ Williams, **"Comprehensive single cell dielectric spectroscopy using , isomotive dielectrophoresis (isoDEP),"** *Proc. 21st International Conference on Miniaturized Systems for Chemistry and Life Sciences (μTAS2017)*, Savannah, GA WA, Oct. 22-26, 2017.

Conference Abstracts, Conference Posters, and Invited Presentations

2020 MZ Rashed, JA Kopechek, MC Priddy, KT Hamorsky, KE Palmer, N Mittal, J Valdez, J Flynn, SJ Williams, **"Electrochemical impedance-based detector for SARS-CoV-2 antibodies,"** *International Conference on Miniaturized Systems for Chemistry and Life Sciences (μTAS2020),* Virtual Oct. 4-9, 2020.

K. Keim M. Rashed, J. Beech, W. Labbichi, T. Ryser, G. Porro, P. Thiriet, J, Tegenefeldt, C. Guiducci, **"Simultaneous use of metal coated three-dimensional SU-8 pillars as passive posts and electrodes,"** *Proc. 24th International Conference on Miniaturized Systems for Chemistry and Life Sciences (μTAS2020),* Virtual Oct. 4-9, (Poster). K. Keim presented.

T. Ryser K. Keim M. Rashed, W. Labbichi, A. Mahul-Mellier, H. Lashuel, C. Guiducci, **"Electrorotation for single cell analysis of membrane damage induced by toxins mimicking the neurodegenerative effect of amyloid beta in the Alzheimer's disease,"** *Dielectrophoresis*, Flagstaff AK, USA.(Oral) T. Ryser presented.

2019 K Keim, MZ Rashed, C Guiducci, **"A parallelized in flow electrorotation platform with individual control on the trapping and release of single cells,"** *Proc. 23rd International Conference on Miniaturized Systems for Chemistry and Life Sciences (μTAS2019)*, Palm Springs, California Oct. 13-18, 2019 (Oral). K. Keim presented.

MZ Rashed, CJ Belott, MA Menze, and SJ Williams, **"Dielectrophoresis based characterization of lEA proteins",** *2019 Colloid & Surface Science Symposium* Atlanta, GA, June 16-19, 2019. (Oral)

MR Jett, K Henson, MZ Rashed, SP Hendricks, SJ Williams, **"Impedance "spectroscopy-based evaluation of phytoplankton health"** *2019 Colloid & Surface Science Symposium*, Atlanta, GA, June 16-19, 2019. (Oral)

MZ Rashed, CJ Belott, MA Menze, and SJ Williams, **"Dielectrophoresis based characterization of lEA proteins",** *13th International Symposium on Electrokinetics (ELKIN)* MIT, Boston, MA June 12-14, 2019. (Oral)

2019 MZ Rashed, NG Green, and SJ Williams, **"Electrohydrodynamic scaling laws analysis in a microfluidic isoDEP device",** *International Symposium on Electrokinetics (ELKIN)* MIT, Boston, MA June 12-14, 2019. (Poster)

MR Jett, K Henson, MZ Rashed, SP Hendricks, SJ Williams, **"Impedance spectroscopy-based evaluation of phytoplankton health",** *Kentucky Water Resources Annual Symposium*, Lexington, KY, March 23, 2019 (Poster).

2018 MZ Rashed, CJ Belott, MA Menze, and SJ Williams, **"Dielectrophoresis based characterization of lEA proteins",** *Dielectrophoresis*, Surrey, UK, July 23-25, 2018 (Poster).

MZ Rashed, SP Hendricks, SJ Williams, **"Dielectrophoresis-based characterization of phytoplankton cells"** *Dielectrophoresis*, Surrey, UK, July 23-25, 2018 (Poster).

MZ Rashed, KC Grome, SP Hendricks, SJ Williams, **"Isomotive dielectrophoresis-based characterization of chlamydomonas cells",** *Kentucky Water Resources Annual Symposium*, Lexington, KY, March 19, 2018 (Poster).

MZ Rashed, KC Grome, SP Hendricks, SJ Williams, **"Isomotive dielectrophoresis-based characterization of chlamydomonas cells",** *Graduate Student Regional Research Conference*, Louisville, KY, March 2-3 2018 (Oral).

2017 MZ Rashed, KC Grome, SP Hendricks, SJ Williams, **"Isomotive dielectrophoresis-based characterization of chlamydomonas cells,"** textitAIChE *Annual Meeting of the American Electrophoresis Society*, Minneapolis, MN, Oct. 29-Nov. 3, 2017 (Oral).

MZ Rashed, KC Grome, SJ Williams, **"Electrohydrodynamic scaling laws analysis in a microfluidic isoDEP device",** *AIChE Annual Meeting of the American Electrophoresis Society*, Minneapolis, MN, Oct. 29-Nov. 3, 2017 (Poster).